Imperial College London

Department of Earth Science and Engineering

The influence of inherited structural relief on the architecture of early post-rift deepwater systems

Timothy James Lewis Wigan

Submitted in partial fulfilment of the requirements for the degree of Doctor of Philosophy (PhD)

March 2025

To anyone who has been told they cannot achieve something due to a learning disability. Remember that your learning disability does not define you, nor does it limit your potential.

The copyright of this thesis rests with the author. Unless otherwise indicated, its contents are licensed under a Creative Commons Attribution-Non Commercial 4.0 International Licence (CC BY-NC). Under this licence, you may copy and redistribute the material in any medium or format. You may also create and distribute modified versions of the work. This is on the condition that: you credit the author and do not use it, or any derivative works, for a commercial purpose. When reusing or sharing this work, ensure you make the licence terms clear to others by naming the licence and linking to the licence text. Where a work has been adapted, you should indicate that the work has been changed and describe those changes. Please seek permission from the copyright holder for uses of this work that are not included in this licence or permitted under UK Copyright Law.

Declaration

The work presented below is produced by the author unless where otherwise cited. The material contained has not been previously submitted to this or any other institution.

Timothy J.L. Wigan

Abstract

Deep-water submarine fans represent the largest sediment accumulations on Earth and serve as key reservoirs for hydrocarbons and carbon storage. Their morphology and architecture are strongly influenced by interactions with topography, particularly in rift basins where inherited structural relief affects sediment routing and deposition. However, uncertainties remain regarding how syn-rift topography controls the distribution and evolution of deep-water systems during early post-rift basin infill. This study investigates two contrasting early post-rift deep-water systems: the Angel Formation (North West Shelf, Australia) and the Agat Formation (North Sea, Norway). An integrated approach utilizing 3D seismic reflection, well logs, core data, and spectral reflectance analysis provides insights into sediment distribution from basin to bed scale. Results indicate that the degree of basin infill critically controls channel and lobe deposition. In underfilled basins, fault topography strongly influences sediment entry points and sandstone distribution, resulting in sand-rich lobe complexes that abruptly pinch out against fault scarps. Pinch-out rates vary due to rugose topography, but compensational stacking increases as the basin fills. In more infilled basins, direct fault interactions are less pronounced, but fault topography exerts a lasting influence by generating compaction hinges over buried faults. These hinges impact sediment pathways, with their effects varying according to fault geometry and throw. This research underscores the role of inherited structural relief in shaping deep-water deposits and highlights the importance of basin-fill state at rift cessation in controlling early post-rift sedimentation. These findings enhance our ability to predict reservoir architecture and connectivity in rift basins, with implications for hydrocarbon exploration and carbon sequestration.

Acknowledgements

I would like to express my sincere gratitude and acknowledgement to the individuals and organisations who have played a significant role in the completion of my PhD. Their guidance, support, and encouragement have been invaluable throughout this journey.

I would like to thank my primary investigator, Chris Jackson, for his exceptional guidance and support. Chris your expertise and mentorship have been instrumental in shaping my understanding of geology/geoscience and life, and for that I am truly grateful. I would also like to extend my gratitude to my Lobe3 supervisors, Dave Hodgson, Ian Kane, and Steve Flint. Our extensive discussions on the Lobe3 field workshops have been enlightening experiences that I will always cherish. Your valuable insights and feedback have significantly contributed to the success of my research. A special thank you goes to Howard Johnson, who joined the project midway. Howard, your drive and wisdom have had a profound impact on improving the quality and the actual completion of my research.

To my peers at Imperial College, Joe, Mike, Sian, Bailey, Andy, Kartik, David, Aurio, Harya, Nan, Sinead, and Ahmed, I would like to express my appreciation for the thoughtful discussions we shared, your support and maintaining my sanity during this project. I am also indebted to everyone involved in the Basins Research Group for their support and constructive criticism during our weekly seminars. To my fellow Lobe3 students, Ander and Zoë, I want to express my gratitude for your companionship and support. Your distant presence and collaboration have been essential in reaching this milestone.

I am deeply grateful to my sponsors, AkerBP, bp, Equinor, Hess, Neptune Energy, Petrobras, PetroChina, Total, Vår Energi, and Woodside, without which this project would not have been possible.

To my wife, Rosie, and my sons, Alfred and Edward, I want to express my heartfelt appreciation for your unwavering love and understanding. Your sacrifices and encouragement have allowed me to focus on this project, even during extremely challenging times. I promise to make up for the lost time and holidays, and I am truly grateful for your support. To my parents, including my parents, Mum, Dad, Sacha and my rother Chris, I want to thank you for your unending support throughout this endeavour. Lastly, I would like to express my gratitude to my late grandmother, 'Dita.' I am deeply grateful for her support in helping me get to a position where I could pursue a PhD. Her presence is missed, but her impact on my life and academic journey will always be remembered.

Contents

1 Introduction 1

1.1 Rationale 1

1.2 Research Aims and Objectives 2

1.2.1 How can early post-rift inherited structural relief effect the architecture and distribution of lobes? 3

1.2.2 How do sand-rich lobes pinch out against post-rift topography? 4

1.2.3 How can inherited early post-rift structural relief effect the architecture and routing of channels? 4

1.3 Thesis Overview 5

2 Literature Review 7

2.1 Introduction 7

2.2 Sediment gravity flows 10

2.3 Deepwater Lobes 12

2.3.1 Lobe sub-environments 13

2.4 Deep-water systems in rift basins 15

3 Submarine lobe complex distribution and pinch out styles: an example from the early post-rift Angel Formation, NW Shelf Australia 19

3.1 Abstract 19

3.2 Introduction 20

3.3 Tectonostratigraphic evolution of the Dampier Sub-basin 23

3.4 Controls on deepwater deposits 23

3.4.1 Late Triassic – Middle Jurassic (Syn-rift) 24

3.4.2 Late Jurassic - Early Cretaceous (Post-rift) 24

3.4.3 Angel Formation 25

3.5 Data and methodology 25

3.5.1 Seismic reflection data 26

3.5.2 Core data 26

3.5.3 Well-log data 27
3.5.4 Palynology data 27
3.5.5 Architectural elements 28
3.6 Results 29
3.6.1 Tectono-stratigraphic Evolution 29
3.6.2 Sedimentary facies analysis and well-log response 34
3.6.3 Facies associations: sedimentology, distribution and petrophysics 39
3.6.4 Vertical and lateral relationships between facies association 45
3.6.5 Lateral rates of change 50
3.6.6 Sandstone distribution 51
3.7 Discussion 57
3.7.1 Controls on depositional patterns 57
3.7.2 Pinch out style and rates 59
3.8 Conclusions 61
4 The curious case of the missing thin-beds: discriminating between lobe fringe environments and hemipelagic drapes in intensely bioturbated successions using reflectance spectroscopy 62
4.1 Abstract 62
4.2 Introduction 63
4.3 Geological context 64
4.4 Data and Methods 65
4.5 Results 68
4.5.1 Spectral reflectance 68
4.5.2 Comparison to previous studies (as above) 69
4.5.3 Thermal infrared (TIR) classification 70
4.5.4 Depositional environments 71
4.6 Discussion 73
4.6.1 Application to deepwater siliciclastics 73

4.6.2 Reconstruction of thin beds 73
4.6.3 Distribution 74
4.7 Conclusion 75
5 Factors controlling deep-water sediment routing and facies variations in the early post-rift – a case study of the Lower Cretaceous Agat Formation, North Sea, Norway 77
5.1 Abstract 77
5.2 Introduction 78
5.3 Geological setting 80
5.3.1 Paleogeography and stratigraphy of the Aptian-Albian 83
5.4 Data and methodology 85
5.5 Agat seismic character and distribution 85
5.5.1 The Lower Agat Horizon 88
5.5.2 The Upper Agat Horizon 90
5.6 Topographic controls 90
5.7 Well Correlation 93
5.8 Southern Agat Formation sedimentology 96
5.8.1 Well 36/7-4 97
5.8.2 Well 35/9-3T2 100
5.8.3 Facies Associations 102
5.9 The Agat Depositional model 103
5.10 Conclusions 104
6 Discussion & Conclusion 106
6.1 How does inherited structural relief effect the architecture and distribution of sand-rich lobes? 106
6.2 How does topography effect the sand pinch out in sand-rich lobes? 107
6.3 How does inherited structural relief effect the architecture and distribution of channels? 108
6.4 Controls on early post-rift deep water architecture 109

6.5 Proposal for future work 111
6.5.1 Investigation of the suitability of the Angel Formation for carbon storage..... 111
6.5.2 Quantitative assessment of pinch out geometry in sand reservoirs. 112
6.5.3 Expand the application of reflectance spectroscopy 113
6.6 Conclusion..... 113
7 References 116

List of Tables

Table 3.1: Core facies table..... 35
Table 3.2: Transition matrix of facies associations..... 48
Table 3.3: Lateral rates of change of sand units between wells along D-D'. ROC is calculated towards the pinchout i.e from Bounty-2. E.G. Mutineer-2 ROC is from Mutineer-1B to Mutineer-2. Orange indicates maximum rate of change. Green indicates minimum rate of change. 49
Table 4.1: Selected points for comparison of thin-section (T-S), X-Ray Diffraction (XRD),shortwave infrared (SWIR) and thermal infrared spectral reflectance(TIR) results. Results are limited in the SWIR and TIR by what minerals are detectable in that spectrum (NR = Not readable), therefore they are relativistic and not absolute values. For example, Wanaea-1, 2833.6m, 30% Tourmaline does not reflect the actual sample is 70% tourmaline but of the few minerals recordable in the SWIR spectrum &0% has been recorded as Tourmaline but it is overall dominated by carbonates. 69
Table 5.1: Agat Formation facies table. 96

List of Figures

Fig. 1.1: Outline of thesis structure, highlighting key questions, with bullet points highlighting key links between chapters. 3
Fig. 2.1: Examples of deepwater systems and their geomorphic features on varying slope complexities (Brooks et al., 2018b) 8
Fig. 2.2: Idealised examples of deepwater deposits, linking depositional process to associated deposits (adapted from Kane and Clare, 2019)..... 9

Fig. 2.3: Summary of low- and high-density turbidity currents and their associated deposits (from Talling et al. 2012).....10
Fig. 2.4: Lobe architecture and hierarchy in (A) unconfined and (B) confined settings, illustrating variations in compensational and aggradation stacking and lateral termination style. C) Sediment gravity flow types and their flow characteristics and resulting interaction with topography and onlap style (from Fuhrmann et al., 2022). 12
Fig. 2.5: Schematic lobe illustrating locations of various sub-environments and compensational stacking patterns (from Hansen et al., 2019). 14
Fig. 2.6: Illustration of idealised seismic cross-section through a half-graben. Rift initiation is equivalent to early syn-rift, rift-climax is equivalent of late syn-rift. (From Prosser, 1993)...16
Fig. 2.7: Schematic diagram of deep-water sedimentation influenced by inherited fault scarp with sea floor expression in the Cromarty area (From Law et al. 2000). 17
Fig. 2.8: Schematic diagrams of various North Sea post-rift deep-water depositional systems with controlling processes illustrated. 1-2) illustrate systems directly interacting with inherited syn-rift topography. 3-8) are systems not in the immediate post-rift that are still influenced by inherited syn-rift topography (not to scale) From Martinsen et al. 2005.....18
Fig. 3.1: Location of the study area. A) Regional map of the NW shelf, Australia. Red indicates Dampier sub-basin, white box indicate area shown in B & C. B) Structural element map of the Dampier sub-basin, structural blocks in grey (modified from Lech, 2013; Spencer et al., 1992) with key seismic reflection surveys in blue and secondary (used for basin cross-sections) seismic reflection surveys in red. Sub-basin boundary purple dashed line. **C)** Well location map, colour indicated data available; green – core and well-logs, orange wells – core only, pink – well-logs only. **D)** Zoomed in well location map for the Mutineer & Exeter area. A-A' and B-'B displayed in Fig. 3.3.....21
Fig. 3.2: A) Stratigraphy of the Lower Jurassic to Lower Cretaceous succession of the Dampier sub-basin (modified from Geoscience Australia, 2021), megasequences from Deng and McClay (2020), with seismic horizons used in this study. B) Late Jurassic paleogeography of the Northern Carnarvon Basin. 22
Fig. 3.3: Line A-A', NW-SE seismic cross-section of the Dampier sub-basin in the northern section of the study area (see Fig. 3.1B for location). Line B-B'; NW-SE seismic cross-section in the central part of the study area. The Angel Formation lies between H2 and H3. Line locations illustrated in Fig. 3.1B. 30
Fig 3.4: A-E) Depth structure maps of Horizon (H) 1-5. F-I) Isochron maps of Seismic unit (SU) 1-4. Contours at 40 m intervals. Map show a combined surface across two key surveys,

white dashed line shows the survey join. Discrepancies across the surveys are due to the processing differences between the two surveys. 32
Fig. 3.5: A) Biostratigraphic zonation scheme used based off Bint and Marshall, (1991) and Helby et al., (2004), sub-zones are ca. <250,000 years. B) Intervals used in this study next to an example Gamma Ray log. C) Location of cored interval in proportion to bio 33
Fig. 3.6: Representative core facies images with a pie chart highlighting the facies proportions of total core thickness 36
Fig. 3.7: Summary of petrophysical properties of cored interval of Angel Fm. facies highlighting the skew of data towards massive and dewatered sandstone and bioturbated heterolithics, and the challenge in distinguishing the limited depositional variability across the Angel Fm. 38
Fig. 3.8: A) Facies make up of facies associations. B) Correlated core cross-section through the Dampier sub-basin (NE-SW) with interpreted facies associations. Sand bodies are not correlated due to distance between wells. 40
Fig. 3.9: Base Angel Fm. surface highlighting location of cores and the relative thickness of the cored intervals and facies association proportions.....41
Fig. 3.10: A) Enlarged base Angel Fm. (H2) depth map of the Mutineer area (Fig. 3.1D). Dashed lines indicate underlying normal faults. B) Isochron thickness map of SU2. C-C'; seismic cross section from Norfolk North 1 to Bounty 3. D-D' seismic cross section from Mutineer 2 to Bounty 2. Wells showing gamma ray logs are tied to seismic, wells without sonic logs are shown as an approximate location (black line). Horizons are colour-coded, as shown in Fig. 3.3. 43
Fig. 3.11: Correlated well cross-section of Fig. 3.10 C-C' of SU2 (yellow to green horizons). Biostratigraphic zones are correlated using palynology sample points (black diamonds) and are colour-coded by palynological subzones (as Fig. 3.5). Flattened on top of Tithonian-aged sandstone. Palynology and gamma ray characteristics were used to correlate sandstones where possible. Possible advancing pinch out in Biozone 3 and compensational stacking in Biozone 4.....44
Fig. 3.12: Correlated well cross-section of Fig. 11 D-D' of SU2 (Green to red/yellow horizons.. Biostratigraphic zones are correlated using palynology sample points (black diamonds) and are colour coded by palynological subzone (as Fig. 6). Flattened on top Tithonian-aged sandstone. Palynology and gamma ray characteristics used to correlate sandstones where possible. 46

Fig. 3.13: Mutineer pinch-out in 3-dimensions highlighting the changes in sub-environment and stacking pattern. Dotted colours lines relate to biostratigraphic intervals, colour coded to Fig. 3.6. 47
Fig. 3.14: Lateral thickness changes of lobe complexes (Units) in Mutineer area highlighting rapid variations in thickness. Unit relative thicknesses displayed. Basal gradients in red. Total sandstone thickness in grey with sandstone percentage. Numbered lines correspond to Unit numbers as in Fig. 3.12 and 3.13. 50
Fig. 3.15: A) Base Angel Fm. surface (H2), B) Angel formation isochron (SU2). Highlighting location of wells that fully intersect the whole Angel Formation interval, identifying their thickness and sand percentage. 52
Fig. 3.16: Base Angel Fm. surface (H2) with wells log sand percentage for each biostratigraphic interval. This includes maps covering the total basin-fill (c. 110 x 45 km) and an enlargement of the more densely drilled northeastern area (Mutineer-Bounty area, c. 25 x 17 km). 54
Fig. 3.17: Paleogeographic maps of the Angel Formation. Interpretation is based on Fig. 3.16 with sub-environments loosely based on facies associations. Sub-environments transitions are shown with hard boundaries but are likely to be more gradual. 55
Fig. 3.18: Summary of sand-rich lateral punchout against a basin margin (cf. Fig.2.4) 60
Fig. 4.1: A) Location map of study area, NW Shelf Australia. White box shows location of B) Map of Dampier sub-basin illustrating main structural features modified from Spencer et al 1992. C) Stratigraphic column of Dampier basin. Angel Formation highlighted in orange. ..64
Fig. 4.2: Results panel from Mutineer-1B showing core images, core log, alongside visible to near infrared (VNIR), shortwave infrared (SWIR) and thermal infrared (TIR) mineral assemblages. Pie charts showing type relative proportion distribution across the three studied wells. VNIR and SWIR is limited in minerals detectable. Core image A) = Type 1, B) Type 2A, C) Type 3 and D), dark mudrock = Type 4.....66
Fig. 4.3: Results panel for Wanaea-1, showing core log alongside HyLogger-3TM results and core images of key TIR types. Core image A: ungraded medium grained massive sandstone with Type 1 TIR response, B: Mottled bioturbated heterolithics with Type 2A TIR response, C: Mottled bioturbated heterolithics with Type 3 TIR response, D) Bioturbated mudrock with type 4 TIR response. 67
Fig. 4.4: Detailed results from Mutineer-1B (3136.22-3136.35m; 0.13m thick) Type 2A showing every sample reading at 4mm intervals. Interpreted core image shows a possible interpretation for reconstructed thin beds. 70

Fig. 4.5: Detailed reconstruction of heavily bioturbated interval from Mutineer-1B with an interpreted depositional environment. Core log key and TIR colours as in Fig. 4.2. Red beds indicate post-depositional injections. P = Pyrite. 74
Fig. 5.1: Location map Northern North Sea. Well locations (yellow) and main Cretaceous structures and faults shown. Seismic surveys outlined in red. Modified from Jackson et al., (2021). A-A', B-B', C-C' dipslayed on Fig. 5.8. D-D' dipalyed on Fig. 5.9. 79
Fig. 5.2: Stratigraphic column of the Måløy Slope with interpreted seismic horizons. Intermediate horizons between H2 & H1 were picked locally aid interpretation. Modified from Jackson et al.,(2021). Additional seismic horizons colours correlate to Figs. 5.3 & 5.10..... 80
Fig 5.3:Seismic cross section of the North of the study area highlighting the main tectonic structures and seismic horizons H2 not shown due to overlap and proximity to H3. Main structural features are the Måløy Slope, Sogn Graben and Tampen Spur. 81
Fig. 5.4: Current understanding of spatial distribution of sand fairways of the Agat Formation, as mapped in (A) Bugge et al., (2001), (B) Martinsen et al., (2005), and (C) Jackson et al., (2021). Black dashed line highlights the Agat sediments deposited on the Måløy Slope . GG= Gjøa Graben, GFZ = Gjøa Fault Zone 84
Fig. 5.5: Key seismic horizon surfaces and isochrons. Key basement faults are identified in the basement surface. 86
Fig. 5.6: Seismic facies present across the Agat isochrone. Red = positive hard kick. SF1 displays the GR log for 36/7-4, SF2 displays the GR for well 35/6-2S. Sf3 displays the GR log for 35/9-3T2. See fig 5.1 for well locations. 87
Fig. 5.7: RMS amplitude maps (A &D) and spectral decomposition (B&E) of the upper (A,B &C) and lower Agat (D,E,&F) Interpretations assisted by seismic facies analysis. 89
Fig. 5.8: Fence diagram showing path of channel in Southern area viewing down depositional dip. Location of lines displayed on Fig 5.1. Top of seismic lines cut at -2100ms..... 91
Fig. 5.9: Close up of the southern area covering the Gjøa Graben, highlighting location of channel thalwegs (green) and fault interpretation from Reeve et al, (2015). A) basement surface (ms), B) Agat isochrone (ms), C) RMS Amplitude, D) Spectral decomposition, E) basement faults with channel thalwegs, F) throw-distance profile of the Gjøa Fault Zone Fig. 5B from Reeve et al., (2015). D-D' Line location for Fig. 5.11. 92
Fig. 5.10: Seismic cross-section across Gjoa Graben. Colours are as Fig. 5.7. Note pinching and swelling in Agat Formation (Yellow) West to the left of the image. Red reflection = red hard kick..... 94

Fig 5.11: Modified from Jackson et al. (2021). Seismic line of cross section is displayed in Fig. 5.9. Core sections displayed in Fig. 5.13 and Appendix 5.....95
Fig. 5.12: Facies images, see Table 1 for full description.....97
Fig. 5.13: Condensed logged core intervals with interpreted facies associations. See Appendix 4 for complete logs.....98
Fig. 5.14: Facies association composition of the cored wells. Facies <1% not labelled.....100
Fig. 6.1: Schematic illustration of key early-post rift tectonics and influences on deep-water sedimentation.....110

1 Introduction

1.1 Rationale

Seafloor topography plays a significant role in shaping the pathways and depocenters of deep-water sediment gravity flows. As a result of this influence, the morphology and architecture of resulting deposits can differ significantly from similar but more unconfined systems, highlighting the importance of a detailed understanding of the impact of seafloor topography on sediment gravity flows in predicting the characteristics and distribution of deep-water deposits. Ancient deposits in the subsurface often act as reservoirs for hydrocarbons, have the potential for carbon sequestration. Whereas modern sediment gravity flows pose a significant geohazard to offshore infrastructure. Moreover, recent studies have recognised their capacity to transport anthropogenic pollutants to deep-water environments (e.g. Kane & Clare, 2019). Therefore, understanding the impact of seafloor topography on deep-water deposits is critical for predicting the reservoir distribution in subsurface geology and anticipating the distribution of potential pollutants on the modern seafloor.

The morphology of the seafloor is shaped by a complex interplay of geological processes, including tectonic deformation (pre- or syndepositional), as well as the influence of existing sediment in a basin. For instance, mass transport deposits, salt or mud kinematics, and lithological variations which can generate relief or variations in sediment thickness, leading to differential compaction and ultimately affecting the seafloor morphology. Understanding these processes and their impact is important for paleogeographic reconstruction and identifying potential reservoirs.

We define the early post-rift, as the phase in an extensional basin where fault growth has ceased or has starting to cease in the area of deep-water deposition (as often fault death is not instantaneous across a basin). In this early-post-rift phase the failed rift basin still has an expression on the seafloor topography, before complete burial and the commencement of the sag phase. This early post-rift stage offers a unique timespan in which significant tectonic-related topography exists with limited to no structural movement. The degree to which the fault-related topography will be affected depends upon the relationship between the rate of subsidence and the rate of sedimentation. Often these basins can be underfilled at this stage (subsidence has outpaced sedimentation) and therefore the basin will have a significant water depth and a complex seabed topography with exposed faults and/or topographic highs on horst

blocks or crests of rotated fault blocks (*sensu* Gabrielsen *et al.*, 2001; incipient post-rift). Even if the basin is filled or into the (*sensu* Gabrielsen *et al.*, 2001; middle post-rift), a greater amount of compaction commonly will occur within the grabens compared to the basement highs causing subtle rift-related topography. This early post-rift phase also offers relatively quiescent period where sedimentation patterns are not affected by fault growth, enabling the study of deep-water sediment gravity flows interacting with relatively 'static' topography and improve understanding of how deep-water sediments heal topography. Early post-rift deep water systems contain proven prolific reservoirs (e.g. Angel Formation, Dampier-Sub-basin) and are a current focus for hydrocarbon resource renewal and may house sites for carbon storage (e.g. Angel Formation, Dampier-Sub-basin and Kopervik Sandstone, Captain Field, North Sea).

Numerous idealised geometries of sandstone pinch outs against topography have been suggested (e.g. Bakke *et al.*, 2013), however relatively little quantification of the rates at which sandstones pinch out has been published. Quantification of pinch outs are typically limited to outcrop which may lack the wider context and only measured in 2-dimensions or calculated at a seismic scale which lacks sedimentological detail (Marini *et al.*, 2015; Nagatomo & Archer, 2015; Fryer & Jobe, 2019; Hansen *et al.*, 2019; Kus *et al.*, 2021). These pinch out zones can impact the sandstone proportion and quality of reservoirs (e.g. Bell *et al*., 2018), and understanding the rates at which they occur can aid in identifying and predicting the location and characteristics of reservoirs. By integrating various scales of subsurface datasets, such as well logs and seismic reflection attributes, geoscientists can identify, and map facies distributions more accurately and better understand the subsurface geology of a given area. This can help in identifying and targeting potential reservoirs with preferential characteristics, such as good porosity and permeability or increase reservoir volumes. This in turn may lead to improved future well placement and therefore limit seal penetrations, which important for preventing leaks and ensuring reservoir integrity especially for carbon sequestration, thereby minimising potential environmental damage.

1.2 Research Aims and Objectives

This thesis focuses on three main questions (Fig. 1) with the goal of improving the understanding of how deep-water sediment gravity flows interact with inherited topography. Central to these questions is how inherited tectonic relief affects the architecture and distribution of channel and lobe systems, and how inherited relief affects the sand pinch-out zone. These questions will be addressed at a range of scales, from the basin-scale down to sandstone composition.

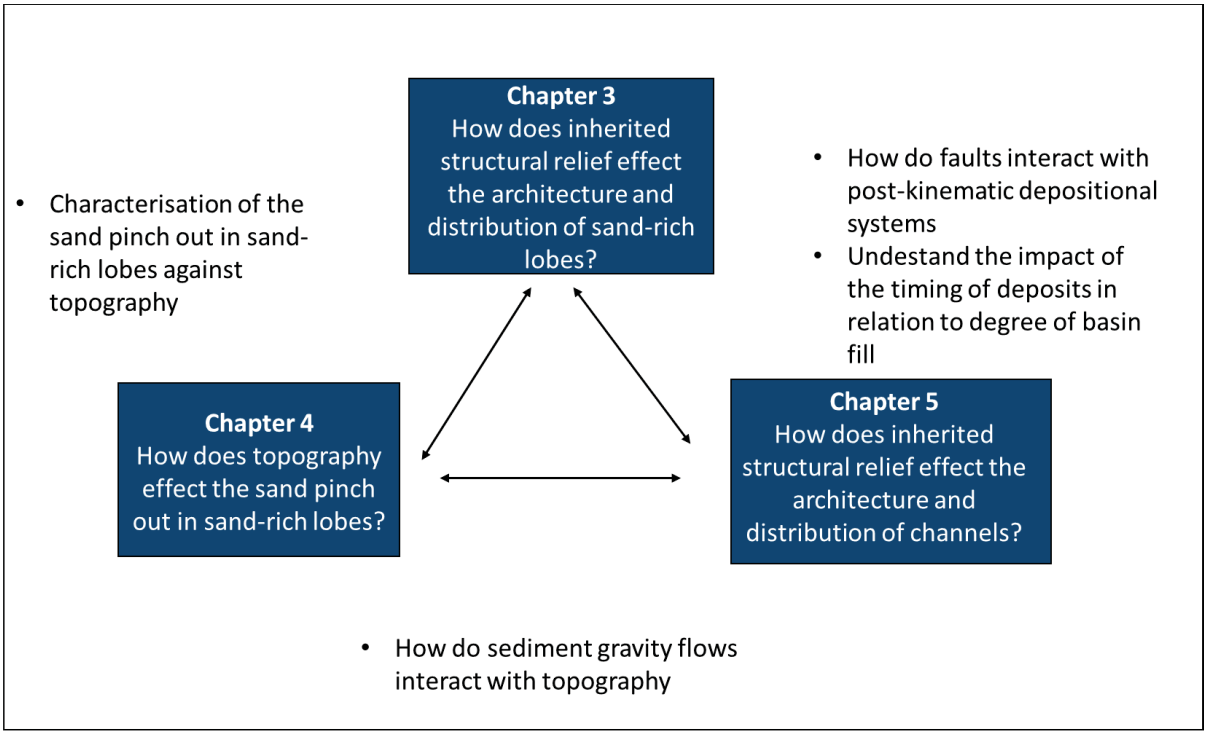


***Fig. 1.1**: Outline of thesis structure, highlighting key questions, with bullet points highlighting key links between chapters.*

1.2.1 How can early post-rift inherited structural relief effect the architecture and distribution of lobes?

Aims:

- Determine the controls on depositional patterns within structurally confined lobe complexes and how inherited topography is healed.
- Quantify how a lobe complex pinches out against topography.

Objectives: These aims will be achieved using an integrated dataset of core, well logs, palynology and 3D seismic reflection data of the Angel Formation, Dampier sub-basin, NW Shelf Australia, a deep water lobe system at an economic burial depth.

- Analyses the basin structure and timing of rifting using seismic reflection data.
- Characterise the Angel Formation using core logging to determine the lithology, texture, bed thicknesses and stacking patterns.
- Identify a suitable location to evaluate the lateral variations in sedimentology at a lateral pinch out against topography using well cross section constrained by palynology.
- Apply sedimentological interpretations tied into seismic reflection data to understand the distribution of facies and the effect of paleotopography on lobe complex distribution.

- Develop gross depositional environment maps to show key depocenters and sediment routing.

1.2.2 How do sand-rich lobes pinch out against post-rift topography?

Aims:

- Test the application of reflectance spectroscopy in deep water clastic systems.
- Determine the origin of the heavily bioturbated heterolithic facies observed in the Angel Formation.
- Investigate how confinement affects the lobe fringe sub-environment.

Objectives:

- Compare reflectance spectroscopy results to mineralogical data sets typically utilised in the subsurface to assess accuracy.
- Identify mineral abundances and assemblages that may define different lobe sub-environments.
- Add these newly identified sub-environments to improve my prior interpretation how lateral facies transition at a lateral pinch out.
- Evaluate the potential mechanism for facies transitions.

1.2.3 How can inherited early post-rift structural relief effect the architecture and routing of channels?

Aims:

- Determine how inherited rift-related faults influence the architecture of early post-rift deepwater channel systems.
- Assess the interaction between axial and transverse systems in early post-rift settings.

Objectives:

- Map the distribution and architecture of the Agat Formation across the Måløy Slope and Sogn Graben.

- Analyse how rift-related fault networks influence channel morphology and routing using seismic mapping and seismic geomorphology.
- Characterise the sedimentology and facies association of the Agat Formation using core logging and well logs.
- Develop gross depositional environment maps illustrating the evolution of sediment routing across the Agat Formation.

1.3 Thesis Overview

In **Chapter 2**, relevant literature is reviewed that relates to the research objectives. Specifically, this includes an examination of the models and nomenclature, of sediment gravity flow and deposits in deep water systems, as well as an evaluation of the evolution of rift basins and the shift in sedimentation patterns from syn- to early post-rift.

Chapter 3, "Submarine lobe complex distribution and pinch out styles: an example from the early post-rift Angel Formation, NW Shelf Australia" offers a basin-scale to bed-scale, subsurface case study of sand-rich lobe complexes from the early post-rift. The primary focus of this chapter is to provide a detailed description of the sedimentology and distribution of these lobe complexes, as well as an evaluation of the pinch out of sand-rich lobe complexes against lateral topography. This chapter is presented in the form of a research paper intended for submission to the academic journal Basin Research.

Author contributions

- Wigan, T.J.L.: Main author, responsible for analysis, wrote manuscript
- Jackson, C. A-L.: In-depth discussion, assisted core logging and manuscript review
- Hodgson, D.M.: In-depth discussion and manuscript review
- Johnson, H.D.: In-depth discussion and manuscript review
- Flint, S.S.: Manuscript review

Chapter 4, "The curious case of the missing thin-beds: discriminating between lobe fringe environments and hemipelagic drapes in intensely bioturbated successions using reflectance spectroscopy" focuses on the mineralogical scale of the Angel Formation to determine the origin of the bioturbated heterolithic facies, in order to improve our understanding of facies evolution at a lateral pinch out. This chapter is presented as a research paper intended for submission to a short form academic journal such as Geology.

Author contributions

- Wigan, T.J.L.: Main author, responsible for analysis, wrote manuscript
- Jackson, C. A-L.: In-depth discussion and manuscript review
- Hodgson, D.M.: In-depth discussion and manuscript review
- Johnson, H.D.: In-depth discussion and manuscript review

Chapter 5, titled "Underlying fault controlled deep-water sediment routing and facies variations in the post-rift – a case study of the Lower Cretaceous Agat Formation, North Sea, Norway," presents a detailed analysis of an early post-rift channel and lobe system. The chapter offers a comprehensive basin-scale to bed-scale examination of the Agat Formation, including an evaluation of the controls on channel distribution and facies variability, as well as the seismic geomorphology of interaction of axial and transverse deep-water systems. The findings from this chapter are intended for publication as a research paper in the academic journal Basin Research.

Author contributions

- Wigan, T.J.L.: Main author, responsible for analysis, wrote manuscript
- Jackson, C. A-L.: In-depth discussion
- Hodgson, D.M.: In-depth discussion

Chapter 6 serves as a reflection on the research presented in the preceding chapters, highlighting the key findings and major contributions made to the field of deep-water sedimentology. Specifically, this chapter brings together the results of Chapters 3, 4, and 5 to provide a comprehensive overview of the controls on sediment gravity flows in post-rift basins. The synthesis of these findings reveals important insights into the spatial and temporal variability of depositional systems in deep-water environments. Finally, Chapter 6 also identifies potential areas for future research.

2 Literature Review

This chapter briefly outlines the key literature used as a foundation for this study. It introduces the concept of deep-water clastic sedimentology followed by an explanation of common processes and depositional environments focussing on deep-water lobes and their common controls.

2.1 Introduction

The deep-water sedimentology is the study of the sedimentary processes and depositional environments in the deep-water, which is defined as below the storm wave base (>200m) and is typically located beyond the continental shelf. The reason for the presence of coarser-grained sediments in deep-water was uncertain until Kuenen and Migliorini (1950) established a link between graded beds and turbulent currents. Since then understanding of deep-water environments has developed significantly over the last 70 years (eg. Bouma, 1962; Biscaye, 1965; Seilacher, 1967; Piper, 1970; Hampton, 1972; Mutti, 1977; Lowe, 1982; Wetzel, 1984; Hiscott, 1994; Kneller & Branney, 1995; Clark & Pickering, 1996; Baas & Best, 2002; Mayall *et al.*, 2006; Kane *et al.*, 2007; Stow & Faugères, 2008; Haughton *et al.*, 2009; Prélat *et al.*, 2009; Bell *et al.*, 2018; Boulesteix *et al.*, 2019; Soutter *et al.*, 2019; Stevenson *et al.*, 2020; Heijnen *et al.*, 2022; Nugraha *et al.*, 2022; Pope *et al.*, 2022).

Deep-water systems form some of the most volumetric (e.g. the Bengal Fan) and economically important sedimentary deposits on Earth (Normark & Piper, 1969; Shanmugam & Moiola, 1988; Weimer & Pettingill, 2007). Sediment is delivered to the deep-water under the force of gravity acting on density contrasts between a sediment laden flow and the ambient water, this transportation process is termed subaqueous ‘sediment gravity flow’ (Middleton & Hampton, 1973; Lowe, 1982; Haughton *et al.*, 2009). These sediment gravity flows can amount to the largest single event transporters of sediment on Earth (Rothwell *et al.*, 1998; Talling *et al.*, 2007; Nugraha *et al.*, 2022). Due to water depths and the destructive capacity of sediment gravity flows, a limited number of direct measurements of flows have been possible, although recent technological advances have significantly improved the number of measurements (Shepard *et al.*, 1977; Piper *et al.*, 1999; Azpiroz-Zabala *et al.*, 2017; Simmons *et al.*, 2020).

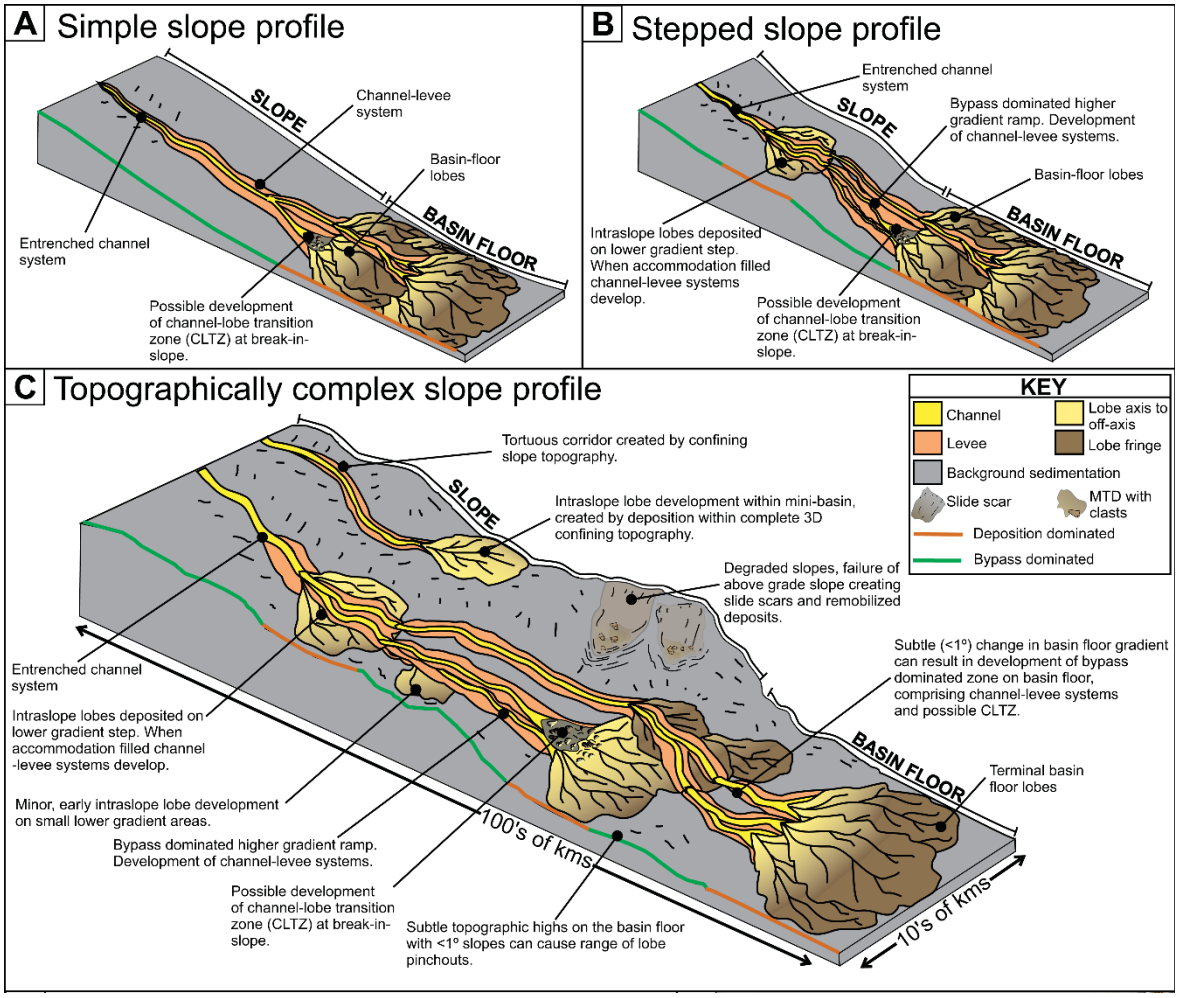


Fig. 2.1: *Examples of deepwater systems and their geomorphic features on varying slope complexities (Brooks* et al.*, 2018b)*

Geomorphic features associated with sediment gravity flows are typically more erosional in proximal areas and more depositional in distal areas. Sediments destined for delivery to deep-water are typically sourced into shelfal areas by fluvial systems, littoral drift, or directly into incised canyons, gullies, or fluvial deltas (Carlson & Karl, 1988; Paull *et al.*, 2002; Blum & Hattier-Womack, 2009; Prélat *et al.*, 2015; Talling *et al.*, 2022). These point sources pass into channel-levee systems towards the lower part of the slope (Fig. 2.1), which act as conduits for sediment transport further into the basin (Babonneau *et al.*, 2002). Channels typically terminate in submarine fans which are considered the ultimate sink of sediments in deep water (Normark, 1978; Walker, 1978; Reading & Richards, 1994). The transition between the channel-levee

system and a submarine lobe has been termed a Channel-Lobe Transition Zone or Channel Mouth Expansion Zone (Mutti & Normark, 1991; Wynn *et al.*, 2002; Hodgson *et al.*, 2022).

	Process / flow type	Bed type	Bed type description	Interpretation
Background	Hemipelagic settling	Hemipelagite	Grain size: clay, minor silt. Sedimentary structures: structureless or laminated.	Suspension settling from water column.
Individual sediment gravity flow deposits	Low-density turbidity current	Low-density turbidite	Grain size: silt-lower medium sand. Sedimentary structures: plane-parallel and ripple-cross lamination throughout, normally-graded.	Competence-related deposition and tractional working by low density turbidity current (Lowe, 1982; Hiscott, 1994).
	High-density turbidity current	High-density turbidite	Grain size: medium to very coarse and granular. Sedimentary structures: dominantly structureless.	Deposition from a high density turbidity current (sensu Lowe, 1982).
	Hybrid flow	Hybrid bed	Grain size: fine to medium sand. Sedimentary structures: banding, dewatering structures.	Deposition from flows with characteristics of turbidity currents and debris flows (Haughton et al., 2003; Talling, 2004; Haughton et al., 2009).
	Debris flow	Debrite	May include grains of all sizes. Sedimentary structures: diamictic, plastic deformation – fold and shear structures.	Deposition from debris flows where matrix strength is the main particle support mechanism (Lowe, 1982; Sohn, 1997).
	Slump	Slump deposit	Structures include evidence of plastic deformation, including folding and overturned beds.	Gravitational instability of un-lithified sediments which move downslope for a limited distance and begin to disintegrate but retain original structures.
	Slide	Slide deposit	Structures include coherent bedding with thrust planes, sheared bedding contacts, extensional and compressional features.	Gravitational instability of sediments which move downslope initially as a coherent mass and may retain internal structures.
Reworked deposits	Tractional lag	Tractional lag deposit	Grain size: silt-granular. Sedimentary structures: weak irregular stratification, erosional remnants, lenticular, clean but with mud-clasts, anomalously coarse, sharp base and top.	Winnowed tractional deposit formed at the base of a channel, scour or bedform trough typically by the passage of multiple flows leaving their coarsest material behind.
	Bottom current reworked	Bottom-current reworked sst	Grain size: silt to fine sand. Sedimentary structures: plane-parallel and ripple-cross lamination, mud draped foresets and laminae, variable grading, internal erosion surfaces, bioturbated.	Deep water sediment gravity flow silts and sands reworked by tractional currents attributed to bottom currents (thermohaline flows).
	Bottom current reworked	Drift deposit	Grain size: clay to silt. Sedimentary structures: plane-parallel and low angle dipping lamination, may be entirely bioturbated, or lack bioturbation.	Deep water sediment gravity flow clays and silts, and hemipelagite, reworked by quasi continuous thermohaline circulation (bottom currents) (e.g. Stow & Faugères, 2008).

Fig. 2.2: *Idealised examples of deepwater deposits, linking depositional process to associated deposits (adapted from Kane and Clare, 2019).*

2.2 Sediment gravity flows

Sediment gravity flows and their associated deposits have been reviewed numerous times and are often subdivided based on flow cohesiveness, flow state and/or density of particles (Fig. 2.2; eg. Dott, 1963; Middleton & Hampton, 1973; Lowe, 1982; Kneller & Buckee, 2000; Mulder & Alexander, 2001; Talling *et al.*, 2012). Understanding the link between processes and their deposits is crucial as the problem faced by geologists is that studies are typically limited to deposit-based observations in outcrops or core, where flow parameters cannot be interpreted. However, one way to link deposits to the flow process is through laboratory modelling (Baas *et al.*, 2011; Baker *et al.*, 2017; Ferguson *et al.*, 2020; Soutter *et al.*, 2021).

Turbidity currents are sediment-laden flows, where sediment is supported by flow turbulence and can be subdivided by the density of particles in the flow: high and low-density (Lowe, 1982; Talling *et al.*, 2012).

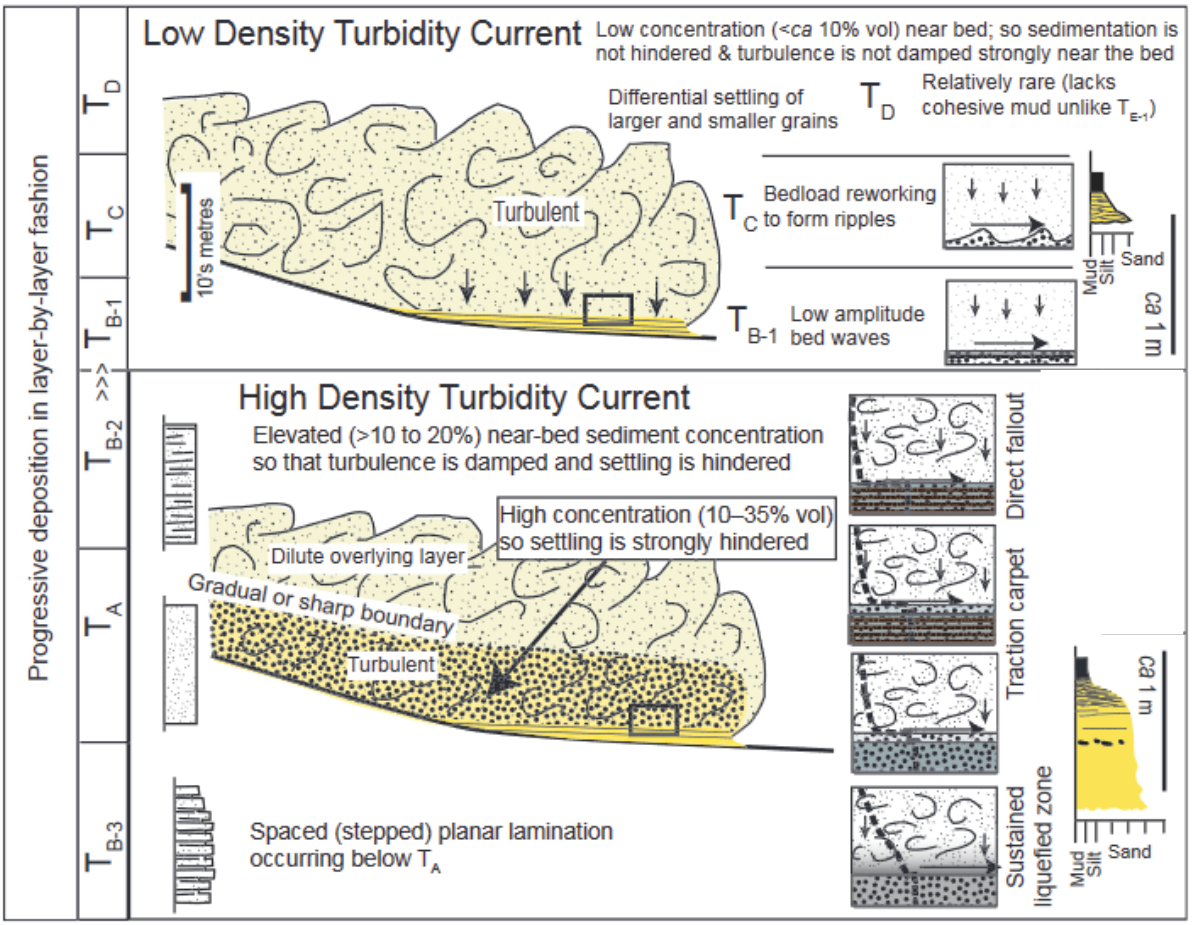


***Fig. 2.3**: Summary of low- and high-density turbidity currents and their associated deposits (from Talling et al. 2012)*

High-density turbidity currents comprise a dense basal layer, where sediment is supported by grain-to-grain interaction or dispersive pressures, and an overlying more dilute cloud of

sediment, where turbulence supports sediment suspension (Fig. 2.3), where deposition occurs in a layer-by layer fashion (Kneller & Branney, 1995; Talling *et al.*, 2012; Azpiroz-Zabala *et al.*, 2017). In contrast, low-density turbidity is deposited by a waning turbulent flow with relatively low sediment concentrations, which leads to vertical particle sorting (Fig. 2.3) (Lowe, 1982; Mulder & Alexander, 2001).

This density contrast leads to variations in their deposits (known as turbidites), where high-density turbidites typically comprise massive, ungraded or graded sandstone at the base of the deposit (i.e. Bouma's T_a) due to the effect of dampening of turbulence by sediment concentrations (Bouma, 1962; Lowe, 1982; Stow & Johansson, 2000). This massive sandstone unit may show evidence of dewatering features such as consolidation laminae, dish and pipe structures caused by rapid deposition of liquified sediments (Lowe, 1975; Hurst & Cronin, 2001). This massive sandstone unit may then be overlain by a low-density turbidite associated with the overlying turbulent cloud. Low-density turbidites may lack a basal massive sandstone and commonly have traction sedimentary structures such as planar laminations and ripples (Fig. 2.3).

However, more recent studies have identified intermediate flow types between these two end-members, so called 'hybrid flows' that deposit 'hybrid beds' (Fig. 2.2, (Haughton *et al.*, 2003, 2009; Stevenson *et al.*, 2020). Two types of hybrid event beds are typically described: 'linked debrites' and transitional flow deposits. Linked debrites have a basal massive sandstone which is overlain by a typically clast-bearing, muddy sandstone which form due to changes in flow rheology by entrainment of a muddy substrate (Kane *et al.*, 2017). Transitional flow deposits are banded with interleaved bands of clean sandstone and muddy sandstone which are thought to be a product of a fluctuation flow state between turbulent and laminar flow states (Stevenson *et al.*, 2020). Flows can transform both spatially and temporally through the natural deceleration of a flow (e.g. Kane & Pontén, 2012), and/or interaction with topography (e.g. Kneller *et al.*, 1991; Hodgson & Haughton, 2008; Haughton *et al.*, 2009; Patacci *et al.*, 2014; Southern *et al.*, 2015; Soutter *et al.*, 2019).

Cohesive flows are typically mud-rich and freeze *en masse* leading to a chaotic fabric in clast-bearing flows (Fig. 2.2). These flows are laminar, tend to follow topographical lows, and are able to transport sediment 100kms on low slope gradients into a basin (Laberg & Vorren, 2000; Talling *et al.*, 2012).

2.3 Deepwater Lobes

There have been many models focusing on submarine fans. Classically, lobes are fed by a single feeder channel with a channelised proximal lobe area and a tabular distal lobe deposits (Normark, 1978). Generally, models have also accounted for end-members based on grain-size where mud-rich systems have longer runouts than coarser grained systems (Reading & Richards, 1994; Bouma, 2000; McHargue *et al.*, 2021).

Deep-water lobes are convex-up lobate-shaped deposits formed by sediment gravity flows that transport sediment from the shelf to the basin floor (Fig. 2.4; Prélat *et al.*, 2009). Lobe sizes can vary from a few km's to >10's km in length and width (Prélat *et al.*, 2010). The width and level of confinement can be related to the thicknesses of lobes. Confined lobes may have a width-to-thickness ratio of c. 100:1, and unconfined lobes may be over 1000:1 (Prélat *et al.*, 2010).

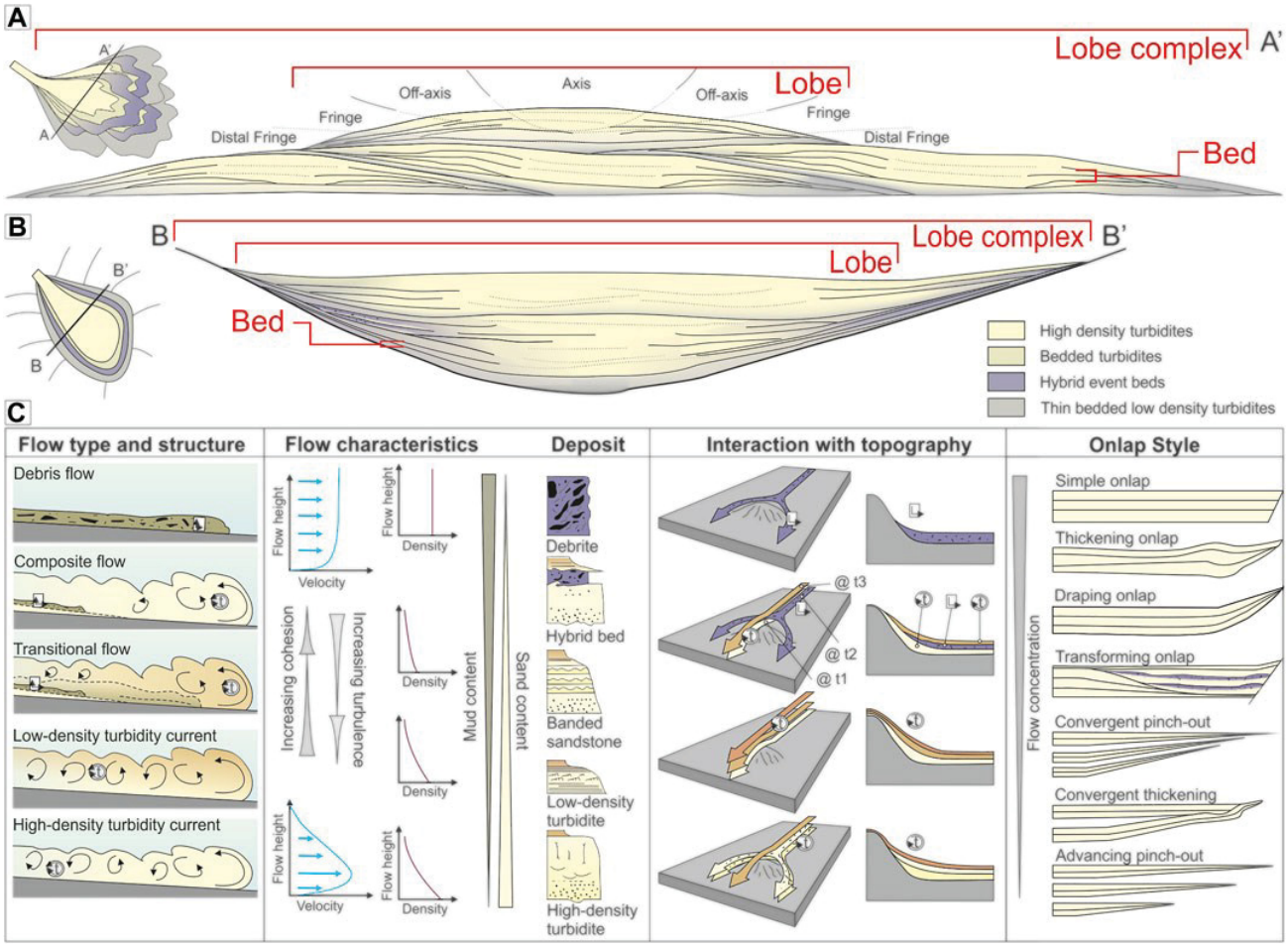


Fig. 2.4: *Lobe architecture and hierarchy in (A) unconfined and (B) confined settings, illustrating variations in compensational and aggradation stacking and lateral termination style. C) Sediment gravity flow types and their flow characteristics and resulting interaction with topography and onlap style (from Fuhrmann* et al.*, 2022).*

Deep-water lobes can be deposited on the slope (i.e. intraslope), at the toe of slope, or on the basin floor (Fig. 2.1). Intraslope lobes that are fully-confined are described as 'ponded' (Prather *et al.*, 2012). Semi-confined to unconfined intraslope lobes are described as 'perched' (Plink-Björklund & Steel, 2002; Prather *et al.*, 2012; Jobe *et al.*, 2017; Brooks *et al.*, 2018b; Privat *et al.*, 2021) and these types may exhibit initial ponding of deposits before developing a wedge shape and finally exhibiting bypass as accommodation is filled (Prather *et al.*, 1998; Beaubouef & Friedmann, 2000; Pirmez *et al.*, 2000; Casagrande *et al.*, 2022).

The morphology, distribution, character and evolution of deepwater deposits are governed by both allogenic (external) and autogenic (internal) factors (Baas *et al.*, 2005; Bouma, 2008). Allogenic controls includes; tectonic settings, sea-level changes and sediment supply (eg. Reading & Richards, 1994; Gawthorpe & Leeder, 2000; Normark *et al.*, 2006). Autogenic controls include examples such as compensational stacking (eg. Straub & Pyles, 2012; Prélat & Hodgson, 2013), remobilisation events such as slumps, slides and mass transport complexes (eg. Moscardelli *et al.*, 2006; Armitage *et al.*, 2009; Steventon *et al.*, 2021; Martinez-Doñate *et al.*, 2023), and subsurface movement of salt and mud (eg. Armentrout *et al.*, 2000; Davis *et al.*, 2009; Doughty-Jones *et al.*, 2017; Cumberpatch *et al.*, 2021b).

2.3.1 Lobe sub-environments

Four different sub-environments can be identified across a lobe based on facies and degrees of bed amalgamation (Fig. 2.5). These are lobe axis, off-axis, proximal fringe, and distal fringe, with the transition between these zones being gradual over 10s m (Fig. 2.4; Prélat et al., 2009). The axis, typically, is a zone of high bed amalgamation, dominated (85-100%) by coarser-grained structureless sandstone deposited by high-density turbidites, and can be traceable over several 100s metres down-dip and laterally (Spychala *et al.*, 2017b). Off-axis represents the zone around the lobe axis. The off-axis is defined by moderate bed amalgamation, 50-85% stratified sandstone with tabular geometries, and can be traced for several 100s metres laterally and longitudinally (Prélat *et al.*, 2009; Spychala *et al.*, 2017b). Medium to thin-bedded successions of structureless sandstone, hybrid-event beds and debrites with no amalgamation are present in the proximal fringe, with 20-50% sandstone (Kane *et al.*, 2017; Spychala *et al.*, 2017b). The distal fringe is a 'halo' around the lobe which is dominated by thin-beds of

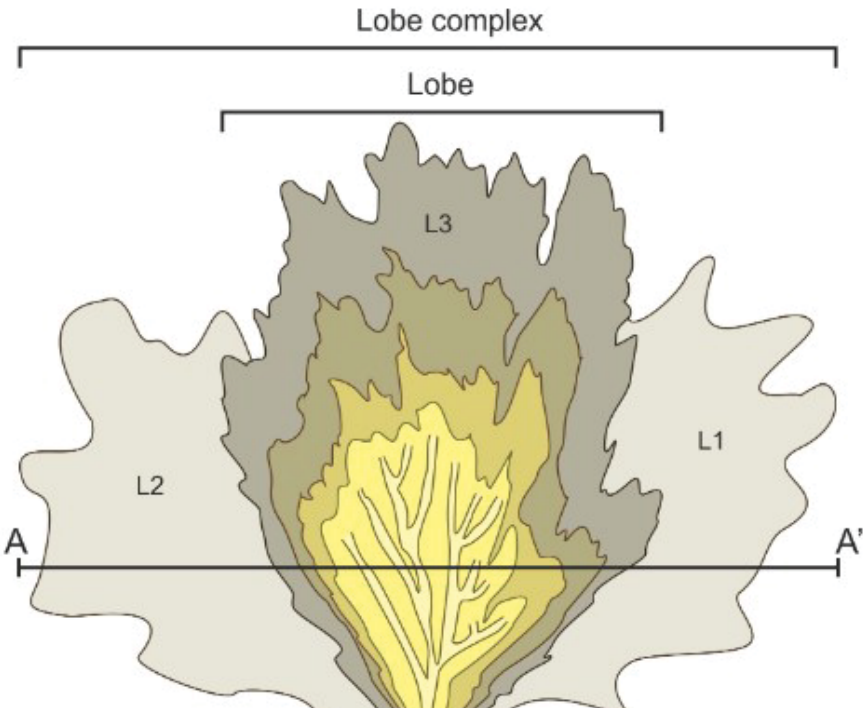
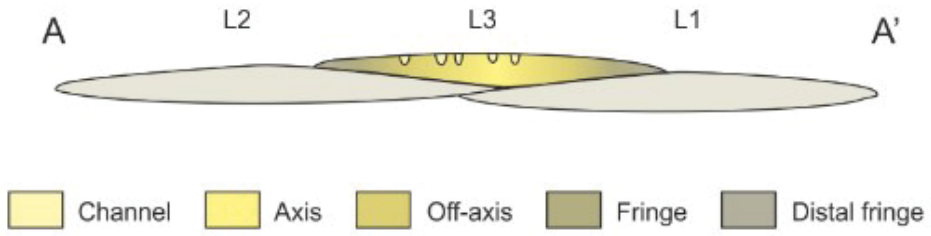


***Fig. 2.5**: Schematic lobe illustrating locations of various sub-environments and compensational stacking patterns (from Hansen et al., 2019).*



siltstone and occasional (<20%) fine sand beds that can extend for several kilometres (Spychala *et al.*, 2017b; Boulesteix *et al.*, 2020). Addition longitudinal variations from proximal to medial and distal lobe positions identify increased erosion, amalgamation and channelisation in proximal areas whereas in more distal areas erosional contacts are rare (Sullivan *et al.*, 2000; Saller *et al.*, 2008; Doughty-Jones *et al.*, 2017).

Two subtypes of lobe fringes can commonly be identified: frontal fringe and lateral fringe. The degree of confinement effects the facies and geometry in each of these settings. In an unconfined setting, the frontal fringe is dominated by hybrid-event beds and high-density turbidites that can abruptly pinch out, whereas the lateral fringes are classified as having no amalgamation and heterolithic deposits that progressively taper out (Spychala *et al.*, 2017c). In confined settings, lateral fringes have the tendency to aggrade and onlap topography and can have a variety of geometries, such as abrupt terminations and pinch-and-swell geometries (Fig. 2.4 B&C), the geometry is typically controlled by the confining slope geometry and flow

rheology, where less cohesive and low-density slows can override topography (Bakke *et al.*, 2013; Patacci *et al.*, 2014; Soutter *et al.*, 2019).

2.4 Deep-water systems in rift basins

As tectonics plays an important role in the generation of accommodation and uplift of source regions for sediments, an understanding of the initiation, development and termination of rift basins is crucial for predicting reservoir distribution both spatially and temporally where tectonics (eg. Prosser, 1993; Nottvedt *et al.*, 1995; Gawthorpe & Leeder, 2000; Gabrielsen *et al.*, 2001; Steel, 2010). The periods of rifting are commonly described in terms of megasequences; pre-rift (prior to extension), syn-rift (during active extension) and post-rift (after extension), with each displaying distinct sedimentation patterns which are controlled by climate, tectonic framework and sea level (Prosser, 1993; Gawthorpe & Leeder, 2000; Wonham *et al.*, 2014). Syn-rift sedimentation is typically controlled by the rate of fault growth and development of a structural framework for the rift basin, illustrated in Fig 2.5 (Gawthorpe & Leeder, 2000). Typically documented during the syn-rift are relatively immature transverse sedimentation from local fault scarp uplift and degradation and axial systems which stack adjacent to footwall scarps which may be source via antecedent drainage though sediment transfer zones that developed in relay ramps and between fault segments (Fig. 2.5 B, C, D; Ravnås & Steel, 1997; Gawthorpe & Leeder, 2000; McArthur *et al.*, 2016). The Gawthorpe and Leeder model (2000) is limited in its interpretation of deep-water sedimentation focusing on primary rifts, whereas often rift basins undergo multiple phases which have the potential for oblique stretching to existing faults generating complex fault networks eg. the North Sea and Dampier Sub-basin NW Shelf Australia (eg. Hocking *et al.*, 1987; Badley *et al.*, 1988; McHarg *et al.*, 2018; Phillips *et al.*, 2019). More mature, hinterland sourced, deep-water systems have recently been interpreted to be are well established by the late syn-rift stage on a faulted slope or terraces slope dominated by transverse systems with rare axial systems documented (Fig. 2.7, Tillmans *et al.*, 2021). Initial early syn-rift deep-water sandstone deposition is controlled locally by active normal faults leading to ponding in rift generated accommodation, which are commonly overfilled, expressing limited seafloor relief (Fig. 2.7 ; Tillmans *et al.*, 2021). Tillmans *et al.* (2021) recognized greater subsidence and footwall uplift in the late syn-rift, which was focused on fewer normal faults leading to routing of deep-water flows through transfer zones across fault segments (Fig. 2.7).

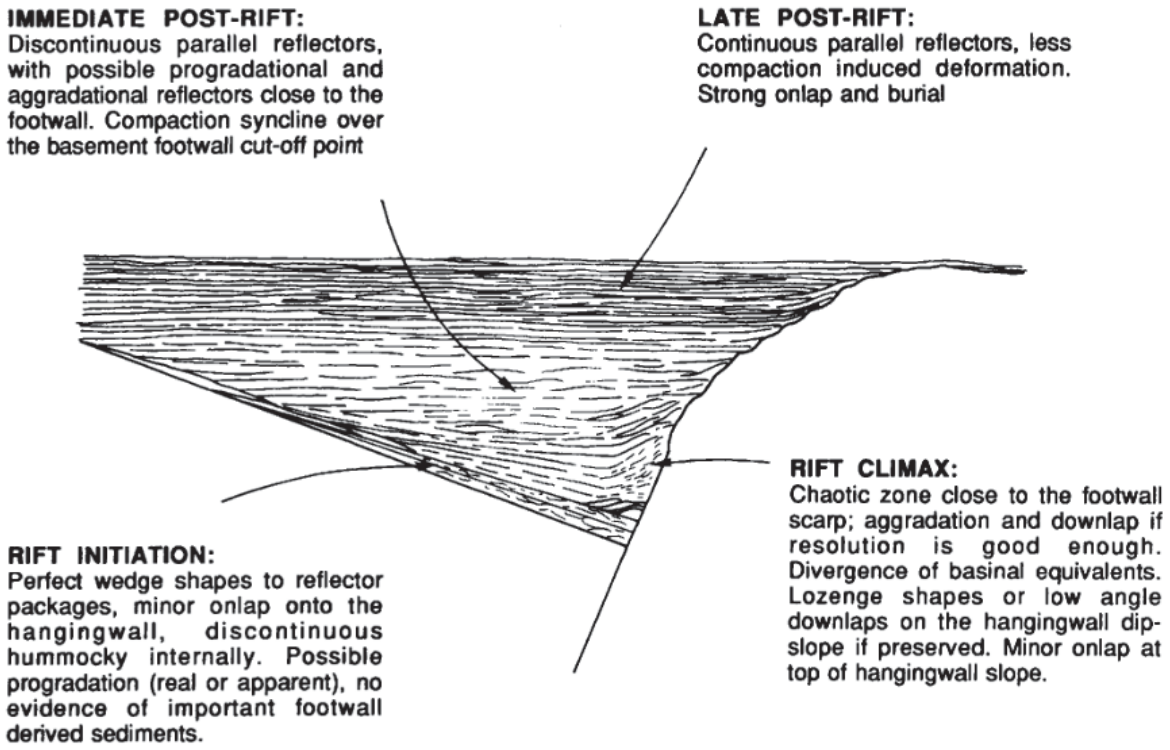


***Fig. 2.6**: Illustration of idealised seismic cross-section through a half-graben. Rift initiation is equivalent to early syn-rift, rift-climax is equivalent of late syn-rift. (From Prosser, 1993)*

Understanding the transition from syn-rift to post-rift is essential and often marked by a significant onlap surface in seismic data known as a post-rift unconformity (Prosser, 1993). The immediate or early post-rift phase is characterised by the cessation of faulting and a transition to subsidence driven by thermal relaxation or sediment loading, although this may not occur uniformly across a basin with fault death diachronous across the basin (Gabrielsen *et al.*, 2001). Key diagnostic criteria include the end of tilting and fault displacement and infilling of remaining rift topography (Prosser, 1993). In seismic commonly parallel reflections dominate although variations can be attributed to depositional processes and subsequent compactional deformation (Prosser, 1993). The inherited structural features in the early post-rift phase acts as a major control on the routing and distribution of sedimentary systems (Gabrielsen *et al.*, 2001). Late post-rift deposits result from the peneplanation of inherited fault related topography, although the underlying rift may continue to influence sediment routing through differential compaction between the rift infill and basement highs, seismically, these deposits often appear as parallel reflections (Prosser, 1993; Gabrielsen *et al.*, 2001).

Inherited syn-rift structures provide the main influence on post-rift deposition (Zachariah *et al.*, 2009). Direct interaction of deep-water sediments with tectonic structures in the early post-rift is relatively under documented even though they may act as excellent reservoirs (Fig. 2.8

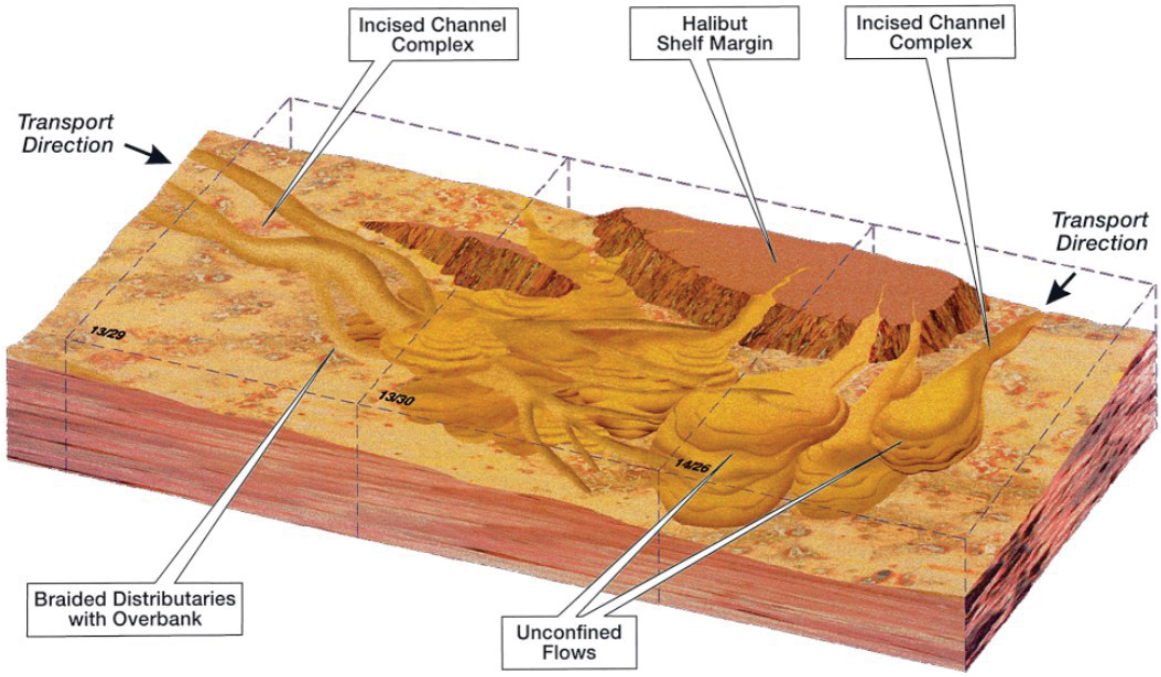


***Fig. 2.7**: Schematic diagram of deep-water sedimentation influenced by inherited fault scarp with sea floor expression in the Cromarty area (From Law et al. 2000).*

& 2.9 1-2; Argent *et al.*, 2000; Law *et al.*, 2000; Martinsen *et al.*, 2005). However numerous studies have focused on sedimentation in the later post-rift once syn-rift structures are buried leading to subtle rift-related topographical controls (Fig. 2.9, 3-8; Martinsen *et al.*, 2005; Rose & Pyle, 2014; McKie *et al.*, 2015; Hansen *et al.*, 2021b; Privat *et al.*, 2021).

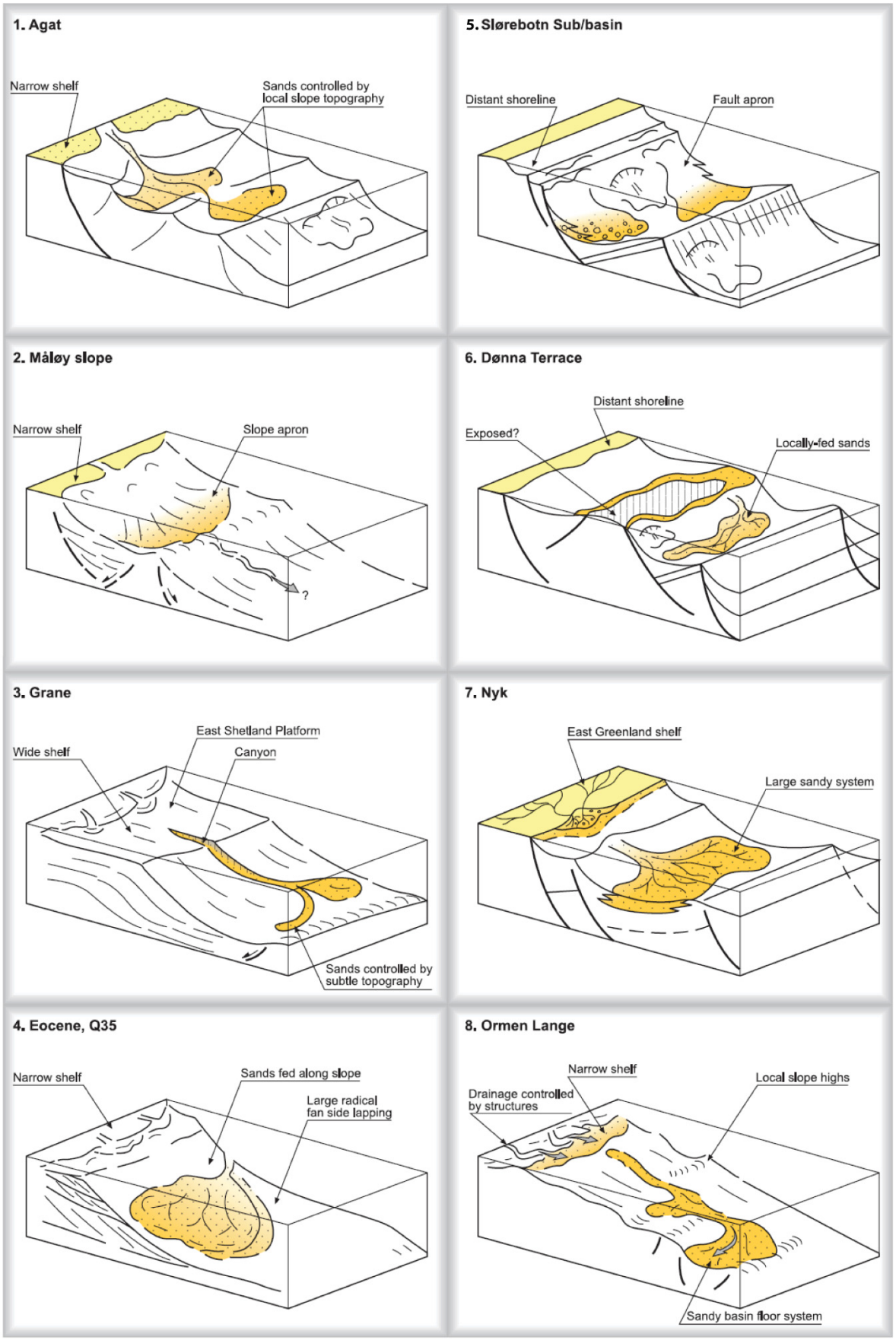


***Fig. 2.8**: Schematic diagrams of various North Sea post-rift deep-water depositional systems with controlling processes illustrated. 1-2) illustrate systems directly interacting with inherited syn-rift topography. 3-8) are systems not in the immediate post-rift that are still influenced by inherited syn-rift topography (not to scale) From Martinsen et al. 2005.*

3 Submarine lobe complex distribution and pinch out styles: an example from the early post-rift Angel Formation, NW Shelf Australia

Timothy J. L. Wigan[1*], Christopher A-L. Jackson[1], David M. Hodgson[2], Howard D. Johnson[1]

[1]Basins Research Group (BRG), Department of Earth Science and Engineering, Imperial College London, SW7 2BP, United Kingdom

[2] School of Earth and Environment, University of Leeds, Leeds, LS2 9JT, United Kingdom

3.1 Abstract

Deep-water post-rift basins inherit syn-rift topography due to underfilling during rifting or differential compaction above fault blocks. The resulting intra-basin topography influences sediment gravity flows and dispersal patterns, and therefore, the sedimentary architecture and stacking patterns of submarine lobes and channels that form in topographic lows. Such a setting characterises the Angel Formation (Late Jurassic), which represents stacked sand-rich submarine lobe complexes in the Dampier Sub-basin, NW Shelf Australia. A comprehensive and geologically diverse subsurface dataset, comprising regional 3D seismic reflection, well-log, biostratigraphic, and core data, has enabled reconstruction of the spatial and temporal distribution of lobes and lobe complexes in the Angel Formation. The depositional system comprises one major axial fan (lobe complex sets), and five smaller oblique fans, that share a single sediment source area. These fans were deposited on a SW-dipping tectonically controlled basin laterally confined by inherited and degraded syn-rift-related structures. Our study illustrates the impact of evolving rift-related topography on stacking patterns, reservoir architecture, and degree of amalgamation of submarine fans, with stratigraphic change from abrupt to tapered pinch out of lobes, and increased compensational stacking patterns, as inherited relief was healed.

Keywords*: Lobe pinch out, Confined basin, Angel Formation, Deep-water fans*

3.2 Introduction

Seabed topography controls the location and orientation of lobes and lobe complexes in submarine fans (Smith, 2008; Prélat *et al.*, 2010; Prather *et al.*, 2012; e.g. Marini *et al.*, 2015; Soutter *et al.*, 2021) because turbidity currents are sensitive to changes in the gradient and orientation of seabed topography. Therefore, the stacking pattern and style of pinch out of lobes has been used as a record of evolving physiography in: i) syn-rift basins, in which relief is generated by normal faults (Ravnås *et al.*, 2000; Jackson *et al.*, 2011; e.g. Cullen *et al.*, 2019; Tillmans *et al.*, 2021), ii) post-rift basins, in which relief is inherited from the syn-rift phase (Rose, 1999; e.g. Bergslien, 2002; Dmitrieva *et al.*, 2018; Dodd *et al.*, 2019; Privat *et al.*, 2021)), iii) salt-influenced slopes (Oluboyo *et al.*, 2014; Rodriguez *et al.*, 2019; Cumberpatch *et al.*, 2021b; Howlett *et al.*, 2021; e.g. Casagrande *et al.*, 2022) , iv) deep-water fold-thrust belts (e.g. Howlett et al., 2019), and v) intra-basin relief above mass transport complexes (e.g. Armitage *et al.*, 2009; Martínez-Doñate *et al.*, 2021; Steventon *et al.*, 2021).

Several factors influence the facies and geometry of lobe pinch out, including: i) flow characteristics (e.g. flow height, composition, and magnitude) (eg. McCaffrey & Kneller, 2001; Barker *et al.*, 2008; McHargue *et al.*, 2021) , ii) gradient and incidence angle of the flow with respect to seabed topography (e.g. Amy *et al.*, 2004; Patacci *et al.*, 2014; Southern *et al.*, 2015; Spychala *et al.*, 2017c) and iii) substrate erosion (e.g. Gardiner, 2006; Stevenson *et al.*, 2020). Previous quantification of the rate of thinning of lobes and the style of pinch-out have largely come from outcrop data (Drinkwater *et al.*, 2001; Marini *et al.*, 2015; Fryer & Jobe, 2019; Hansen *et al.*, 2019). However, many exposures are two-dimensional, therefore three-dimensional relationships are inferred. Experimental (Soutter *et al.*, 2021) and numerical modelling (Cumberpatch *et al.*, 2021a) approaches provide insights into the three-dimensional relationship between topography, lobe geometry, and pinch-out rate and style, but their predictions require testing against natural datasets. Subsurface datasets, in particular 3D seismic reflection data supported by a dense network of wells and associated well-log, biostratigraphic, and core data, provide an opportunity to characterise lobe pinch outs in three dimensions and constrain the evolving three-dimensional physiography of sedimentary basins.

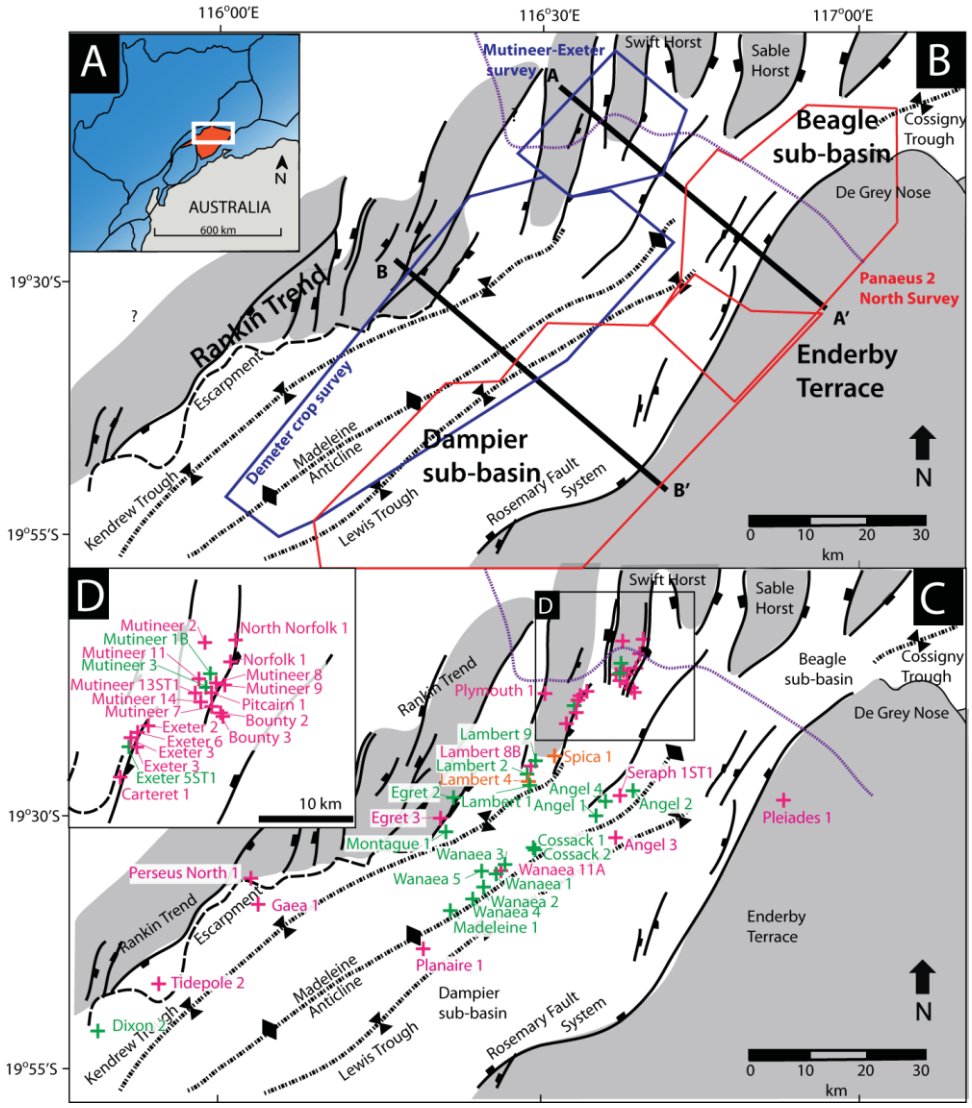


Fig. 3.1: *Location of the study area. A) Regional map of the NW shelf, Australia. Red indicates Dampier sub-basin, white box indicate area shown in B & C. B) Structural element map of the Dampier sub-basin, structural blocks in grey (modified from Lech, 2013; Spencer et al., 1992) with key seismic reflection surveys in blue and secondary (used for basin cross-sections) seismic reflection surveys in red. Sub-basin boundary purple dashed line.* ***C)*** *Well location map, colour indicated data available; green – core and well-logs, orange wells – core only, pink – well-logs only.* ***D)*** *Zoomed in well location map for the Mutineer & Exeter area. A-A' and B-'B displayed in Fig. 3.3.*

The Angel Formation (Late Jurassic), Dampier Sub-basin, NW Shelf, Australia (Fig. 3.1A) is a set of sandstone-rich, early post-rift, submarine fans that has been extensively explored for hydrocarbons since the 1970's (eg. Hocking *et al.*, 1987; Bint, 1991). As such, it is sampled by an exceptionally rich dataset comprising 3D seismic reflection surveys (c. 2000 km^2), 50 wells, and c. 1 km of core (Fig. 1C and D). We used this 3D subsurface dataset to i) reconstruct the spatial and temporal evolution of the Angel Formation deep-water depositional system, ii) evaluate the relative impact of allogenic and autogenic controls on lobe deposition, including the role of intra-basin relief, and iii) assess the influence of inherited topography on bed geometries, pinch-out rate, and three-dimensional lobe architecture.

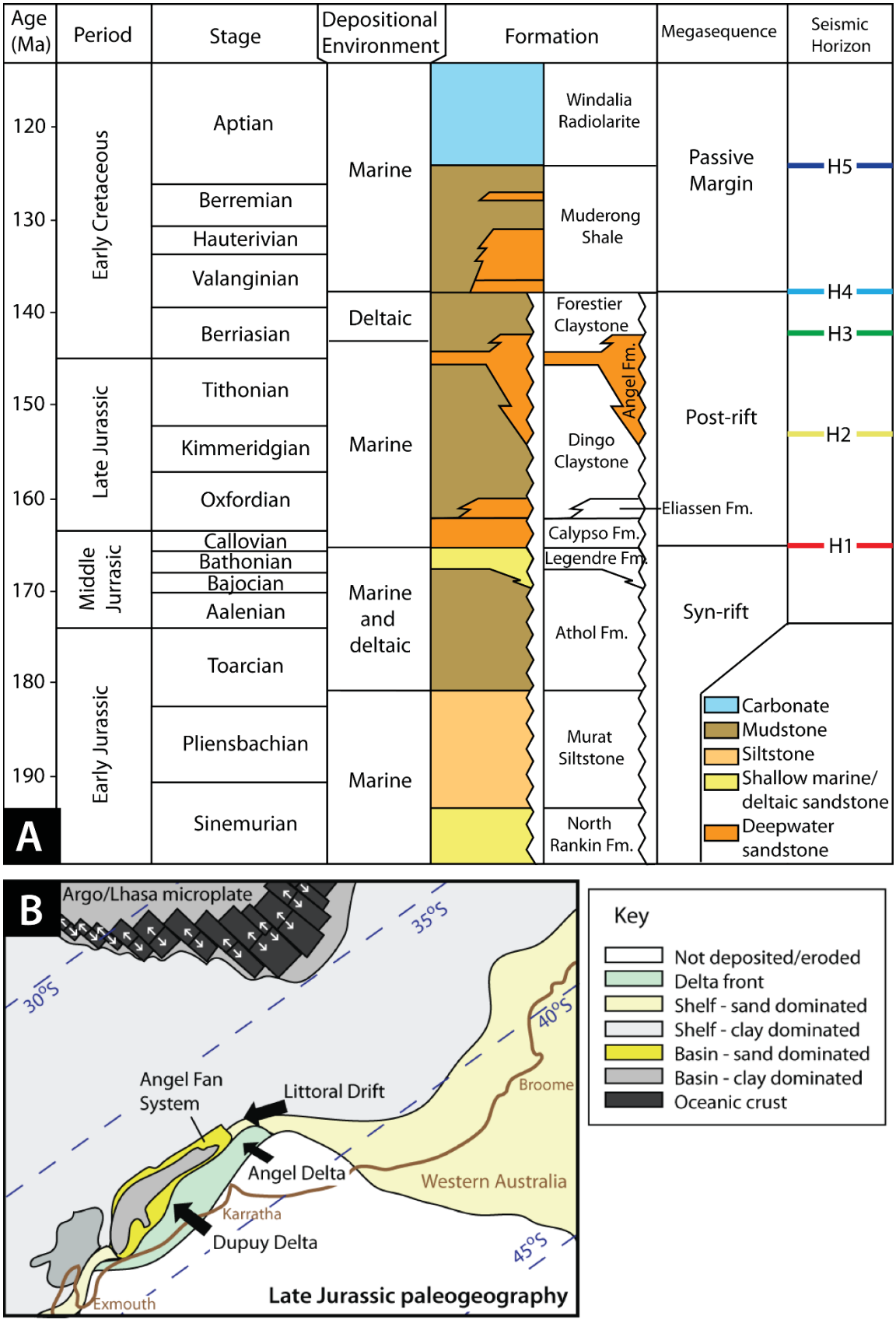


Fig. 3.2: *A) Stratigraphy of the Lower Jurassic to Lower Cretaceous succession of the Dampier sub-basin (modified from Geoscience Australia, 2021), megasequences from Deng and McClay (2020), with seismic horizons used in this study. B) Late Jurassic paleogeography of the Northern Carnarvon Basin.*

3.3 Tectonostratigraphic evolution of the Dampier Sub-basin

The present-day Dampier Sub-basin is an inboard failed rift basin that forms a part of the wider North Carnarvon Basin. An initial phase of rifting occurred during the Late Carboniferous to Late Triassic, during which time a network of NE-SW-striking faults developed, forming the regional Westralian Superbasin (eg. Hocking *et al.*, 1994; Longley *et al.*, 2002). A subsequent rifting period during the Late Triassic-to-Middle Jurassic lead to the formation inboard subbasins with the Northern Carnarvon Basin which the Dampier Sub-basin is one of (Fig. 3.2, Elders et al., 2016). Below, we provide a review of the key structural elements and events associated with, and immediately after, the Late Triassic-to-Middle Jurassic rifting.

3.4 Controls on deepwater deposits

The morphology, distribution, character and evolution of deepwater deposits are governed by both allogenic (external) and autogenic (internal) factors (Baas *et al.*, 2005; Bouma, 2008). Allogenic controls includes; tectonic settings, sea-level changes and sediment supply (eg. Reading & Richards, 1994; Gawthorpe & Leeder, 2000; Normark et al., 2006). Autogenic controls include examples such as compensational stacking (eg. Straub & Pyles, 2012; Prélat & Hodgson, 2013), remobilisation events such as slumps, slides and mass transport complexes (eg. Moscardelli *et al.*, 2006; Armitage *et al.*, 2009; Steventon *et al.*, 2021; Martinez-Doñate *et al.*, 2023), and subsurface movement of salt and mud (eg. Armentrout *et al.*, 2000; Davis *et al.*, 2009; Doughty-Jones *et al.*, 2017; Cumberpatch *et al.*, 2021b).

This thesis will focus one of the key allogenic controls, tectonic setting in the form of extensional basins. These basins are significant sedimentary sinks with high potential for preserving records of climatic changes, sedimentation, and sea level interactions in relation to fault activity, and contain significant subsurface hydrocarbon accumulations and potential carbon storage sites (eg. the Kopervik, North Sea). The completeness of rifting in rift basins plays a key role on the development of sedimentary systems, in that if the rift is ‘completed’ and therefore develops into a passive margin or ‘fails’ and lacks the development of oceanic crust. Additional complexity can be added to the failed rift basin in the form of salt and volcanism. This thesis will focus on ‘failed’ rift basins that lack the additional complexity of volcanism and salt deposition.

3.4.1 Late Triassic – Middle Jurassic (Syn-rift)

The Dampier Sub-basin formed in response to crustal extension during the early Mesozoic (Fig. 3.1A). The basin margins are defined by the Rankin Fault Zone (in the NW) and the Rosemary Fault System (in the SE), which separate the basin from the structural highs of the Rankin Trend and Enderby Terrace, respectively (Fig. 3.1B). These fault systems trend NNE-SSE and are oblique to the Late Carboniferous-to-Late Triassic rift fault trend, with the causal oblique extension resulting in the formation of *en echelon* faults along the Rankin Trend (Fig. 3.1B). These faults detach in the Locker Shale (Early-to-Middle Triassic) and link to the Rankin Fault via fault-bend or ramp-flat fault geometry (Romine *et al.*, 1997; McHarg *et al.*, 2018). The cross-sectional geometry of the Rankin Fault gives rise to a hanging wall anticline, the Madeleine Anticline, which runs along the basin axis, and originates in the NE and terminates to the SW, beyond the Madeleine-1 well (Fig. 3.1C). The along-strike termination of the anticline is attributed to the along-strike change in the faults geometry, from ramp-flat to planar (McHarg *et al.*, 2018). The Madeleine Anticline subdivides the basin into two depocenters: the Lewis and Kendrew troughs (Fig. 3.1B) (Spencer *et al.*, 1992; McHarg *et al.*, 2018). The early rift basin-fill thins across the Madeleine Anticline (Fig. 3.3B), suggesting that faulting and related folding occurred during the Early Jurassic (Longley *et al.*, 2002; McHarg *et al.*, 2018). Toward the end of the syn-rift, the Legendre Delta (Middle Jurassic) prograded over the Dampier Sub-Basin and surrounding sub-basins before a major transgression and shift in the locus of rifting occurred, with strain localised along the inboard sub-basins of the Northern Carnarvon Basin (Hocking, 1992; Heine & Müller, 2005; Marshall & Lang, 2013).

3.4.2 Late Jurassic - Early Cretaceous (Post-rift)

The base of the post-rift succession is defined by a major unconformity over the Kendrew Trough that merges with an older, Triassic unconformity over the basin-bounding structural highs that marks the end of the syn-rift phase and a shift to thermal relaxation driven subsidence (Deng & McClay, 2020),. The Dampier sub-basin was likely underfilled at this stage, given the fact that: i) the flanking Triassic fault scarps are degraded (Deng & McClay, 2020), ii) the Dingo Claystone (Fig. 3.2A) is confined to the Dampier Sub-basin and onlaps the structural highs (Hocking, 1992); iii) deep-water clastics of the Eliasson Formation are restricted to the Lewis Trough, indicating that the Madeline Anticline acted as a submarine high at this time (Hocking, 1992). During the Tithonian, clastic supply to the Dampier Sub-basin increased, with multiple channelised turbidite systems feeding the deep-water lobes of

the Angel Formation, which were sourced from a sand-rich shelf to the NE (Fig. 3.2B, (Longley *et al.*, 2002). From the Early Cretaceous onwards, a passive margin setting was established across the wider North Carnarvon Basin and minor subsidence occurred in the Dampier sub-basin, driven by thermal subsidence (Marshall & Lang, 2013; Deng & McClay, 2020)

3.4.3 Angel Formation

Previous work on the Angel Formation has focused on its general context within the wider Dampier Sub-basin stratigraphy (e.g. Hocking, 1992; Hocking *et al.*, 1994; Marshall & Lang, 2013) and initial field discoveries (e.g. Bint, 1991) and biostratigraphy (eg. Bint & Marshall, 1994; Helby *et al.*, 2004). Studies focusing exclusively on the sedimentology and stratigraphy of the Angel Formation are limited to di Toro (1995), well reports, and an unpublished PhD thesis (Deller, 2011). These studies describe the Angel Formation sandstones as pale-grey, fine-to-medium-grained sandstones which are interpreted to have been deposited by high-density turbidity currents in a submarine fan environments that overall fine southward (Hocking, 1992; di Toro, 1995; Deller, 2011). The interbedded mudstones are heavily bioturbated to the extent that any original depositional fabric is overprinted (Deller, 2011). As a result of hydrocarbon exploration, the most extensively documented area of the Angel Formation is the NE of the Dampier Sub-basin, on the flanks of the Rankin Trend, and on the Madeleine Anticline. Sandstone-bearing intervals are typically thin and fine to the SE (di Toro, 1995). Potential sediment source areas were structural highs in the Beagle Sub-basin (NE), Rankin Trend (NW), De Grey Nose, and Enderby Terrace (E) (Fig. 3.1B), with sandstones pinching out before the centre of the Dampier Sub-Basin (i.e. by the Madeleine 1 well) (Hocking *et al.*, 1987; Barber, 1994; di Toro, 1995; Stephenson *et al.*, 1998; Marshall & Lang, 2013). A large submarine fan has previously been interpreted to have existed in the NE section of the Madeleine Anticline (Fig. 3.1), which form part of the Angel, Cossack, and Wanaea fields, that were sourced from the Enderby Terrace to the NE and thins to the SE (Hocking, 1992). Smaller oblique submarine fans have been identified in the SW, sourced directly off the Rankin Trend, along with an axial (fault-parallel) channel that transported sediment to the SW (Chen *et al.*, 2020).

3.5 Data and methodology

In this study, we used four 3D seismic reflection surveys: 50 wells, 956 m of core, and 766 palynology sample points. The seismic reflection data was interpreted to define the early post-rift structural configuration of the basin, and the large-scale stratigraphic architecture and filling patterns. Core data was used to constrain the sedimentology of the Angel Formation,

and stratigraphic panels, constrained by biostratigraphic data, to understand the lateral and vertical relationships between sandstone units and the basin structure. Rates of stratigraphic thinning were then calculated, and the style of lateral pinch-out was characterised to understand how sediment gravity-flows were influenced by syn-depositional topography.

3.5.1 Seismic reflection data

All CVSN06 Mutineer_Exeter 3D MSS (2006) and part Demeter 3D MSS (2004); two pre-stack time-migrated seismic reflection surveys (Fig. 3.1B) are used covering a total area of 2090 km^2, imaging the Kendrew Trough, Madeleine Anticline, and Rankin Fault Zone, in the central and northern parts of the Dampier Sub-basin (Fig. 3.1B). The quality of the surveys varied, with the Mutineer_Exeter survey imaging the key seismic horizons, whereas the Demeter survey was of poorer quality and lacked reliable imaging of deeper horizons (Fig. 3.3). Two additional surveys (Panaeus 1 MCDMSS from 1997 and Panaeus 2 North MSS from 1998) surveys to construct basin-scale structural cross-sections (Fig. 3.3). We tied stratigraphic information from 20 wells (Fig. 3.1C & 3.1D) to seismic reflection data employing synthetic seismograms (Appendix 2). By interpreting key seismic horizons, we are able to: i) define the present basin structure; ii) determine the large-scale stratigraphic filling of the basin by calculating sediment thickness maps (i.e. isochrons); and iii) map the regional distribution of the Angel Formation. The five mapped horizons are; H1) an unconformity consisting of Top Athol Fm./Legendre Fm./Base Dingo Claystone; H2) Top Dingo Claystone merging with the underlying unconformity over structural highs; H3) Top Angel Formation; H4) Top Forestier Claystone; H5) Top Muderong Shale (Appendix 2). H1 and H2 are composite surfaces consisting of the post-rift Oxfordian Unconformity and base Angel Formation, respectively. H1 was only picked in the Mutineer_Exeter survey because of poor illumination and lateral connectivity of reflections in the Demeter survey (Fig. 3.4A). H2 over the Demeter survey is a low-confidence pick in the south away from well control, there is good confidence in all other picks.

3.5.2 Core data

An extensive core database (956 m of core from 22 wells; Fig. 3.1, Appendix 1) forms the sedimentological observations and interpretations that underpin our assessment of the main depositional processes and environments recorded within the Angel Formation. Each core was logged at a 1:50 scale, with emphasis on sediment texture and sedimentary structures, facies,

and the level and type of bioturbation (MacEachern & Bann, 2008; Knaust, 2017), the presence of accessory minerals, and the nature of bedding contacts.

3.5.3 Well-log data

Well-logs were calibrated to the core-based facies scheme to enable facies interpretation to be extended to all uncored intervals (45 wells, Fig. 3.1). Key well-logs included caliper (CAL), gamma-ray (GR), density (RHOB), neutron porosity (NPHI), sonic (DT), and deep resistivity (ResD). Core logs are tied to well-logs, with depth corrections made by linking high-value, positive spikes in the gamma ray log with mudstone-rich intervals. For well-log correlation, we applied biostratigraphic constraints to separate similarly aged sand-rich (<70 API GR) packages that we called units. These units are subdivided into subunits that represent individual beds or bedsets. Interpretation was guided by palynological data (which provided age constraints; see below) and gamma-ray log patterns. Detailed analysis of the well-log correlation panels allowed the relationship between sandstone unit thicknesses and paleotopography to be investigated, in addition to the rate of thickness change (RoC) between adjacent wells (Equation 1). The basal gradient is assumed based on a flat top of the Angel Formation. Where x is the difference in distance between two wells along the cross-section, and y is the thickness variation of the sand unit.

$$Equation\ 1: RoC = \frac{y_2 - y_1}{x_2 - x_1}$$

Regional mapping of the Angel Formation and mapping of discrete sand-rich fairways were made using a sand/mud ratio derived from gamma ray logs (i.e. >70 API = mudstone-dominated; <70 API = sandstone-dominated).

3.5.4 Palynology data

A palynological dataset (766 samples from 42 wells) provides a biostratigraphic framework to aid the correlation of stratigraphic intervals between wells. This includes six dinocyst zones and 13 dinocyst subzones across the Angel Formation (Fig. 3.5A), with each subzone estimated to represent an approximate duration of <250 kyr (Helby et al., 2004). The sample quantity and quality varied between wells. Samples are from core, sidewall core, and drilling cuttings, with sampling rates ranging from 10 cm up to 30 m intervals, typically with an irregular sampling density. Where we have a higher data resolution, we apply the Bint and Marshall (1994) scheme; however, these intervals are not traceable across the basin. Therefore, we have

combined multiple subzones from the scheme used in well reports (Bint & Marshall, 1994; Helby *et al.*, 2004) into four informal biozones (Fig. 3.6B) that can be identified in each well across the basin (from oldest to youngest): Biozone 1 spans an interval of ca. 1.5 Myr (6 subzones) and is comparable with the lower D.*jurassicum* and O.*montgomeryi* zones; Biozones 2 and 3 span ca. 0.75 Myr (3 subzones) and ca. 0.5 Myr (2 subzones), respectively, and split the upper D.*jurassicum*; Biozone 4 spans an interval of ca. 1 Myr (4 subzones) and is comparable to P.*iehiense*.

3.5.5 Architectural elements

Hierarchical schemes of architectural elements aid comparison of scales, processes, and stacking patterns across different datasets (Miall, 1988; e.g. Clark & Pickering, 1996), and have been developed for submarine lobe systems, a major component of submarine fan successions, using bounding surfaces marked by abrupt facies changes and thicknesses and/or lateral extent (Gervais *et al.*, 2006; Deptuck *et al.*, 2008; Saller *et al.*, 2008; Prélat *et al.*, 2009; Mulder & Etienne, 2010; Straub & Pyles, 2012; Prélat & Hodgson, 2013; Cullis *et al.*, 2018). We applied the widely adopted Prélat et al. (2009) scheme to the Angel Formation. Typically, one depositional event, such as a turbidite, is classed as a 'bed' (c. 0.5 m thick), and a few beds combine to a 'lobe element' (c. 2 m thick), lobe elements stack into a 'lobe' (c. 5 m thick), and multiple lobes stack into a 'lobe complex' (10's m thick). Thin-bedded finer grained 'interlobe' units (0.2-2 m thick) are interpreted as the distal lobe fringe of compensationally stacked lobes (*sensu* Prélat & Hodgson, 2013).

Here, we define sharp-based sandstone packages (~5 m thick) as lobes, which are grouped based on biostratigraphic subzones into lobe complexes. We used the four informal biozones to group the lobe complexes as 'lobe complex sets'. These lobe complex sets (*sensu* Prélat and Hodgson, 2013) are based on more regionally identified biostratigraphic picks. Given the biostratigraphic resolution and intense bioturbated nature of the fine-grained intervals, there is some uncertainty when discriminating between distal lobe fringe settings and more regional periods of reduced sand supply that are used in other studies to define strata that represent periods of reduced sand supply (e.g. Prélat *et al.*, 2009). Nonetheless, the approach combining lobe complexes into lobe complex sets where there are no significant regional breaks in sand supply is consistent with the identification of lobe complex sets at outcrop (e.g. Spychala *et al.*, 2017a), but with an added planform control of lobe complexes being sourced from axial and transverse margins during the same biozone. The persistent location, thickness, and duration

of the lobe complexes across multiple biozones (~3.75 Myr) were used to define multiple submarine fans that comprise the Angel Fm.

3.6 Results

3.6.1 Tectono-stratigraphic Evolution

The Dampier Sub-basin is characterised by a graben flanked by a relatively broad, flat shelf in the SE and several *en echelon* horst blocks in the NW (i.e. the Rankin Trend; Fig. 3.3). The horst blocks that define the Rankin Trend are eroded immediately adjacent to the block-bounding normal fault, suggesting that they have been subjected to fault scarp degradation (Fig. 3.3A). This erosion likely occurred during the syn-rift and/or early post-rift, similar to other NW Shelf examples (Bilal *et al.*, 2018; Barrett *et al.*, 2021). Five horizons (H1-5) (Fig. 3.3) divide the syn- to post-rift stratigraphy into four seismic units (SU1-4), that ultimately characterise the post-rift fill of the sub-basin (see below and Fig. 3.4).

SU1 (c. 165.6-152.1 Ma)

SU1 is bound by H1 and H2 and is only present within the axis of the sub-basin (i.e. it is absent on the flanking structural highs). Poor seismic imaging meant that we could not reliably map H1 in the Demeter survey; therefore, no surface map or isochrone could be made (Fig. 3.4A). In the North, the sub-basin is split into two depocenters separated by a central structural high (Fig. 3.3, A-A'). This central structural high is defined by a tilted fault block bound by a NW-dipping normal fault that terminates close to the northeastern end of the Madeleine Anticline (Fig. 3.1B).

SU1 onlaps onto the Rankin Trend (Fig. 3.4F) and central high (Fig. 3.3A) and does not thicken towards faults bounding the Rankin Trend. These observations suggest that fault movement ceased by the time this unit was deposited (i.e. the unit is early post-rift) and that accommodation was driven by thermal subsidence. In contrast, south-eastward thickening of SU1 (SE of the Pleiades 1 well; Fig. 3.3A) indicates that the eastern margin fault remained active at this stage.

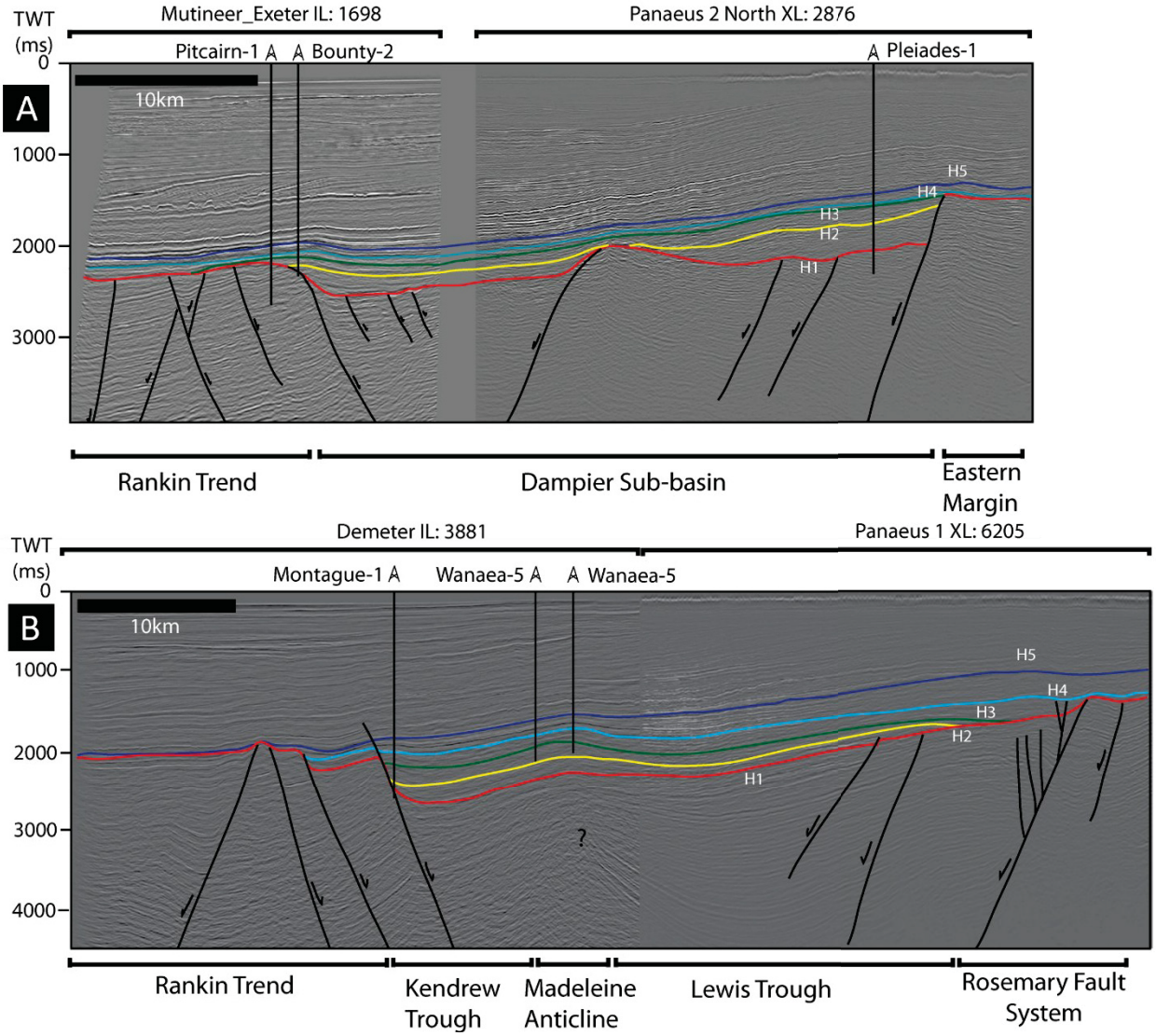


Fig. 3.3: *Line A-A', NW-SE seismic cross-section of the Dampier sub-basin in the northern section of the study area (see Fig. 3.1B for location). Line B-B'; NW-SE seismic cross-section in the central part of the study area. The Angel Formation lies between H2 and H3. Line locations illustrated in Fig. 3.1B.*

SU2 (c. 152.1-145.0 Ma)

SU2, which represents the Angel Fm. is the focus of this study and is bound by H2 and H3. SU2 is not present over the Rankin Trend, but thickens overall to the south, except across the

Madeleine Anticline where thinning is observed (Fig. 3.4G). SU2 thins more gradually against the Rankin Trend faults than SU1 and infills the degraded fault scarps of the Rankin Trend in the north (Fig. 3.3A). In the north, SU2 has a relatively consistent thickness, with minor thinning observed over the structural highs (Fig. 3.3A). In the south, minor thickening of SU2 toward the Rankin Trend and minor thinning over the Madeleine Anticline are observed alongside significant displacement and thickening across Rankin Trend faults (Fig. 3.3B).

In the north of the study area, SU2 documents the ongoing (over)filling of the sub-basin and the eventual burial of locally degraded, fault-bound structural highs typical of post-rift strata (e.g. Prosser, 1993). In contrast, in the south of the study area, SU2 thins over structural highs (e.g. across the Madeline Anticline), suggesting that these features had seabed relief during this time, possibly related to ongoing rift-related tectonics and/or passive infilling of relict relief. Significant steps in displacement and thickness across the southern Rankin Trend faults may highlight continued fault movement in the south of the basin at this time. Regional thickness trends in SU2 indicate an apparent palaeoslope dipping to the SW; this is important for our later assessment of the Angel Formation source area and depositional patterns.

SU3 (c. 145.0-137.9 Ma)

SU3 is bound by H3 and H4 and is widely deposited across the sub-basin. In the north, only very minor thinning over the structural highs is observed (Fig. 3.4H). In the south, SU3 thins over the Rankin Trend and the Madeleine Anticline (Fig. 3.3B). The widespread deposition of SU3 indicates complete filling of the sub-basin by this time, except over the largest horst blocks inherited from the preceding rift event (NW of Egret 3 well). Minor thinning over these structural highs indicates that accommodation was driven by thermal subsidence and/or differential compaction across underlying structures (Fig. 3.4H).

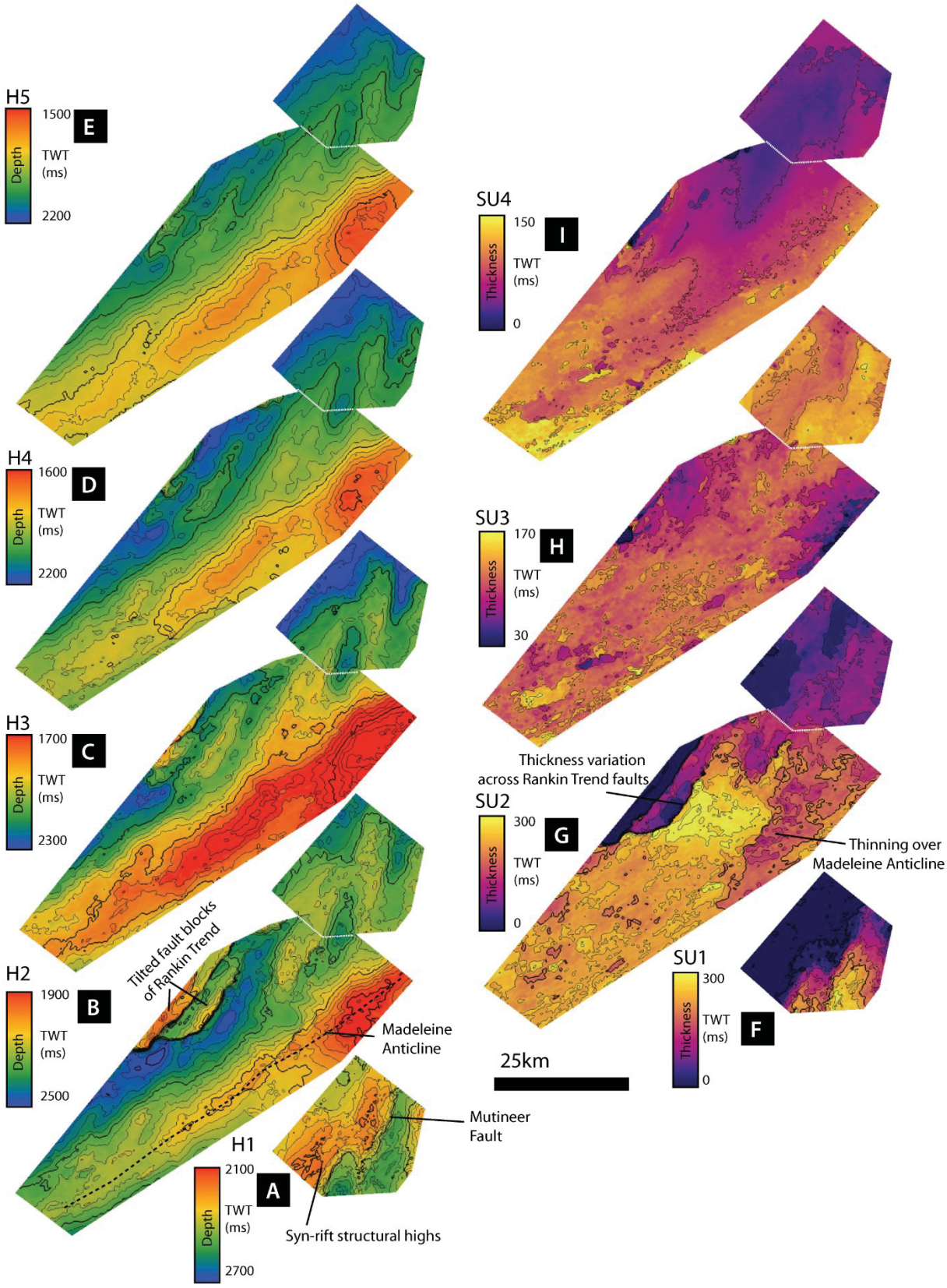


***Fig 3.4**: A-E) Depth structure maps of Horizon (H) 1-5. F-I) Isochron maps of Seismic unit (SU) 1-4. Contours at 40 m intervals. Map show a combined surface across two key surveys, white dashed line shows the survey join. Discrepancies across the surveys are due to the processing differences between the two surveys.*

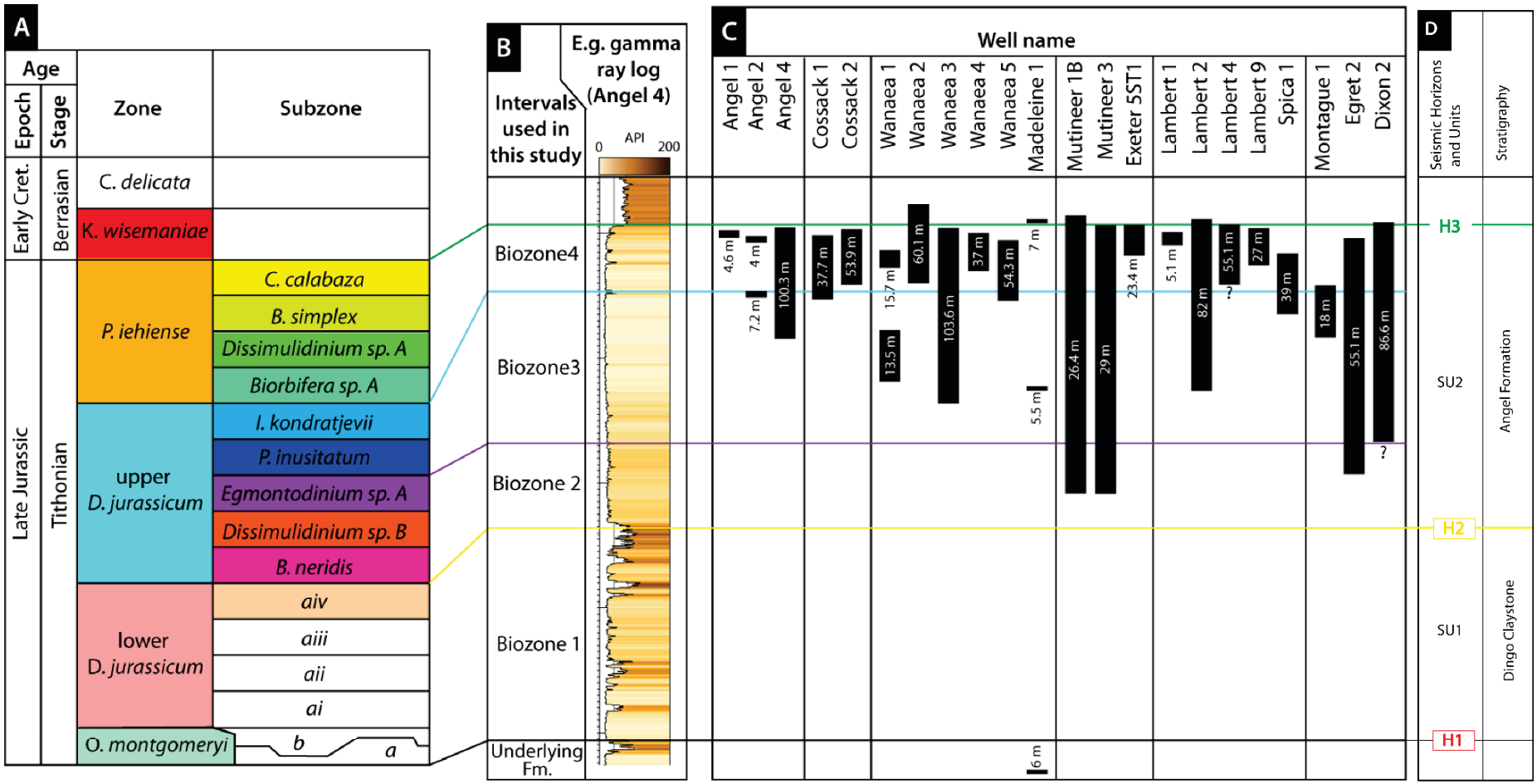


***Fig. 3.5**: A) Biostratigraphic zonation scheme used based off Bint and Marshall, (1991) and Helby et al., (2004), sub-zones are ca. <250,000 years. B) Intervals used in this study next to an example Gamma Ray log. C) Location of cored interval in proportion to bio*

SU4 (c. 137.9-123.3 Ma)

SU4 is bound by H4 and H5 and overall thins to the north (Fig. 3.4I). In the south, SU4 displays minor thinning over the Rankin Trend (Fig. 3.3B). Close to Montague 1 (Fig. 3.3B), local thickness changes across a normal fault identify SU4 as a period of minor fault reactivation in the South of the basin (Fig. 3.3B). Clinoforms prograding from the west indicate a change in sediment delivery (Fig. 3.3).

This unit represents the complete burial and peneplanation of the Dampier Sub-basin leading to a change in sedimentation pattern as the sub-basin is incorporated into the wider North Carnarvon Basin. Westward progradation of clinoforms due to sediments source from the Australian continent (cf. Deng & McClay, 2020).

3.6.2 Sedimentary facies analysis and well-log response

Sedimentary facies analysis was based on 956 m of core from 22 wells (Fig. 3.6) and identified 11 facies (Table 3.1). The facies are summarised below as well as their respective petrophysical properties support the interpretation of the Angel Formation having been deposited from a range of sediment gravity-flow processes within a sand-rich submarine lobe complex (further details in Table 3.1, facies listed in order of abundance and Fig. 3.6 & 3.7).

Two sandstone facies dominate the cored intervals (61%, Fig. 3.6): i) Massive Sandstone (SM: 46% of the cored intervals) facies comprise texturally- and mineralogically-mature, structureless sandstones, occurring in single beds (c. 1-3 m thick) that are ungraded or weakly graded, and which are commonly amalgamated to form units up to 30 m thick; and ii) Dewatered Sandstone (SDw: 15%) facies, which are compositionally similar to the SM sandstone, but is distinguished by abundant dewatering features, including consolidation laminae, dish and pipe structures and floating quartz granules. These two facies are interpreted as deposits of high-density turbidity currents, with the lack of internal structure, combined with.

Table 3.1: Core facies table

Facies code	Facies	Core Proportion (Total Thickness)	Lithology	Sedimentology	Thickness Range	Petrophysics (mean) (See Figure 9)	Interpretation
SM	**Structureless Sandstone**	46.9% (439.53 m)	Medium grained sandstone, rarely coarse-grained sandstone.	Massive sandstone, rare faint lamination. Typically, ungraded occasionally normally graded. Moderately to well sorted, sub-rounded to rounded. Common isolated floating quartz granules. Occasional floating organic matter, and mud clast. No bioturbation observed.	7 cm - 21 m	GR = 44 API RHOB = 2.38 g/cc Neutron = 0.145 m3/m3 DT = 88 US/ft ResD = 50.7 Ohm/m	Deposited by basal part of high-density turbidity currents (e.g. Lowe 1982) either en masse or by aggradation of flows with dampened turbulence due to high sediment concentrations.
BH	**Bioturbated Heterolithics**	26.3% (246.52 m)	Fine silt to medium sandstone	Mottled texture, poorly sorted, heavily to completely bioturbated (BI 5-6).	7 cm - 13.5s m	GR = 105 API RHOB = 2.48 g/cc Neutron = 0.178 m3/m3 DT = 83 US/ft ResD = 8.9 Ohm/m	Uncertain due to level of bioturbation, possible hemipelagic background/bioturbated thin beds/alternative sediment input.
SDw	**Dewatered Sandstone**	15.1% (142.02 m)	Medium grained sandstone.	Consolidation laminae, dish and pipe structures. Typically, ungraded occasionally normally graded. Moderately to well sorted, sub-rounded to rounded. Common isolated floating quartz granules. Occasional floating organic matter, and mud clast. No bioturbation observed.	10 cm -8.5 m	GR = 46 API RHOB = 2.42 g/cc Neutron = 0.145 m3/m3 DT = 82 US/ft ResD = 17.3 Ohm/m	Deposited by high density turbidity currents, high sedimentation rate lead to dewatering during or immediately after deposition(n Hurst and Cronin, 2001).
SCr	**Clast-rich Sandstone**	4% (37.4 m)	Medium grain sandstone with cm-mm sized clasts	Massive sandstone, ungraded. Cm-mm scale angular clasts often reverse graded, typically in bed tops, occasionally increase in detrital mud to bed top. Clasts can be angular to wispy laminations, comprised of mud or carbonaceous material. Clast occasionally show evidence of previous bioturbation.	10 cm - 1.4 m	GR = 66 API RHOB = 2.43 g/cc Neutron = 0.162 m3/m3 DT = 81 US/ft ResD = 19.8 Ohm/m	Clasts located at bed tops indicate flows were erosional updip with clasts segregated to the upper parts of flows (Haughton et al., 2003) or rip-down clasts related to dewatering (Johansson and Stow, 1995) or shearing from liquefaction of unconsolidated sand-rich beds creeping downslope.
SA	**Argillaceous Sandstone**	3.3% (30.95 m)	Claystone to medium grained sandstone	Chaotic mud-rich sandstone, no grading, poorly sorted, often heavily bioturbated (BI 2-6)	10 cm - 5.5 m	GR = 73 API RHOB = 2.5 g/cc Neutron = 0.146 m3/m3 DT = 87 US/ft ResD = 7.0 Ohm/m	Deposited by cohesive debris flow (Talling et al., 2012).
SDc	**Discontinuous Sandstone**	2.1% (19.23 m)	Medium grained sandstone	Massive, non-graded well sorted, low % detrital mud, laterally and vertically discontinuous, often ptygmatic, no bioturbation	mm - 10 cm	GR = 96 API RHOB = 2.48 g/cc Neutron = 0.172 m3/m3 DT = 81 US/ft ResD = 7.4 Ohm/m	Sand injectites from over-pressurised sandstone due to rapid burial, or unstable overburden. Observed within BH and SA
SS	**Structured Sandstone**	1.2% (11.13 m)	Fine to medium grained sandstone.	Mm scale argillaceous or carbonaceous planar to wavy laminations. Typically, normally graded. Well sorted, sub-rounded to rounded Structures are not preserved whole, either effected by bioturbation or shearing.	1 - 10 cm	GR = 55 API RHOB = 2.44 g/cc Neutron = 0.157 m3/m3 DT = 91 US/ft ResD = 21.8 Ohm/m	Deposited by low-density turbidity currents or waning high-density turbidity currents (e.g. Lowe, 1982; Hiscott, 1994)
SB	**Banded Sandstone**	0.6% (5.46 m)	Medium grained sandstone	Alternating cm - 3 cm scale bands of higher detrital mud and cleaner sandstone, occasionally crosscut by dewatering pipes.	40 -50 cm	GR = 62 API RHOB = 2.45 g/cc Neutron = 0.157 m3/m3 DT = 81 US/ft ResD = 8.0 Ohm/m	Slurry or banded hybrid-beds (Guy and Lowe, 2000: Haughton et al., 2009)
SG	**Granular Sandstone**	0.2% (2.11 m)	Coarse to granular sandstone	Massive, typically normally graded, occasionally inversely graded. Moderately sorted. No bioturbation.	30 cm - 90 cm	GR = 37 API RHOB = 2.34 g/cc Neutron = 0.141 m3/m3 DT = 84 US/ft ResD = 78.5 Ohm/m	Gravel lag deposits related to flow bypass (e.g. Gardner et al, 2003; Stevenson et al, 2015).
RB	**Remobilised Beds**	0.2% (1.97 m)	Silt and sandstone	High angle or folded beds	40 -50 cm	GR = 70 API RHOB = 2.50 g/cc Neutron = 0.166 m3/m3 DT = 79 US/ft ResD = 51.5 Ohm/m	Soft sediment deformation or slumping.
M	**Mudstone**	0.2% (1.43 m)	Claystone to fine silt	Occasionally laminated, Typically bioturbated (BI 3-6). Occasional siderite cementation.	5 cm - 40 cm	GR = 70 API RHOB = 2.69 g/cc Neutron = 0.170 m3/m3 DT = 73 US/ft ResD = 51.5 Ohm/m	Hemipelagic background deposition or deposits by dilute turbidity currents (Boulesteix et al., 2019). Increased anoxic conditions decreasing biogenic activity.

the abundance of dewatering structures, reflecting very high rates of sediment deposition and/or hindered settling in traction carpets (Lowe, 1975; Sohn, 1997).

Bioturbated Heterolithic (BH: 26%) facies represents the second most common facies and consists of an intensely bioturbated (Bioturbation Index, BI, 5-6 of MacEachern and Bann, 2008) mixture of siltstone to medium-grained sandstone of varying proportions, with a mottled fabric. Individual beds are difficult to discern, probably because of the lack of preservation resulting from intense bioturbation (Fig. 3.6). For example, subtle changes in mottled fabric

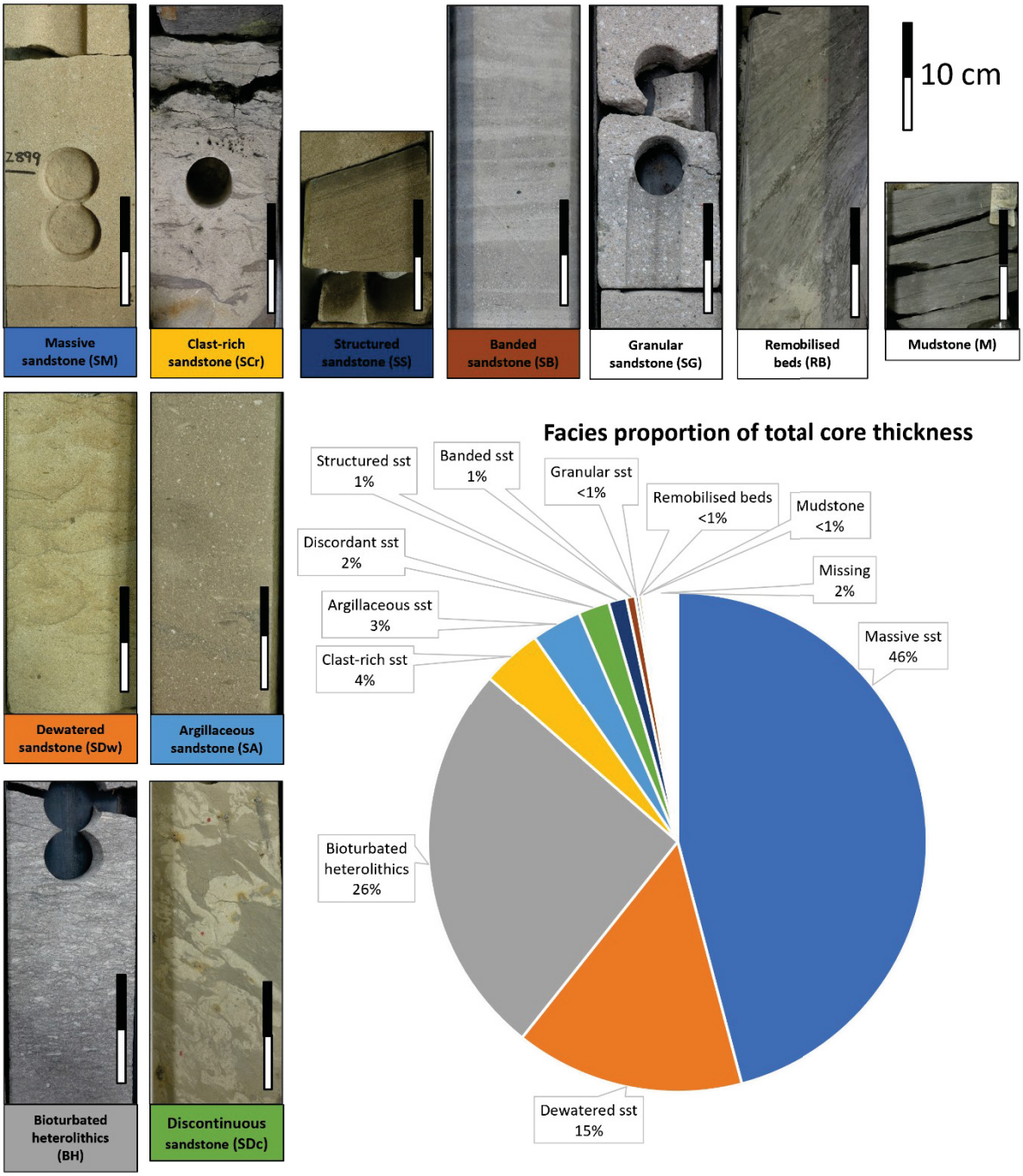


Fig. 3.6: *Representative core facies images with a pie chart highlighting the facies proportions of total core thickness*

colour suggest remnants of thin beds (<5 cm thick). Intervals with a lower bioturbation index (BI = 4) preserve examples of *Chondrites*, *Planolites*, *Thalassinoides*, and *Zoophycus* trace fossils. The ichnofauna suggests a tiered system of Cruziana to Nereites ichnofacies, which supports an offshore to basin floor environment (Seilacher, 1967), whereas the low diversity of ichnofacies suggests relatively stressed conditions, possibly caused by frequent and relatively rapid sedimentation (Wetzel, 1984). Intercalation of the BH facies with the SM and SD facies across sharp facies breaks on a decimetre to meter scale (Fig. 3.8) supports their close genetic relationship, with the finer-grained BH facies consistent with an overall lower energy and more distal setting. The high frequency and intensity of bioturbation support a rapid re-establishment of infauna after deposition and/or long periods of non-deposition between depositional events in a well-oxygenated setting with abundant nutrient supply.

The remaining eight facies are subordinate, accounting for only 13% of the total cored intervals. They comprise seven sandstone-rich facies (SCr, SA, SDc, SS, SB, SG, and RB) and one mudstone-rich facies (M) (Table 1). The five sandstone-rich facies (SCr, SDc, SS, SB, SG) are genetically linked to high-density turbidites (SM and SDw) and provide a more detailed understanding of related flow processes. For example, clast-rich sandstones (SCr) are interpreted to record updip erosion and entrainment of seabed material before their deposition as linked debrites (e.g. Haughton *et al.*, 2003). Banded sandstones (SB) are interpreted as representing transitional or hybrid flows (e.g. Haughton *et al.*, 2009; Stevenson *et al.*, 2020) (e.g. Haughton et al., 2009; Stevenson et al., 2020). In contrast, structured sandstones (SS) include planar and current ripple cross-lamination at the top of high-density turbidites, and are interpreted as waning low-density turbidity current deposits (Lowe, 1982; e.g. Hiscott, 1994). Other facies comprise debris flows (SA), remobilised beds (RB), and sandstone injectites (SDc), which support previous interpretations of relatively rapid deposition, including the development of overpressure, dewatering, and remobilisation (Hurst & Cronin, 2001). The

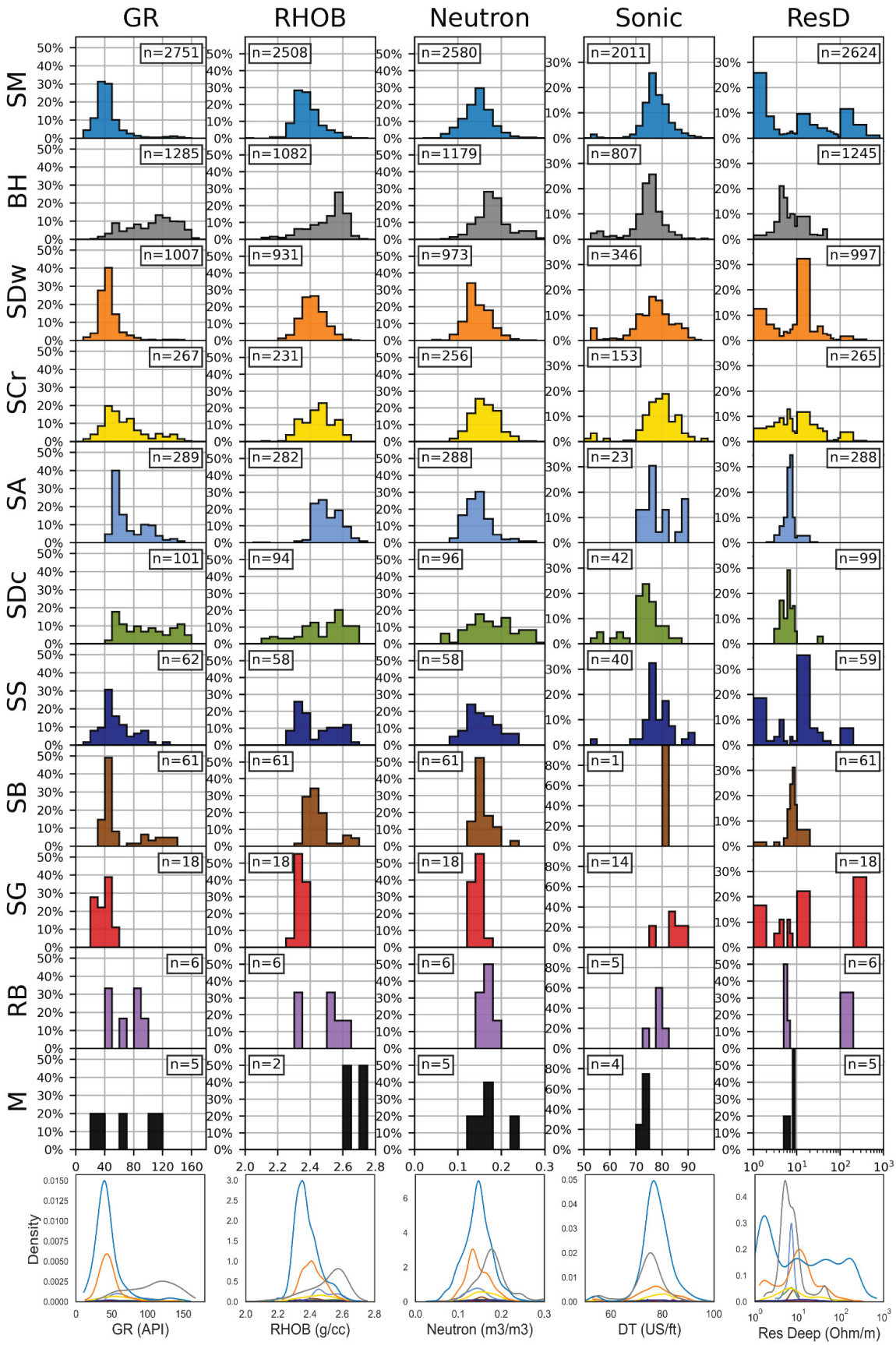


Fig. 3.7: *Summary of petrophysical properties of cored interval of Angel Fm. facies highlighting the skew of data towards massive and dewatered sandstone and bioturbated heterolithics, and the challenge in distinguishing the limited depositional variability across the Angel Fm.*

abundant in some of the uncored intervals, which regionally encase coarser-grained, sandstone-dominated facies. Overall, these facies record deposition from a range of gravity flows, which is shown later to have occurred in a sand-rich submarine lobe complex setting.

3.6.3 Facies associations: sedimentology, distribution and petrophysics

The 11 facies were grouped into four facies associations (FA), with characteristic vertical facies and well-log patterns (Fig. 3.8). i) FA1: lobe axis (comprising 52% of the gross cored interval), ii) FA2: lobe off-axis (17%), iii) FA3: proximal lobe fringe (13%), and iv) FA4: distal lobe fringe (18%). These are discussed below in terms of their facies proportions, thickness, distribution, and petrophysical characteristics (Fig. 3.7). Petrophysical analysis (Fig. 3.7) at the facies scale highlights the difficulty of expanding our facies-level interpretation beyond the cored intervals. By upscaling to a facies association-level interpretation, we applied our interpretation to uncored intervals based on gamma-ray log character and inferred bed thickness (Figs. 3.8 and 3.9). The overall trend from FA1 to FA4 reflects a decrease in sandstone occurrence away from the lobe axis and towards mudstone-rich distal lobe fringe settings. This is analysed further in terms of vertical and lateral relationships of the four FAs.

3.6.3.1 FA1: Lobe axis

Observations: FA1 is sandstone-rich and consists of medium-to coarse-grained, ungraded to weakly normally graded sandstone (SM 72%, SDw 20%) with centimetre-thick granular layers (SG facies). Other sand-rich facies (SG, SCr, SA, SDc, SB, c. 3% total) and mud-rich facies (BH and M, c. 3%) were less common. Typically, SM and SDw are amalgamated to form 5-15 m-thick packages (Fig. 3.8). FA1 is dominant in the east around the Angel wells (Fig. 3.9), generally decreasing in proportion towards the SW (Fig. 3.10).

Interpretation: The dominance of SM and SDw facies, and the presence of erosional bed bases and rare granular layers (SG facies), are consistent with deposition by high-density turbidity currents (eg. Lowe, 1982; Ilstad *et al.*, 2004; Breien *et al.*, 2011). Intervals containing repeated dewatering features suggest deposition by multiple flows, with cryptic amalgamation surfaces

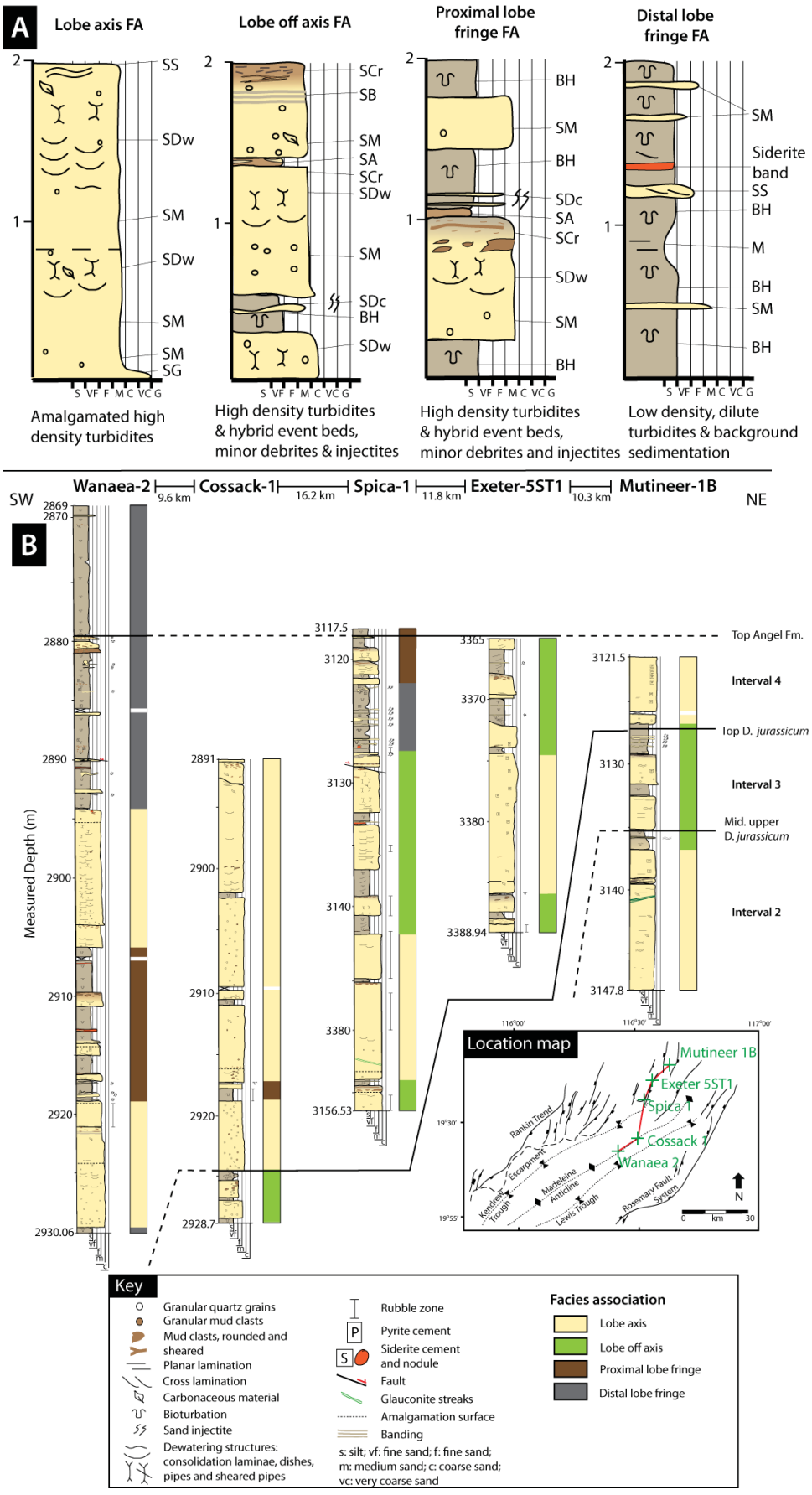


Fig. 3.8: *A) Facies make up of facies associations. B) Correlated core cross-section through the Dampier sub-basin (NE-SW) with interpreted facies associations. Sand bodies are not correlated due to distance between wells.*

eroding into now-truncated, dewatered bed tops (e.g.Wanaea-2, Fig. 3.8B). Amalgamation of

sandstones into up to 30 m-thick packages suggests that any finer-grained facies was eroded and redeposited down-dip into deeper water; this is supported by rare granular facies interpreted to record sediment bypass-related gravel lags (Gardiner, 2006; Stevenson *et al.*, 2015). The blocky well-log response is consistent with the textural and mineralogical homogeneity, plus relatively uniform rock properties. The sandstone-rich character of FA1, and the dominance of deposition from high-density turbidites with high levels of amalgamation, is consistent with deposition in a lobe axis sub-environment (Prélat *et al.*, 2009), including the likely amalgamation of multiple lobes into lobe complexes where >10m thick.

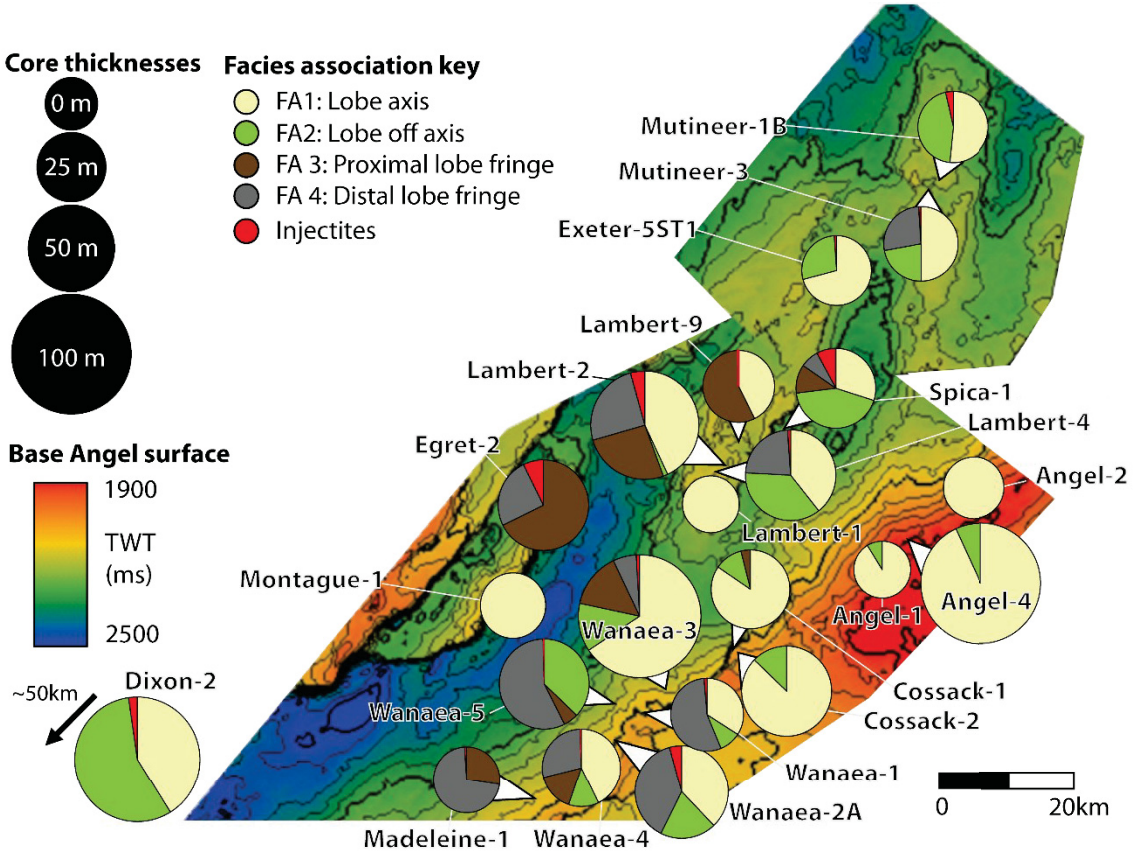


Fig. 3.9: *Base Angel Fm. surface highlighting location of cores and the relative thickness of the cored intervals and facies association proportions*

3.6.3.2 FA2: Lobe off-axis

Observations: FA2 is also sandstone-rich, consisting mainly of (i) 0.5-5 m-thick sandstone beds and bedsets, the latter formed through the cryptic amalgamation of individual beds (Fig. 3.8), and (ii) thinner interbeds of finer-grained and more mud-rich facies with a diverse range of facies types. The overall facies occurrence is much more diverse compared to FA1: SM (38%), BH (25%), SDw (20%), SCr (9.9%), SB (2.7 %), SS (1.6%), and SA (0.8%). Many of the

thinner interbedded sandstones display primary sedimentary structures, or more argillaceous, clast-rich bed tops (e.g., SB and SCr). FA2 is apparently most common in the NE (Mutineer area) and towards the centre of the study area (Fig. 3.9). FA2 is defined by low, blocky GR well-log pattern, with thin intervals of higher GR likely corresponding to the interbedded, bioturbated, more heterolithic facies (Fig. 3.8).

Interpretation: Sandstone beds with sedimentary structures or beds with more argillaceous, clast-rich bed tops (e.g. SB and SCr) are interpreted to be deposited by high-density turbidity currents and hybrid event beds, such as turbidites with linked debrites, respectively (e.g. Haughton *et al.*, 2003; Talling *et al.*, 2012). The wider array of facies types, thinner sandstone beds, and higher argillaceous content places FA2 in a relatively lower and more variable energy setting compared to FA1. In addition to the lower sand proportion, relatively minor bed amalgamation (including preserved bed tops), the presence of banded beds (SB), and frequent interbedding with BH facies, supports a reduction on the size and frequency of individual gravity flows. The vertical and lateral distributions of FA1 and FA2 suggest their close physical relationship (Figs. 3.11 & 3.12), which supports the interpretation that FA2 represents a lobe off-axis environment (Prélat *et al.*, 2009).

3.6.3.3 FA3: Proximal lobe fringe

Observations: FA3 is the least common facies association in the Angel Formation, with the main facies components being BH (c. 50%), SM (c. 30%) and SDw (c. 10%). Sandstone beds are typically normally graded, <0.5 m thick, medium-grained, and topped by planar and minor ripple-scale cross-lamination (Fig. 3.9A). Sandstones are interbedded with intervals of BH. FA3 is also characterised by <5 cm thick zones of sub-vertical, ptygmatically folded injectites (SDc, 3%). FA3 is commonly observed in the west, with injectites most frequently observed in close proximity to underlying faults (Fig. 3.9B, e.g. Egret-2). FA3 exhibits a serrated GR well-log character (Fig. 3.11).

Interpretation: The overall increase in finer-grained facies, most notably BH facies, and the frequent preservation of primary sedimentary structures implies a lower energy depositional environment with a lower rate of sediment supply compared to FA1 or FA2. The increase in mudstone-rich facies (BH and M), and the lack of sandstone bed amalgamation and are also consistent with a more distal setting. The overall facies characteristics and their close physical relationship with FA1 and FA2 leads to the conclusion that FA3 was deposited in a proximal lobe fringe environment. The paucity of thin beds (<5 cm) that are typical of such settings

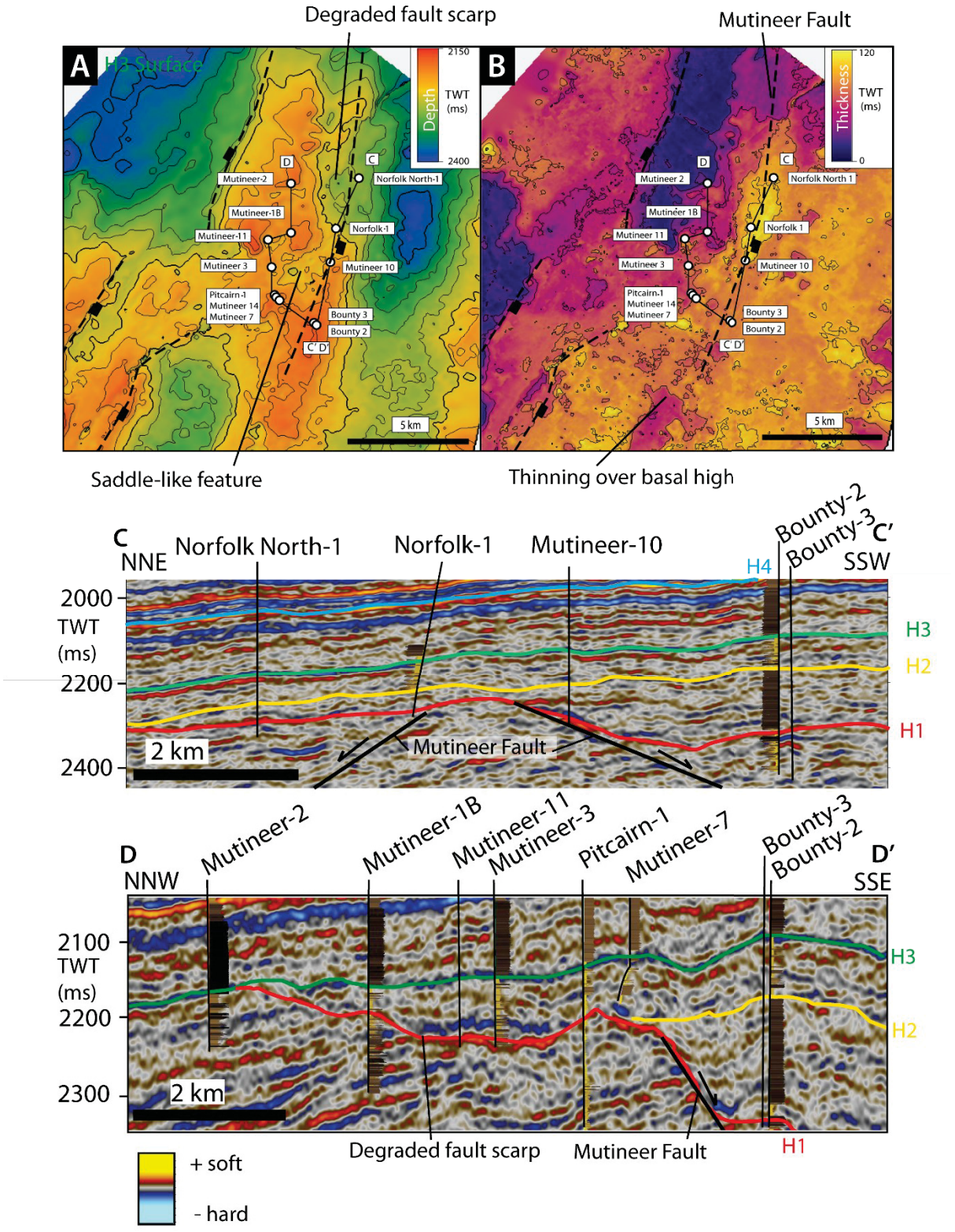


Fig. 3.10: *A) Enlarged base Angel Fm. (H2) depth map of the Mutineer area (Fig. 3.1D). Dashed lines indicate underlying normal faults. B) Isochron thickness map of SU2. C-C'; seismic cross section from Norfolk North 1 to Bounty 3. D-D' seismic cross section from Mutineer 2 to Bounty 2. Wells showing gamma ray logs are tied to seismic, wells without sonic logs are shown as an approximate location (black line). Horizons are colour-coded, as shown in Fig. 3.3.*

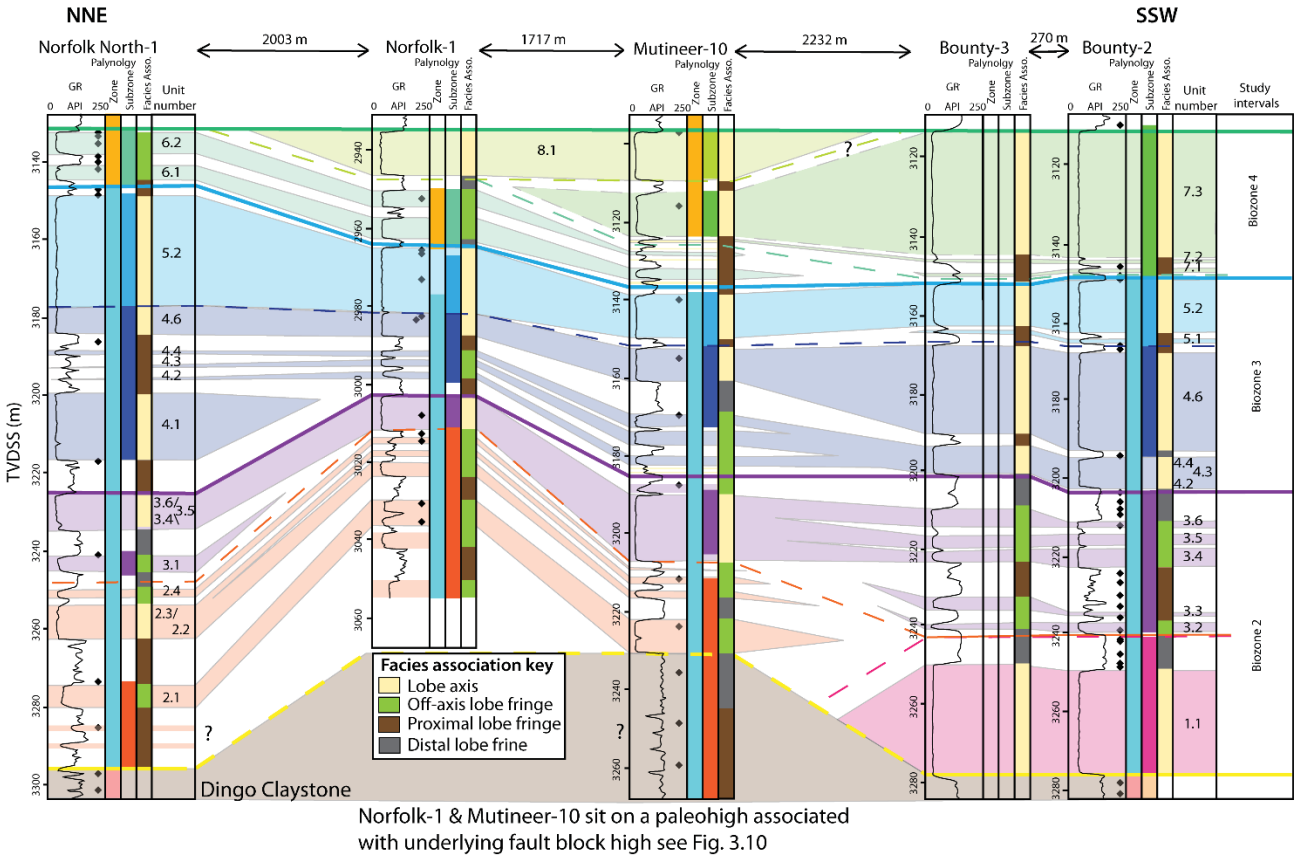


Fig. 3.11: *Correlated well cross-section of Fig. 3.10 C-C' of SU2 (yellow to green horizons). Biostratigraphic zones are correlated using palynology sample points (black diamonds) and are colour-coded by palynological subzones (as Fig. 3.5). Flattened on top of Tithonian-aged sandstone. Palynology and gamma ray characteristics were used to correlate sandstones where possible. Possible advancing pinch out in Biozone 3 and compensational stacking in Biozone 4.*

(Spychala *et al.*, 2017c; Boulesteix *et al.*, 2019) may reflect a combination of high levels of bioturbation, confined basin topography with reduced runout of gravity flows and/or the sand-rich nature of the flows causing rapid flow collapse.

3.6.3.4 FA4: Distal lobe fringe

Observations: FA4 comprises moderately thick intervals (>5 m) of BH (c. 90%), c. 7% SDc and the largest proportion of M (0.8%) that locally contains siderite-cemented zones. Within FA4, BH is typically poorer in sandstone with a lower BI (3-5 BI) than FA3 (distal lobe fringe). Commonly, *Chondrites* are the only trace fossil present. FA4 is dominant in the SW, with injectites (SDc) most common in these areas or close to underlying faults (Fig. 3.9). Petrophysically, this FA has the highest GR response and has a smooth to slightly serrated character (Fig. 3.11).

Interpretation: The dominance of facies deposited by dilute turbidity currents (i.e. BH) and hemipelagic fallout (i.e. M) suggests an overall lower-energy depositional environment. The increase in finer-grained-rich facies (BH and M) and decrease in sandstone beds (Fig. 3.8),

relative to FA1-3, suggest that FA3 was deposited in a more distal location and represents the lowest energy FA observed in this study. FA4 is interpreted to represent the distal fringes of lobes or record periods of regional decreases in sand delivery to the basin. Local decreases in bioturbation intensity and diversity may suggests stressed conditions caused by the shutdown of sand-delivery and nutrients to the deep-water, and a more reducing environment supported by the presence of siderite. These interpretations are consistent with FA4 recording deposition within a slope-to-basin floor during a hiatus of sand supply (Boulesteix *et al.*, 2020, 2022).

3.6.4 Vertical and lateral relationships between facies association

We investigated the vertical and lateral relationships between the facies associations described above using two approximately N-S oriented, well-log correlation panels (Figs. 3.11 and 3.12; see location of panels C-C' and D-D' in Fig. 3.10). Our interpretations are based on the integration of three elements to construct a framework: i) units, which are defined by biostratigraphically (palynology) constrained stratigraphic surfaces of known age (subzones; Fig. 3.5A); ii) core- and log-based facies associations, enabling a genetic stratigraphic interpretation of both sections of wells that are cored and those which are not (e.g. Fig. 3.8), and iii) well-log driven correlations of the main sand bodies, based on thickness and GR log character, which allows us to subdivide the succession into sub-units (e.g. 3.1-3.6, etc.), and that can be applied to reservoir-scale mapping and lateral sand body pinch out rate estimations. We have identified 8 informal units based on biostratigraphic data (Fig. 3.5A), and 4 biozones using the most regionally extensive biostratigraphic picks. The biozones are typically at a lobe complex scale in terms of thickness (c. 20-50 m at thickest point), whereas the sharp based and topped sandstone sub-units (e.g. 4.1, 4.2, 4.3) are typically at a lobe axis scale (c. 5-15 m thick) (Prélat et al., 2009). In some cases, sub-units (eg. 1.1, 4.6, 5.2, 7.3 in C-C', Fig. 3.11) exceed this (c. 20-30m) and likely form lobe complexes in themselves. These interpretations provide a stratigraphic framework for reservoir mapping (Figs. 3.13 and 3.14). Panel C-C' (Fig. 11) orientation (NNE-SSW) is slightly oblique to the paleoflow direction (NE to SW) and includes the Mutineer Fault, which underlies the Norfolk-1 and Mutineer-10 wells (Fig. 3.10C). Panel D-D' (Fig. 3.12) orientation (NNW-SSE) is close to perpendicular to paleoflow (from NE to SW) that steps onto the footwall of the Mutineer Fault between Bounty-3 and Mutineer-7 (Fig. 3.10D). The base of the Angel Formation to the north of Mutineer-7 forms a rugose surface (Fig. 3.10D), which is interpreted as a degraded fault scarp (discussed earlier). This rugose basal surface has a prominent basal high around Mutineer-14 and Pitcairn-1 (Fig. 3.10D) with a saddle-like feature between Pitcairn-1 and Mutineer-1B.

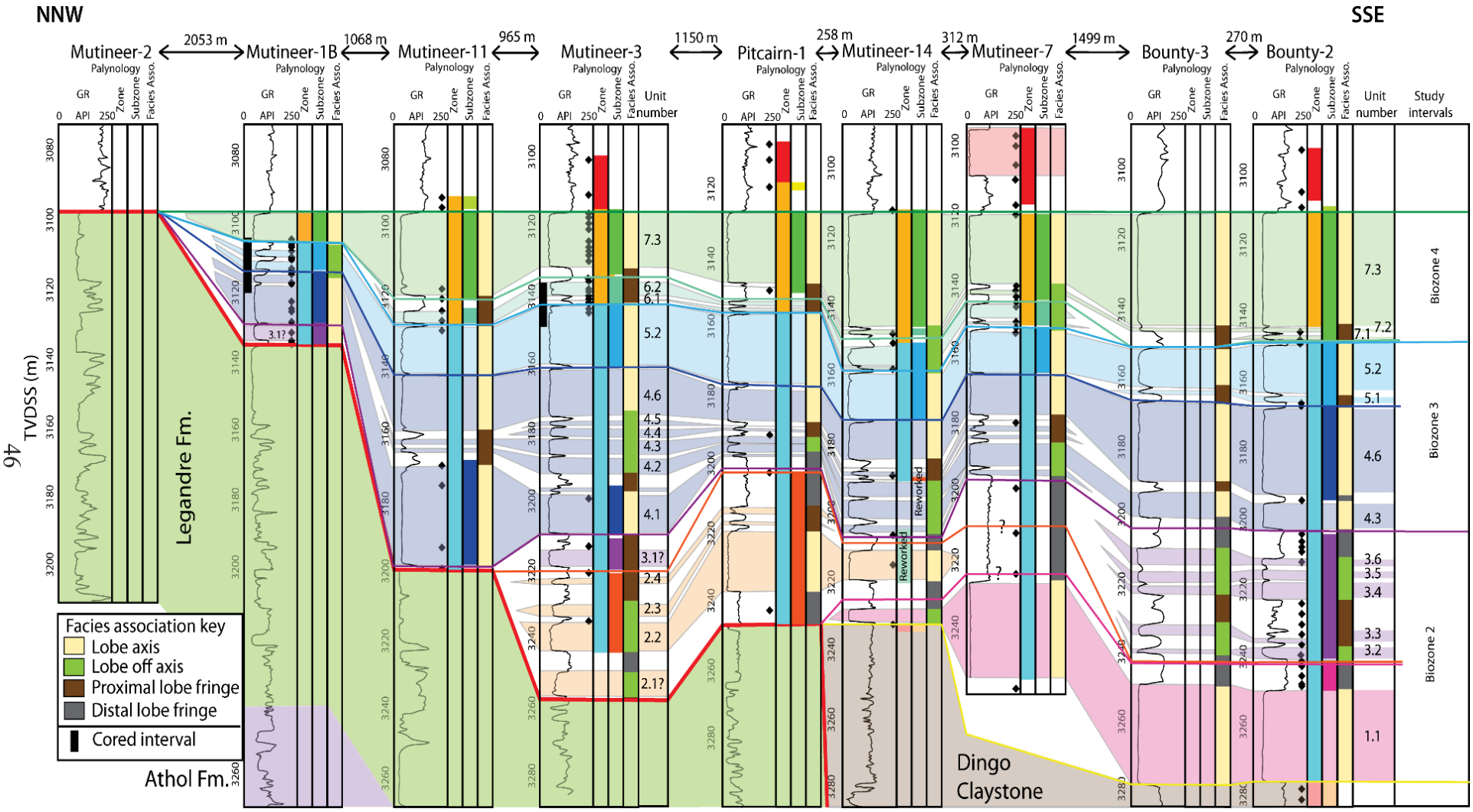


***Fig. 3.12**: Correlated well cross-section of Fig. 11 D-D' of SU2 (Green to red/yellow horizons.. Biostratigraphic zones are correlated using palynology sample points (black diamonds) and are colour coded by palynological subzone (as Fig. 6). Flattened on top Tithonian-aged sandstone. Palynology and gamma ray characteristics used to correlate sandstones where possible.*

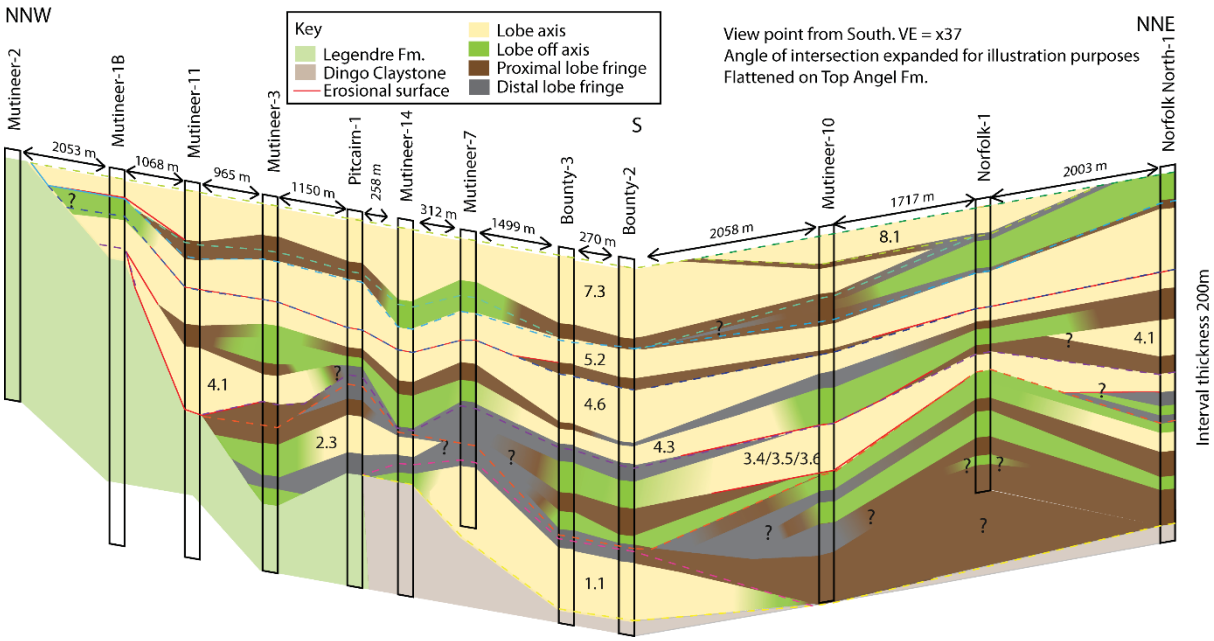


Fig. 3.13: *Mutineer pinch-out in 3-dimensions highlighting the changes in sub-environment and stacking pattern. Dotted colours lines relate to biostratigraphic intervals, colour coded to Fig. 3.6.*

Observations: Initial deposition of sandstone units was restricted to the sub-basin underlain by the Dingo Claystone (Unit 1, Fig. 3.11 & 3.12). Sub-units 2.1-3.1 were deposited within the sub-basin in the north and restricted to the degraded fault scarp in the west. Sub-units 3.2-3.6 were deposited within the sub-basin. Sub-unit 4.1 was restricted to the degraded fault scarp area. Sub-units 4.2- 8.1 are widely deposited across the sub-basin and the degraded fault scarp. Sub-units 4.1, 4.6 and 5.2 show evidence of amalgamation in Mutineer-1B and Mutineer-11.

Typically, sub-unit facies associations transition laterally from lobe axis through lobe off-axis to proximal lobe fringe and finally to distal lobe fringe (Fig. 3.13). The most varied lateral transitions are associated with the thinner sandstone sub-units (e.g. Units 4.2-4.4). In lower sub-units (e.g. Unit 1.1) close to topography, we observe the lobe axis transition to lobe off-axis and then pinch out. In upper sub-units, we commonly observe minimal facies transitions associated with the lobe axis (e.g. Unit 7.3). Lateral transition from proximal lobe fringe to distal lobe fringe are difficult to reliably correlate but is observed, for example between sub-units 4.4 and 4.6 in Mutineer-10 and Norfolk-1 (Fig. 3.11).

Overall, the Angel Formation does not display a clear trend in vertical stacking patterns (Table 2). The most common upward transition is lobe axis overlying proximal lobe fringe. The least common upward transitions are from proximal lobe fringe to distal lobe fringe and vice versa.

Transtion Matrix		Overlying FA			
		FA1: LA	FA2: LOA	FA3: PLF	FA4: DLF
Underlying FA	FA1: LA	-	14	12	13
	FA2: LOA	16	-	11	16
	FA3: PLF	25	10	-	7
	FA4: DLF	14	16	4	-

Table 3.2: *Transition matrix of facies associations.*

Interpretation: Initial depositional patterns are interpreted to be strongly controlled by topography with preferential infill of topographic lows within the basin and the saddle-like feature. Unit 2 and sub-unit 4.1 that initially infilled the saddle-like feature appear to be diverted onto the degraded fault scarp around Norfolk North-1. Erosion of units deposited on the degraded fault scarp is common (Fig. 3.13). Subsequent sub-units are interpreted to be less effected by the basal topography with aggredational and compensation stacking patterns (Units 4 to 8).

The vertical distribution of sub-environments that switch from proximal lobe fringe to axis deposits FAs is interpreted to record increase in sediment supply after a period of reduced sediment supply as opposed to the typical compensational stacking model which is discounted due to confining topography (*sensu* Cumberpatch *et al.*, 2021b).

There are two styles of lateral transitions observed: (i) minimal FA change with abrupt pinch out of sandstone units, which is interpreted as a simple onlap pinch out style (Bakke *et al.*, 2013; Patacci *et al.*, 2014) that is common in thicker sandstone sub-units (lobes); and (ii) gradual lateral FA transitions from FA1 through to FA4 with a more tapered pinch out (Patacci *et al.*, 2014).

The depositional nature of the sandstones within the Angel Fm. *ie*. lack of erosion surfaces and lag deposits and tabular nature of the sandstones suggest a lobe depositional environment is preferred. Minor lobe distributary channelisation (eg. 8.1) indicating lobe progradation.

Rates of Change	Distance along D-D' (km)									
m/km	0	2.053	3.121	4.086	5.236	5.494	5.806	7.305	7.575	**Maximum thickness (m)**
	Mutineer-2	**Mutineer-1B**	**Mutineer-11**	**Mutineer-3**	**Pitcairn-1**	**Mutineer-14**	**Mutineer-7**	**Bounty-3**	**Bounty-2**	
Unit 7	-3.78	-14.83	8.69	-4.28	-52.36	37.53	-9.43	2.59	n/a	36.07
Unit 6		-3.14	-0.31	2.14	-15.00	1.44	2.36	1.93	n/a	5.06
Unit 5	-1.70	-8.93	-4.98	-1.57	24.96	2.56	0.79	-12.59	n/a	19.66
Unit 4	-6.38	-33.62	11.41	17.40	-21.55	3.91	-5.35	-5.63	n/a	49
Unit 3	-2.08	3.99	-11.81	9.91			-11.61	9.74	n/a	17.41
Unit 2			-17.46	-8.65	71.05	27.15			n/a	26.8
Unit 1					-14.46	-75.74	-1.12	10.52	n/a	29.04
Total unit ROC	-13.94	-56.54	-14.47	14.95	-7.36	-3.14	-24.36	6.56		
Total gross sandstone thickness ROC	-35.94	-11.49	13.51	1.12	-7.26	25.05	-6.25	3.16		
Angel Fm ROC equivalent to basal gradient(m/km)	-18.89	-60.52	-38.94	18.64	1.78	-50.13	-21.22	1.74		
Basal gradient (deg)	1.08	3.46	2.23	1.07	0.10	2.87	1.22	-0.10		

***Table 3.3**: Lateral rates of change of sand units between wells along D-D'. ROC is calculated towards the pinchout i.e from Bounty-2. E.G. Mutineer-2 ROC is from Mutineer-1B to Mutineer-2. Orange indicates maximum rate of change. Green indicates minimum rate of change.*

3.6.5 Lateral rates of change

Sandstone thicknesses for each unit (i.e., lobe complex-scale; *sensu* Prélat et al., 2009) were used to calculate rates of change (RoC, Equation 1) for each unit along D-D' (Fig. 3.12) to investigate the effect of lateral topography (Table 3.3 and Fig. 3.14). We focused on the rate of change (RoC) towards the pinch out in the Mutineer area, along transect D-D' (Fig. 3.12), extending for c. 7.6 km from Bounty-2 in the south to Mutineer-2 in the north. The results are shown in Fig. 3.14, with positive and negative values indicating thickening and thinning towards the pinch out, respectively. Slope angle was calculated assuming a flat top to the oldest Tithonian-aged sandstone unit (Fig. 3.14, Unit 7).

Calculating the total Angel Formation thickness including interbedded mudstones provides an overview of the pinch out with a RoC of -24 m/km onto an average linear slope of 1.39° (Bounty-3 to Mutineer-1B), with total gross sandstone thickness assuming all thinning is due to topography. However, such a trend is not linear and is impacted by the rugosity of the basal surface (Fig. 3.10A). Hence, more precise estimates are required for the pinch out at the lobe and lobe complex level.

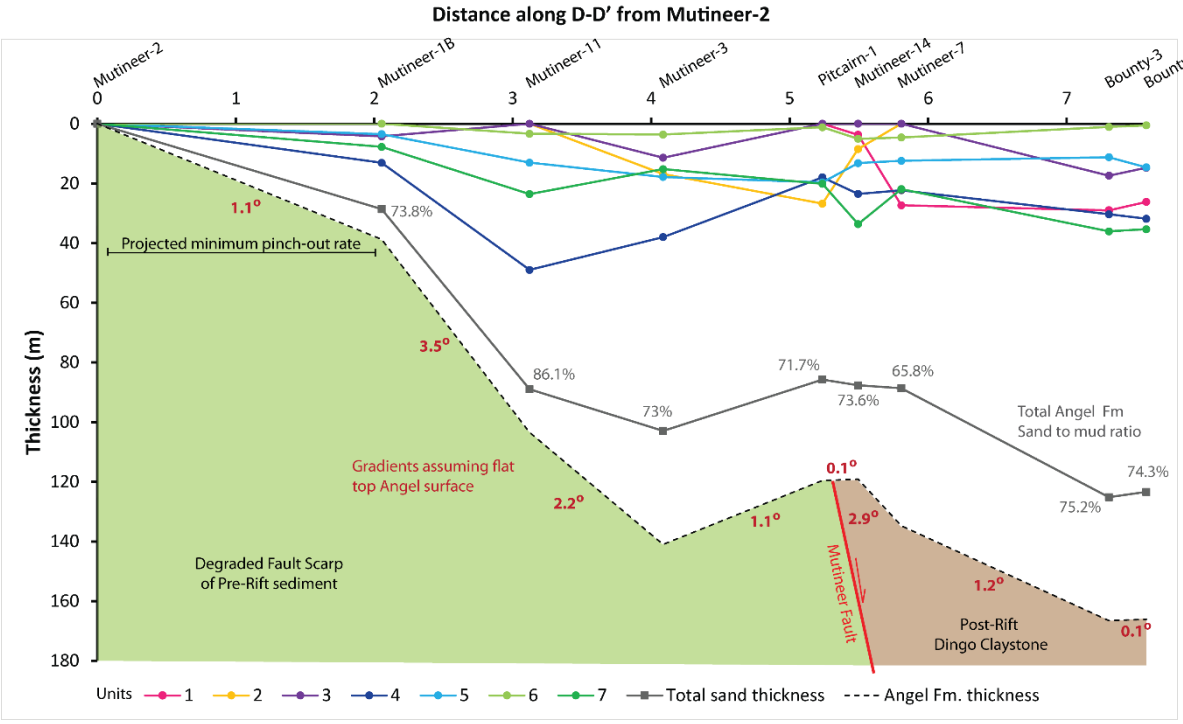


Fig. 3.14: *Lateral thickness changes of lobe complexes (Units) in Mutineer area highlighting rapid variations in thickness. Unit relative thicknesses displayed. Basal gradients in red. Total sandstone thickness in grey with sandstone percentage. Numbered lines correspond to Unit numbers as in Fig. 3.12 and 3.13.*

The lowermost Units (1 & 2), which are directly in contact with basal surface, are where the largest RoC are observed (-70 to -75 m/km, Table 3). Unit 1 abruptly pinches out against the Mutineer Fault basal high around Mutineer-14 (Fig. 3.14), whereas Unit 2 pinches out in the opposite direction infilling part of the degraded fault scarp. Unit 3 has a limited expression likely due to no axial deposits in the Mutineer area. Unit 4 displays rapid RoCs when directly deposited on the degraded fault scarp. In Units 1 to 4, the trend of largest RoC shifts from Muntineer-14 to Mutineer-1B, moving towards the pinch out as basin was healed (highlighted orange, Table 3.2, Fig. 3.14).

The highest RoC in the overlying Units 5, 6 & 7, are observed in Pitcairn-1 which directly overlies the Mutineer Fault. In these units, the largest ROC above the Mutineer Fault may have acted as a hinge point between the deposits within the sub-basin and those on the degraded fault scarp. In this scenario, it would signify greater available accommodation within the sub-basin likely due to increased compaction.

Despite the high degree of variability at the unit scale (described above) the overall sandstone percentage displays minimal variability up to the pinch out 74.3% and 75.2% in Bounty 2&3 respectively to 73.8% in Mutineer 1B (closest well to the pinch out). The highest overall sandstone percentage (86.1%) is closest to the pinch out at Mutineer-11.

3.6.6 Sandstone distribution

We have established the main sand fairways based on well-based interval thickness and gross facies trends across the sub-basin, constrained by the chronostratigraphic framework represented by the four biozones (Figs. 3.15 and 3.16). The preceding facies analysis has linked sandstone percentage and depositional environment as follows: (i) >75% = lobe axis), (ii) 75-50% = proximal lobe fringe, (iii) 50-25% = distal lobe fringe, and (iv) <25% = slope to basin floor. In map view (Fig. 3.17), each biozone, describes the sandstone distribution at a lobe complex set scale (*sensu* Prélat & Hodgson, 2013). The persistent location and duration of deposition across biozones (~3.75 Myr) and different stacking patterns supports the identification of submarine fans that comprise multiple lobe complexes.

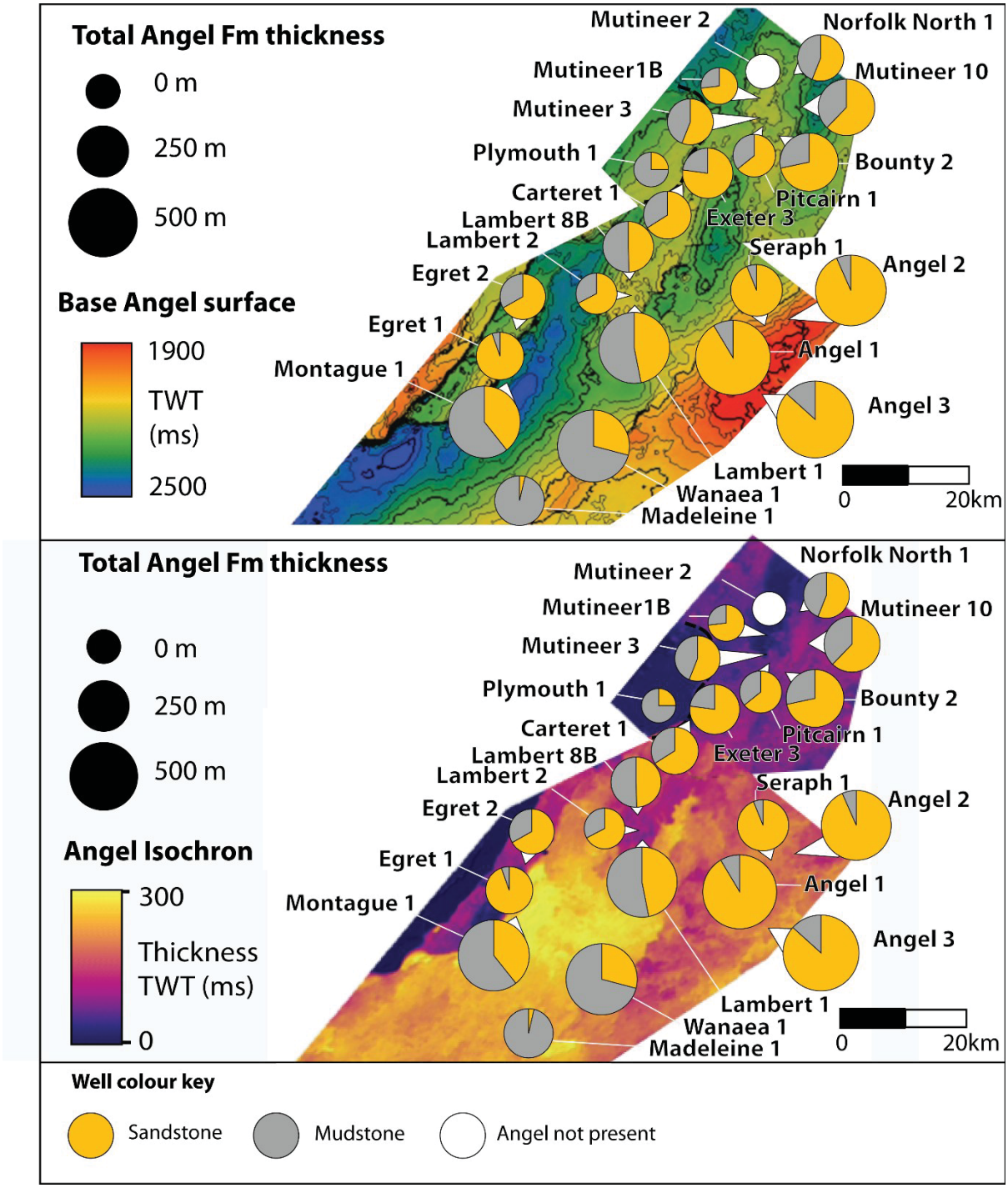


Fig. 3.15: *A) Base Angel Fm. surface (H2), B) Angel formation isochron (SU2). Highlighting location of wells that fully intersect the whole Angel Formation interval, identifying their thickness and sand percentage.*

Across the entire Angel Fm., the overall sandstone proportions decrease to the SW. Six separate sandstone-rich fans (i.e., multiple lobe complex sets with durations across biozones) within a mud-rich basin floor setting (Fig. 3.17A). Multiple sediment entry points are interpreted from patterns of sandstone thickness and fining; one to the east, sourcing the axial Angel fans, and four fans around the northern-western periphery of the basin, sourcing the Egret, Montague, Lambert, Exeter and Mutineer fans (listed SW to NE). Individual fans are aligned broadly

subparallel to the dominant NE-SW structural fabric of the basin. The axial Angel fan trends along the centre of the basin (Fig. 3.17). The Angel fan runs along the axis of the Madeline Anticline, and thins and pinches out to the SW, which was probably an active structure at this time and exhibiting positive seafloor relief (Fig. 3.4G). Oblique fans, sourced from the NW-NE via outboard horst blocks, demonstrate major thickness variations across the basin margin faults, indicating the presence of fault-related topography and basin confinement (Fig. 3.15B, cf. Montague-1 and Egret-1&2).

There is considerable lateral variability in both sandstone proportion and thickness, which is partly linked to proximity to intra-basin structures (Figs. 3.15, 3.16 and 3.17). Sandstone distribution trends, which represent multiple lobe complexes that may or may not stack to form lobe complex sets, are discussed below for each biozone, highlighting spatial and temporal changes in this fan-dominated, deep-water depositional setting (Fig. 3.17).

3.6.6.1 Biozone 1 (<1.5 Myr, No prior designated Intervals)

The thickest lobe complex set succession accumulated in the axial Angel fan, with 455 m in Angel-3 indicating a maximum sediment accumulation rate of c. 0.30 m/kyr. The Egret and Montague lobe complexes sets are interpreted to be separated by the crest of a tilted fault block at this time due to non-deposition in Egret-1 (Fig. 3.4G). The Lambert fan is routed southwards down a southward-dipping horst block of the Rankin Trend, whereas the Exeter and Mutineer lobe complexes sets are sourced from the northeast and appear to be confined laterally, on their NW margins by horst blocks (Fig. 3.12 & 3.17A,B).

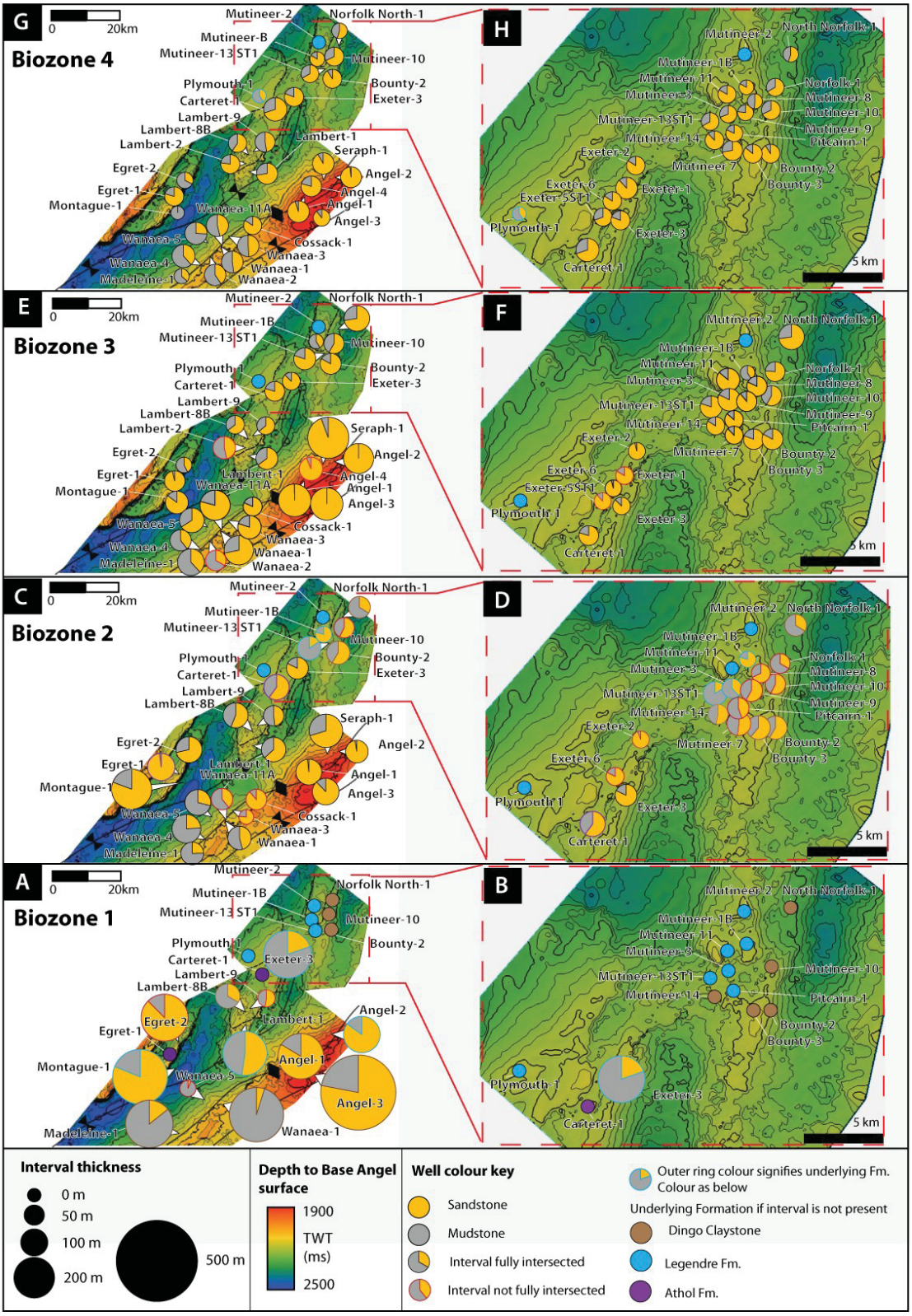


Fig. 3.16: *Base Angel Fm. surface (H2) with wells log sand percentage for each biostratigraphic interval. This includes maps covering the total basin-fill (c. 110 x 45 km) and an enlargement of the more densely drilled northeastern area (Mutineer-Bounty area, c. 25 x 17 km).*

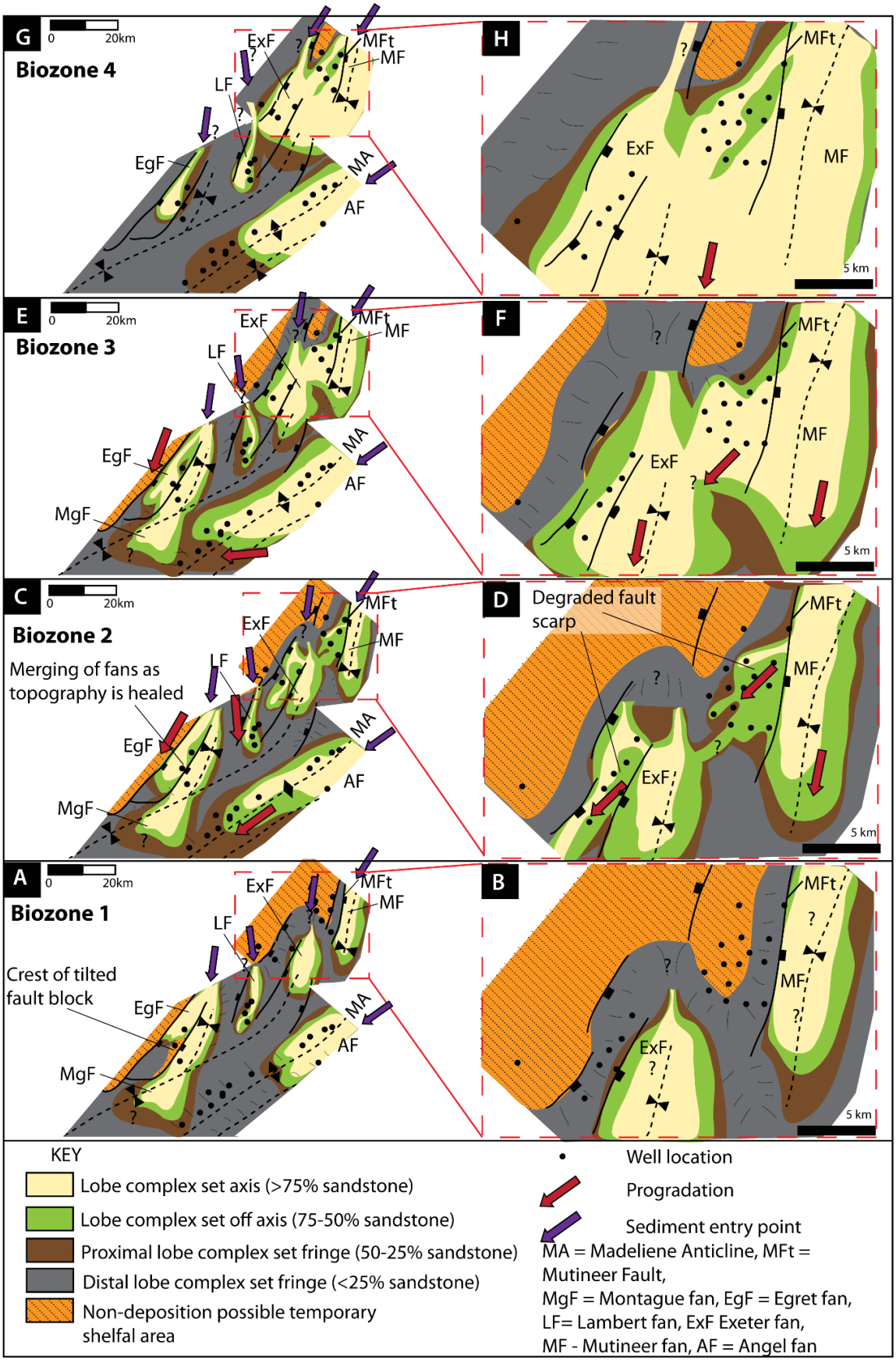


Fig. 3.17: Paleogeographic maps of the Angel Formation. Interpretation is based on Fig. 3.16 with sub-environments loosely based on facies associations. Sub-environments transitions are shown with hard boundaries but are likely to be more gradual.

3.6.6.2 Biozone 2 (<0.75 Myr, Intervals 1, 2 & 3)

The Angel fan prograded south-westwards along the Madeleine Anticline (Fig. 3.16C). The thickest lobe complex set succession of Biozone 2 is found in the Montague fan (176 m thick), defining a maximum sediment accumulation rate of 0.23 m/kyr. Along the northern flank of the sub-basin, sand deposition in the Egret and Mutineer fans extended south-westwards with lobe complexes overlapping the crest of the tilted fault block (Fig. 3.17C) that was starved of sediment during Biozone 1 (Fig. 3.17A). In the Lambert fan, sandstone proportions are more uniform across the sub-basin than in Biozone 1, possibly recording the infill of any relict, rift-related topography by these post-rift depositional systems. In the Exeter fan, routing along a degraded fault scarp occurred leading to a split in the lobe complex set in this location. In the Mutineer area, sandstones pinch out onto a degraded fault scarp (Figs. 3.12 and 3.16H). The more uniform thickness patterns observed across the Rankin Trend faults is interpreted to record the infill and eventual burial of rift-related topography. However, the highest horst blocks in the NW still exhibit influence on the sandstone distribution as there was still non-deposition at this time (Fig. 3.17D, Mutineer-11 & Plymouth-1).

3.6.6.3 Biozone 3 (<0.5 Myr, Intervals 4 & 5)

The Angel fan continued to prograde axially, towards the SW, with the thickest lobe complex set succession (204 m) indicating a maximum sediment accumulation rate of 0.40 m/kyr, the highest rate observed in any of the biozones. The Angel fan also remains the most sand-rich. Regarding the oblique fans, a relatively uniform thickness succession of lobe complexes sets is encountered, which is thinner than that of Biozone 2 (Fig. 3.16E). The lobe complex sets of the Egret and Montagues fans coalesce downdip to the southwest, whereas the Lambert lobe complex set likely stepped a few kilometres to the east, away from the locus of deposition characterised in the Biozone 2 (Fig. 3.17E). The lobe complex sets of the Exeter and Mutineer fans also may coalesce southwards, with their geometry and thickness less influenced by fault scarp-related topography compared to that observed in Biozone 1 (Fig. 3.11, 3.12 and 3.17F).

3.6.6.4 Biozone 4 (<1 Myr, Intervals 6, 7 & 8)

Biozone 4 shows an overall increase in mud proportion compared to Biozone 3. The lobe complex set in the axial Angel fan back-steps north-eastwards, although it remains sandy (Fig. 3.16G). There is no observed sandstone deposition in the lobe complex set of the Montague fan and no backstepping is observed in the lobe complex set in the Egret fan (Fig. 3.16G). The Lambert fan reaches its maximum areal extent in this biozone, with the greatest proportion of sandstone occurring in the most southernly Lambert wells (Fig. 3.16G). The thickest succession

encountered within this biozone occurs in the lobe complex set of the Exeter fan, where a 71 m-thick succession indicates a maximum sediment accumulation rate of 0.07m/kyr, the lowest of all the biozones. The Exeter and Mutineer fans continue to prograde and widen, with the high well-density suggesting the sandstone units become more sheet-like (Fig. 3.12, e.g. unit 7.3).

3.7 Discussion

3.7.1 Controls on depositional patterns

Sediment Source

During the Late Jurassic, the Dampier Sub-basin received a major influx of coarse clastic sediment, supplied by sand-rich gravity flows. Our analysis has identified at least six coeval submarine fans: (i) an axial fan (Angel fan) trending parallel to the Madeleine Anticline, and (ii) five smaller, oblique fans (Mutineer, Exeter, Lambert, Egret and Montague fans) fed via the northern margin of the Rankin Trend (Fig. 3.17).

The uniformity in texture and mineralogy (Hocking, 1992) of the sandstones in the axial and oblique fans suggest a single sediment source. Two possible sources are recognised; i) a large single shelfal source area to the east that is linked to the outboard Rankin Trend (Fig. 3.2B and Longley *et al.*, 2002), or ii) the Angel Formation is sourced from a previous basin-wide sandstone-rich deposit, such as the Legendre Fm, that was eroded and reworked on structural-highs of the Rankin Trend and up-dip Beagle Sub-basin (Lech, 2013; Chen *et al.*, 2020) and directed SW by the *en echelon* fault blocks. The oblique fans deposited sub-parallel to the *en echelon* fault blocks (Fig. 3.17) of the Rankin Trend as the fans coalesced and curve downdip to the SW and merge over structural highs as seabed relief was healed (e.g. Montague/Egret).

Previous work focusing on early post-rift settings shows that axial and oblique to transverse systems can operate simultaneously (Chiarella & Joel, 2021; Hansen *et al.*, 2021b), but that this interplay of two sediment dispersal pathways is more widely reported in syn-rift strata (Barrett et al., 2021; Cullen et al., 2019; McArthur et al., 2016). In this study, we do not observe thin beds interfingering the axial and oblique systems of the Angel Formation, this may be due poor seismic control or limited run out of sand-rich flows. Additional well control and higher-quality 3D seismic reflection data, the latter potentially permitting a detailed seismic geomorphological analysis of the system, may reveal a more complex stratigraphic architecture. An improved understanding of the nature and distribution of the bioturbated

heterolithic (BH) facies may also be beneficial, given the lack of thin-beds typically associated with lobe fringe environments which may represent interfingering of systems.

Structural Architecture

The sub-basin's tectonic configuration was a major control on the distribution of the Angel Formation's sand-rich gravity flows. The flows were confined by *en echelon* horst blocks of the Rankin Trend, and to a lesser degree by the Madeleine Anticline in the centre of the sub-basin. This confinement, along with a tectonically controlled slope dipping to the SW, controlled the NE-SW orientation of the lobe complex sets (each Biozone) and fans (across all 4 biozones).

Although more common in underfilled rift basins during the syn-rift stage (e.g. Hodgson & Haughton, 2008; McArthur *et al.*, 2016; Tillmans *et al.*, 2021), tectonically inherited topography has been documented in post-rift systems controlled by differential compaction over underlying rift structures leads to intra-formational onlaps (e.g. Færseth & Lien, 2002; Dmitrieva *et al.*, 2018; Dodd *et al.*, 2019; Hansen *et al.*, 2021b; Privat *et al.*, 2021). In early post-rift systems, such as the Angel Formation, accommodation driven by differential compaction took place within the sub-basin lows (Lewis and Kendrew Trough, Fig. 3.3); however, basin-margin onlapping of reflections indicate fans directly abut fault scarps and degraded footwalls exposed on the paleo-seafloor (Fig. 3.13). Such basin-margin onlapping is documented in other early post-rift deep-water systems such as the Lange and Lyr Formations (Moscardelli *et al.*, 2013), and the Wick Sandstone Formation in the North Sea (Argent *et al.*, 2000). This indicates that it is more important to understand sediment supply, tectonic configuration, and the related topography at specific points in the basin at specific times when studying early post-rift deep-water depositional patterns, than it is to formally define the stratigraphic boundary between syn- and post-rift strata.

Other depositional controls

Compensational stacking plays a varying role in the Angel Formation. Sandstone units initially prograde and aggrade when highly confined laterally by fault-related topography. After the fault-related topography was infilled, the rugose nature of the degraded fault scarp resulted in tortuous corridors with sandstone filling the topographic lows. The uppermost sandstone units show some evidence of compensational stacking away from topographical constraints (Fig. 3.11, Biozone 4). Thus, as the topography heals, compensational stacking becomes more

prevalent into the post-rift, although this is not a linear trend as degraded fault scarp topography can cause an intermediate complex stacking pattern.

No mass-transport deposits (MTDs) or complexes (MTCs) are observed in seismic reflection or well data. The apparent absence of cohesive mass-flows is likely related to the early post-rift timing of deposition with fault scarps unable to locally source mass-flows because of degradation in the syn-rift, an interpretation consistent with other studies in the surrounding Northern Carnarvon Basin (Bilal *et al.*, 2018; Barrett *et al.*, 2021).

The high level of bioturbation in the Angel Fm. is enigmatic for deep-water deposits. This high-degree of bioturbation and the limited diagnostic evidence from ichnofacies brings into question the depth of the basin at time of deposition. This high-level of bioturbation may suggest a shallower water depth, more conducive to biological activity indicating that the lobes of the Angel Fm. might be intraslope lobes.

3.7.2 Pinch out style and rates

The lobe scale pinch outs of the Angel Formation show minor to no facies transitions occurring towards a lateral confining slope (Fig. 3.11), and the lobes (and lobe complexes) maintaining high sandstone percentages (>70%) up to the pinch out (Fig. 3.14).

Several studies that quantify rate of change (RoC) in submarine fans focus on intra-lobe thinning rates (Fryer & Jobe, 2019) or on thin-bedded sandstones at the pinch out (Kus *et al.*, 2021). Three previous examples have documented lateral pinch outs onto basin-floor relief: i) Skoorsteenberg Formation, Karoo Basin (Hansen et al., 2019); ii) Laga Formation, Laga Basin (Marini *et al.*, 2015); and iii) Forties Sandstone Member of the Sele Formation, North Sea Basin (Davis *et al.*, 2009; Nagatomo & Archer, 2015). These examples are from outcrop (i and ii) and subsurface (iii) studies. The very-fine to fine grained Skoorsteenberg Formation is a relatively unconfined system with gradual lateral facies transitions from c. 80% high-density turbidites (axis) to 70% hybrid beds (at pinch out) with a RoC of c. 0.2 m/km against a 0.11º slope. The medium- to coarse-grained Laga Formation is of a similar grainsize to that observed in sandstone beds in this study, with our example becoming progressively less confined as topography was infilled. Lateral RoC against a 1-3º slope averages 0.6-0.7 m/km, with a maximum of 12 m/km. In the very fine- to fine-grained Forties Sandstone, the approximate RoC is c. 0.15 cm/m and c. 0.1 cm/m against a 2.6º and 1.2º lateral paleoramp, respectively, with facies transitioning from axial, sandstone-rich beds to mud-prone, hybrid event beds on a lateral slope (Davis *et al.*, 2009; Nagatomo & Archer, 2015).

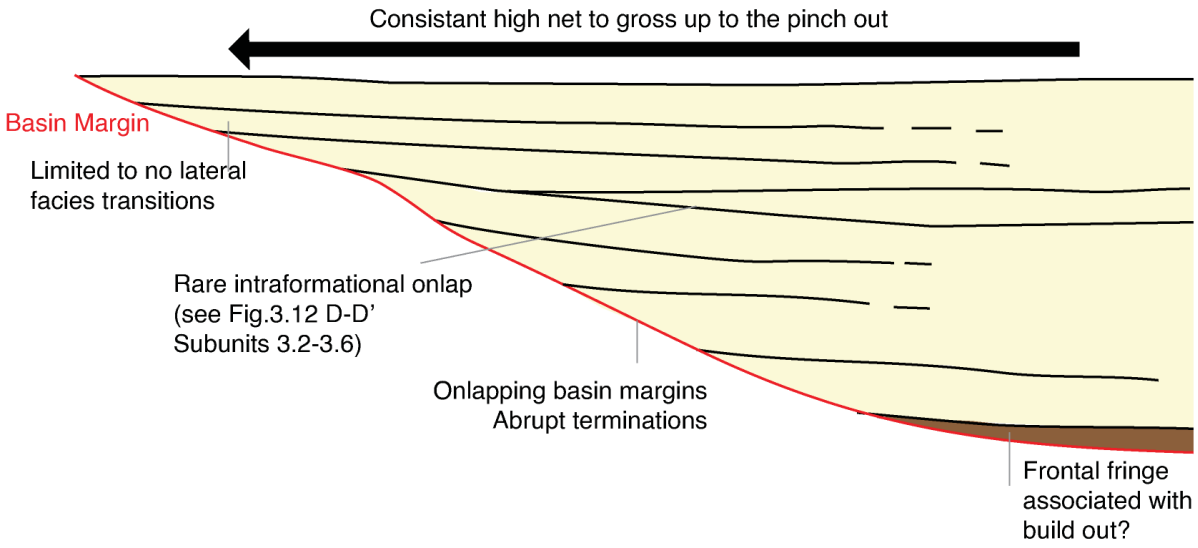


***Fig. 3.18**: Summary of sand-rich lateral punchout against a basin margin (cf. Fig.2.4)*

The Angel Formation also demonstrates significant rates of change (RoC, Table 3) on a more rugose slope profile than the three discussed studies, which were characterised by comparable slope angles. The cause of the high RoC maybe four-fold; due to the more rugose nature of the slope with steep slope sectors, not identified by our linear predictions between wells, the sand-rich nature of the flows that were sea-floor hugging and unable to ride up and deposit on adjacent slopes (Ilstad *et al.*, 2004; Breien *et al.*, 2011; Talling *et al.*, 2012), efficient downstream flow stripping of the more dilute part and finer part of density stratified flows against a lateral slope. Similarly, limited facies transition and maintenance of high sandstone percentages are seen in other intraslope examples (Spychala *et al.*, 2015; Jobe *et al.*, 2017; Privat *et al.*, 2021) and is possibly diagnostic for intraslope lobes where underlying inherited gradients are a few degrees. This interpretation relies on the assumption of a flat top to the Angel Formation and our stratigraphic interpretation of the well-based cross-sections. Alternative models could be made if we allow for greater flexibility of biostratigraphic constraints caused by reworking and possible sample mixing (from drill cuttings), or large-scale (m) post-depositional remobilisation by injectites. Another limitation of our study, which merits further investigation relates to the bioturbated heterolithic (BH) facies, as we are unable to interpret whether the sand-rich flows evolved or collapsed at the pinch out due to the level of bioturbation of the interbedded silty sandstones.

3.8 Conclusions

We have documented the enigmatic sandstone-rich submarine fans of the Angel Formation (Tithonian), Dampier Sub-basin, NW Shelf Australia. Mapping of 3D seismic reflection data revealed inherited rift topography was expressed on the paleo-seafloor during the syn- to post-rift transition. Detailed core descriptions allowed identification of 11 facies, which are dominated by massive and dewatered sandstones that were deposited as high-density turbidites and a heavily bioturbated heterolithic facies of uncertain origin, respectively. We grouped these 11 facies into four facies associations: lobe axis, lobe off-axis, proximal lobe fringe, and distal lobe fringe. Six submarine fans have been identified; the axial Angel Fan and smaller oblique fans five (Mutineer, Exeter, Lambert, Egret and Montague) entering obliquely to the basin from the outboard Rankin Trend. Lobes are shown to be confined by inherited rift topography, in the form of a hangingwall anticline (Madeleine Anticline), and variably degraded fault scarps or the Rankin Trend inherited from the preceding rift phase. Over ca. 3.75myr, lobe complex sets initially highly confined prograded and aggraded over a ca. 1.75 Myr period, before shutting down over ca. 1 Myr. The sandstone-rich flows initially deposit in topographic lows have high pinch out rates (up to 75m/km) against a ~3° slope. Once rugose basal topography was healed, lobes become more sheet-like and possibly channelised and begin to compensationally stack away from topography with lower pinch out rates (15 m/km, non-channelised) against an ~1° slope. At pinch outs against topography, sandstone units are interpreted to maintain high sandstone proportions with little facies transitions and pinch out at extremely high rates of thinning (up to 75 m/km). This study highlights identifies the high potential of rapid abrupt pinch outs against inherited topography in these settings and highlighting the potential for greater reservoir volumes.

Acknowledgements

The authors would like to thank Geoscience Australia for supplying and hosting open access data and Schlumberger for academic software license to Petrel. This work forms a part of TW's PhD, supported by the LOBE 3 consortium, that is gratefully funded by Aker BP, BHP, bp, Equinor, HESS Neptune Energy, Petrobras, PetroChina, Total, Vår Energi and Woodside. Expenses to log core in Perth, Australia were partly covered by an AAPG grant in aid, which the authors are grateful for. We are also thankful for Kerrie Deller's thoughtful discussions in the core store.

4 The curious case of the missing thin-beds: discriminating between lobe fringe environments and hemipelagic drapes in intensely bioturbated successions using reflectance spectroscopy

Timothy J. L. Wigan[1*], Christopher A-L Jackson[1], David M. Hodgson[2], Howard D. Johnson[1]

[1]Basins Research Group (BRG), Department of Earth Science and Engineering, Imperial College London, SW7 2BP, United Kingdom

[3]School of Earth and Environment, University of Leeds, Leeds, LS2 9JT, United Kingdom

4.1 Abstract

Packages of thin-bedded turbidites are a common feature in many deep-marine successions and can provide important paleoenvironmental records and support paleogeographic reconstructions. However, uncertainties can arise in the absence of thin-bedded turbidites through intense bioturbation. We use spectral reflectance, a technique not previously applied to deepwater siliciclastics, to investigate the striking paucity of thin-bedded turbidites in the Jurassic syn-to-post-rift Angel Fm., offshore Australia. We tested this novel technique against thin-section and XRD to assess its accuracy in identifying mineral assemblages across three bandwidths. Thermal infrared was used to identify five types based on mineralogy to characterise lobe environments: 1) lobe axis/off-axis, 2A) a heavily bioturbated lobe fringe, 2B) sandstone injectites, 3) distal lobe fringe, 4) hemipelagic mudstone, 5) siderite cemented zone. The identification of rare type 2A, not identifiable in core due to heavy bioturbation, demonstrate that lobe fringe environments with sandstone beds <5 cm were deposited but are masked by heavy bioturbation. The identification of previously unidentifiable lobe fringe environments indicates there was limited flow transformation when sand-rich flows interacted with topography and limited compensation stacking due to confinement by inherited rift topography. We have highlighted the useful application of spectral reflectance data on

understanding deepwater systems as well as the techniques usefulness for rapid reservoir characterisation.

4.2 Introduction

Deep-water submarine fans have are exploited as hydrocarbon reservoirs (e.g. Weimer & Pettingill, 2007), recent climate change is beginning to refocussed these, often depleted reservoirs, as potential carbon storage sites (e.g. Wilkinson, 2022). Understanding the architecture and depositional context is key to predicting reservoir distribution and siting injector wells. Fringe areas of submarine fans are thin-bedded and record a more complete palaeoenvironmental archive than axial areas because there's commonly less erosion here. Therefore they can be used to explain how flow events evolve, compensationally stack and pulses in sediment supply (e.g. Kane & Pontén, 2012; Straub & Pyles, 2012; Soutter *et al.*, 2022). However, bioturbation is often observed in lobe fringe environments from ancient (e.g. Cummings & Hodgson, 2011) and modern submarine fan successions (e.g. Wetzel, 1984), which can hinder interpretations of deep-water environments by mixing of sediments and destruction of primary sedimentary structures and if bioturbation intensity is sufficiently high then it can lead to the homogenisation of thin bedded intervals that results in muddy sandstone or sandy mudstone with a mottled texture. Bioturbated heterolithic successions have previously been interpreted as background sedimentation (e.g. Bruhn & Walker, 1995) but more recently they have been interpreted as the deposits of channel and lobe sub-environments (e.g. Heard *et al.*, 2014; Boulesteix *et al.*, 2020). In intensely bioturbated areas, interpretations rely on visual colour changes to infer changes in composition and dominant grain size, with time consuming and costly techniques (e.g. thin sections, QEMSCAN) used to preform detailed analysis on discrete sample points. Reflectance spectroscopy is a novel technique in sedimentology that is fast (500 m in 8 hrs), non-destructive, and a relatively inexpensive method to collect mineralogical information at a fine scale (1 cm). Similar techniques have recently been applied to support interpretations of carbonates (McCormick *et al.*, 2021), volcanic/volcaniclastic (Mauger *et al.*, 2012) and fluvial to marine bitumen-stained sandstone successions (Shchepetkina *et al.*, 2017), but has not previously been applied to deep-water siliciclastics.

We use reflectance spectroscopy to document a bioturbated deep-water siliciclastics succession, the Angel Formation, Dampier Sub-basin, NW Shelf Australia. We aim to i) test the accuracy of reflectance spectroscopy on deep-water siliciclastics against other techniques; ii) interpret a bioturbated heterolithic interval of unknown origin; iii) apply our new

understandings of the bioturbated heterolithics to refine the depositional model of the Angel Formation; and iv) assess the implications from a reservoir perspective .

4.3 Geological context

The early post-rift Angel Formation is confined laterally to the northwest by inherited syn-rift topography from structural highs of the Rankin Trend (Fig. 4.1B). The Angel Formation sandstone has previously been interpreted to be routed from the NE via the Rankin Trend (Hocking, 1992; Deller, 2011; Chapter 3) and overall thins and fines to the SW (di Toro, 1995). The early post-rift Angel Formation is largely bimodal in sedimentary facies, and

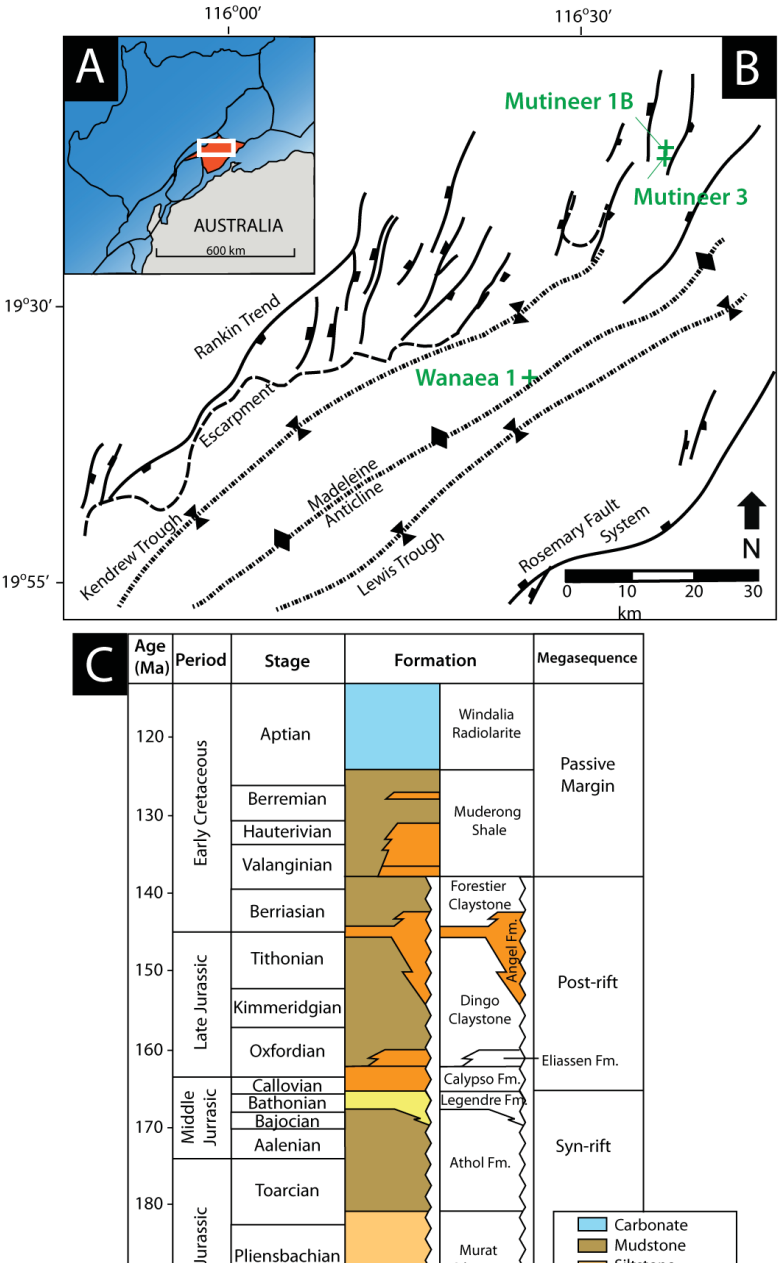


Fig. 4.1: *A) Location map of study area, NW Shelf Australia. White box shows location of B) Map of Dampier sub-basin illustrating main structural features modified from Spencer et al 1992. C) Stratigraphic column of Dampier basin. Angel Formation highlighted in orange.*

predominantly comprises either i) medium-grained, moderately-to-well-sorted, quartz arenite to subarkose sandstone, or ii) bioturbated heterolithic facies (Deller, 2011; Chapter 3). The sandstones are often massive or dewatered and highly amalgamated (Fig. 4.2, core image A), up to 35 m thick (Chapter 3) and are interpreted to be high-density turbidity current deposits (Hocking, 1992; Longley *et al.*, 2002; Deller, 2011; Chapter 3). The sandstones are interleaved with a heavily bioturbated heterolithic facies (Fig. 4.2, core image B and C), which comprises siltstone and sandstone with a mottled texture, and level 5-6 Bioturbation Index (MacEachern & Bann, 2008). Therefore, the primary sedimentology has largely been destroyed, and the depositional processes and environmental setting of the bioturbated silty sandstone is not clear. Previous interpretations have speculated that thin-bedded (<5 cm) turbidites have been masked by bioturbation (Deller, 2011; Chapter 3), although there is limited evidence put forward for interpretation beyond simple colour variations and minor grain-size variation. Within the bioturbated heterolithic facies mm-cm scale clastic injectites and rare sandstone beds are observed (Chapter 3). Subsidiary sedimentary facies include clast-rich sandstones and laminated mudstone (Fig. 4.2, core image D).

4.4 Data and Methods

We used three cored wells of the Angel Formation in this study; Mutineer-1B (26.38 m, Fig. 4.2), Mutineer-3 (29 m, Appendix 3), and Wanaea-1 (13.5m & 15.8m, Fig. 4.3). The cored intervals of the Mutineer wells have been previously interpreted to be the lateral fringe of a lobe complex fringe and Wanaea-1 as the frontal fringe of a lobe complex (Chapter 3, Fig. 1B).

Thirty-five point-counted thin-section (T-S) point counts, three x-ray diffraction (XRD) analyses, and permeability (216 samples) and porosity (202 samples) data (Appendix 4) from well reports (Woodside, 1989; Pitman, 1999, 2003) and Wawryk & Hancock (2017) provide valuable compositional information to compare against. To allow direct comparison with HyLogger-3^{TM} data (see below), which does not identify porosity and variations in mineral origin, T-S point counts have been normalised by removing porosity and including authigenic minerals in the total percentage. For example, authigenic quartz was added to quartz grains for a total quartz percentage. The previous well report results have focused on the mineralogy of sandstone-rich intervals (36 of 38 samples). The remaining two samples are from the bioturbated heterolithic intervals and consist of one T-S point count and one XRF sample. The mineral assemblages for a sandstone interval typically consist of >75% quartz with minor (<5%) glauconite and feldspar (Table 4.1, T-S and XRF). Carbonates have a varying

abundance. In heterolithic intervals, quartz percentage is lower (~35%) with dominance of phyllosilicate clays (~46%).

Reflectance spectroscopy core scanning was performed by the Geological Survey of Western Australia at the Perth Core Library as part of the Australian National Virtual Core Library project using the CSIRO HyLogger-3™. The HyLogger-3 ™ is a reflectance spectrometer that

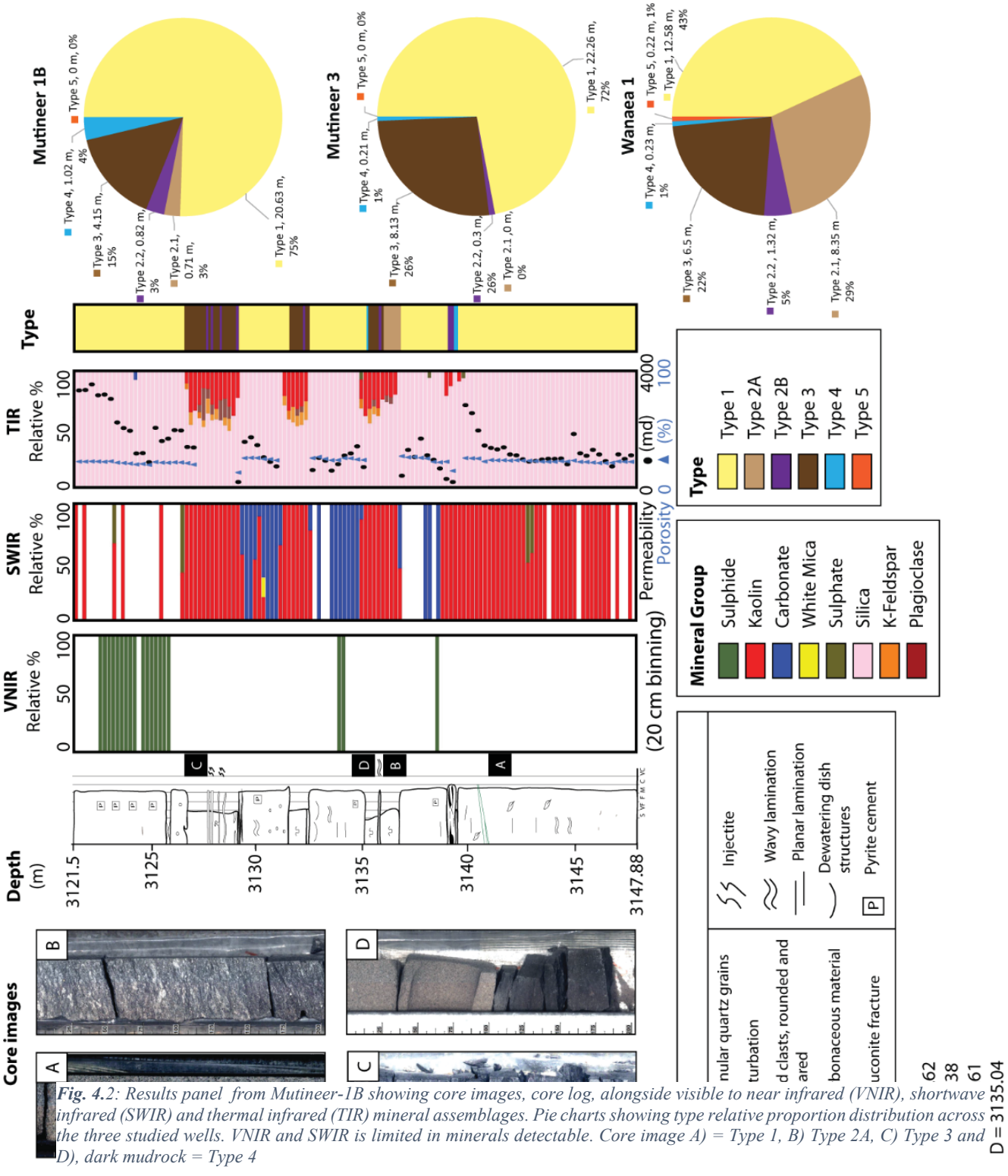


Fig. 4.2: Results panel from Mutineer-1B showing core images, core log, alongside visible to near infrared (VNIR), shortwave infrared (SWIR) and thermal infrared (TIR) mineral assemblages. Pie charts showing type relative proportion distribution across the three studied wells. VNIR and SWIR is limited in minerals detectable. Core image A) = Type 1, B) Type 2A, C) Type 3 and D), dark mudrock = Type 4

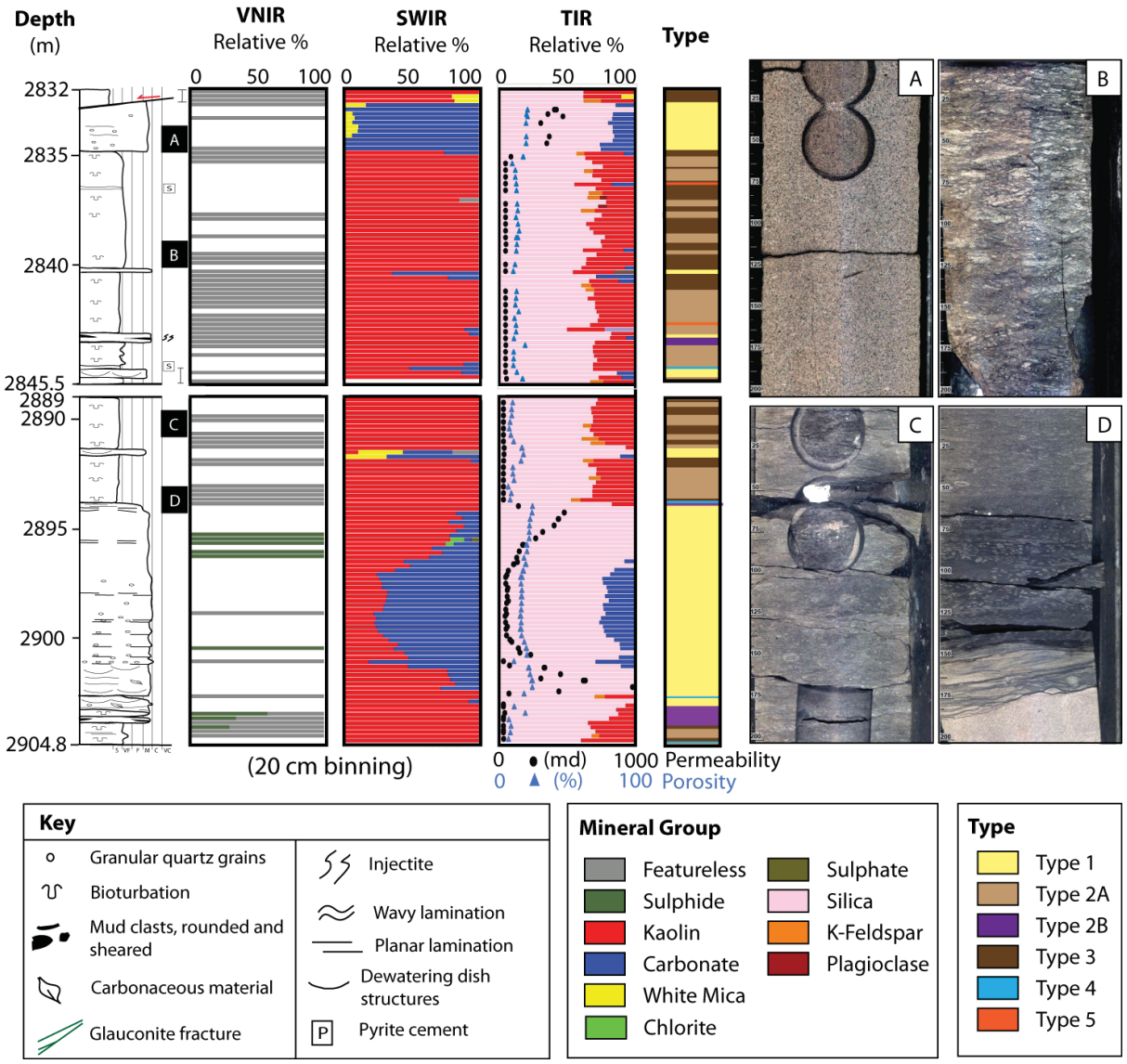


Fig. 4.3: *Results panel for Wanaea-1, showing core log alongside HyLogger-3TM results and core images of key TIR types. Core image A: ungraded medium grained massive sandstone with Type 1 TIR response, B: Mottled bioturbated heterolithics with Type 2A TIR response, C: Mottled bioturbated heterolithics with Type 3 TIR response, D) Bioturbated mudrock with type 4 TIR response.*

takes rapid non-destructive measurements in the infrared spectrum. The HyLogger-3 ™ measures the relative response of minerals and cannot give absolute values of mineral assemblages. Measurements were taken every 4 mm (field of view 1 cm^2) across three bandwidths: visible-near infrared (VNIR, 800-1000 nm), shortwave infrared (SWIR, 1000 to 2500 nm) and thermal infrared (TIR, 6000-14,500 nm) (Schodlok *et al.*, 2016). The chemical composition of the measured minerals influences the absorption features (dips at specific bandwidth location) in VNIR-SWIR or reflectance peaks (spikes at specific bandwidth locations) in TIR. The spectral response is compared to a known user-specified spectral library (Appendix 3) to identify the mineral assemblages, only minerals detectable in the given spectrum are recorded. As Minerals are not detected across all bandwidths but may span two

bandwidth or are only observed in one, this limits the application of some bandwidths for this study. For example quartz, and feldspars are only detectable in the TIR bandwidth. Most typical minerals in deep-water systems are detectable with the key absence of illite. The spectral responses may be affected by particle size, roughness and chemical properties of a sample (Rivard *et al.*, 2008). To counter these factors, multiple spectra for each mineral are available within the library. Spectral responses from multiple minerals are unmixed using a Constrained Least Squares (CLS) method with a minimum resolution for a mineral is set at 5% (Schodlok *et al.*, 2016). For a full description on core processing and the HyLogger-3^{TM} system see Schodlok *et al.,* (2016).

We defined a maximum of 5 minerals groups to be identified based on thin-section analysis (Silica *ie*. quartz, Feldspars *ie*. K-feldspar & plagioclase, carbonate *ie*. calcite and micas, Appendix 3). Minerals included in the user-defined spectral library comprised of minerals identified from previous well reports (as above) as well as typical minerals observed in deep-water siliciclastics (e.g. Amin, 1979; Spears & Amin, 1981; Pearce & Jarvis, 1992; Porten *et al.*, 2016; Steventon *et al.*, 2021).

We initially assess results from the three spectral bandwidths, which identify different minerals, to the logged core for direct comparison to lithology. We then compared the results to previous mineralogical well reports, and defined a classification for TIR results to aid and improve previous environmental interpretations for Angel Formation deposition.

4.5 Results

4.5.1 Spectral reflectance

The most insightful results are from the TIR bandwidth, due to the variety of minerals observable. We observe a typical mineral assemblage of silica (quartz), feldspars, carbonates and kaolin. We have compared the most common mineral proportions against the logged core. The sandstone intervals are typically 100% quartz (silica, Fig. 2.2 below 3140m). Heterolithic intervals typically maintain high proportions of quartz along with a more diverse range of minerals, such as feldspars, kaolin and carbonates (Fig. 4.2 and 4.3). Further analysis of the TIR results follows our comparison to other mineralogical studies.

A highly limited array of minerals is identified in SWIR, including phyllosilicate clays and micas, carbonates, and sulphate (gypsum). Kaolin and carbonates dominate the responses, with

kaolin present in sandstone and heterolithics in the cored intervals, whereas carbonates are typically only present in sandstone intervals (Fig. 4.3).

The readings from VNIR are limited by the minerals identified, and most of the results are null. We only identify infrequent sulphide in the form of pyrite in the sandstone intervals in this bandwidth (Fig. 4.2 and 4.3).

Table 4.1: *Selected points for comparison of thin-section (T-S), X-Ray Diffraction (XRD),shortwave infrared (SWIR) and thermal infrared spectral reflectance(TIR) results. Results are limited in the SWIR and TIR by what minerals are detectable in that spectrum (NR = Not readable), therefore they are relativistic and not absolute values. For example, Wanaea-1, 2833.6m, 30% Tourmaline does not reflect the actual sample is 70% tourmaline but of the few minerals recordable in the SWIR spectrum &0% has been recorded as Tourmaline but it is overall dominated by carbonates.*

	Mutineer-3: 3147.9 m				Wanaea-1: 2833.6 m			Wanaea-1: 2841.1 m		
Cored description	Sandstone interval				Sandstone interval			Heterolithic interval		
Sampling technique	**T-S**	**XRD**	**SWIR**	**TIR**	**T-S**	**SWIR**	**TIR**	**T-S**	**SWIR**	**TIR**
Quartz	87%	97%	NR	100%	75%	NR	81%	35%	NR	63%
Feldspar	4%	1%	NR		5%	NR		5%	NR	19%
Glauconite	3%		NR		4%	NR		7%	NR	
Carbonate	3%	Tr	51%		11%	70%	19%			
Phyllosillicate clays	Tr	1%	49%					46%	100%	18%
Tourmaline						30%				
Other	4%	1%			2%			7%		

4.5.2 Comparison to previous studies (as above)

Table 4.1 highlights three samples for comparison between the three sampling techniques, (thin section, XRD and spectral reflectance). Thin section analysis represents the most common analysis perform and is therefore used as the baseline for comparison. SWIR is not directly representative of the thin section samples due to the minerals that can be measured in this bandwidth but may aid understanding of minor mineral relative proportions such as carbonate vs phyllosilicate clay (e.g. Mutineer-3, Table 4.1). Both XRD and TIR over-represent the most abundant minerals and under-represent the least abundant minerals. In the case of the TIR results, this is due to the minimum detection resolution so low abundant minerals (<5%) are not measured, leading to an overrepresentation of the minerals observed. One limitation is that spectral reflectance data was measured after core plugs for thin section analysis were removed. As a result, the spectral reflectance data is from the closest measurement to the removed core plugs. The absence of the detectability of illite in the HyLogger^{TM}, that typically seen in deep-water clastic systems is an obvious absence and limitation to the data, however with the sparsity of calibration data (thin-section and XRD) not detecting/describing illite, we conclude that the results are representative for further investigation for thin bed analysis in this study.

4.5.3 Thermal infrared (TIR) classification

We have focused our analysis on the TIR results as silica is the dominant mineral group detected along with kaolin and feldspar. Five 'types' have been identified based on TIR mineralogy and silica abundance (Fig. 4.2 and 4.3). We describe the mineral assemblage, boundaries to surrounding types, porosity and permeability and distribution for each type.

Type 1 (63% of cored interval)

Type 1 is 75-100% silica with secondary carbonate minerals such as siderite, calcite and dolomite, and forms sharp contacts to surrounding Types. Type 1 is the only Type with high porosity and permeability, although zones with secondary carbonates (Wanaea-1; Table 4.1, and Fig. 4.4) are associated with a decrease in porosity and permeability due cementation during diagenesis. Type 1 is the most abundant type in all wells and accounts for ~75% in the proximal Mutineer wells and 42% in the distal Wanaea-1 well (Fig. 4.2).

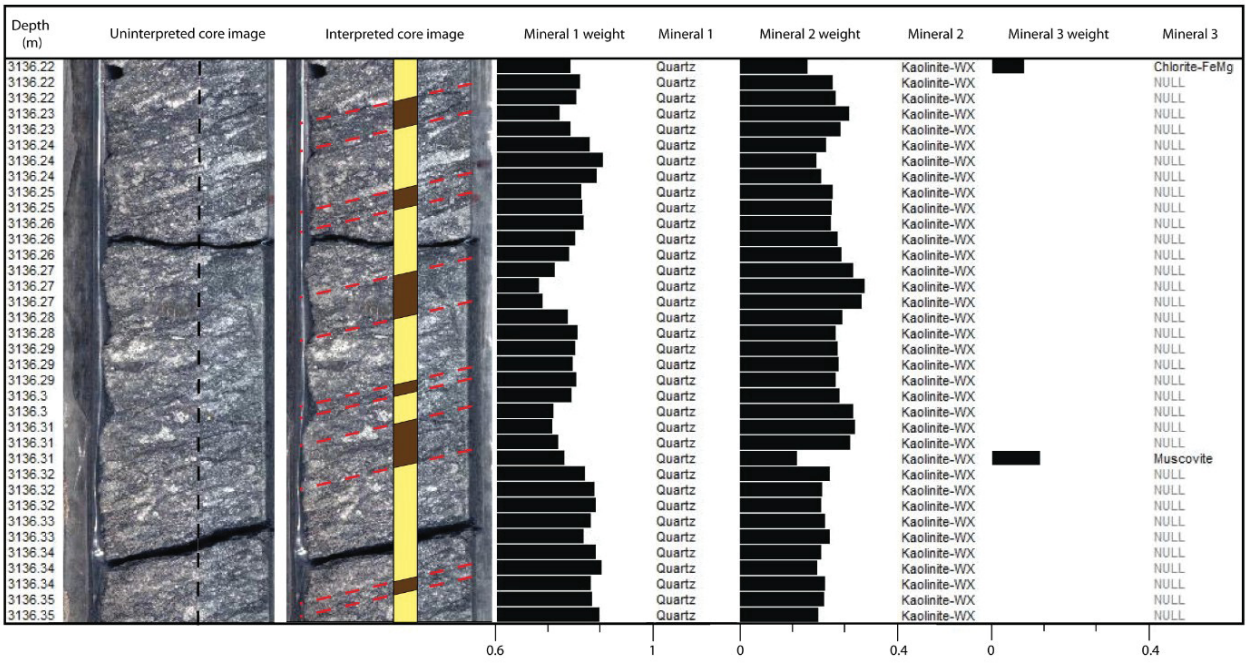


Fig. 4.4: Detailed results from Mutineer-1B (3136.22-3136.35m; 0.13m thick) Type 2A showing every sample reading at 4mm intervals. Interpreted core image shows a possible interpretation for reconstructed thin beds.

Type 2A (10% of interval)

Type 2A consists of 65-90% silica, secondary kaolin with occasional feldspars and white-mica. Within Type 2A, an undulating silica abundance is observed (Fig. 4.4), these intervals (<5 cm) of high quartz proportions are interleaved with intervals of lower quartz proportions. Where quartz abundance drops kaolin increases reflecting the colour tone in the core. This Type typically has gradual contact where intercalated with Type 3 and forms sharp contacts to other

types. Type 2A has low porosity and permeability (Fig. 4.3). Type 2A is most abundant in Wanaea-1 but it is very minor (<5%) to not observed in the Mutineer wells (Fig. 2).

Type 2B (3% of interval)

Type 2B is compositionally the same as 2A with 65-90% silica, secondary kaolin with occasional feldspars and white-mica (Fig. 4.3, 2904m). Type 2B contacts are gradual with Type 2A and 3, but sharp to other types. Porosity and permeability are variable, with moderate to low porosity and average to poor permeability. This type is seen in all wells at ≤5% but is most abundant in Wanaea-1(Fig. 2).

Type 3 (21% of interval)

Type 3 is classified as 40-65% silica with secondary kaolin, K-feldspars, and plagioclase. Quartz abundances are variable but less than in Type 2A. The 65% silica cut-off is arbitrary but is required as the extremes between Type 2A and Type 3 are significantly different (40% to 90% silica). The boundary to Type 2A is typically gradual and sharp to others. Type 3 has low porosity and permeability. Type 3 represents a relatively consistent proportion of all the facies in all the wells ranging from 15-26% (Figs. 4.2, 4.3).

Type 4 (2% of interval)

Kaolin is the dominant mineral group in Type 4 with secondary silica, smectite, K-feldspar, and plagioclase (Fig. 4.5, 3135.0-3135.2m). Sharp contacts to other types are observed. This type has poor porosity and permeability. Type 4 is most dominant (4%) in Mutineer-1B and 1% in other wells.

Type 5 (<1% of interval)

Siderite is the dominant mineral in Type 5 with minor silica, k-feldspar, plagioclase and kaolin. Sharp contacts to other types are observed. This type has poor porosity and permeability. This type is only observed in Wanaea-1 (1%).

4.5.4 Depositional environments

The Angel Formation is an unusual deepwater system in that it has units with very high sandstone proportion interpreted as deep-water lobe complexes, intercalated with a bioturbated heterolithic facies and extremely rare thin-bedded turbidites (Hocking, 1992; Deller, 2011; Chapter 3). Our results from TIR reflectance spectroscopy have been divided into 5 types which are generally comparable to lobe sub-environments.

Type 1 is linked to sand-rich intervals with massive or dewatering structures and no bioturbation. The silica-rich deposits of Type 1 are linked with what has previously been interpreted as high-density turbidites, typically amalgamated and deposited in a lobe axis or an off-axis environment where more stratified (Chapter 3).

Type 2A is part of the mottled bioturbated heterolithic facies but spans sections lightest in colour. The overall high silica composition for Type 2A indicates a higher energy environment compared to Types 3, 4 and 5. Type 2A intervals with high and variable silica proportions (Fig. 5) are interpreted to be thin (cm-scale) sandstone beds with muddy caps and/or interbedded sandstones and mudstones or that have been heavily bioturbated. An exact cut-off silica percentage for an individual sandstone bed cannot be identified as it is affected by the blurring of the measurements taken every 4 mm by the 1 cm^2 sampling window, and by the surrounding substrate composition, e.g. if there are multiple sandstone beds thinly interbedded with mudstone then there will be an overall higher quartz proportion than one isolated sandstone bed surrounded by mudstone. Type 2A is highly bioturbated with a where the bioturbation level is sufficiently high where no individual burrows remain and only a mottle texture, common ichnofauna of *Chondrites*, *Planolites*, *Zoophycus* and *Thalassinoides*. These ichnofauna have previously been observed in offshore to basin floor to lobe fringe environments (Cummings & Hodgson, 2011). Overall, the high-silica, bioturbated thin-sandstone beds and ichnofauna are diagnostic of a proximal lobe fringe environment (Prélat & Hodgson, 2013).

Type 2B is visually associated with cm-scale non-horizontal discordant sandstones surrounded by bioturbated heterolithic facies and rare horizontally bedded thin (<5 cm) sandstones that are not bioturbated. We have interpreted Type 2B to be clastic injectites, extremely rare turbidites and/or hybrid beds. Similar features are observed in distal lobe fringes, particularly around paleo-topography (Privat *et al.*, 2021). This type highlights the similarity of thin sandstone beds to the high-silica bioturbated intervals of Type 2A as they have the same mineral composition.

Type 3 covers part of the heavily bioturbated heterolithic facies and is visually similar to Type 2A except for a darker colour. Ichnofauna is identical to Type 2A. Type 3 has been interpreted to be deposited by dilute turbidites in a distal lobe fringe (Spychala *et al.*, 2017b; Boulesteix *et al.*, 2019) due to the lower proportion and variable silica abundance and ichnofauna . The increase in feldspar proportions in this type compared to Type 1 and 2A may indicate segregation of feldspar into the upper parts of flows leading to bypass of feldspar deposition to more distal areas.

Type 4 is visually the darkest type and is associated with laminated mudstone intervals. Bioturbation levels are reduced with only *Chondrites* observed. We have interpreted this as hemipelagic deposition during regional reduced sand supply to the deep basin).

Type 5 aligns with zones effected by early post-depositional siderite cementation evidenced by a red colour and circular, uncompacted *Chondrites* burrows. This type is associated with finer grained units and indicates the basin was subject to anoxic events.

4.6 Discussion

4.6.1 Application to deepwater siliciclastics

The results of our comparison of spectral reflectance to other mineralogical techniques have demonstrated that the technique is valid and can be applied to deepwater clastics (Table 1 & Appendix 4). The TIR bandwidth is the most useful for the typical mineral assemblages expected in these environments but is typically dominated by quartz which is often overrepresented by c. 13%, either due to a larger grain size, or the overall dominance of the quartz response 'drowns out' other responses. In more heterolithic intervals, the quartz over representation maybe due to the limited amount of minerals detected and the overall abundance of quartz is accounting for the wider array of minerals that are not detected. Further work is required into the effects of grain size.

4.6.2 Reconstruction of thin beds

We have reconstructed a heavily bioturbated interval from Mutineer-1B (Fig. 4.6) to investigate smaller scale heterogeneities within the bioturbated units. Types were assigned based on mineral assemblages with bioturbated thin beds interpreted within Types 2A and 3 at silica peaks in order to identify the largest of the thin beds as fine beds deposited by 'dilute' turbidites would be below the resolution of the HyLogger^{TM}. Within the heterolithic unit the depositional environment alternating between a proximal lobe fringe and distal lobe fringe and overlain by a drape. This overall fining upward trend either demonstrates a waning sediment supply or successive stacking of lobes in a lobe complex away from Mutineer-1B (Chapter 3). The interpretation of this, and other Type 2A and 3 dominated intervals, suggests that the Angel Formation comprises more proximal lobe fringe and distal lobe fringe environments than previously understood, with the presence of several lobe complex fringes. Furthermore, the interpretation of low-density and dilute turbidity currents suggests a physical connection to high-density turbidites in lobe axes, which do not abruptly pinch out. We have demonstrated

that heavy bioturbation can mask not only thin (<5cm) , but also complete lobe fringe facies associations.

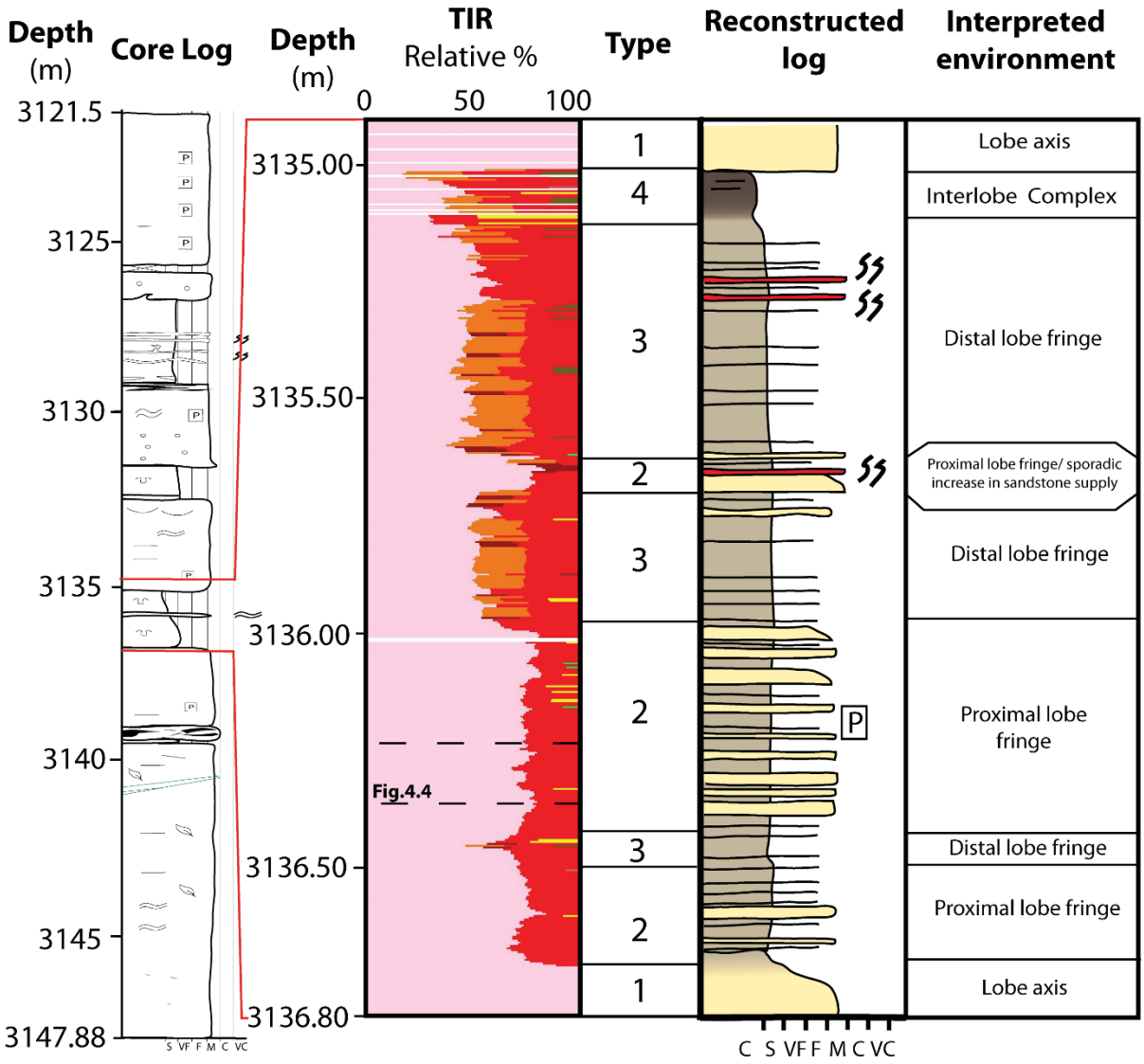


Fig. 4.5: *Detailed reconstruction of heavily bioturbated interval from Mutineer-1B with an interpreted depositional environment. Core log key and TIR colours as in Fig. 4.2. Red beds indicate post-depositional injections. P = Pyrite.*

4.6.3 Distribution

The proximal wells (Mutineer-1B and Mutineer-3) are close to lateral paleo-topography, with Mutineer-1B the closest well to a lateral pinch out against a pre-rift horst block (Chapter 3). We observe a dominance of the axial deposits in both wells (Fig. 4.2, pie charts) with a greater variability closer to the lateral pinch out with increased proportions of proximal lobe fringe and interlobe deposits. We also observe an increase in injectites and hybrid beds closer to the pinch out in Mutineer-1B (as in Chapter 3). The decreased abundance of lower-energy environments away from the pinch out (Mutineer-3) indicates the flows may have been erosive leading to the

removal of these types and/or there was limited compensation stacking with units typically aggrading due to confinement caused by topography as described in Chapter 3.

Wanaea-1 has previously been interpreted as in a frontal fringe fan position away from lateral topographical constraints (Chapter 3). Axial deposits (43%) still dominate although proximal lobe fringe deposits form a much higher proportion than in the proximal wells (29%, Fig. 4.2). This represents a significant change in depositional style possibly linked to the increased distance to topography allowing a higher degree of compensational stacking of lobes, and preservation of lobe fringe units.

This identification of lobe sub-environments based on mineralogy offers the potential to expand our Type-base packaging of intervals beyond the core interval if they are correlatable to log responses. Some well logs respond to lithological changes (e.g. gamma ray, density, neutron porosity and sonic logs), therefore comparison of these logs to our environmental interpretation may enable new insights into the morphology and distribution of the Angel Formation.

4.7 Conclusion

This study documents a novel approach to interpreting deep-water siliciclastics using reflectance spectroscopy of well cores from the Angel Formation, NW shelf, Australia. A combination of reflectance spectroscopy with core descriptions, thin-section, XRD, porosity, and permeability have been used to analyse 3 cored wells. TIR results are the most applicable due to the minerals (*ie*. quartz, K-feldspar, plagioclase and kaolin) detected in in the bandwidth and are offer the most accurate when compared with thin-section analysis.

The depositional environments of five types have been interpreted based on TIR mineral assemblages. The key insight from the TIR results is the subdivision of the bioturbated heterolithic facies into proximal and distal lobe fringes and the level of bioturbation was sufficient to mask sandstone beds <5 cm thick and complete lobe fringe environments. This improved analysis of the Angel Formation has identified the sediment gravity flow deposits had a greater degree of variation than previously thought.

The absence of the detectability of illite in the HyLogger^{TM}, adds uncertainty to the results, further work should increase the XRD calibration points in the bioturbated heterolithics. Further work into the application of spectral reflectance to widen the application to deep water siliciclastics should focus on less compositionally mature sandstones to test mineral

identification in more varied heterolithic sandstones and assess the impact of grain size on results. To enhance our understanding of the Angel Formation comparison of our results to petrophysical well logs may enhance our understanding of the compositional distribution of the deep-water fans.

Acknowledgements

The authors acknowledge the Government of Western Australia for the open accessibility of the data and CISRO for the use of an educational license for The Spectral Geologist Software.

5 Factors controlling deep-water sediment routing and facies variations in the early post-rift – a case study of the Lower Cretaceous Agat Formation, North Sea, Norway

5.1 Abstract

Understanding the transition from axial sediment transportation in the syn-rift to a more dominant transverse sedimentation pattern in the post-rift, is vital when predicting subsurface deep-water reservoirs for hydrocarbons and CO_2 storage. In the early post-rift inherited rift topography is a major influence on sediment distribution, however this influence declines as the basin are infilled. This study investigates how rift related structures affected the early post-rift deep-water Agat Formation across the Måløy Slope and Sogn Graben in the North Sea. Seismic attributes and spectral decomposition interpretation supports the interpretation of a Southern axial deepwater channel feeding a base of slope frontal lobe, which was subsequently bypassed to the North where there was interaction with a E-W transverse system. Two cored wells supported by seismic interpretation over the Southern area, identify confined stacked channel complexes, and a channel margin or overbank environment with an abundance climbing ripples, indicating loss of confining topography. Underlying fault segmentation and geometry played a key role in determining where the confined channel crossed the compaction hinge zone associated with the underlying Gjøa Fault Zone. The reinterpretation of the paleogeography of the Agat Formation highlights the important role that rift generated topography particularly fault segmentation can play in reservoir distribution the early post-rift.

5.2 Introduction

Topography is a major control on the architecture and morphology of deep-water deposits numerous factors influencing basin topography range in scale and include: tectonics, mass transport complexes (MTCs), salt and mud diapirism, differential compaction of sediment, and compensational stacking (e.g. Adeogba et al., 2005; Gervais et al., 2006; Moscardelli et al., 2006; Jackson et al., 2008; Armitage et al., 2009; Davis et al., 2009; Clark & Cartwright, 2012; Howlett et al., 2019; Privat et al., 2021) with subtle gradient changes effecting the routing of sediment gravity flows and therefore their deposits (e.g. Argent et al., 2000; Stevenson et al., 2013; Spychala et al., 2017c; Hansen et al., 2019). Understanding the transition from direct influence of tectonically-generated escapements in the syn-rift to a more subtle controlling influence in the later post-rift is important in predicting distribution and character of sandstone-rich deposits for hydrocarbons and CCS reservoirs in early post-rift reservoirs. During the syn-rift, the distribution and morphology of deepwater sediment gravity flows are influenced strongly by fault characteristics such as propagation, growth, linkage and death (Ravnås & Steel, 1997; Gawthorpe & Leeder, 2000). In the late syn-rift and early post-rift, deposits have been documented to interact directly with exposed fault escarpments (McArthur *et al.*, 2016; Tillmans *et al.*, 2021; Chapter 3,) and buried faults, where compaction hinges have been documented to effect the sedimentation and morphology in the late post-rift (Martinsen *et al.*, 2005; Southern *et al.*, 2017; Dmitrieva *et al.*, 2018; Hansen *et al.*, 2021b; Privat *et al.*, 2021).

The main aims of this study are to investigate an early post-rift system to understand the effect of inherited rift-related faults can influence deep-water deposits and sedimentation. To do this we will re-evaluate the Agat depositional model by remapping the Agat Formation and improve the understanding of how inherited structural relief in the early post-rift influences the architecture and morphology of deep-water channels and lobes. The Early Cretaceous Agat Formation is an example of an early post-rift deepwater system and a target for recent hydrocarbon exploration (Bugge *et al.*, 2001; Martinsen *et al.*, 2005; Hansen *et al.*, 2021a; Azzam *et al.*, 2022). We have focused on the Southern area (blocks 35/7, 35/9, Fig. 5.1) as the sedimentology of the Northern area (block 35/3) has been previously studied in detail (Shanmugam *et al.*, 1994; Skibeli *et al.*, 1995; Nystuen, 1999; Bugge *et al.*, 2001; Martinsen *et al.*, 2005). Although the Southern area has recently been the subject of analysis from reservoir quality perspective (Hansen *et al.*, 2021a; Azzam *et al.*, 2022), there is a lack of understanding of the sedimentology and relationship between the Southern area and the

Northern area. Our study area is in the Northern North Sea, offshore Norway and comprises the westward-dipping Måløy

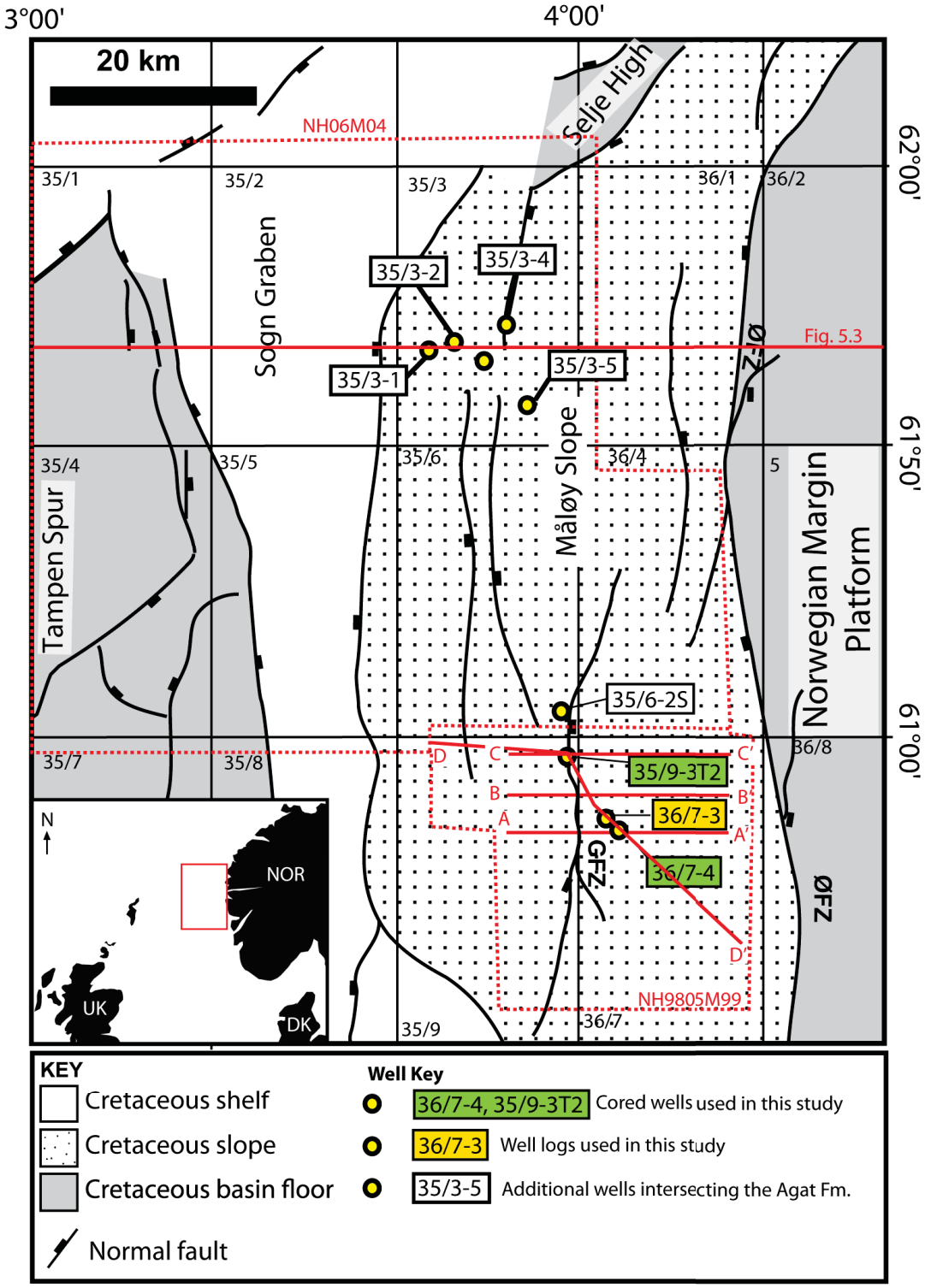


Fig. 5.1: *Location map Northern North Sea. Well locations (yellow) and main Cretaceous structures and faults shown. Seismic surveys outlined in red. Modified from Jackson et al., (2021). A-A', B-B', C-C' dipslayed on Fig. 5.8. D-D' dipalyed on Fig. 5.9.*

Slope in the east, the Jurassic Sogn Graben rift basin with the Tampen Spur the western boundary (Fig. 5.1).

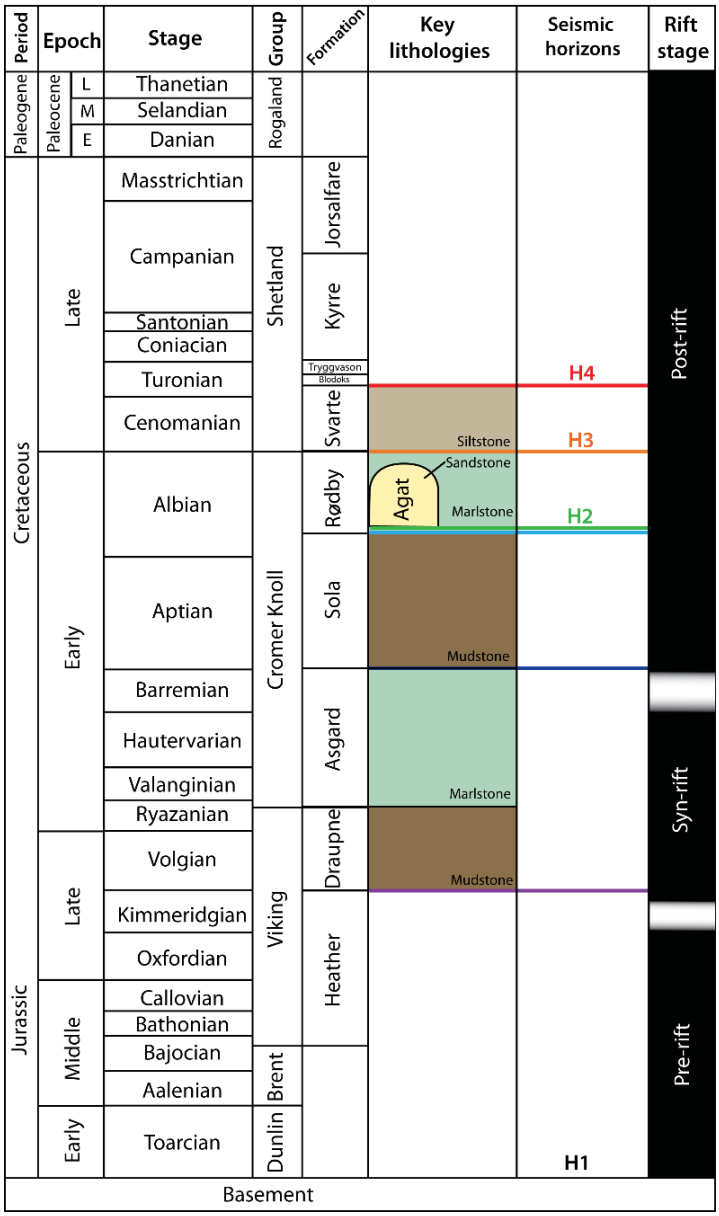


Fig. 5.2: *Stratigraphic column of the Måløy Slope with interpreted seismic horizons. Intermediate horizons between H2 & H1 were picked locally aid interpretation. Modified from Jackson et al.,(2021). Additional seismic horizons colours correlate to Figs. 5.3 & 5.10.*

5.3 Geological setting

The North Sea is a multiphase tripartite failed rift basin with the Måløy Slope and Sogn Graben located to the northeast of the northern branching Viking Graben. The North Sea comprised two rifting phases, first in the Permian to the Middle Triassic (not part of this study) and later in the Late Jurassic to the Early Cretaceous (Fig. 5.2, eg. Badley *et al.*, 1988; Nottvedt *et al.*, 1995; Færseth, 1996; Gabrielsen *et al.*, 2001).

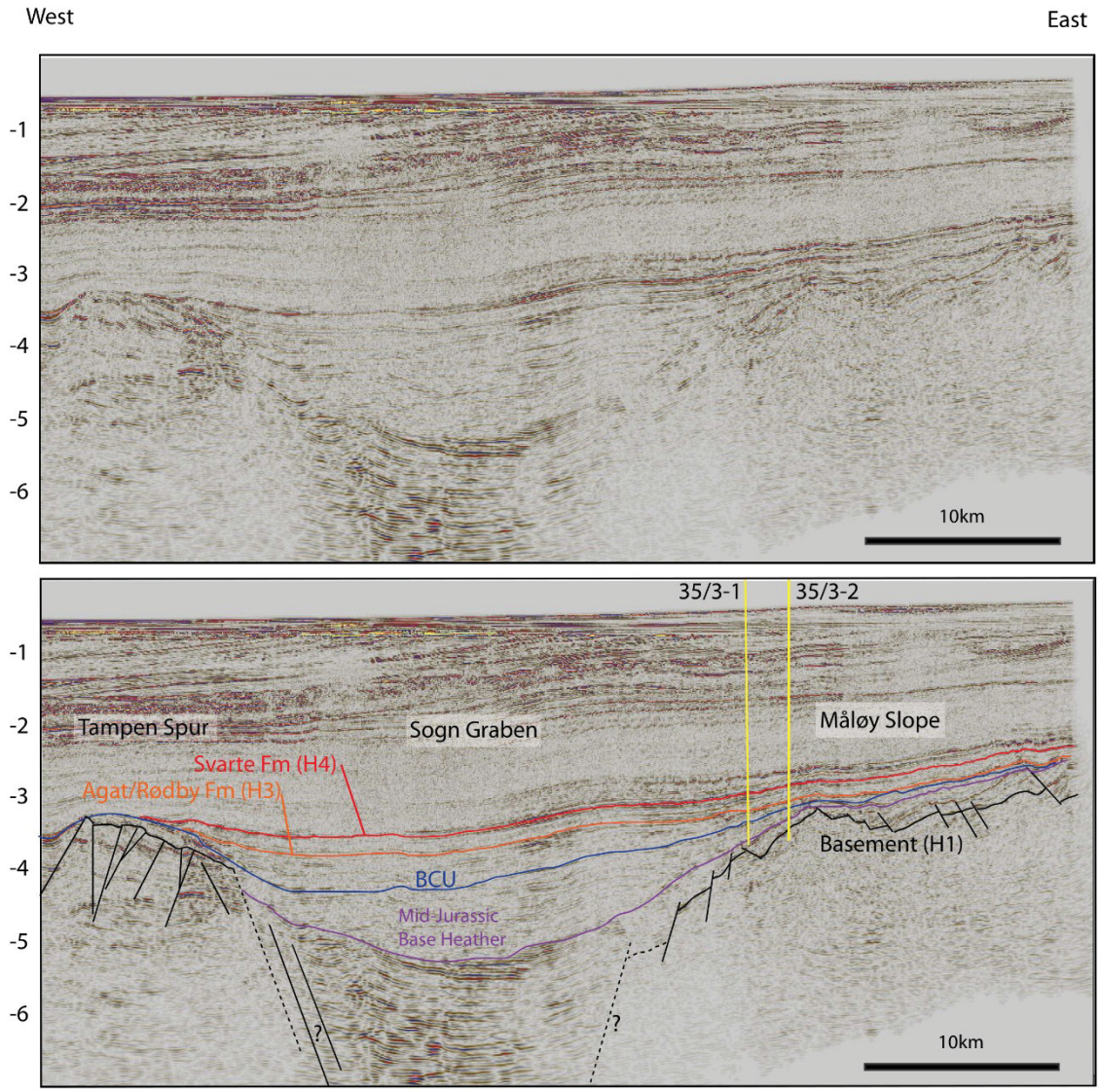


***Fig 5.3**:Seismic cross section of the North of the study area highlighting the main tectonic structures and seismic horizons H2 not shown due to overlap and proximity to H3. Main structural features are the Måløy Slope, Sogn Graben and Tampen Spur.*

The first (Permo-Jurassic) rift period is understood to have an E-W extension direction with oblique faults striking N-S and NNW-SSE, whereas the later extension was oblique with a NW-SE or WNW-ESE extension (Færseth *et al.*, 1997). This later oblique rifting led to a series of NNE-SSW *en échelon* rift segments with the focus of extension in the Viking and Sogn grabens (Færseth *et al.*, 1997; Phillips *et al.*, 2019). New fault development was common in the second stage of rifting alongside fault reactivation, although the reactivation of faults was not uniform (Færseth, 1996; Bell *et al.*, 2014). New NNE-SSW fault development occurred on the Måløy Slope and was likely a structural high during the Devonian, as the youngest strata observed are from the Early Jurassic (Reeve *et al.*, 2013, 2015; Bell *et al.*, 2014). This led to the Måløy Slope having a series of perched half grabens and grabens on the Måløy Slope such as the Gjøa Graben (Fig. 5.3, Martinsen *et al.*, 2005; Sømme *et al.*, 2013; Reeve *et al.*, 2015;

Wahyuni *et al.*, 2019; Jackson *et al.*, 2021). The North Sea's expression of transition to the post-rift is complex, with diachronous cessation of rifting where the 'incipient' or early post-rift phase lasted the entire Early Cretaceous period (*sensu* Gabrielsen *et al.*, 2001). The early post-rift is characterised by large relief and localised deep basins with shallow and emergent fault blocks where extensive erosion occurred (Nottvedt *et al.*, 1995).

Regionally the start of the early post-rift is marked by the 'base Cretaceous unconformity' (BCU), however locally and in our study area the nature of this unconformity is complex (Kyrkjebø *et al.*, 2001; Jackson *et al.*, 2021), due to a threefold combination of the; BCU, the so called Upper Jurassic Unconformity (UJUNC, Jackson *et al*., 2008) and a Late Abian-Cenomanian unconformity that often combine to form composite surfaces (Sømme & Jackson, 2013; Jackson *et al.*, 2021). The exact cause of the UJUNC and the Aptian Unconformity remains uncertain nut the former is linked to a potential fall in sea level and subsequent period of subaqueous slope failure of erosion by sediment gravity flows (Jackson *et al.*, 2021).

The underlying basement to the Måløy Slope is comprised of crystalline igneous and metamorphic rocks (Slagstad *et al.*, 2008; Reeve *et al.*, 2013). Lower Jurassic sediments on the Måløy Slope consist of the pre-rift fluvial-deltaic and shallow marine Dunlin and Brent Group and the Heather Formation of the Viking Group deposited in a shallow marine basin (Vollset & Dore, 1984; Helland-Hansen *et al.*, 1992; Brekke *et al.*, 2001; Fig. 5.2). These sediments were deposited as part of the primary rift megasequences.

The syn-rift sequence comprised of the shale-rich Draupne Formation and claystone and marl-rich Asgard Formation, which signify a significant deepening and transition to open marine environment in the basin which accounts for around 400m of sediment on the Måløy Slope and >800 m in the Sogn Graben (Fig. 5.3, Isaksen & Tonstad, 1989; Brekke *et al.*, 2001; Bugge *et al.*, 2001). High rates of post-rift subsidence led to the margin tipping steeply to the W-NW (Somme *et al*., 2013). The early post-rift was infilled by marine mudstones of the Sola, Formations and into the post-rift by the mudstone Svarte and Blodoks Formations where subsidence was driven by thermal relaxation. These mudstones of the early post-rift Rødby formation are interspersed with deep water sandstones of the Agat Formation. By the early post-rift the basement highs of the syn-rift were buried with mudstone of at latest Aptian age (e.g. Sola Formation, (Martinsen *et al.*, 2005; Jackson *et al.*, 2021).

5.3.1 Paleogeography and stratigraphy of the Aptian-Albian

During the Early Cretaceous the Måløy Slope was a westerly dipping low-gradient slope that terminated in the Søgn Graben (Shanmugam *et al*., 1994; Bugge *et al*., 2001) which had a water depth of c. 500 m (Gabrielsen *et al*, 2001; Roberts *et al.,* 2009). The Øygarden Fault Complex (ØFC, Fig 5.1) acted as a 'hinge zone' separating a shallow basin to the east and the ramp of the Måløy Slope into the deep-water basin to the west (Fig. 5.3, Færseth, 1996; Bugge *et al.*, 2001; Jackson *et al.*, 2008). Mudstone deposition generally dominates the post-rift succession with deepwater sandstones for the Agat Formation (Aptian-Albian). The deep-water sandstones of the Agat Formation have been documented spanning the Måløy Slope and into the Søgn Graben covering approximately 200km^2, however the mode of deposition was initially disputed (Fig. 5.4, Isaksen & Tonstad, 1989; Gulbrandsen & Nyborkken, 1991; Shanmugam *et al.*, 1994; Skibeli *et al.*, 1995; Nystuen, 1999; Bugge *et al.*, 2001; Martinsen *et al.*, 2005; Hansen *et al.*, 2021a; Azzam *et al.*, 2022).

Initially the Agat Formation was interpreted as localised sandy slumps and sandy debris flows on a upper slope location which explained the poor lateral extensiveness of the sand bodies (Shanmugam *et al.*, 1994; Skibeli *et al.*, 1995). Later interpretations, identified the Agat as mass-flow events deposited in paleovalleys or local slump scars by turbidites and sandy debris flows (Nystuen, 1999; Bugge *et al.*, 2001). Martinsen *et al.* (2005) recognised channel and lobe systems traversing down the Måløy Slope in seismic and highlighted the possibility of turbidity currents being captured in local topography controlled by differential subsidence related to major basin faults.

Most previous work (cited above), focused on the northern area (35/3 area; Fig. 5.1) where a series of intraslope channels and lobe have been mapped in seismic reflection and penetrated by wells (Martinsen *et al.*, 2005; Lien *et al.*, 2006). Here, the Agat Formation was likely sourced from a (now eroded) narrow 20-40km wide shelf which has been speculated to be sourced from small drainage basin (8000km^2) on the western Norwegian mainland, (Bugge *et al.*, 2001; Fonneland *et al.*, 2004; Martinsen *et al.*, 2005).

Recent work has focused on the southern area 35/6,7,9 (Fig. 5.1) where a channel system has been described which is chlorite and glauconite-rich and sourced by a series of canyons inherited from a Kimmeridgian-aged unconformity (Hansen et al., 2021a; Jackson et al., 2021; Azzam et al., 2022). Analysis of clay coating of sandstone grains supports a lateritic-rich drainage basin. However, chlorite abundance decreases upward though the Agat Formation

suggesting a variation in the sediment source over time (Hansen et al., 2021; Azzam et al., 2022).

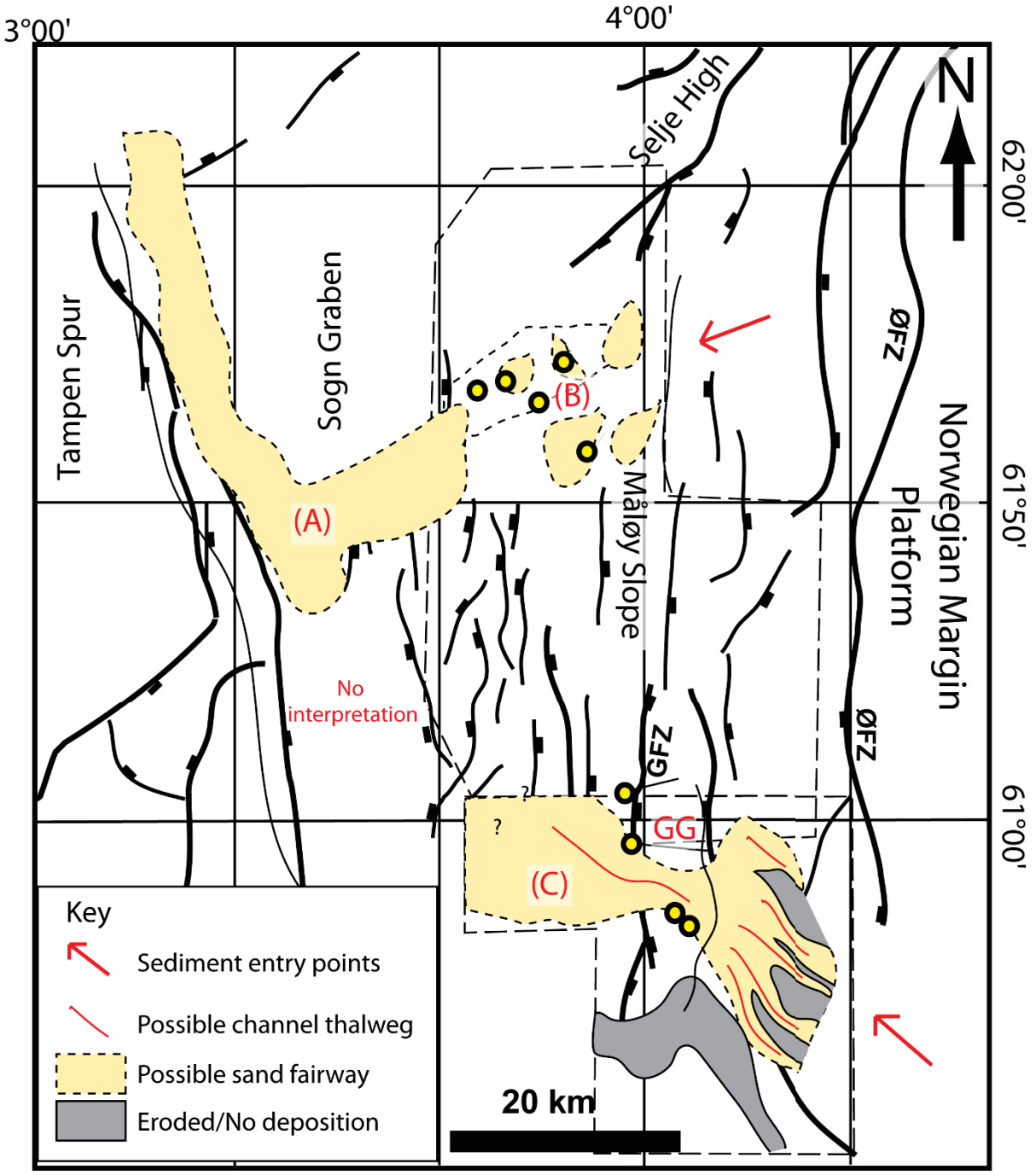


Fig. 5.4: *Current understanding of spatial distribution of sand fairways of the Agat Formation, as mapped in (A) Bugge et al., (2001), (B) Martinsen et al., (2005), and (C) Jackson et al., (2021). Black dashed line highlights the Agat sediments deposited on the Måløy Slope . GG= Gjøa Graben, GFZ = Gjøa Fault Zone*

We have combined all the interpretations of the mapped the sandstone distribution of the Agat Formation across the Måløy Slope and Sogn Graben (Fig. 5.3). From this we can identify two possible sediment inputs both from the west but one in the north and one in the south of the

study area. There currently is a lack of understanding in how the southern system is routed and how these two systems interact.

5.4 Data and methodology

A multiscale approach was used for our study from core to well logs and seismic reflection data. Two cored wells along with seven additional wells over two 3D seismic reflection volumes (NH06M04 and NH9805M99) that covers the study area of c. 4500 km^2 (Fig. 5.1). Our study area covers the Måløy Slope to the East, the Tampen Spur to the West and the Sogn Graben from the Gjøa Fault Zone in the South to the Selje High in the North (Fig. 5.1).

The thickness and seismic character of the Agat Formation across the study area was mapped using seismic horizons, isochrons, and seismic attributes (RMS amplitude and spectral decomposition). Seismic facies for each facies associations were based on reflection amplitude, frequency, lateral continuity and geometry. Rift faults were picked where they underlie the Agat Formation to assess the proximity to tectonic structures. A combined interpretation of seismic attributes and mapping of isopachous slicing between the Top Agat and Base Agat lead to the gross depositional environment maps for the Lower and Upper Agat.

Well logs were tied to core to seismic and to understand the petrophysical characteristics of each facies association and enable interpretation outside the cored intervals in well logs. Two wells have been cored in the Agat Formation in the South of the study area. We logged a total of c.185 m (35/9-3T2; 67.8m, 36/7-4; 117.6 m). 36/7-4 was logged at 1:50 and 35/9-3T2 at 1:20, to capture the greater heterogeneity. The grain size, lithology, fabric and colour were used to designate lithological facies and facies associations. This was used to calibrate the well logs of the three wells in the South to aid correlation from proximal to distal to illustrate the changes in facies associations down-dip and in relation to tectonic structures. Third party biostratigraphic data sourced from micropalaeontology and palynology from cuttings sampled at a resolution of 10 m was used to aid the correlation (Jackson *et al*., 2021).

From this multiscale dataset we evaluated the link between the sediment routing of the Agat Formation and the underlying rift related tectonic structures.

5.5 Agat seismic character and distribution

Four key surfaces have been interpreted basin-wide to analyse distribution and morphology of the Agat Formation (Fig. 5.2); top basement (H1), base Agat Formation (H2) which is a composite surface, top Agat Formation (H3) and Top Svarte Formation (H4), with relevant

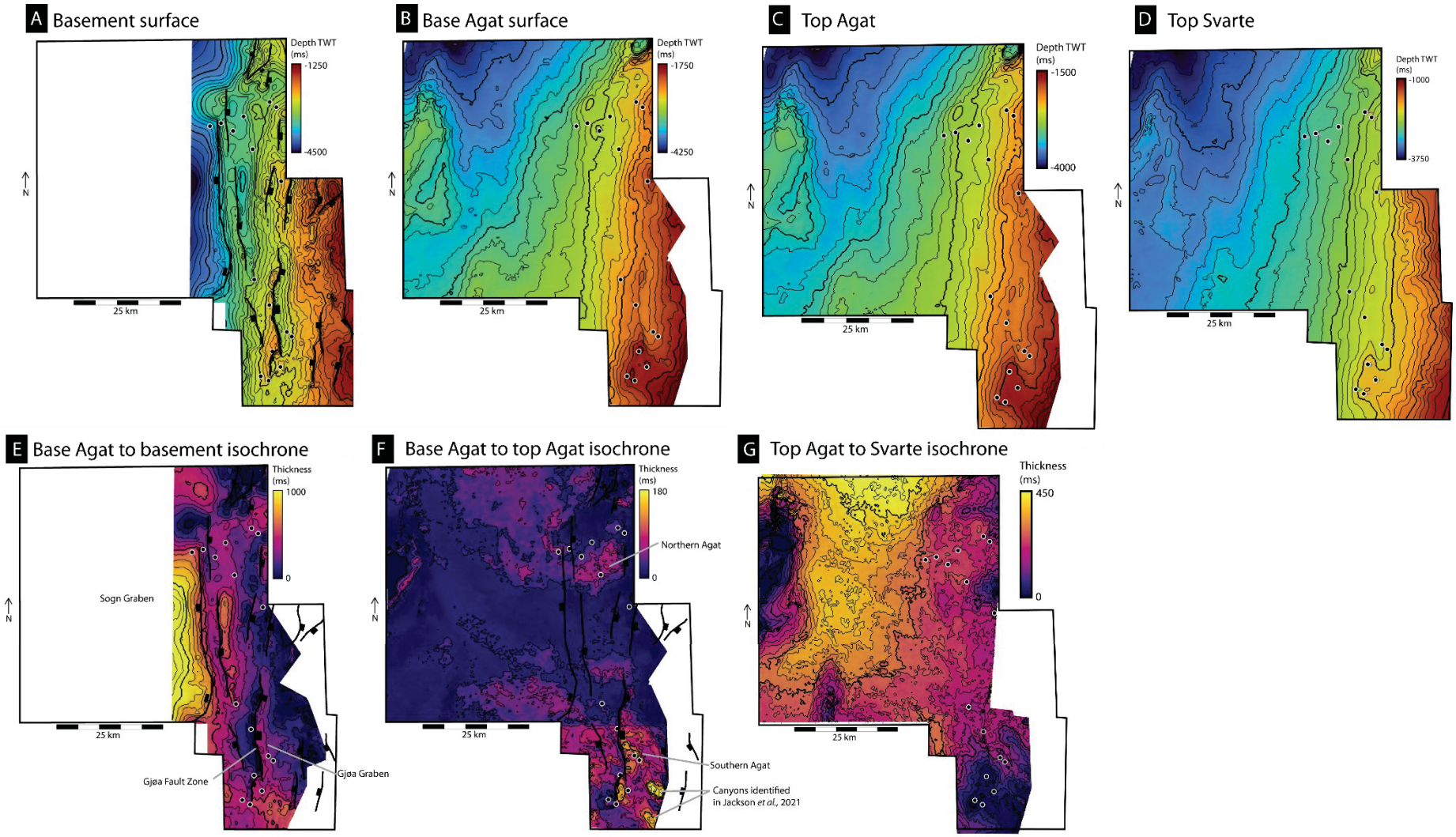


***Fig. 5.5**: Key seismic horizon surfaces and isochrons. Key basement faults are identified in the basement surface.*

isochrones (Fig. 5.5). These surfaces were selected to identify the distribution of the Agat Formation and to identify relationships between the Agat Formation and basement structures.

The basement (Fig. 5.5A) has been mapped over the Måløy Slope and highlights the underlying rift-related structures, once the basement deepens into the Sogn Graben any interpretation is highly uncertain due to poor resolution and is therefore not shown. The basement surface comprises a series of N-S trending faults that define a series of graben and half graben depressions (Fig. 5.5A). These grabens and half grabens exhibit thickening into them and thinning over basement highs (Fig. 5.5E). The basal Agat surface onlaps onto the basement in the west and dips the west before becoming more northerly dipping (Fig. 5.5C). The Agat isochron (Fig. 5.5F) shows two areas of significant thickness in the south and the north. The southern area appears to be mostly restricted the Gjøa Graben and thins to the northwest. The northern area has isolated areas of thicker Agat on the Måløy Slope before bending northward within the Sogn Graben. The Agat thicknesses appear to be related to underlying basement faults being confined in the south by the GFC and in the north by underlying faults on the slope.

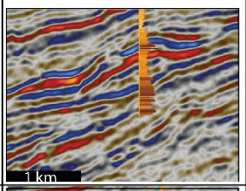
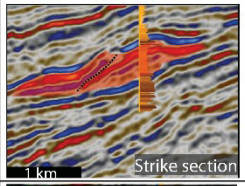
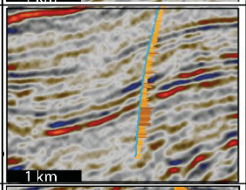
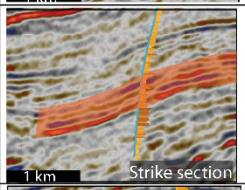
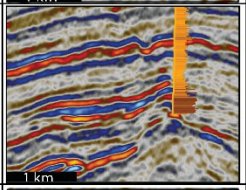
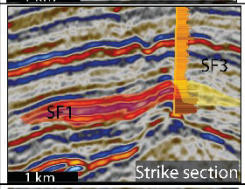
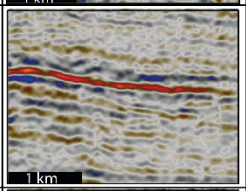
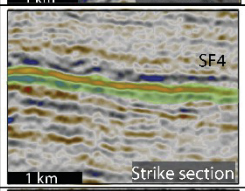
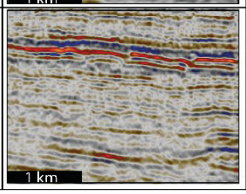
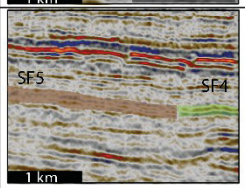
Seismic Facies	Uninterpreted	Interpreted	Description	Interpretation
SF1 Stacked confined channel complexes			Semi-continuous high amplitude, moderate frequency. Laterally pinching and dimming. Ribbon-like in planform. Example is hydrocarbon filled. Black dash line indicates boundary between two stacked channels.	Stacked channel complexes in a confined setting
SF2 Unconfined channel complex			Semi continuous moderate with laterally variable amplitude, high frequency reflections. Ribbon-like in planform.	Dispersed to stacked channels in a weakly confined setting
SF3 Channel complex overbank			Moderate to weak amplitude reflectors adjacent to SF1. Laterally pinching out.	Overbank deposits of confined channels
SF4 Lobe complex			Laterally continous high amplitude, moderate frequency reflections, dim laterally with occasionall swelling (thickening).	Lobe complex deposits, occasionally channelised
SF5 Background			Discontinuous weak amplitude, high freqency refelctions.	Mud-rich background sedimentation or distal lobe fringe

***Fig. 5.6**: Seismic facies present across the Agat isochrone. Red = positive hard kick. SF1 displays the GR log for 36/7-4, SF2 displays the GR for well 35/6-2S. Sf3 displays the GR log for 35/9-3T2. See fig 5.1 for well locations.*

Thicker areas are also identified in the southeast and are associated with the canyons identified by Jackson *et al.* (2021).

Five seismic facies (SF, Fig. 5.6) have been identified alongside RMS amplitude and spectral decomposition (Fig. 5.7) to interpret the character and to assist the mapping of the distribution of the of the Agat Formation. The Agat Formation was split into a lower (Fig. 5.7 A, B, C) and upper (Fig. 5.7 D, E, F) horizon to understand how the system evolved.

In the location where wells have intersected sand-rich intervals, the seismic expression is commonly a high amplitude with varying frequencies depending on their exact depositional environment (Fig. 5.6, SF1, 2, 3). Channel-form features (SF1 & SF2, Fig.5.6) are typically semi-continuous whereas lobes and background deposits have more continuous reflections (Fig. 5.6, SF4). SF1 is only observed in the Gjøa Graben. Outside the Gjøa Graben area, SF1 rapidly transitions to SF2. This is likely due to a decrease in confinement outside of the Gjøa Graben, with confined channels (SF1) having a stacked mounded expression and unconfined channels are more tabular and less likely to be vertically stacked. The proximity of SF3 to SF1 supports a channel margin or overbank interpretation (core facies described later in section 5.8.2).

5.5.1 The Lower Agat Horizon

Description: The Lower Agat horizon displays two distinct areas of sediment input, one in the north and one in the south, indicated by high amplitudes and overlapping frequencies. In the southeast, multiple small-scale linear features are present, trending NW-SE, which are associated with SF1 and continue to the northwest where they expand in the centre of the study area before narrowing again and continuing to the northwest where SF2 and SF4 are present (Fig. 5.6 A&B). In the northwest, it may interact with an E-W trending linear high amplitude feature with moderate frequencies that bifurcates in the west by bending northward. A possible halo of low amplitude (grey) and low frequency (dark) around this linear feature is present.

Interpretation: In the south, a sand-rich fairway running SE-NE appears to be sourced via a canyon system in the southeast. Confined channels are present within the Gjøa Graben close to the canyon system, which transition to a more unconfined channel system and a possible base

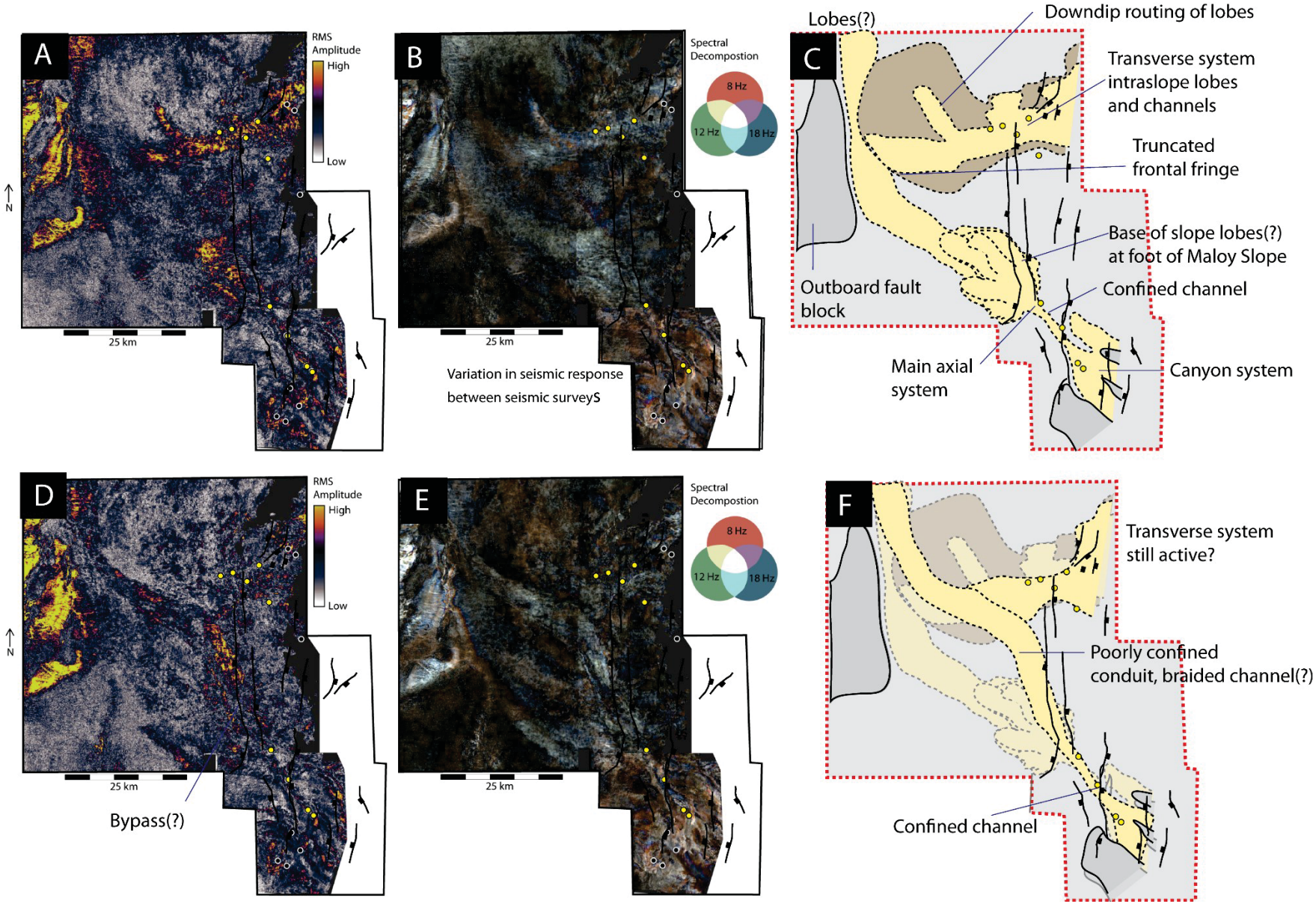


Fig. 5.7: RMS amplitude maps (A &D) and spectral decomposition (B&E) of the upper (A,B &C) and lower Agat (D,E,&F) Interpretations assisted by seismic facies analysis.

of slope lobe complex or intraslope lobe complex. This base of slope lobe system likely is a product of the change in gradient at the base of the Måløy Slope. However, the system continues to the northwest where it potentially interfingered with the transverse system. The transverse system is indicated by the high amplitude linear feature and has been previously mapped on the (Bugge *et al.*, 2001; Martinsen *et al.*, 2005).

5.5.2 The Upper Agat Horizon

Description: The Upper Agat horizon (Fig. 5.7 D&E) displays similar linear high amplitude features in the southeast that extend towards the northwest. The linear high amplitude feature with moderate frequencies remains in proximity to the east of the basin before curving towards the west close to the Tampen Spur. The northeast is more uncertain compared to the lower Agat horizon, exhibiting a less discernible amplitude and frequency. Nevertheless, it may indicate the system shifted southward, merging with the linear feature from the southeast. **Interpretation**: The southern channel system seems to stay close to the eastern basin or remains on the Måløy Slope (Fig. 5.7F). This might be due to the base of slope lobes (identified in the Lower Agat horizon) positive topography rerouting the channel towards the north before subsequently shifting back across, near the Tampen Spur. The two systems may interacted, with sediment from the northeast truncating the distal lobe of the northern transverse system or the north system ceased activity by this point in time.

5.6 Topographic controls

The main topographical control on the Agat Formation is the Måløy Slope that acts as a westerly ramp into the basin. Topography associated with grabens and half grabens on the slope acted to confine flows and pond sediment (Fig. 5.3 & 5.7 and Martinsen *et al.*, 2005). Our observations suggest that the confined channel system within the Gjøa Graben exhibited a different configuration and thickness than the channels outside of this region (cf. SF1 & SF2, Fig. 5.6). We infer that the Gjøa Fault Zone, the outboard fault network of Gjøa Graben, was a topographical high that acted to confine the channel (Fig. 5.8). This is supported by the shape of the channel, which transitions from the canyon system in the southeast to trending north before crossing the Gjøa Fault Zone (GFZ) and curving northeast (Fig. 5.7 B,C,D). The evidence suggests the channel system crossed the fault at this location due to the underlying rift configuration.

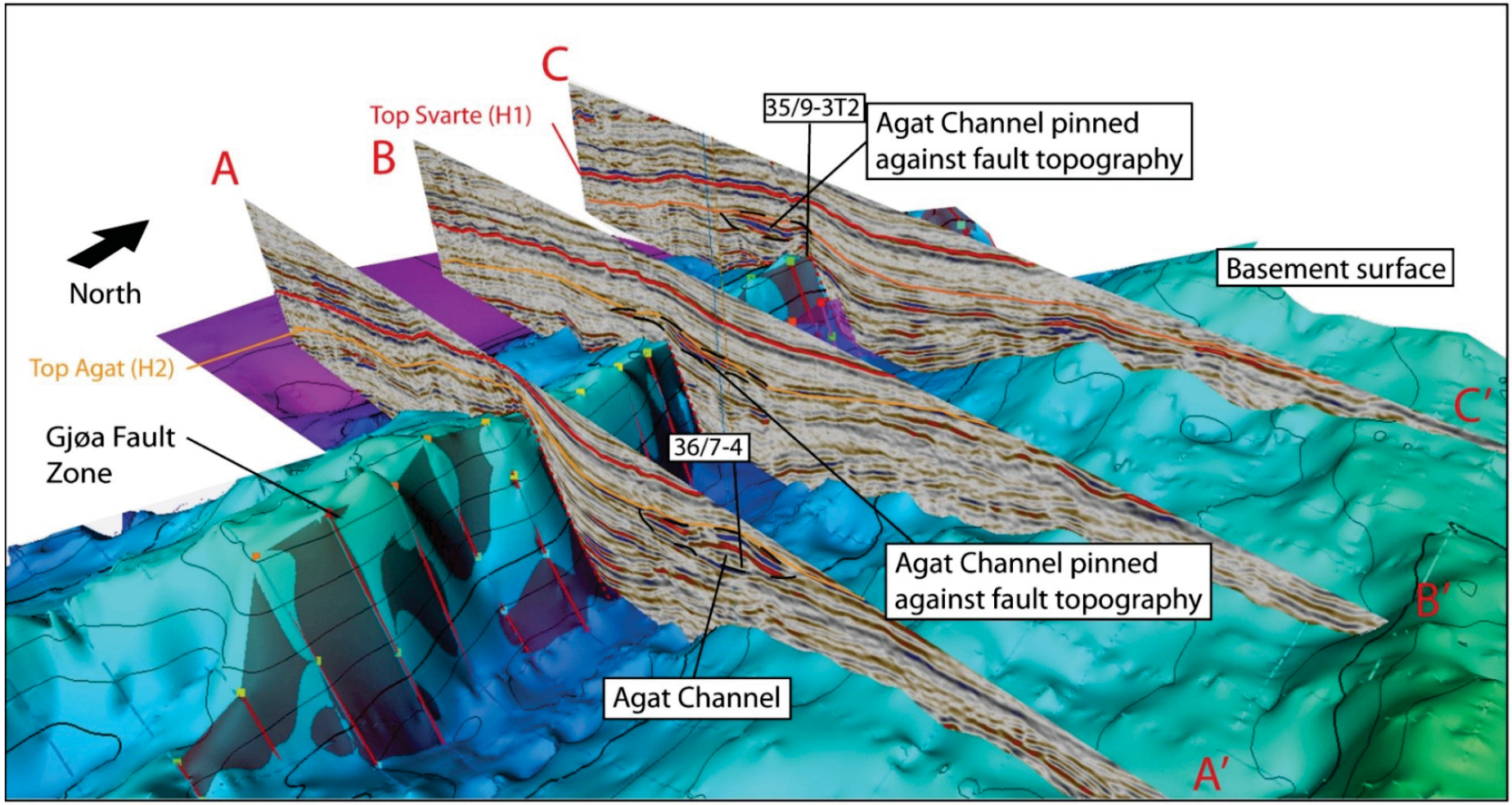


***Fig. 5.8**: Fence diagram showing path of channel in Southern area viewing down depositional dip. Location of lines displayed on Fig 5.1. Top of seismic lines cut at -2100ms.*

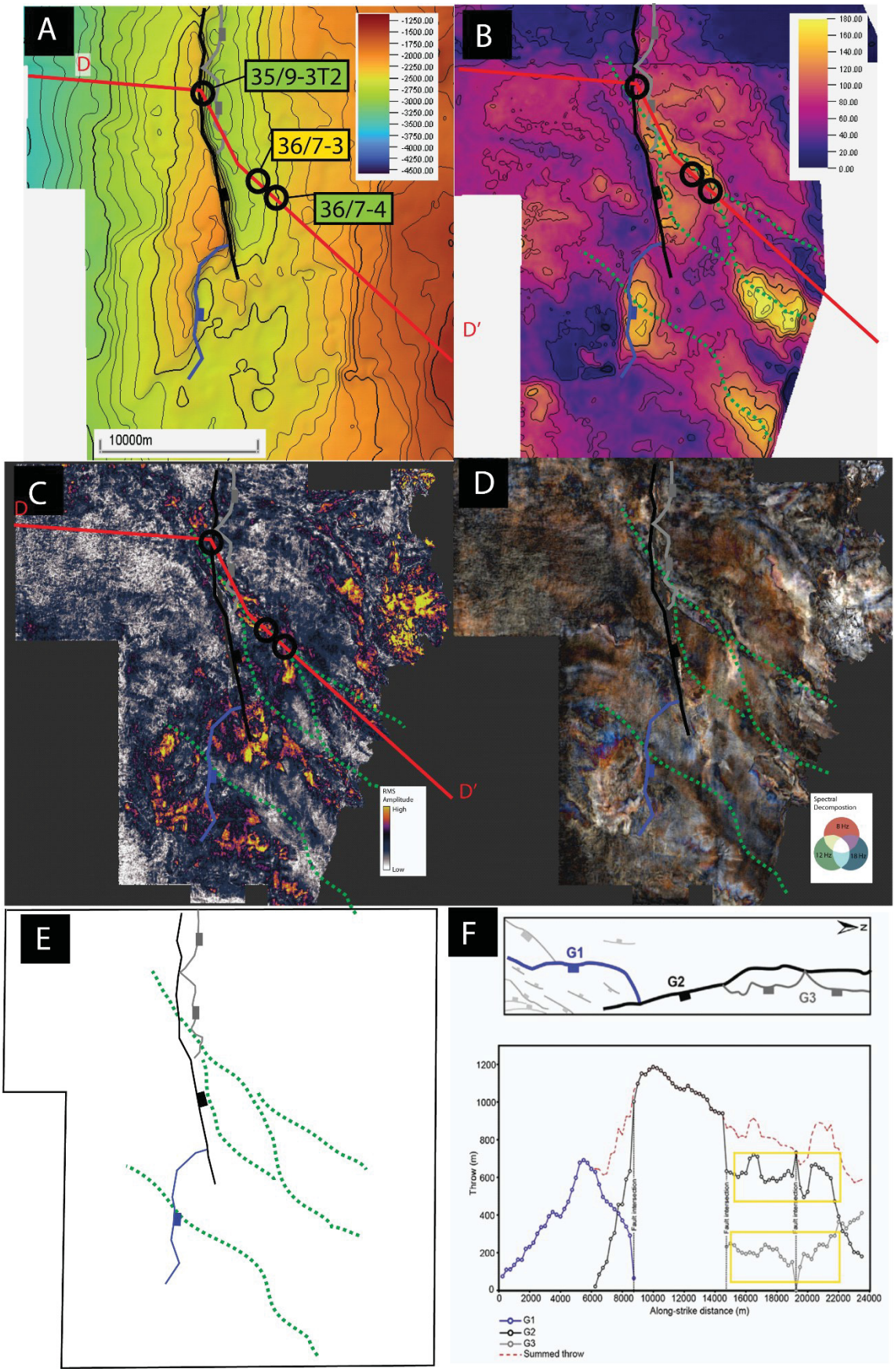


***Fig. 5.9**: Close up of the southern area covering the Gjøa Graben, highlighting location of channel thalwegs (green) and fault interpretation from Reeve et al, (2015). A) basement surface (ms), B) Agat isochrone (ms), C) RMS Amplitude, D) Spectral decomposition, E) basement faults with channel thalwegs, F) throw-distance profile of the Gjøa Fault Zone Fig. 5B from Reeve et al., (2015). D-D' Line location for Fig. 5.11.*

A detailed investigation of the Gjøa Fault Zone by Reeve et al. (2015) revealed that the GFZ consists of multiple segments with a complex fault geometry and throws that trend north-south with dips between 40-50° E, forming a kinematically linked system (Fig. 5.9F). The largest fault segment (G2, Fig. 5.9F, as in Reeve et al., 2015) bifurcates into two smaller fault segments to the north (G3, Fig. 5.9F, as in Reeve et al., 2015), causing a reduction of fault throw on the main fault (G2) due to some of the throw being taken up by the smaller fault segments (Fig. 5.9F yellow boxes). We propose that fault segmentation acted as a wider hinge zone and a lesser topographical step due to less differential compaction between the hanging wall and the fault segments compared to the hanging wall and the main fault (G2). This identifies that even thought the GFZ was buried and inactive at the time of Agat deposition there was still a seabed expression of the fault network that had an influence on sediment gravity flows.

5.7 Well Correlation

Three wells have been correlated (Fig. 5.10 & 5.11) in the Southern area using GR logs, seismic with biostratigraphy from Jackson et al., (2021). No biostratigraphy is available for 36/7-4. The top Svarte Formation, representing the end of the early post-rift (Gabrielsen *et al.*, 2001) has been used as a reference horizon due to its widespread and strong seismic character (Fig. 5.3).

In the northwest well 35/9-3T2 has penetrated a succession on a basement high associated with the GFZ with missing syn-rift (Asgard Fm. & Draupne Fm) sediments indicating this was a structural high before being draped by mudstone in the late Aptian (Fig. 5.10 & 5.11). The other two wells (36/7-3, 36/7-4) penetrated the Gjøa Graben and intersect sediments down to the Draupne Formation (Fig. 5.11).

The Måløy Slope's basement (Fig. 5.10, black horizon) dips to the west which is interrupted by a large fault zone known as the Gjøa Fault Zone which delineates the western limit of the Gjøa Graben. The sediments below the UJUNC are present inboard and outboard of the Gjøa Fault zone and is offset by multiple small scale faults that offset reflections. The varying thickness of this unit is likely caused by the high degree of erosion associated with the UJUNC (Fig. 5. 9). The overlying Asgard Formation is also highly variable in thickness due to infilling of the UJUNC and the overlying erosional Aptian Unconformity. The Sola Formation is the first sediments that are present on the Gjøa Fault high overlying the basement (Fig. 5.9 and 5.10).

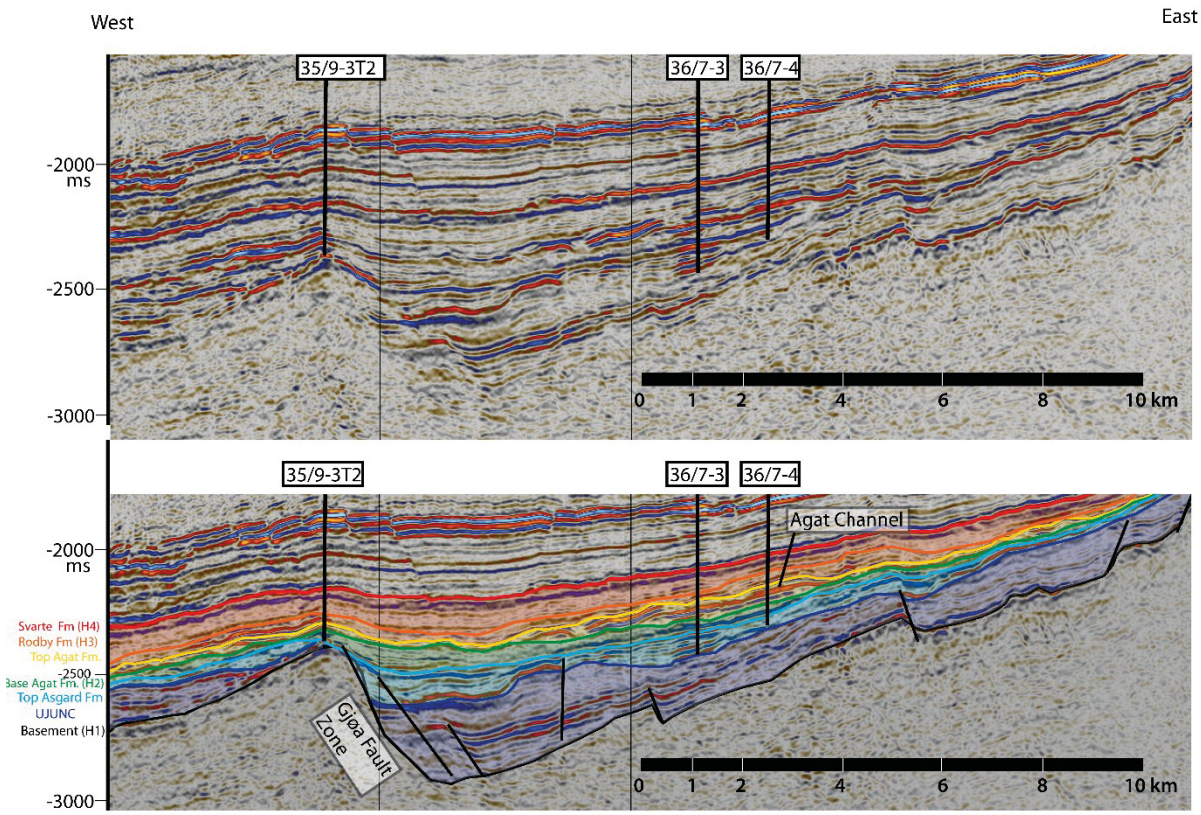


Fig. 5.10: *Seismic cross-section across Gjoa Graben. Colours are as Fig. 5.7. Note pinching and swelling in Agat Formation (Yellow) West to the left of the image. Red reflection = red hard kick*

Sediments deposited after the Aptian Unconformity (Top Asgard) thin and onlap to the East onto the Måløy Slope (Fig. 5.10 and 5.11) except for the Rødby and Agat Formations. The Aptian Unconformity down to the UJUNC shows significant thickness changes and wedge shaped geometries against the Gjøa Fault, as does the Asgard Formation (Fig. 5.10 light blue).

The Sola Formation appears to thicken into the Gjøa Graben (Fig. 5.10, green) indicating infilling of topographic lows. The distribution of the Rødby and Agat Formations is varied with thinning onto the basement associated with the Gjøa Fault Zone and thickens where Agat channels are intersected (Fig. 5.11). The Agat Formation shows a thinning towards 35/9-3T2 in the northwest on the basement high. The Agat Formation thins from the channel-fill deposits in 126m in 36/7-4, to 77m in 36/7-3, and to 45m of channel margin and overbank deposits in 35/9-3T2. However, this relationship in this cross-section underrepresents the rate of thinning as adjacent to 35/9-3T2 on the basement high a channel-form body is observed in seismic (Fig. 5.6, SF3 & 5.8 C-C').

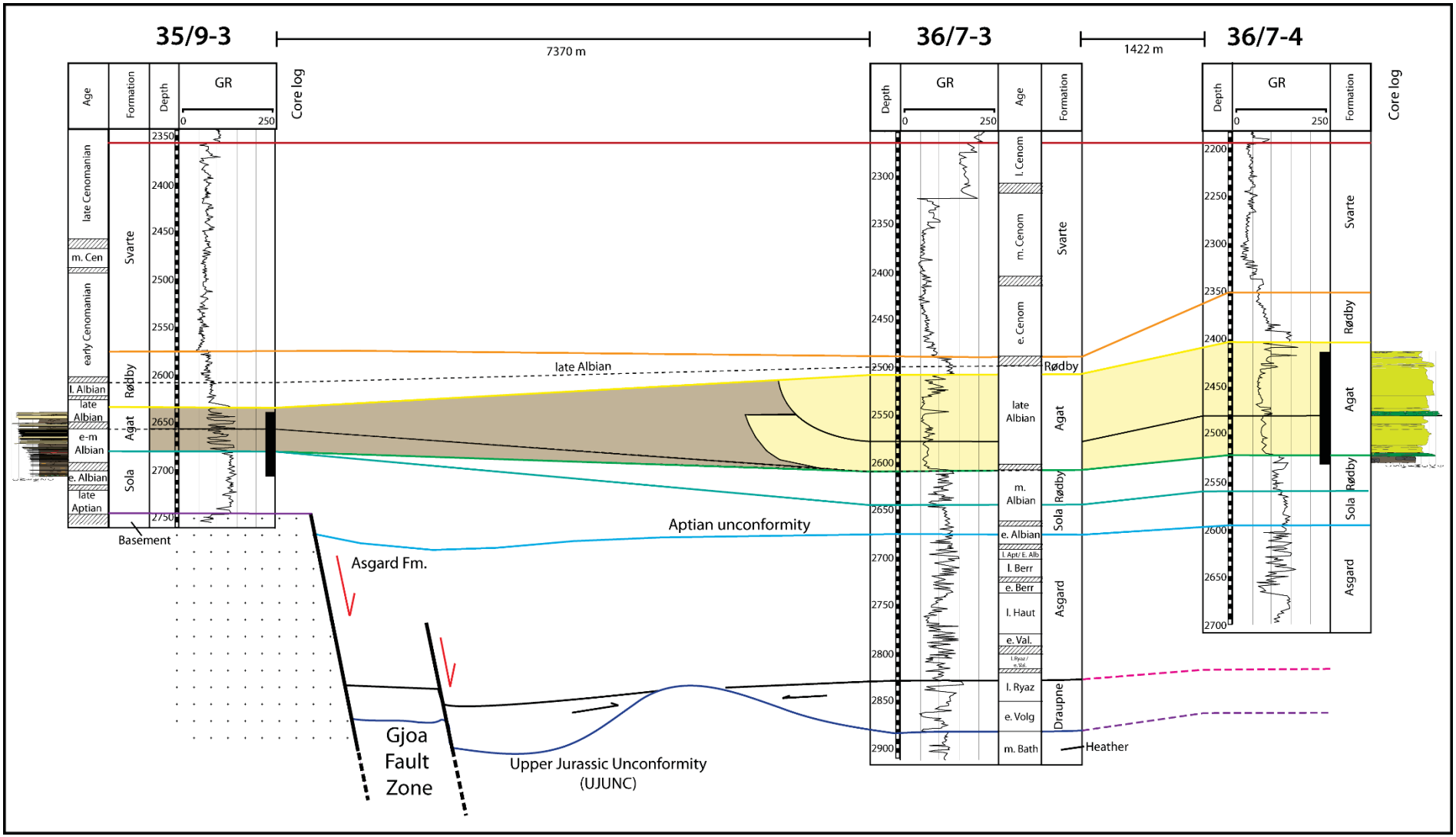


***Fig 5.11**: Modified from Jackson et al. (2021). Seismic line of cross section is displayed in Fig. 5.9. Core sections displayed in Fig. 5.13 and Appendix 5*

5.8 Southern Agat Formation sedimentology

Table 1 provides a summary of the facies (Fig. 5.12) described in the cored intervals (Fig 5.13. The deposits observed are typical of deep-water systems with high-density and low-density turbidites, hybrid event beds (transitional flow events and high-density turbidites with linked debrites), debrites and remobilised heterolithics and mudstones (Fig. 5.12).

C	Conglomerate	Conglomeratic medium to very coarse grained sandstone matrix with cm-dm clasts	Clast-supported conglomeratic sandstone. Clasts: angular to rounded, cm to dm clasts included green, dark grey mudstones and siderite/phosphatic nodules. Martix: medium to very coarse grained sandstone, poorly sorted	Deposited as basal lag deposits
SG	Granular sandstone	Medium to very-coarse grained sandstone	Sandstone with granular grains. Poorly sorted. Gluconitic and chlorite-rich in 36/7-4	Deposited by high denisty turbidity currents
SM	Massive sandstone	Fine to coarse grained sandstone	Moderately sorted, well sorted in finer grained, rare faint sandstone laminations. Gluconitic and chlorite-rich in 36/7-4	Deposited by high-density turbidity currents
SS	Structured sandstone	Fine to medium grained sandstone	Sandstone with planar to wavy and rippled laminations, typically mud draped occasionally with a coarse grained reddish mineral drape.	Deposited by dilute turbidity currents
SCr	Clast-rich sandstone	Medium to coarse grained sandstone with floating clasts	Clast-rich sandstone with green and dark grey mudclasts (sometimes armoured), commonly in discreate intervals, lithic and bioclastic clasts. Clasts are mm to 50 cm thick and are sub angualr to rounded or wispy (compacted).	Variable size and compostion of mudclasts, indicate a variety of sources, likely from local erosion of paleo-seabed.
SB	Banded sandstone	Fine to medium grained sandstone	Alternating bands (cm) of 'cleaner' sandstone and 'dirty' (high detrial claystone).	Banding indicates flutuation between turbulence and laminar flows (Stevenson et al., 2020)
HB1	Hybrid bed 1	Fine to medium grained sandstone with and overlying mudstone cap	Mud draped ripples to wavy laminated sandstone with an overlying 'linked' sandy mudrock	Couplets of low density (tractional) turbidites with an overlying linked debrite
HB2	Hybrid bed 2	Fine to medium grained sandstone with and overlying mudstone cap	A massive sandstone with an overlying linked debrite	Hybrid bed with a linked debrite (Haughton, 2003)
MM	Massive mudstone	Mudstone	Massive mudstones, commonly bioturbated (BI 1-3) with mud-filled burrows occaionally laminated.	Mudstone deposited by hemipelagic fallout or mud settleing from a waning flow (Boulesteix et al., 2019)
MC	Clast-rich mudstone	Mudstone with clasts	Mud-clast typically supported in a muddy matrix with a chaotic fabric	Deposited by mud-rich debris flows (Talling 2012)
DH	Deformed hetrolithics	Mudstone to medium sandstone	Hetrolithics exhibiting evidence of slumping. Discontinous/contineous sandstone or mudstone intervals which demonstrate contorted or steeply dipping lamination.	Slide or slumped beds remobilised due to gravity on glide planes indicated by the rotation of beds.

***Table 5.1**: Agat Formation facies table.*

Two styles of hybrid event beds are observed. Hybrid Bed 1 typically consists of a basal sandstone which may have a relatively thin massive sandstone, overlain by structured sandstone with mud draped discontinuous ripples/climbing ripples and planar laminations (as in Structured Sandstone facies) which typically make up most of the bed thickness. The beds are typically capped with a mudstone which may be massive or mudclast-rich and may show evidence of small-scale sand injection. Hybrid Bed 2 consists of a basal massive sandstone with an overlying massive mudclast-rich mudstone which may show evidence of sand injection. The sandstones of Hybrid Bed 2 typically have a whiter/cleaner appearance is likely be caused by depositional processes rather than a different source. Hybrid Bed 2 has a typical composition to previous documented linked debrites (*sensu* Haughton *et al.*, 2003) whereas

Hybrid Bed 1 is more enigmatic with climbing ripples indicating rapid loss of confinement typically seen in levee deposits, with a linked debrite cap potentially indicating rapid flow transition into a debris flow due to sandstone depletion.

The two cored wells have distinctly different character. Each well has been divided into successions which are made up of sections which may be further divided into units.

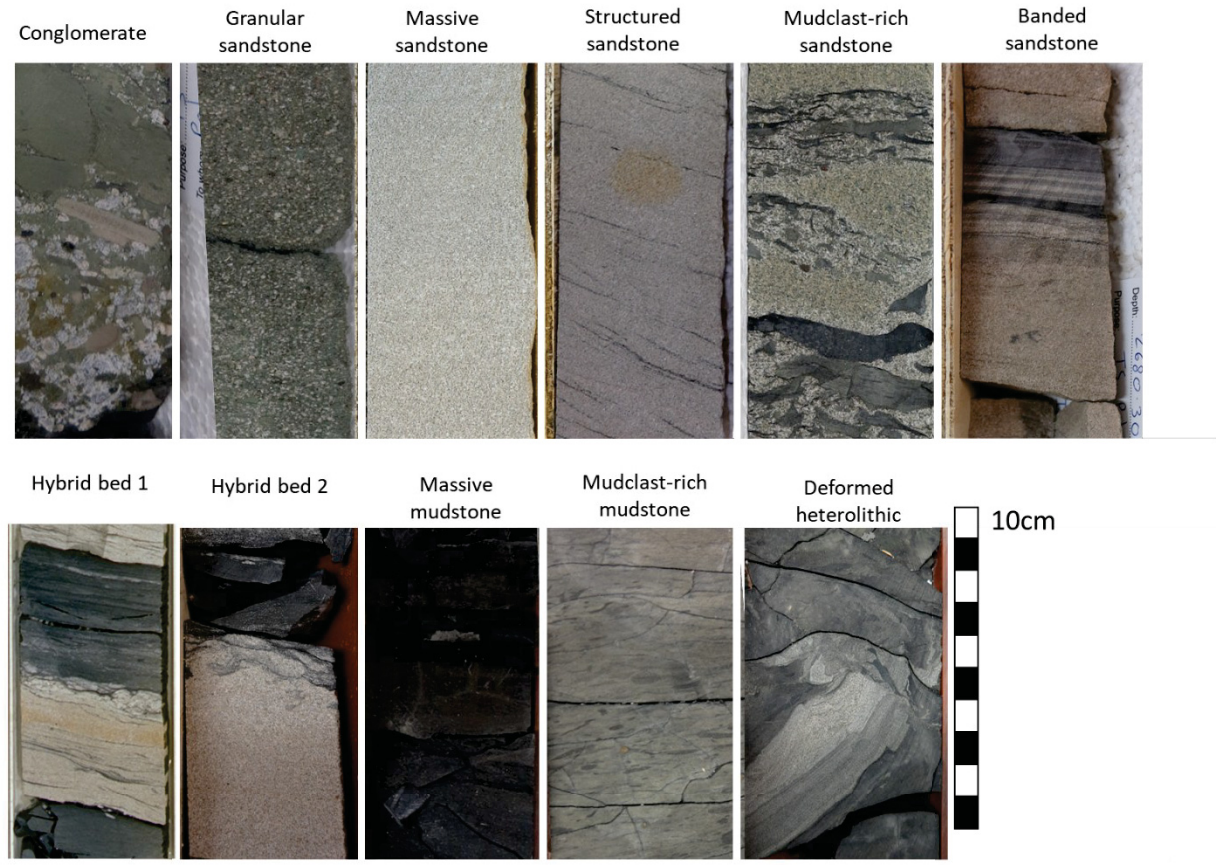


***Fig. 5.12**: Facies images, see Table 1 for full description*

5.8.1 Well 36/7-4

Description: This well's cored interval can be divided into two successions, a lower mud-rich and heterolithic succession (2547.6-2554.6m) and an upper sandstone-rich succession (2437-2547.6m, Fig 5.13). The lower succession (7m thick) of the core interval is dominated Mudclast-rich Mudstones (MC = 79%), Deformed Heterolithics (DH = 13%) and Massive Mudstones (MM = 8%, Fig. 5.14). The upper (110.6 m thick) succession is comprised of Granular Sandstones (SG = 54%), Massive Sandstones (SM = 14%), Clast-rich Sandstones (SCr= 17%). This succession is comprised of two similarly stacking sections (A and B), split by the conglomeratic interval (C = 1 % of cored interval) which are further subdivided into units picked on grain size breaks (Fig. 5.13). The lowest section (A = 42.7 m) can be divided

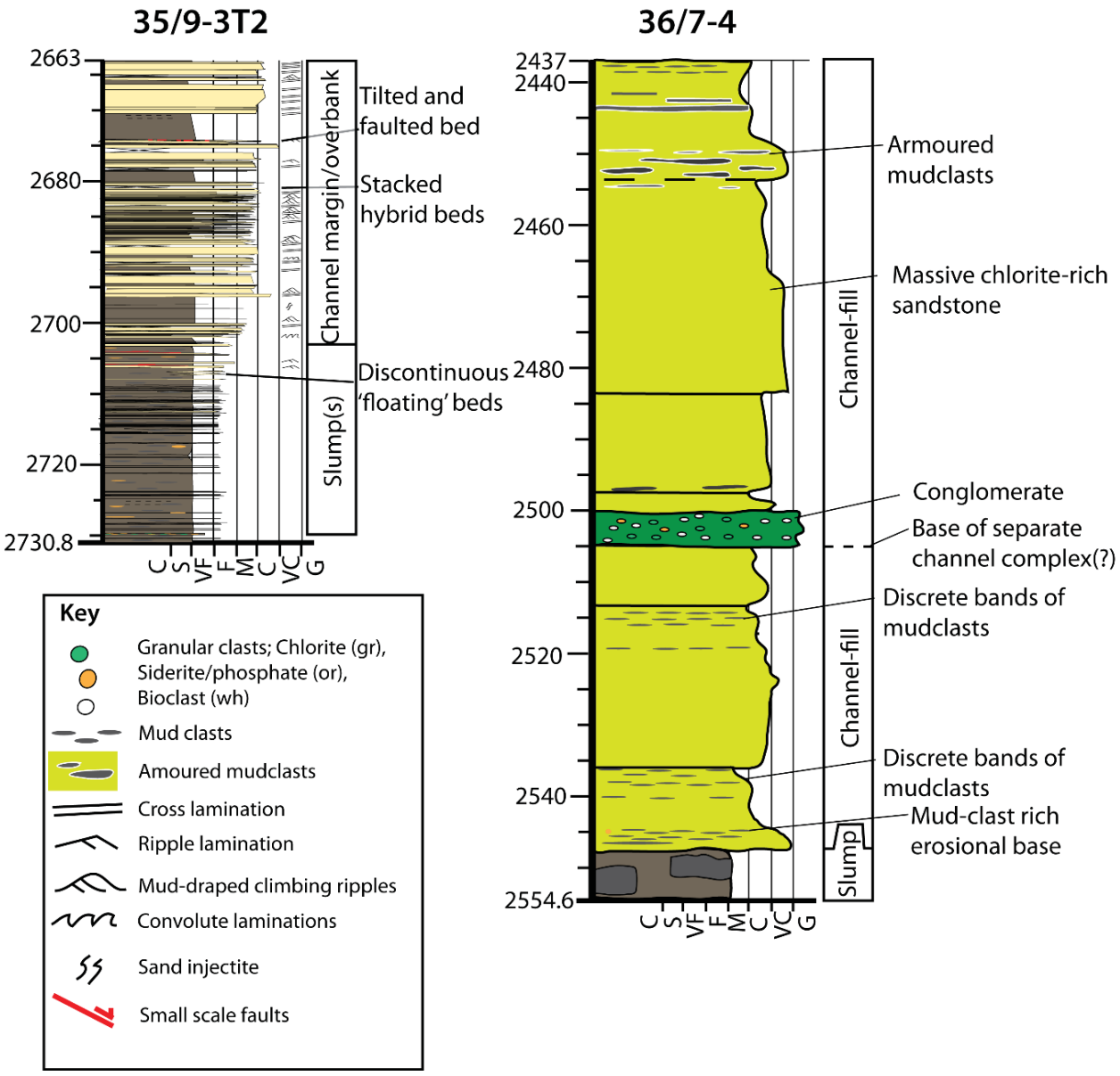


Fig. 5.13: Condensed logged core intervals with interpreted facies associations. See Appendix 5 for complete logs.

into possibly three discrete fining upward units. 1) The lowest unit (A.i. = 11.7 m thick) has an erosional base cutting into the underlying succession with an overlying granular sandstone rich in dark grey mudclasts that fines upwards. At the base of unit A.i. mudclasts are platy to blocky and can be pebble to core spanning (10cm vertically), in contrast to the top of the unit where dark grey mudclast accumulate in discrete horizons. The intermediate unit (A.ii. = 21.3 m thick) has a sharp grainsize break at the base and is inversely graded becoming normally graded with discrete dark grey mudclast horizons towards the unit top. The uppermost unit (A.iii. = 9.7m thick) is also inversely graded at the base becoming normally graded and has no mudclasts present. The upper section (B = 67.9 m thick) can be split into four units. The basal unit (B.i. =7.8m thick) has a conglomeratic base that fines upward into granular sandstones. The conglomerate is mostly matrix-supported mudclast within a granular sandstone matrix is

occasionally clast-supported. Clasts comprised of siderite and bioclastic material as well as dark grey and green mudstones. Dark grey mudclasts are blocky to platy whereas siderite, bioclastic material and green mudclasts are rounded and rarely platy. Overlying this conglomeratic unit is a normally graded unit (B.ii. 13.9 m thick) with a platy to wispy mudclast-rich base. Unit B.iii. is the thickest unit in the core (29.9 m thick), it composed of massive to granular sandstones which are relatively devoid of character and is normally graded. The uppermost unit (B.iv. 16.3 m thick) is different to the rest of the well in that dark grey mudclasts may be armoured with quartz grains, some mudclasts are massive or can be comprised of mudclast-rich mudstone, deformed heterolithic facies. Towards the top of this unit the mudclasts are the more typical, platy to wispy dark grey mudclasts.

The mudclast appear to have a bimodal nature typically either dark grey with a wispy fabric or rounded with a more varied lithology (green mudstone, bioclastic or siderite). The wispy dark grey clasts indicate they were likely not lithified and may be a result of local seabed erosion. Whereas the more rounded clasts were likely more resistant to erosion during transportation due to the lithified nature, possibly indicating transportation from further, possibly a shelfal catchment area, which is also supported by the bioclastic composition of some of the clasts.

Interpretation: The extensively deformed character of the lower succession supports the interpretation that these are a mud-rich remobilised slump facies association with occasional sandstone beds that retain the original depositional structure. The fining-upward, erosional bed bases, sand-rich nature, mudclast-rich horizons and conglomerates of the upper succession suggests a high-energy channelised environment. Based on thicknesses, units have been interpreted to be channel-fills with sections A & B (described above) equating to channel complexes (Sprague *et al.*, 2005; McHargue *et al.*, 2011). The variation between mudclast-poor rich and mudclast-rich and sandstones is interpreted to be due to channel story migration, with mud-clast-poor deposits suggesting an axial location and mud-clast rich sandstone with distinct horizons representing the channel off-axis (*sensu* Hubbard *et al.*, 2014). The conglomerate unit likely represents a lag deposit, marking the base of a channel complex (Mayall *et al.*, 2006). In well 36/7-4 this would suggest that there are two vertically stacked channel complexes each comprising of at least three to four axial channel fills. The underlying slump deposits may or may not represent a basal channel deposit or was deposited prior to channel activation.

5.8.2 Well 35/9-3T2

Description: This well is also divided into two successions; a lower mudstone-rich (2703.2-2730.8m, 27.6 m thick) and an upper (2663-2703.2m, 40.2m) thin-bedded sandstone succession (Fig. 5.13). The lower succession is dominated by Mudclast-rich Mudstone (MC = 56%) and Deformed Heterolithics (DH = 43%) facies (Fig. 5.14). The Mudclast-rich Mudstone has a contorted fabric and mudclasts are of a dark grey colour and oval to platy or wispy in shape. Deformed Heterolithics are typically fine-grained thin (c. 10cm) laminated sandstone beds interbedded with mudstones and may be over-steepened or overturned. The sandstone beds are occasionally discontinuous across the core with a contorted fabric that is rarely microfaulted. The original depositional character of the sandstone beds is occasionally still

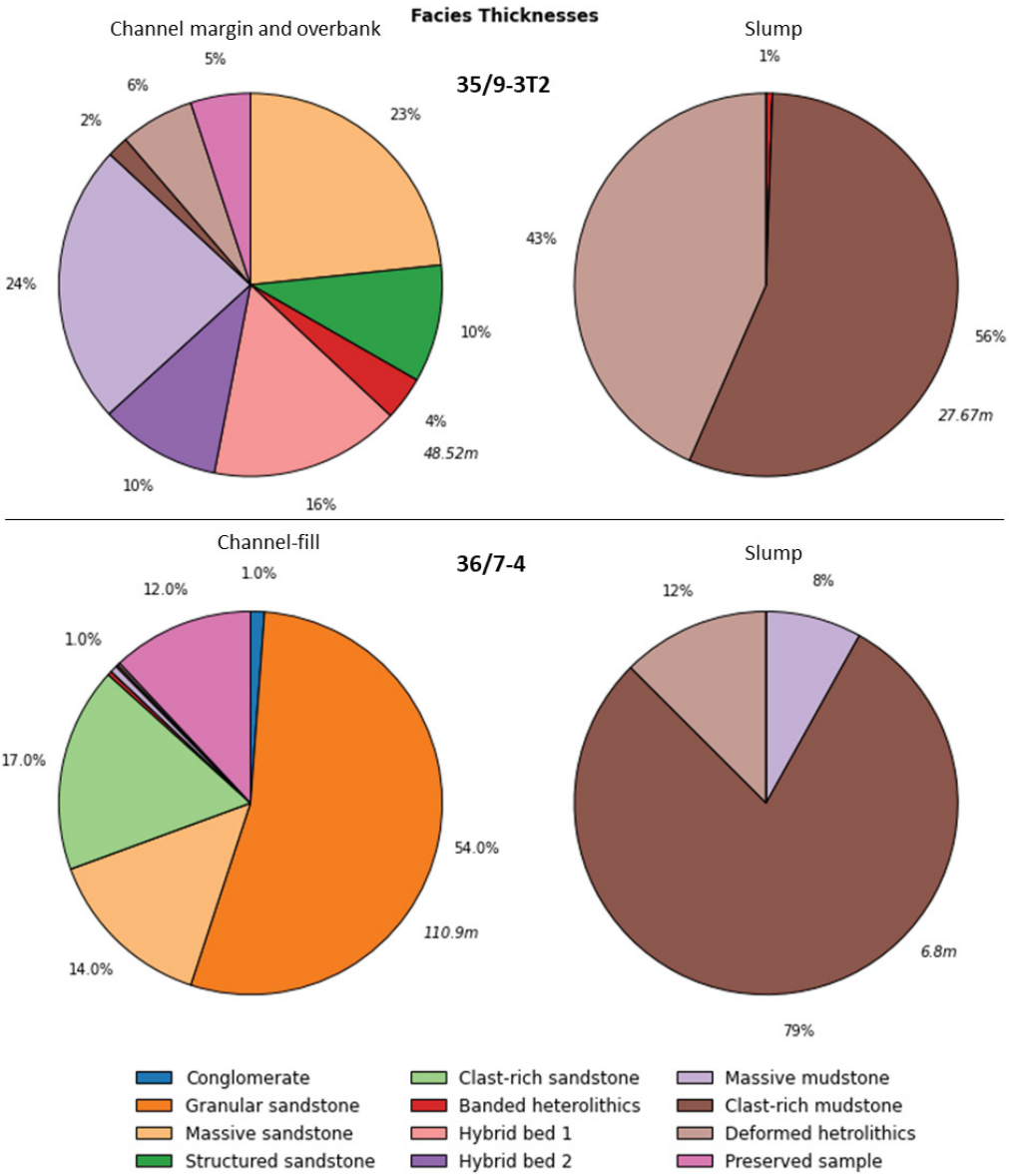


Fig. 5.14:*Facies association composition of the cored wells. Facies <1% not labelled.*

apparent, typically they are fine-grained normally graded beds of Structured Sandstone (SS) or Banded Sandstones (SB). The upper section is highly variable with Massive Mudstone (MM=24%) and Massive Sandstone (SM=23%) dominating with subordinate Hybrid Beds 1 and 2 (16% and 10% respectively) and structured sandstones (SS= 10%). This section is also made up of minor (<10%) Banded Heterolithics, Deformed Heterolithics and Clast-rich Mudstone. The thinly bedded sandstones average c.35 cm thick and are interbedded with Massive Mudstones and to a less extent Deformed Mudstones (c.65cm). Both styles of hybrid beds are observed in this section and may be interbedded with each other forming bed stacks. These bed stacks are often thin and fine upwards with the muddy debrite cap increasing in proportion upwards.

Interpretation: The lower succession in 35/9-3T2 is comparable to the lower succession in 36/7-4, in that the sediments are predominantly deformed and mud-rich. However, there is a high proportion of sandstone beds retaining the original depositional fabric than in 36/7-4. This supports the interpretation of a remobilised slide facies association.

Within this succession there are mud-rich deformed units interbedded with the sandstone intervals which are likely to represent remobilised mudstone such as slumps or slides. This signifies that there is likely to have been local topography, which may also be influencing sediment gravity flows into this area. This disorganised arrangement of beds indicates an area where high energy and lower energy flows can interact. The presence of interbedded slide deposits indicates there was topography that was present thought deposition of the sandstones.

The upper succession is not comparable to the 36/7-4, being dominated by thinnly bedded sandsstones which display a increase in hybrid event beds and low-density turbidites. This supports a lower energy environement. The presence of climbing ripples indicates rapid depostion of sandstone a result of loss of confinement (Kane & Hodgson, 2011; Jobe *et al.*, 2012). This interpretation is supported by the wells intersection of the flank of a channel body (Fig 5.6, SF3) indicating a levee or overbank depositional environment.

The reason for the variation between the two hybrid beds remains uncertain. The hybrid beds thicknesses remain similar and upward fining indicating the flows were of similar competence and size. Hybrid event beds 1 are enigmatic in that a low-density turbidity current with tractional structures is overlain by a linked debris flow. This style of hybrid event bed may represent a separation of flows, with a forerunning low density turbidity current chased by a

debris flows which are separated enough to enable tractional structures to be deposited as see in the Windermere Group (Ningthoujam *et al.*, 2023). This would be counterintuitive to a levee environment in that it is unlikely that a debris flow confined in a channel would escape into a levee environment Hybrid bed 2 are consistent with previous interpretation of hybrid event beds and are not commonly describe in levee deposits (Haughton *et al.*, 2003; Kane & Hodgson, 2011). Hybrid event beds are commonly documented at slope gradient changes at frontal lobe fringes and lobes influenced by topography (Davis *et al.*, 2009; Spychala *et al.*, 2017a) as well as in CTLZ (Brooks *et al.*, 2018a, 2022) and in levee environments exposed to pulsing flows (Ningthoujam *et al.*, 2023). Due to the proximity of channels lobe interpretations are discounted therefore, the presence of hybrid event beds in this channel margin or overbank location may be a result of the underlying fault influencing slope gradients potentially leading to pulsed flows trigger by topography as see in the Windermere group (Ningthoujam *et al.*, 2023).

5.8.3 Facies Associations

From our facies analysis we have identified three facies associations: remobilised slump deposits, channel-fill, and channel margin and overbank. The channel-fill facies association in the upper section in 36/7-4 represent stacked axial channel-fill deposits (e,g, Mayall *et al.*, 2006; Bakke *et al.*, 2008; Hubbard *et al.*, 2014) and is also supported by seismic geomorphology, (Fig. 5.7). Whereas the channel margin and overbank facies association in the upper section in 35/9-3T2, represent a channel margin and overbank depositional environment likely in a terrace environment within incised channel indicated by the complex ripple arrangement and underlying the slide deposit which may be derived bank collapse from an external levee (e.g. Hansen *et al.*, 2017), this interpretation is also supported by seismic geomorphology interpretation on the flank of a channel body (Fig. 5.7). Both wells have a lower succession that is comprised of a remobilised deposit facies association. Underlying the channel margin and overbank facies association the remobilised deposits are more intact with oversteepened beds suggesting less travel distance than the more disaggregated remobilised deposits underlying the axial channel-fill deposits.

Sandstone colour variations: The sandstones vary in colour between the two wells, in 36/7-4 the sandstones are green in colour whereas the sandstones in 35/9-3T2 are light brown. Previous analysis on 36/7-4 well (Azzam et al. 2022 and Hansen et al 2021) has identified the presence of chlorite grain coatings that were inherited prior to transportation to the deep-water.

Therefore, the absence of the chlorite coatings in 35/9-3T2 may be due to two reasons. Firstly, the sediment supplied to the area may have varied over time, as channel overbanks are deposited by bypassing flows and initial flows were not chlorite/glauconite-rich (Hodgson *et al.*, 2016), or due to hydrodynamic fractionation confining the deposition of chlorite coated grains to the channel axis.

5.9 The Agat Depositional model

The channel-fill deposits of 36/7-4 have a low blocky GR character, that spikes where mud-rich conglomerate facies are present in the core. Minor increases in GR are associated with the mudclast-rich horizons (Fig. 5.11). Well 36/7-3, has a similar blocky GR character to 36/7-4 and has been interpreted to be dominated by channel-fill facies association, this interpretation is supported in seismic by an unbroken reflector with similar amplitude and frequency (Fig. 5.7 & 5.10). The channel margin and overbank facies association present in 35/9-3T2 have a serrated GR expression and with biostratigraphy indicating they are older than the channel-fill deposits in the other two wells. This is consistent with some channel environments as the overbank deposits are deposited by bypassing flows utilising the channel whereas the channel-fill represents the later infilling of the channel. The biostratigraphy suggests that the channel-fill deposits are later than the lower channel margin and overbank deposits of 35/9-3T2 (Fig. 5.10) supporting our interpretation (*sensu* Hodgson *et al.*, 2016). Slumping appears to be common likely due to the gradient of the Måløy Slope at time of deposition, although in 36/7-4 it is interpreted to represent the base of the channel system (sensu Mayall *et al.*, 2006)

Deep-water clastic input into the Måløy Slope and Sogn Graben during the Lower Cretaceous represented a significant change from the earlier mud-rich post-rift sediments. The abundance of wells that intersect sediment gravity flow deposits that have been mapped out in channel and lobe/sheet-like sandstones (described above and in Nystuen, 1999; Martinsen *et al.*, 2005) indicate that the Agat Formation was sourced from the East down a slope with a complex morphology due to inherited rift-related features. At two systems have been documented as southerly channelised system that trends northward once into the Sogn Graben and a transverse system that initially deposited sediment in a linear fashion down the slope, before branching northward (Fig. 5.7).

This axial system was sourced by canyons in the southeast which initially routed sediment into the Gjøa Graben area where channels were highly confined laterally by compaction hinges over the outboard Gjøa Fault Zone preventing lateral stacking of channels. This fault zone has a

complex geometry which likely controlled the routing of the channels as we observe the channels crossing the fault zone where throw distances were decreased, and the fault was segmented possibly creating more of a stepped topography (Fig. 5.7). This fault controlled channel routing has been previously documented in gravitational-driven thrusting in passive margins (Pizzi *et al.*, 2023). The system then deposited a possible lobe at the base of the Måløy Slope likely triggered by a change in gradient at the base of the Måløy Slope (*sensu* Pohl *et al.*, 2020). Before prograding and routing sediment to the North outside the study area and possibly interacting with the frontal fringe of the transverse system. Later the channel shifted northward and overlies the lobes of the transverse system.

The transverse system was ponded on the slope in topography created by hinge zones over basement highs leading to a complex distribution (Martinsen *et al.*, 2005). Once this topography was bypassed or infilled the system appears to have a straight linear morphology depositing sediment down the Måløy Slope . At some point in the life of the system the flows were directed northward likely due to the development of topography by the underlying lobes with the direction of avulsion supported by the graben deepening to the North. The frontal fringe of the transverse system appears to be cross-cut by the channelised southern system and latterly the channel appears to override the transverse lobes.

5.10 Conclusions

This study applies an integrated data set including cored and uncored wells alongside seismic reflection data to describe the character and distribution of the Lower Cretaceous Agat Formation in the Northern North Sea specifically focusing around the Gjøa Graben. Two sediment entry points were mapped; a southern axial system dominated by channels sourced by a canyon system and a northern transverse system running perpendicular to the basins axis. The two systems potentially interact at the most distal point of the transverse system where a southern system channel potentially truncates lobes for the northern system. Core analysis from the southern axial system identifies three facies associations; channel-fill, channel margin and overbank, and slump deposits supporting the seismic interpretation of channels. Variation in sandstone colour and minerology between channel-fill and channel margin and overbank deposits may indicate a change in updip sediment source. Rift related topography plays a significant role in the distribution of the Agat Formation potentially influencing the deposition of hybrid event beds in overbank deposits and on routing of the channels, which in the Southern Agat are controlled by the underlying Gjøa Fault Complex. Initially the fault confines and deflected the channel to the north, before crossing the fault complex where the fault zone was

bifurcated leading to a reduced fault throw. This bifurcation of the fault complex may have been less of a topographic obstruction to the channel due to variations in compaction across the fault segments enabling the crossing of the channel into the Sogn Graben. This is contrasted in the northern transverse system which has a straighter more direct routing into the Sogn Graben with faults in the Måløy Slope potentially acting as sites for ponding of intraslope lobes.

Acknowledgements

We thank the Norwegian Petroleum Directorate for access to the data for this study. We also thank the Lobe3 JIP sponsors for funding TW's PhD which this study forms a part of.

6 Discussion & Conclusion

Understanding of the relationship between deep water sediment gravity flows and inherited early post-rift topography has been essential theme running throughout this thesis. In the proceeding chapters, I have analysed subsurface datasets at a range of scales, environments and locations. The deep water lobes of the Angel Formation, NW Shelf, Australia have been analysed at a basin-scale (Chapter 3) to the mineralogical-scale (Chapter 4), whereas the channel system of the Agat Formation has been analysed at a basin-scale to bed-scale (Chapter 5). In the subsequent sections I will deal with the main aims of this thesis and then consider further work.

6.1 How does inherited structural relief effect the architecture and distribution of sand-rich lobes?

In Chapter 3, I investigated the distribution and morphology of the sand-rich lobe complexes in an underfilled early post-rift basin. The main findings from this study were that the main controls on the distribution of lobe complexes were the location of sediment source and the inherited rift related structures. These factors subsequently prompted rapid rates of sand pinch out against the inherited topography.

The exact sediment source of the Angel Formation remains enigmatic. However, the uniform texture and mineralogy indicates a single source. I have speculated on two possibilities for this single source area, a large shelfal to the East that is linked to the outboard horst blocks of the Rankin Trend or the reworking of a basin-wide sand-rich deposits previously deposited over the basement highs such as the Legendre Formation. The sediment source for the Angel Formation was mud-poor as very little mud is observed in the system, this likely had a knock on effect on the rate and style of pinch out we observe, which is discussed below. This wide-spread sediment source with multiple entry points enabled the development of coeval axial and transverse lobe systems which is commonly seen in the syn-rift but is becoming more commonly observed in the early post-rift (Chiarella and Joel, 2021; Hansen *et al.,* 2021). Tectonic related relief was inherited from the Late Triassic to Middle Jurassic period of rifting however the configuration was strongly affected by the underlying Late Carboniferous to Late Triassic rift configuration. This configuration led to the sediments being sourced from the Rankin Trend basement highs and the East. The Rankin Trends e*n echelon* fault orientation guided sediment routing down relay ramps and tilted horst blocks, as well as infilling degraded

fault scarp topography (Fig. 6.1A). The hanging-wall anticline of the Madeleine Anticline appears to have a limited impact on sandstone distribution with thick lobe complexes developing on the top of the structure.

Chapter 3 also focused on a lateral sand pinch out against a degraded fault scarp. The inherited fault related topography impacted the distribution of sandstone deposition across the timespan of the system. High-rates of pinch outs are observed leading to a simple onlap interpretation with no flow transformation observed (e.g. hybrid event beds). This indicates that topography of between 1-3.5° (compacted) can trigger abrupt flow collapse in sand-rich turbidity currents. The rate of the sand pinch out generally decreases as topography is healed. However, as the infilled topography is rugose the pinch out rate does not decrease upward in a linear fashion. This high rate of pinch out can be accounted for by the depositional flows being large in comparison to the confining topography (*sensu* Liu *et al.* 2018; Stanbrook and Bentley, 2022).

This work has important implications for understanding reservoir distributions in the subsurface. The identification of a simple onlap geometry and sand dominance up to inherited relief will be useful in models for calculating the storage capacity of these reservoir rocks for hydrocarbons and carbon dioxide.

6.2 How does topography effect the sand pinch out in sand-rich lobes?

In Chapter 4, I utilised reflectance spectroscopy which has not previously been applied to deep water sedimentology, to characterise the heavily bioturbated heterolithic facies identified in Chapter 3. The key findings were that the technique can identify the relative abundances of quartz, kaolin and feldspars in deep water deposits and that there was relatively little to no flow transition or run-up onto the topographical highs.

Initially, spectral reflectance data was compared to other studies which utilised other techniques this found that in this example the results were reasonably accurate considering the minimum resolution of mineral is >5%. Therefore, this technique is only useful in identifying the main mineral assemblages in this example. Often the relative quartz abundance was over estimated due to two reasons, as the minerals <5% were not counted this automatically overrepresented the minerals that were detected and the possibility of variation in detection due to the relative grain size of the minerals.

The analysis of relative abundance and distribution of the mineral assemblages has developed the interpretation of the Angel Formation from Chapter 3. The abundance of carbonate and

siderite cements within the lobe complexes appears to have a direct relationship with the porosity and permeability of the sandstones, which is to be expected with the development of diagenetic cements. In future studies, this technique could offer a quick initial interpretation that is able to capture the heterogeneities in the rock that may require further analysis e.g., thin-sections analysis.

The identification of zones of possible thin-bedded turbidites, based on quartz abundance, has identified that dilute flows or parts of flows were able to run up topography. Based on the lack of any mudclasts within the bioturbated zones ruling out a hybrid event bed origin, the origin of the thin-beds could two-fold. They may be a result of flow stripping as a result of the topography or separate dilute turbidity current origin. This again supports the model that the sand-rich parts of the flows rapidly collapsed when interacting with topography.

6.3 How does inherited structural relief effect the architecture and distribution of channels?

In Chapter 5, I investigated how subtle topographical confinement can influence the distribution and morphology of a channel and lobe system of the Agat Formation, Norwegian North Sea. The main findings from this study were that subtle confinement associated with variations in geometry of buried underlying rift faults can affect channel routing and lobe distribution and the presence of key lithological variations between channel axis and channel margin and overbanks. In the early post-rift setting we observe an interplay of transverse lobe system and axial channel systems.

The Agat channel system is confined by topography associated with depositional compaction around underlying basement faults. These compaction hinges forming over underlying faults act as subtle confining topography, with fault geometries playing an import role in influencing flows (Fig. 6.1B). Underlying faults are observed to bifurcate into fault segments along strike before re-intersecting. During the time of Agat deposition the channel system which was initially confined to the half graben associated with the Gjøa Fault, crosses over the fault at the point where the fault is segmented. This indicates that there was likely less topography related to depositional compaction over these split fault segments than on the main fault before then being captured by a second fault to the north. This highlighted the importance of understanding the basins tectonic physiography for predicting sediment routing patterns.

A transverse submarine fan is initially deposited perpendicular to the basin axis and may be potentially frontally confined by the outboard fault system of the Sogn Graben. As system

became more established and prograded into the basin, the dip of the basins slope asserted greater control and altered the focus of deposition to a more down dip location as the system.

In a location with a fixed channel position (crossing a compaction hinge), channel margin and overbank deposits are compositionally and sedimentologically significantly different to the channel-fill axis. In terms of compositionally, the earlier channel margin and overbank deposits are poor in chlorite clays and glauconite, whereas the later channel-fill deposits are rich in chlorite clays and glauconite. This indicates a significant change in either the sediment source or how the sediment was routed on the shelf. The increase in glauconite would indicate longer storage on the shelf before remobilisation into the deep water. Whereas chlorite clays are associated with estuarine environments with input from lateritic soils (Azzam *et al.*, 2022). This change in sedimentation may have been linked to the remobilisation of sediments stored on the shelf due to uplift mainland Norway triggered by the initiation of rifting in the North Atlantic or to the continued deepening of the North Sea linking shelfal areas (Gabrielsen *et al.*, 2001; Kyrkjebø *et al.*, 2001).

The channel axis deposits are different to the deposits channel margin and overbank. Channel axis deposits are comprised of amalgamated high density turbidites with lag deposits. Whereas channel margin and overbank deposits are made up of a mixture of transitional flow deposits often displaying complex flow fields and linked-debrite deposits interbedded with slump deposits. The complex flow fields observed are likely linked flows reflecting of surround topography which are likely channel-related as opposed to the subtle topography derived from differential compaction over a hinge zone.

6.4 Controls on early post-rift deep water architecture

I have documented two examples of early post-rift deepwater systems which differ significantly in their grain size, mud content, and post-rift fill stage (Fig. 6.1).

The sand-rich Angel Formation distribution and architecture is governed by its high-sand content and its direct interaction with fault topography in a under filled basin such as abrupt pinch outs against topography and routing through transfer zones associated with *en echelon* faulting (6.1A). Similar routing down transfer zones is observed by coarse-grained high-density turbidity currents in the Lusitanian Basin (Leinfelder & Wilson, 2010). At this stage of the basins fill subtle topography (e.g. the Madeliene Anticline) plays a less significant role than it may play later in the basins fill stage. At a similar under-filled stage, lobes have been documented to stack in depressions in a fill-and spill style model (Argent *et al.*, 2000), this

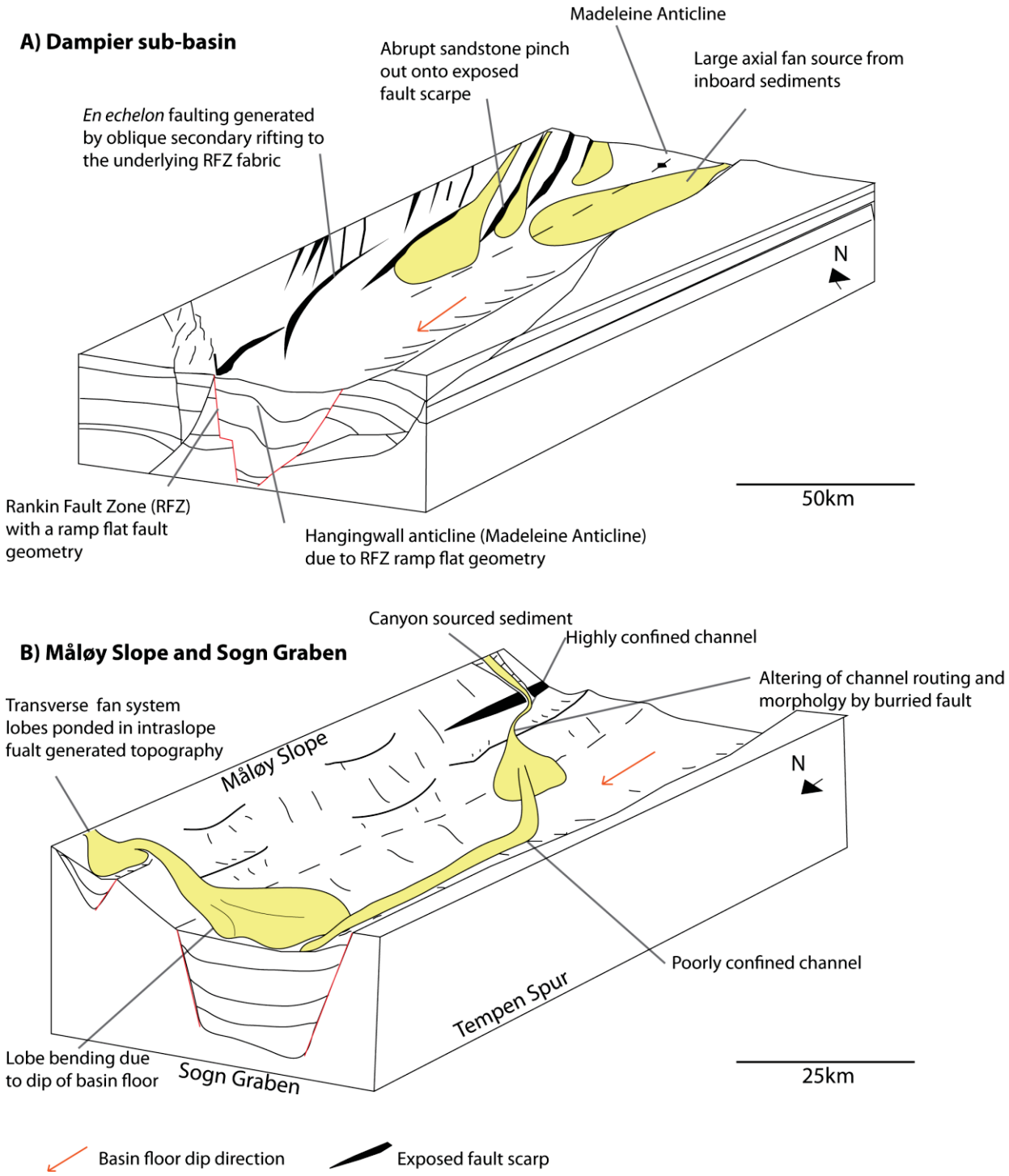


***Fig. 6.1**: Schematic illustration of key early-post rift tectonics and influences on deep-water sedimentation with A) illustrating the Angel Fm. NW Shelf, Australia (basin structures and faults adapted from Deng and McClay, 2020), B) Illustrating the Agat Fm. North Sea.*

may be occurring in the Angel Formation however due to poor seismic we cannot constrain this. Late syn-rift deep-water architecture is similar to this early post-rift underfilled architecture where flows are diverted to topographic lows generated by fault topography with ponding observed in topographic lows (Tillmans *et al.*, 2021)

Whereas the Agat Formation has a higher mud-proportion and is less directly controlled by tectonic structures as the basin is a higher fill state. Compaction hinges that develop over underlying faults appear to largely control the sediment routing (Chapter 5 and Martinsen et al., 2005). Within these compaction hinges fault geometries and configuration plays an important role in dictating the where the sediment is routed especially channel routing and geometries. Similar case of compaction driven fault topography are observed in the early-port rift (Privat *et al.*, 2021; Martínez-Doñate *et al.*,) into the late post-rift (Davis *et al.*, 2009; Eldrett *et al.*, 2015; Dmitrieva *et al.*, 2018) and in a gravitational-driven thrust setting (Pizzi *et al.*, 2023). However, variability in cessation of rifting and sediment routing/source may lead to local variations in fill-level of the basin. Therefore, a continuum is suggested where in syn-rift and underfilled early post-rift basins direct fault interaction can dictate the deep-water architecture, this interaction has a decreasing effect as the basin is progressively infilled and healed.

The mutiphased nature of the rifts plays an important role in influencing the deep water sedimentary systems in both basins. In the Dampier sub-basin, the oblique direction of extension to the underlying tectonic framework led to the complex *en echelon* faulting in the secondary rift which plays a key role in the distribution of the Angel Formation. In the Måløy Slope and Sogn Graben the primary rift plays a reduced role, in that the basins syn-rift deposits are deep-water mudrocks, as the initial phase of rifting enable the rapid deepening to a marine underfilled basin in the secondary rift phase enabling the development of mature deep-water systems to develop (*cf*. Gawthorpe & Leeder, 2000).

6.5 Proposal for future work

The findings from this research have identified two future projects as well as highlighted areas for possible expansion of the application of spectral reflectance.

6.5.1 Investigation of the suitability of the Angel Formation for carbon storage

The aim of this further work is to address the uncertainties surrounding the Angel Formation and assess its suitability for carbon storage. Specifically, the project's aims will focus on:

- Refine the depositional model of the Angel Formation to understand the interaction between the axial and transverse systems and investigate the paleoflow in the system.

- Conducting a risk assessment and model the reservoir to appraise the suitability and capacity of the reservoir to store carbon dioxide.

Objectives:

- Analyse improved seismic data (Fortuna 3D) not available to this study to better constrain the southeastern part of the sub-basin and identify the potential interfingering of axial and oblique systems.
- Analyse paleoflow indicators in borehole imaging to improve the understanding of the paleoflow in the system.
- Conduct a detailed petrological analysis of the Angel Formation to investigate the distribution of fine-grained sandstones and CO2-specific heterogeneities that may be upscaled to spectral reflectance for rapid evaluation across the sub-basin
- Investigate the impacts of intra-reservoir horizons of bioturbated heterolithics on plume morphology with a view to improve placement of CO2 injectors, utilizing production data and the reservoir architecture identified in Chapter 3.

Outcome:

- Improved understanding of the reservoir characteristics of the Angel Formation.
- Identification of potential uncertainties and risks associated with carbon storage in the reservoir.
- Assessment of the suitability and capacity of the reservoir for carbon storage.
- Define CO2 specific reservoir heterogeneities.

6.5.2 Quantitative assessment of pinch out geometry in sand reservoirs.

This will build upon the work done in Chapter 3 where a simple abrupt pinch out against complex slope topography was quantified. The aim of this project would be to:

- Investigate the criteria responsible for controlling the geometry of sand pinch out.
- Quantify the rates of various geometry styles of pinch out.
- Identify the facies variations in different pinch out geometries and rates of change.

Objectives:

- Identify the main criteria that define the style of pinch out and run up distance, such as flow velocity, mud-proportion, style and shape of slope/topography, or location within a system using flume tank experiments (Soutter *et al.*, 2021) and outcrop.
- Quantify the rates of different pinch out geometries using flume tank experiments and field outcrops (e.g. Hansen *et al.*, 2019; Soutter *et al.*, 2019).
- Investigate and quantify facies evolution at the pinch out and the relationship between pinch out geometry and facies evolution rates, following the methodology of Bell et al (2018).

Outcome:

- A better understanding of the criteria governing sand pinch out dimensions.
- This will aid in improving the prediction and interpretation of pinch outs in sand reservoirs in the subsurface.

6.5.3 Expand the application of reflectance spectroscopy

There is a limited scope for the further application of this technique with the lack of the detection of illite, however if this is overcome a test of the reproducibility of the spectral reflectance work performed in Chapter 4 is proposed.

- The sensitivity and reproducibility of the spectral reflectance data by testing the data collection techniques in system rich in lithic fragments or a system with a varied grain size to test the sensitivity of the mineral assemblages. As well as testing it in a less bioturbated system or more mud-rich system to understand how low and dilute turbidity currents are represent. This would require an abundance of XRD data to calibrate the dataset
- Applying the spectral reflectance approach to similar heavily bioturbated systems such as paralic systems (MacEachern *et al.*, 1999), to refine sedimentological interpretations.
- Investigating the application of spectral reflectance data to paleosols with complex mineralogy to improve the characterization and understanding of paleosol development.

6.6 Conclusion

This thesis has investigated the interplay of inherited structural relief has on early post-rift deep-water systems, using two studies: the Angel Formation (NW Shelf, Australia) and the Agat Formation (North Sea). An integrated approach was applied, utilising seismic reflection

data, well logs, and core data. This research has provided new insights into how inherited fault topography can influence sediment entry points, sediment transfer zones, sandbody architecture and connectivity. These findings represent a step forward in the prediction of deep-water reservoirs in underexplore basins, mature basins and for emerging carbon sequestration plays.

Key Findings

1. Impact of inherited syn-rift structural relief on early post-rift sand-rich lobes and channels
    - The Angel Formation is deposited in an underfilled early post-rift basin and displays evidence of direct interaction of deep-water lobe resulting in an abrupt pinch out style to the lobe deposits against fault scarps.
    - Whereas the Agat Formation was deposited in a more infilled basin and illustrates a less direct interaction with inherited syn-rift topography. Here channels of the Agat Formation are redirected by a compaction hinge generated by a buried fault . The underlying fault network geometry and segmentation of the fault has a controlling influence on the routing of the deep-water channel.
    - In both settings, a multiphase nature of the rift played a role on the style of syn-rift faulting which influenced the sediment routing. Oblique secondary rifting in the Dampier sub-basin led to *en echelon* faulting which acted to redirect deep-water deposits. The Agat Formation was deposited in the early-post rift of a secondary phase of rifting leading to a significantly underfilled deep-water basin at time of deposition.

2. Inherited syn-rift structural controls on sand-pinch out and facies distribution
    - Spectral reflectance analysis has provided new insights into facies distribution within the Angel Formation, revealing the complete masking of thin-bedded turbidites in lobe fringes. The high level of bioturbation and limited diagnostic evidence of ichnology may suggest the Angel Fm. lobe complexes around the Mutineer area are intraslope lobes.
    - Angel Formation pinch outs against fault topography are sand-rich and abrupt in the Mutineer area, whereas the Agat Formation this level of abrupt pinchout was not observed due to the initial draping of the fault scarp topography by mudstones. However, as the underlying faults controlled the channel routing it therefore influenced where channel facies are distributed with more confined channels observed updip of the fault generated confinement and more poorly confined downdip.

3. Implications for reservoir connectivity and prediction
    - In multiphase rifts primary rift fabric appears to have a control on the secondary rift tectonic structures. The identification of sediment transfer zones controlled which are controlled by this interaction between primary and secondary rift fabric is key to predicting sediment routing in the early post-rift.
    - The sand-rich nature of pinch outs in the early-post rift identified these intervals as potentially key locations for hydrocarbon reservoir exploration or carbon sequestration.

This research has highlighted the importance of inherited structural relief on the architecture and morphology of deep-water deposits in the early post-rift. Through the integration of multiscale datasets this thesis has provided a framework for improving the prediction and potential reservoir heterogeneity in the rift basins. These findings have underscored the importance of a holistic approach to understanding the controls of sediment routing and the architecture and morphology of deep-water systems in rift basins.

7 References

Adeogba, A.A., **McHargue, T.R.** and **Graham, S.A.** (2005) Transient fan architecture and depositional controls from near-surface 3-D seismic data, Niger Delta continental slope. *AAPG Bull.*, **89**, 627–643.

Amin, M.A. (1979) Geochemistry and mineralogy of Namurian sediments in the Pennine Basin, England. University of Sheffield

Amy, L.A., **McCaffrey, W.D.** and **Kneller, B.C.** (2004) The influence of a lateral basin-slope on the depositional patterns of natural and experimental turbidity currents. *Geol. Soc. Spec. Publ.*, **221**, 311–330.

Argent, J.D., **Stewart, S.A.** and **Underhill, J.R.** (2000) Controls on the Lower Cretaceous Punt Sandstone Members, a massive deep-water clastic deposystem, Inner Moray Firth, UK North Sea. *Pet. Geosci.*, **6**, 275–285.

Armentrout, J.M., **Kanschat, K.A.**, **Meisling, K.E.**, **Tsakma, J.J.**, **Antrim, L.** and **McConnell, D.R.** (2000) Neogene turbidite systems of the Gulf of Guinea continental margin slope, Offshore Nigeria. *Fine-Grained Turbid. Syst.*, 93–108.

Armitage, D.A., **Romans, B.W.**, **Covault, J.A.** and **Graham, S.A.** (2009) The influence of mass-transport-deposit surface topography on the evolution of turbidite architecture: The sierra contreras, tres pasos formation (Cretaceous), Southern Chile. *J. Sediment. Res.*, **79**, 287–301.

Azpiroz-Zabala, M., **Cartigny, M.J.B.**, **Talling, P.J.**, **Parsons, D.R.**, **Sumner, E.J.**, **Clare, M.A.**, **Simmons, S.M.**, **Cooper, C.** and **Pope, E.L.** (2017) Newly recognized turbidity current structure can explain prolonged flushing of submarine canyons. *Sci. Adv.*, **3**, e1700200.

Azzam, F., **Blaise, T.**, **Patrier, P.**, **Elmola, A.A.**, **Beaufort, D.**, **Portier, E.**, **Brigaud, B.**, **Barbarand, J.** and **Clerc, S.** (2022) Diagenesis and reservoir quality evolution of the Lower Cretaceous turbidite sandstones of the Agat Formation (Norwegian North Sea): Impact of clay grain coating and carbonate cement. *Mar. Pet. Geol.*, **142**, 105768.

Baas, J.H. and **Best, J.L.** (2002) Turbulence Modulation in Clay-Rich Sediment-Laden Flows and Some Implications for Sediment Deposition. *J. Sediment. Res.*, **72**, 336–340.

Baas, J.H., **Best, J.L.** and **Peakall, J.** (2011) Depositional processes, bedform development and hybrid bed formation in rapidly decelerated cohesive (mud-sand) sediment flows. *Sedimentology*, **58**, 1953–1987.

Baas, J.H., **McCaffrey, W.D.** and **Knipe, R.J.** (2005) The Deep-Water Architecture Knowledge Base: towards an objective comparison of deep-marine sedimentary systems. *Pet. Geosci.*, **11**, 309–320.

Babonneau, N., **Savoye, B.**, **Cremer, M.** and **Klein, B.** (2002) Morphology and architecture of the present canyon and channel system of the Zaire deep-sea fan. *Mar. Pet. Geol.*, **19**, 445–467.

Badley, M.E., **Price, J.D.**, **Dahl, C.R.** and **Agdestein, T.** (1988) The structural evolution of the north Viking Graben and its bearing upon extensional modes of basin formation (North Sea). *J. - Geol. Soc. Lond.*, **145**, 455–472.

Baker, M.L., **Baas, J.H.**, **Malarkey, J.**, **Jacinto, R.S.**, **Craig, M.J.**, **Kane, I.A.** and **Barker, S.** (2017) The Effect of Clay Type On the Properties of Cohesive Sediment Gravity Flows and Their Deposits. *J. Sediment. Res.*, **87**, 1176–1195.

Bakke, K., **Gjelberg, J.** and **Agerlin Petersen, S.** (2008) Compound seismic modelling of the Ainsa II turbidite system, Spain: Application to deep-water channel systems offshore Angola. *Mar. Pet. Geol.*, **25**, 1058–1073.

Bakke, K., **Kane, I.A.**, **Martinsen, O.J.**, **Petersen, S.A.**, **Johansen, T.A.**, **Hustoft, S.**, **Jacobsen, F.H.** and **Groth, A.** (2013) Seismic modelling in the analysis of deep-water sandstone termination styles. *AAPG Bull.*, **97**, 1395–1419.

Barber, P. (1994) Sequence stratigraphy and petroleum potential of the Upper Jurassic - Lower Cretaceous depositional systems in the Dampier Sub-basin, North West Shelf, Australia. In: *The Sedimentary Basins of Western Australia: Proceedings of Petroleum Exploration Society of Australia Symposium* (Ed. P.G. Purcell and R.R. Purcell), 1059–1070.

Barker, S.P., **Haughton, P.D.W.**, **McCaffrey, W.D.**, **Archer, S.G.** and **Hakes, B.** (2008) Development of Rheological Heterogeneity in Clay-Rich High-Density Turbidity Currents: Aptian Britannia Sandstone Member, U.K. Continental Shelf. *J. Sediment. Res.*, **78**, 45–68.

Barrett, B.J., **Hodgson, D.M.**, **Jackson, C.A.L.**, **Lloyd, C.**, **Casagrande, J.** and **Collier, R.E.L.** (2021) Quantitative analysis of a footwall-scarp degradation complex and syn-rift stratigraphic architecture, Exmouth Plateau, NW Shelf, offshore Australia. *Basin Res.*, **33**, 1135–1169.

Beaubouef, R.T. and **Friedmann, S.J.** (2000) High Resolution Seismic/Sequence Stratographic Framework for the Evolution of Pleistocene Intra Slope Basins, West.

Bell, D., **Kane, I.A.**, **Pontén, A.S.M.**, **Flint, S.S.**, **Hodgson, D.M.** and **Barrett, B.J.** (2018) Spatial variability in depositional reservoir quality of deep-water channel-fill and lobe deposits. *Mar. Pet. Geol.*, **98**, 97–115.

Bell, R.E., **Jackson, C.A.-L.**, **Whipp, P.S.** and **Clements, B.** (2014) Strain migration during multiphase extension: Observations from the northern North Sea. *Tectonics*, **33**, 1936–1963.

Bergslien, D. (2002) Balder and Jotun - Two sides of the same coin? A comparison of two Tertiary oil fields in the Norwegian North Sea. *Pet. Geosci.*, **8**, 349–363.

Bilal, A., **McClay, K.** and **Scarselli, N.** (2018) Fault-scarp degradation in the central Exmouth Plateau, North West Shelf, Australia. *Geol. Soc. Lond. Spec. Publ.*, SP476.11.

Bint, A.N. (1991) Discovery of the Wanaea and Cossack oil fields. *APPEA J.*, **31**, 22–331.

Bint, A.N. and **Marshall, N.G.** (1994) High resolution palynostratigraphy of the Tithonian Angel Formation in the Wanaea and Cossack Fields, Dampier sub-basin. In: *Purcell, P.G. & Purcell, R.R. (Eds), The Sedimentary Basins of Western Australia: Proceedings of Petroleum Exploration Society of Australia Symposium, Perth, WA, 1994*, 543–554.

Biscaye, P.E. (1965) Mineralogy and Sedimentation of Recent Deep-Sea Clay in the Atlantic Ocean and Adjacent Seas and Oceans. *Geol. Soc. Am. Bull.*, **76**, 803–832.

Blum, M.D. and **Hattier-Womack, J.** (2009) Climate Change, Sea-Level Change, and Fluvial Sediment Supply to Deepwater Depositional Systems. In: *External Controls on Deep-Water Depositional Systems* (Ed. B. Kneller, O.J. Martinsen, and B. McCaffrey), *SEPM Society for Sedimentary Geology*, 92, 0.

Boulesteix, K., **Poyatos-Moré, M.**, **Flint, S.S.**, **Hodgson, D.M.**, **Taylor, K.T.** and **Brunt, R.L.** (2022) Sedimentologic and stratigraphic criteria to distinguish between basin-floor and slope mudstones : Implications for the delivery of mud to deep-water environments. Depositional Rec. doi: 10.1002/dep2.191

Boulesteix, K., **Poyatos-Moré, M.**, **Flint, S.S.**, **Taylor, K.G.**, **Hodgson, D.M.** and **Hasiotis, S.T.** (2019) Transport and deposition of mud in deep-water environments: Processes and stratigraphic implications. *Sedimentology*, **66**, 2894–2925.

Boulesteix, K., **Poyatos-Moré, M.**, **Hodgson, D.M.**, **Flint, S.S.** and **Taylor, K.G.** (2020) Fringe or background: Characterising deep-water mudstones beyond the basin-floor fan sandstone pinchout. *J. Sediment. Res.*, **90**, 1678–1705.

Bouma, A.H. (1962) Sedimentology of some flysch deposits. *Agraphic approach to facies interpretation*, *168*.

Bouma, A.H. (2000) Coarse-grained and fine-grained turbidite systems as end member models: applicability and dangers. *Mar. Pet. Geol.*, **17**, 137–143.

Bouma, A.H. (2008) Key controls on the characteristics of turbidite systems. *Geol. Soc. Lond. Spec. Publ.*, **222**, 9–22.

Breien, H., **De Blasio, F.V.**, **Elverhoi, A.**, **Nystuen, J.P.** and **Harbitz, C.B.** (2011) Transport Mechanisms of Sand In Deep-Marine Environments--Insights Based On Laboratory Experiments--Reply. *J. Sediment. Res.*, **81**, 842–843.

Brekke, H., **Sjulstad, H.I.**, **Magnus, C.** and **Williams, R.W.** (2001) Sedimentary environments offshore Norway-an overview. In: *Sedimentary Environments Offshore Norway - Palaeozoic to Recent*, 7–37.

Brooks, H.L., **Hodgson, D.M.**, **Brunt, R.L.**, **Peakall, J.**, **Hofstra, M.** and **Flint, S.S.** (2018a) Deep-water channel-lobe transition zone dynamics: Processes and depositional architecture, an example from the Karoo Basin, South Africa. *Bull. Geol. Soc. Am.*, **130**, 1723–1746.

Brooks, H.L., **Hodgson, D.M.**, **Brunt, R.L.**, **Peakall, J.**, **Poyatos-Moré, M.** and **Flint, S.S.** (2018b) Disconnected submarine lobes as a record of stepped slope evolution over multiple sea-level cycles. *Geosphere*, **14**, 1753–1779.

Brooks, H.L., **Ito, M.**, **Zuchuat, V.**, **Peakall, J.** and **Hodgson, D.M.** (2022) Channel-lobe transition zone development in tectonically active settings: Implications for hybrid bed development. *Depositional Rec.*, **8**, 829–868.

Bruhn, C.H.L. and **Walker, R.G.** (1995) High-resolution stratigraphy and sedimentary evolution of coarse-grained canyon-filling turbidites from the Upper Cretaceous transgressive megasequence, Campos Basin, offshore Brazil. *J. Sediment. Res. B Stratigr. Glob. Stud.*, 426–442.

Bugge, T., **Tveiten, B.** and **Bäckström, S.** (2001) The depositional history of the Cretaceous in the northeastern North Sea. *Nor. Pet. Soc. Spec. Publ.*, **10**, 279–291.

Carlson, P.R. and **Karl, H.A.** (1988) Development of large submarine canyons in the Bering Sea, indicated by morphologic, seismic, and sedimentologic characteristics. *GSA Bull.*, **100**, 1594–1615.

Casagrande, J., **Hodgson, D.M.**, **Peakall, J.** and **Benac, P.M.** (2022) Fill-and-Spill, Tilt-and-Repeat (FaSTaR) cycles: Stratigraphic evolution above a dynamic submarine stepped slope. *Basin Res.*, 1–27.

Chapter 3 Chapter 3.

Chen, H., **Wood, L.J.** and **Gawthorpe, R.L.** (2020) Sediment dispersal and redistributive processes in axial and transverse deep-time source-to-sink systems of marine rift basins: Dampier Sub-basin, Northwest Shelf, Australia. Basin Res. doi: 10.1111/bre.12462

Chiarella, D. and **Joel, D.** (2021) Stratigraphic and sedimentological characterization of the Late Cretaceous post-rift intra Lange Sandstones of the Gimsan Basin and Grinda Graben (Halten Terrace, Norwegian Sea). *Geol. Soc. Lond. Spec. Publ.*, **495**, SP495-2021–72.

Clark, I.R. and **Cartwright, J.A.** (2012) Interactions Between Coeval Sedimentation and Deformation From the Niger Delta Deepwater Fold Belt. *Appl. Princ. Seism. Geomorphol. Cont.-Slope Base--Slope Syst. Case Stud. Seafloor -Seafloor Analog.*, **SEPM Special Publication**, 243–267.

Clark, J.D. and **Pickering, K.T.** (1996) Architectural elements and growth patterns of submarine channels: Application to hydrocarbon exploration. *AAPG Bull.*, **80**, 194–221.

Cullen, T.M., **Collier, R.E.L.**, **Gawthorpe, R.L.**, **Hodgson, D.M.** and **Barrett, B.J.** (2019) Axial and transverse deep-water sediment supply to syn-rift fault terraces: Insights from the West Xylokastro Fault Block, Gulf of Corinth, Greece. *Basin Res.*, 1–35.

Cullis, S., **Colombera, L.**, **Patacci, M.** and **McCaffrey, W.D.** (2018) Hierarchical classifications of the sedimentary architecture of deep-marine depositional systems. Earth-Sci Rev. doi: 10.1016/j.earscirev.2018.01.016

Cumberpatch, Z.A., **Finch, E.** and **Kane, I.A.** (2021a) External signal preservation in halokinetic stratigraphy: A discrete element modeling approach. *Geology*, **49**, 687–692.

Cumberpatch, Z.A., **Kane, I.A.**, **Soutter, E.L.**, **Hodgson, D.M.**, **Jackson, C.A.L.**, **Kilhams, B.A.** and **Poprawski, Y.** (2021b) Interactions between deep-water gravity flows and active salt tectonics. *J. Sediment. Res.*, **91**, 34–65.

Cummings, J.P. and **Hodgson, D.M.** (2011) Assessing controls on the distribution of ichnotaxa in submarine fan environments , the Basque Basin , Northern Spain. *Sediment. Geol.*, **239**, 162–187.

Davis, C., **Haughton, P.**, **McCaffrey, W.**, **Scott, E.**, **Hogg, N.** and **Kitching, D.** (2009) Character and distribution of hybrid sediment gravity flow deposits from the outer Forties Fan, Palaeocene Central North Sea, UKCS. *Mar. Pet. Geol.*, **26**, 1919–1939.

Deller, K. (2011) Sedimentological Lithofacies, Internal Architecture and Evolution of Deep Marine Fans of the Tithonian Angel Formation, Northwestern Dampier Sub-Basin, North West Shelf, Australia. The University of Adelaide

Deng, H. and **McClay, K.** (2020) Tectono-stratigraphy of the Dampier Sub-basin, North West shelf of Australia. *Geol. Soc. Spec. Publ.*, **476**, 259–285.

Deptuck, M.E., **Piper, D.J.W.**, **Savoye, B.** and **Gervais, A.** (2008) Dimensions and architecture of late Pleistocene submarine lobes off the northern margin of East Corsica. *Sedimentology*, **55**, 869–898.

di Toro, G.A.E. (1995) Angel Formation turbidites in the Wanaea field area, Dampier Sub-basin, North-West Shelf, Australia. In: *An atlas of deep-water environments: Architectural style in turbidite systems* (Ed. Pickering K.T., R.N. Hiscott, N.H. Kenyon, F. Ricci Lucchi, and R.D.A.S. Smith), *Chapman & Hall*, London, 260–266.

Dmitrieva, E., **Jackson, C.A.L.**, **Huuse, M.** and **Kane, I.A.** (2018) Regional distribution and controls on the development of post-rift turbidite systems: Insights from the Paleocene of the eastern North Viking Graben, offshore Norway. *Pet. Geol. Conf. Proc.*, **8**, 147–170.

Dodd, T.J.H., **McCarthy, D.J.** and **Richards, P.C.** (2019) A depositional model for deep-lacustrine, partially confined, turbidite fans: Early Cretaceous, North Falkland Basin. *Sedimentology*, **66**, 53–80.

Dott, R.H. (1963) Dynamics of Subaqueous Gravity Depositional Processes. AAPG Bull. doi: 10.1306/BC743973-16BE-11D7-8645000102C1865D

Doughty-Jones, G., **Mayall, M.** and **Lonergan, L.** (2017) Stratigraphy, facies, and evolution of deep-water lobe complexes within a saltcontrolled intraslope minibasin. *AAPG Bull.*, **101**, 1879–1904.

Drinkwater, N.J., **Pickering, K.T.** and **Schlumberger, N.J.D.** (2001) Architectural elements in a high-continuity sand-prone turbidite system, late Precambrian Kongsfjord Formation, northern Norway: Application to hydrocarbon reservoir characterization. *AAPG Bull. V*, **85**, 1731–1757.

Elders, C., **McHarg, S.** and **I'Anson, A.** (2016) Fault Geometry and Deformation History, Northern Carnarvon Basin. *ASEG Ext. Abstr.*, 1–3.

Eldrett, J., **Tripsanas, E.**, **Davis, C.**, **McKie, T.**, **Vieira, M.**, **Osterloff, P.** and **Sandison, T.** (2015) Sedimentological evolution of Sele Formation deep-marine depositional systems of the Central North Sea. *Geol. Soc. Lond. Spec. Publ.*, **403**, 63–98.

Færseth, R.B. (1996) Interaction of permo-triassic and jurassic extensional fault-blocks during the development of the northern North Sea. *J. Geol. Soc.*, **153**, 931–944.

Færseth, R.B., **Knudsen, B.-E.**, **Liljedahl, T.**, **Midbøe, P.S.** and **Søderstrøm, B.** (1997) Oblique rifting and sequential faulting in the Jurassic development of the northern North Sea. *J. Struct. Geol.*, **19**, 1285–1302.

Færseth, R.B. and **Lien, T.** (2002) Cretaceous evolution in the Norwegian Sea - A period characterized by tectonic quiescence. *Mar. Pet. Geol.*, **19**, 1005–1027.

Ferguson, R.A., **Kane, I.A.**, **Eggenhuisen, J.T.**, **Pohl, F.**, **Tilston, M.**, **Spychala, Y.T.** and **Brunt, R.L.** (2020) Entangled external and internal controls on submarine fan evolution: an experimental perspective. *Depositional Rec.*, **6**, 605–624.

Fonneland, H.C., **Lien, T.**, **Martinsen, O.J.**, **Pedersen, R.B.** and **Košler, J.** (2004) Detrital zircon ages: A key to understanding the deposition of deep marine sandstones in the Norwegian Sea. *Sediment. Geol.*, **164**, 147–159.

Fryer, R.C. and **Jobe, Z.R.** (2019) Quantification of the bed-scale architecture of submarine depositional environments. *Depositional Rec.*, **5**, 192–211.

Fuhrmann, A., **Kane, I.A.**, **Schomacker, E.**, **Clare, M.A.** and **Pontén, A.** (2022) Bottom Current Modification of Turbidite Lobe Complexes. *Frontiers in Earth Science*, **9**,

Gabrielsen, R.H., **Kyrkjebø, R.**, **Faleide, J.I.**, **Fjeldskaar, W.** and **Kjennerud, T.** (2001) The Cretaceous post-rift basin configuration of the northern North Sea. *Pet. Geosci.*, **7**, 137–154.

Gardiner, A.R. (2006) The variability of turbidite sandbody pinchout and its impact on hydrocarbon recovery in stratigraphically trapped fields. In: *The Deliberate search for the Stratigraphic Trap* (Ed. M.R. Allen, G.P. Goffey, R.K. Morgan, and I.M. Walker), *Geological Society, London, Special Publication*, 254, 267–287.

Gawthorpe, R.L. and **Leeder, M.R.** (2000) Tectono-sedimentary evolution of active extensional basins. *Basin Res.*, **12**, 195–218.

Gervais, A., **Savoye, B.**, **Mulder, T.** and **Gonthier, E.** (2006) Sandy modern turbidite lobes: A new insight from high resolution seismic data. *Mar. Pet. Geol.*, **23**, 485–502.

Gulbrandsen, A. and **Nyborkken, S.** (1991) Agat Field-Norwegian North Sea, Subplatform North Viking Graben. *AAPG Bull.*, **75**, 20–21.

Hampton, M.A. (1972) The role of subaqueous debris flow in generating turbidity currents. *J. Sediment. Petrol.*, **42**, 775–793.

Hansen, H.N., **Løvstad, K.**, **Lageat, G.**, **Clerc, S.** and **Jahren, J.** (2021a) Chlorite coating patterns and reservoir quality in deep marine depositional systems – Example from the Cretaceous Agat Formation, Northern North Sea, Norway. *Basin Res.*, **33**, 2725–2744.

Hansen, L., **Janocko, M.**, **Kane, I.** and **Kneller, B.** (2017) Submarine channel evolution, terrace development, and preservation of intra-channel thin-bedded turbidites: Mahin and Avon channels, offshore Nigeria. *Mar. Geol.*, **383**, 146–167.

Hansen, L.A.S., **Hodgson, D.M.**, **Pontén, A.**, **Bell, D.** and **Flint, S.** (2019) Quantification of Basin-Floor Fan Pinchouts: Examples From the Karoo Basin, South Africa. *Front. Earth Sci.*, **7**, 1–20.

Hansen, L.A.S., **Hodgson, D.M.**, **Pontén, A.**, **Thrana, C.** and **Obradors Latre, A.** (2021b) Mixed axial and transverse deep-water systems: The Cretaceous post-rift Lysing Formation, offshore Norway. *Basin Res.*, **33**, 2229–2251.

Haughton, P., **Davis, C.**, **McCaffrey, W.** and **Barker, S.** (2009) Hybrid sediment gravity flow deposits - Classification, origin and significance. *Mar. Pet. Geol.*, **26**, 1900–1918.

Haughton, P.D.W., **Barker, S.P.** and **McCaffrey, W.D.** (2003) "Linked" debrites in sand-rich turbidite systems - Origin and significance. *Sedimentology*, **50**, 459–482.

Heard, T.G., **Pickering, K.T.** and **Clark, J.D.** (2014) Ichnofabric characterization of a deep-marine clastic system: A subsurface study of the Middle Eocene Ainsa System, Spanish Pyrenees. *Sedimentology*, **61**, 1298–1331.

Heijnen, M.S., **Clare, M.A.**, **Cartigny, M.J.B.**, **Talling, P.J.**, **Hage, S.**, **Pope, E.L.**, **Bailey, L.**, **Sumner, E.**, **Lintern, D.G.**, **Stacey, C.**, **Parsons, D.R.**, **Simmons, S.M.**, **Chen, Y.**, **Hubbard, S.M.**, **Eggenhuisen, J.T.**, **Kane, I.** and **Hughes Clarke, J.E.** (2022) Fill, flush or shuffle: How is sediment carried through submarine channels to build lobes? *Earth Planet. Sci. Lett.*, **584**, 117481.

Heine, C. and **Müller, R.D.** (2005) Late Jurassic rifting along the Australian North West Shelf: Margin geometry and spreading ridge configuration. *Aust. J. Earth Sci.*, **52**, 27–39.

Helby, R., **Morgan, R.** and **Partridge, A.D.** (2004) Updated Jurassic - Early Cretaceous dinocyst zonation, NWS Australia. *Geosci. Aust. Publ.*, 2.

Helland-Hansen, W., **Ashton, M.**, **Lomo, L.**, and **Steel, R.J.** (1992) Advance and retreat of the Brent delta: recent contributions to the depositional model. In: *Geology of the Brent Group.*, 109–127.

Hiscott, R.N. (1994) Loss of capacity, not competence, as the fundamental process governing deposition form turbidity currents. *J. Sediment. Res.*, **64**, 209–214.

Hocking, R. (1992) Jurassic Deposition in the Southern and Central North West Shelf, Western Australia. *Geological Survey of Western Australia*, 1–108 pp.

Hocking, R., **Moors, H.T.** and **Van De Graaff, J.E.** (1987) Geology of the Carnarvon basin Western Australia.

Hocking, R., **Mory, A.J.** and **Williams, I.R.** (1994) An atlas of Neoproterozoic and Phanerozoic basins of Western Australia. *Sediment. Basins West. Aust. Proc. Pet. Explor. Soc. Aust. Symp. Perth 1994*, 21–44.

Hodgson, D.M. and **Haughton, P.D.W.** (2008) Impact of syndepositional faulting on gravity current behaviour and deep-water stratigraphy: Tabernas-Sorbas Basin, SE Spain. *Geol. Soc. Lond. Spec. Publ.*, **222**, 135–158.

Hodgson, D.M., **Kane, I.A.**, **Flint, S.S.**, **Brunt, R.L.** and **Ortiz-Karpf, A.** (2016) Time-Transgressive Confinement On the Slope and the Progradation of Basin-Floor Fans: Implications For the Sequence Stratigraphy of Deep-Water Deposits. *J. Sediment. Res.*, **86**, 73–86.

Hodgson, D.M., **Peakall, J.** and **Maier, K.L.** (2022) Submarine Channel Mouth Settings: Processes, Geomorphology, and Deposits.

Howlett, D.M., **Gawthorpe, R.L.**, **Ge, Z.**, **Rotevatn, A.** and **Jackson, C.A. -L.** (2021) Turbidites, topography and tectonics: Evolution of submarine channel-lobe systems in the salt-influenced Kwanza Basin, offshore Angola. *Basin Res.*, **33**, 1076–1110.

Howlett, D.M., **Ge, Z.**, **Nemec, W.**, **Gawthorpe, R.L.**, **Rotevatn, A.** and **Jackson, C.A.L.** (2019) Response of unconfined turbidity current to deep-water fold and thrust belt topography: Orthogonal incidence on solitary and segmented folds. *Sedimentology*, **66**, 2425–2454.

Hubbard, S.M., **Covault, J.A.**, **Fildani, A.** and **Romans, B.W.** (2014) Sediment transfer and deposition in slope channels: Deciphering the record of enigmatic deep-sea processes from outcrop. *Bull. Geol. Soc. Am.*, **126**, 857–871.

Hurst, A. and **Cronin, B.T.** (2001) The Origin of Consolidation Laminae and Dish Structures in Some Deep-Water Sandstones. *J. Sediment. Res.*, **71**, 136–143.

Ilstad, T., **Elverhøi, A.**, **Issler, D.** and **Marr, J.G.** (2004) Subaqueous debris flow behaviour and its dependence on the sand/clay ratio: A laboratory study using particle tracking. *Mar. Geol.*, **213**, 415–438.

Isaksen, D. and **Tonstad, K.** (1989) A revised Cretaceous and Tertiary lithostratigraphic nomenclasture for the Norwegian North Sea.

Jackson, C.A.L., **Barber, G.P.** and **Martinsen, O.J.** (2008) Submarine slope morphology as a control on the development of sand-rich turbidite depositional systems: 3D seismic analysis of the Kyrre Fm (Upper Cretaceous), Måløy Slope, offshore Norway. *Mar. Pet. Geol.*, **25**, 663–680.

Jackson, C.A.L., **Larsen, E.**, **Hanslien, S.** and **Tjemsland, A.E.** (2011) Controls on synrift turbidite deposition on the hanging wall of the South Viking Graben, North Sea rift system, offshore Norway. *AAPG Bull.*, **95**, 1557–1587.

Jackson, C.A.L., **McAndrew, A.E.**, **Hodgson, D.M.** and **Dreyer, T.O.M.** (2021) Repeated degradation and progradation of a submarine slope over geological timescales. *J. Sediment. Res.*, **91**, 116–145.

Jobe, Z.R., **Lowe, D.R.** and **Morris, W.R.** (2012) Climbing-ripple successions in turbidite systems: Depositional environments, sedimentation rates and accumulation times. *Sedimentology*, **59**, 867–898.

Jobe, Z.R., **Sylvester, Z.**, **Howes, N.**, **Pirmez, C.**, **Parker, A.**, **Cantelli, A.**, **Smith, R.**, **Wolinsky, M.A.**, **O'Byrne, C.**, **Slowey, N.** and **Prather, B.** (2017) High-resolution, millennial-scale patterns of bed compensation on a sand-rich intraslope submarine fan, western Niger Delta slope. *Bull. Geol. Soc. Am.*, **129**, 23–37.

Kane, I.A. and **Clare, M.A.** (2019) Dispersion, Accumulation, and the Ultimate Fate of Microplastics in Deep-Marine Environments: A Review and Future Directions. Front Earth Sci. doi: 10.3389/feart.2019.00080

Kane, I.A. and **Hodgson, D.M.** (2011) Sedimentological criteria to differentiate submarine channel levee subenvironments: Exhumed examples from the Rosario Fm. (Upper Cretaceous) of Baja California, Mexico, and the Fort Brown Fm. (Permian), Karoo Basin, S. Africa. *Mar. Pet. Geol.*, **28**, 807–823.

Kane, I.A., **Kneller, B.C.**, **Dykstra, M.**, **Kassem, A.** and **McCaffrey, W.D.** (2007) Anatomy of a submarine channel-levee: An example from Upper Cretaceous slope sediments, Rosario Formation, Baja California, Mexico. *Mar. Pet. Geol.*, **24**, 540–563.

Kane, I.A. and **Pontén, A.S.M.** (2012) Submarine transitional flow deposits in the Paleogene Gulf of Mexico. *Geology*, **40**, 1119–1122.

Kane, I.A., **Pontén, A.S.M.**, **Vangdal, B.**, **Eggenhuisen, J.T.**, **Hodgson, D.M.** and **Spychala, Y.T.** (2017) The stratigraphic record and processes of turbidity current transformation across deep-marine lobes. *Sedimentology*, **64**, 1236–1273.

Knaust, D. (2017) Atlas of Trace Fossils in Well Core. *Springer*.

Kneller, B. and **Buckee, C.** (2000) The structure and fluid mechanics of turbidity currents: a review of some recent studies and their geological implications. *Sedimentology*, **47**, 62–94.

Kneller, B., **Edwards, D.**, **McCaffrey, W.** and **Moore, R.** (1991) Oblique reflection of turbidity currents. *Geology*, **19**, 250–252.

Kneller, B.C. and **Branney, M.** (1995) Sustained high-density turbidity currents and the deposition of thick massive sands. *Sedimentology*, **42**, 607–616.

Kuenen, PH.H. and **Migliorini, C.I.** (1950) Turbidity currents as a cause of graded bedding. *J. Geol.*, **58**, 91–127.

Kus, K.B., **Jobe, Z.R.**, **Laugier, F.**, **Walker, W.** and **Sullivan, M.** (2021) Quantifying the Lateral Heterogeneity of Distal Submarine Lobe Deposits, Point Loma Formation, California: Implications for Subsurface Lateral Facies Prediction. *Depositional Rec.*, 1–30.

Kyrkjebø, R., **Kjennerud, T.**, **Gillmore, G.K.**, **Faleide, J.I.** and **Gabrielsen, R.H.** (2001) Cretaceous-tertiary palaeo-bathymetry in the northern North Sea; integration of palaeo-water depth estimates obtained by structural restoration and micropalaeontological analysis. In: *Norwegian Petroleum Society Special Publications*, *Elsevier*, 10, 321–345.

Laberg, J.S. and **Vorren, T.O.** (2000) Flow behaviour of the submarine glacigenic debris flows on the Bear Island Trough Mouth Fan, western Barents Sea. *Sedimentology*, **47**, 1105–1117.

Law, A., **Raymond, A.**, **White, G.**, **Atkinson, A.**, **Clifton, M.**, **Atherton, T.**, **Dawes, I.**, **Robertson, E.**, **Melvin, A.** and **Brayley, S.** (2000) The Kopervik fairway, Moray Firth, UK. *Pet. Geosci.*, **6**, 265–274.

Lech, M.E. (2013) New Observations of the Post-Triassic Succession in the Central Beagle Sub-basin , Northern Carnarvon Basin , North West Shelf , Australia. *Sediment. Basins West. Aust. IV Proc. Pet. Explor. Soc. Aust. Symp. Perth Aust.*, 1–20.

Leinfelder, R.R. and **Wilson, R.C.L.** (2010) Third-Order Sequences in an Upper Jurassic Rift-Related Second-Order Sequence, Central Lusitanian Basin, Portugal. Mesoz Cenozoic Seq Stratigr Eur Basins. doi: 10.2110/pec.98.02.0507

Lien, T., **Midtbø, R.E.** and **Martinsen, O.J.** (2006) Depositional facies and reservoir quality of deep-marine sandstones in the Norwegian Sea. *Nor. J. Geol. Geol. Foren.*, **86**, 71–92.

Liu, Q., Kneller, B., Fallgatter, C., Valdez Buso, V., Milana, J.P., (2018). Tabularity of individual turbidite beds controlled by flow efficiency and degree of confinement. Sedimentology 65, 2368–2387

Longley, I.M., **Buessenschuett, C.**, **Clydsdale, L.**, **Cubitt, C.J.**, **Davis, C.J.**, **Johnson, R.C.**, **Marshall, M.K.**, **Murray, N.M.**, **Somerville, R.**, **Spry, T.B.** and **Thompson, N.B.** (2002) The North West Shelf of Australia - A Woodside Perspective. In: *The Sedimentary Basins of Western Australia 3: Perth, Petroleum Exploration Society of Australia* (Ed. M. Keep and S.J. Moss),

Lowe, D.R. (1982) Sediment gravity flows: II. Depositional models with special reference to the deposits of high-density turbidity currents. *J. Sediment. Petrol.*, **52**, 279–297.

Lowe, D.R. (1975) Water escape structures in coarse-grained sediments. *Sedimentology*, **22**, 157–204.

MacEachern, J.A. and **Bann, K.L.** (2008) The Role of Ichnology in Refining Shallow Marine Facies Models. 73–116 pp.

MacEachern, J.A., **Zaitlin, B.A.** and **Pemberton, S.G.** (1999) A sharp-based sandstone of the Viking formation, Joffre field, Alberta, Canada: criteria for recognition of transgressively incised shoreface complexes.

Marini, M., **Milli, S.**, **Ravnås, R.** and **Moscatelli, M.** (2015) A comparative study of confined vs. semi-confined turbidite lobes from the Lower Messinian Laga Basin (Central Apennines, Italy): Implications for assessment of reservoir architecture. *Mar. Pet. Geol.*, **63**, 142–165.

Marshall, N.G. and **Lang, S.C.** (2013) A New Sequence Stratigraphic Framework for the North West Shelf, Australia. *Sediment. Basins West. Aust. IV Proc. Pet. Explor. Soc. Aust. Symp. Perth Aust.*, 1–23.

Martínez-Doñate, A., **Kane, I. a.**, **Hodgson, D. m.**, **Privat, A.M.-L.J.**, **Jackson, C. a-L.**, **Schwarz, E.** and **Flint, S. s.** Stratigraphic change in flow transformation processes recorded in early post-rift deep-marine intraslope lobe complexes. Sedimentology. doi: 10.1111/sed.13086

Martínez-Doñate, A., **Privat, A.M.-L.J.**, **Hodgson, D.M.**, **Jackson, C.A.-L.**, **Kane, I.A.**, **Spychala, Y.T.**, **Duller, R.A.**, **Stevenson, C.**, **Keavney, E.**, **Schwarz, E.** and **Flint, S.S.** (2021) Substrate Entrainment, Depositional Relief, and Sediment Capture: Impact of a Submarine Landslide on Flow Process and Sediment Supply.

Martinez-Doñate, A., **Soutter, E.L.**, **Kane, I.A.**, **Poyatos-Moré, M.**, **Hodgson, D.M.**, **Ayckbourne, A.J.M.**, **Taylor, W.J.**, **Bouwmeester, M.J.** and **Flint, S.S.** (2023) Submarine crevasse lobes controlled by lateral slope failure in tectonically-active settings: an exhumed example from the Eocene Aínsa depocentre (Spain). Sedimentologika. doi: 10.57035/journals/sdk.2023.e11.1068

Martinsen, O.J., **Lien, T.** and **Jackson, C.** (2005) Cretaceous and Palaeogene turbidite systems in the North Sea and Norwegian Sea basins: Source, staging area and basin physiography controls on reservoir development. In: *Petroleum Geology Conference Proceedings*, *Geological Society of London*, 6, 1147–1164.

Mauger, A.J., **Gordon, G.A.**, **Reid, A.** and **Kitto, J.** (2012) Quantifying downhole silicate mineralogy – HyLogger with thermal infrared. *ASEG Ext. Abstr.*, **2012**, 1–6.

Mayall, M., **Jones, E.** and **Casey, M.** (2006) Turbidite channel reservoirs-Key elements in facies prediction and effective development. *Mar. Pet. Geol.*, **23**, 821–841.

McArthur, A.D., **Hartley, A.J.**, **Archer, S.G.**, **Jolley, D.W.** and **Lawrence, H.M.** (2016) Spatiotemporal relationships of deep-marine, axial, and transverse depositional systems from the synrift Upper Jurassic of the central North Sea. *AAPG Bull.*, **100**, 1469–1500.

McCaffrey, W. and **Kneller, B.** (2001) Process controls on the development of stratigraphic trap potential on the margins of confined turbidites systems and aids to reservoir evaluation. *Am. Assoc. Pet. Geol. Bull.*, **85**, 971–988.

McCormick, C.A., **Corlett, H.**, **Stacey, J.**, **Hollis, C.**, **Feng, J.**, **Rivard, B.** and **Omma, J.E.** (2021) Shortwave infrared hyperspectral imaging as a novel method to elucidate multi-phase dolomitization, recrystallization, and cementation in carbonate sedimentary rocks. *Sci. Rep.*, **11**, 1–16.

McHarg, S., **Elders, C.** and **Cunneen, J.** (2018) Origin of basin-scale syn-extensional synclines on the southern margin of the Northern Carnarvon Basin, Western Australia. *J. Geol. Soc.*, **176**, 115–128.

McHargue, T., **Pyrcz, M.J.**, **Sullivan, M.D.**, **Clark, J.D.**, **Fildani, A.**, **Romans, B.W.**, **Covault, J.A.**, **Levy, M.**, **Posamentier, H.W.** and **Drinkwater, N.J.** (2011) Architecture of turbidite channel systems on the continental slope: Patterns and predictions. *Mar. Pet. Geol.*, **28**, 728–743.

McHargue, T.R., **Hodgson, D.M.** and **Shelef, E.** (2021) Architectural Diversity of Submarine Lobate Deposits. *Front. Earth Sci.*, **9**, 1–22.

McKie, T., **Rose, P.T.S.**, **Hartley, A.J.**, **Jones, D.W.** and **Armstrong, T.L.** (2015) Tertiary deep-marine reservoirs of the North Sea region: an introduction. *Geol. Soc. Lond. Spec. Publ.*, **403**, 1–16.

Miall, A.D. (1988) Architectural elements and bounding surfaces in fluvial deposits: anatomy of the Kayenta formation (Lower Jurassic), Southwest Colorado. Sediment Geol.

Middleton, G.V. and **Hampton, M.A.** (1973) Part I. Sediment Gravity Flows: Mechanics of Flow and Deposition. In: Marine Sediment Transport and Environmental Management (Ed. by D. J. Stanley and D. J. P. Swift), 197-218. Wiley, New York.

Moscardelli, L., **Ramnarine, S.K.**, **Wood, L.** and **Dunlap, D.B.** (2013) Seismic geomorphological analysis and hydrocarbon potential of the Lower Cretaceous Cromer Knoll Group, Heidrun field, Norway. *AAPG Bull.*, **97**, 1227–1248.

Moscardelli, L., **Wood, L.** and **Mann, P.** (2006) Mass-transport complexes and associated processes in the offshore area of Trinidad and Venezuela. *AAPG Bull.*, **90**, 1059–1088.

Mulder, T. and **Alexander, J.** (2001) The physical character of subaqueous sedimentary density flows and their deposits The physical character of subaqueous sedimentary density flows and their deposits. *Sedimentology*, **48**, 269–299.

Mulder, T. and **Etienne, S.** (2010) Lobes in deep-sea turbidite systems: State of the art. *Sediment. Geol.*, **229**, 75–80.

Mutti, E. (1977) Distinctive thin-bedded turbidite facies and related depositional environments in the Eocene Hecho Group (South-central Pyrenees, Spain). *Sedimentology*, **24**, 107–131.

Mutti, E. and Normark, W.R., (1991) An integrated approach to the study of turbidite systems. In *Seismic facies and sedimentary processes of submarine fans and turbidite systems.* 75-106. New York, NY: Springer New York.

Nagatomo, A. and **Archer, S.** (2015) Termination geometries and reservoir properties of the Forties Sandstone pinch-out, East Central Graben, UK North Sea. *Geol. Soc. Lond. Spec. Publ.*, **403**, 133–155.

Ningthoujam, J., **(Bill) Arnott, R.W.C.** and **Wearmouth, C.** (2023) Systematic vertical organization of matrix-rich and associated matrix-poor sandstones in ancient deep-marine slope and basin-floor deposits. *Geosphere*, **19**, 558–582.

Normark (1978) Fan Valleys, Channels, and Depositional Lobes on Modern Submarine Fans: Characters for Recognition of Sandy Turbidite Environments. *Am. Assoc. Pet. Geol. Bull.*, **62**, 912–931.

Normark, W.R. and **Piper, D.J.W.** (1969) Deep-Sea Fan-Valleys, Past and Present. *GSA Bull.*, **80**, 1859–1866.

Normark, W.R., **Piper, D.J.W.** and **Sliter, R.** (2006) Sea-level and tectonic control of middle to late Pleistocene turbidite systems in Santa Monica Basin, offshore California. *Sedimentology*, **53**, 867–897.

Nottvedt, A., **Gabrielsen, R.H.** and **Steel, R.J.** (1995) Tectonostratigraphy and sedimentary architecture of rift basins, with reference to the northern North Sea. *Mar. Pet. Geol.*, **12**, 881–901.

Nugraha, H.D., **Jackson, C.A.-L.**, **Johnson, H.D.**, **Hodgson, D.M.** and **Clare, M.A.** (2022) Extreme erosion by submarine slides. *Geology*, **50**, 1130–1134.

Nystuen, J.P. (1999) Submarine sediment gravity flow deposits and associated facies: Core examples from the Agat Formation. In O. J. Martinsen &. In: *Sedimentary environments offshore Norway – Palaeozoic to recent. Extended abstracts* (Ed. O.J. Martinsen and T. Dreyer), *Norwegian Petroleum Society/NPF Conference, Bergen, Norway, May 3– 5*, 211–215.

Oluboyo, A.P., **Gawthorpe, R.L.**, **Bakke, K.** and **Hadler-Jacobsen, F.** (2014) Salt tectonic controls on deep-water turbidite depositional systems: Miocene, southwestern Lower Congo Basin, offshore Angola. *Basin Res.*, **26**, 597–620.

Patacci, M., **Haughton, P.D.W.** and **McCaffrey, W.D.** (2014) Rheological Complexity In Sediment Gravity Flows Forced To Decelerate Against A Confining Slope, Braux, SE France. *J. Sediment. Res.*, **84**, 270–277.

Paull, C.K., **Ussler, W.**, **Greene, H.G.**, **Keaten, R.**, **Mitts, P.** and **Barry, J.** (2002) Caught in the act: the 20 December 2001 gravity flow event in Monterey Canyon. *Geo-Mar. Lett.*, **22**, 227–232.

Pearce, T.J. and **Jarvis, I.** (1992) Composition and provenance of turbidite sands: Late Quaternary, Madeira Abyssal Plain. *Mar. Geol.*, **109**, 21–51.

Phillips, T.B., **Fazlikhani, H.**, **Gawthorpe, R.L.**, **Fossen, H.**, **Jackson, C.A.-L.**, **Bell, R.E.**, **Faleide, J.I.** and **Rotevatn, A.** (2019) The Influence of Structural Inheritance and Multiphase Extension on Rift Development, the NorthernNorth Sea. *Tectonics*, **38**, 4099–4126.

Piper, D.J.W. (1970) Transport and deposition of Holocene sediment on La Jolla Deep Sea Fan, California. *Mar. Geol.*, **8**, 211–227.

Piper, D.J.W., **Cochonat, P.** and **Morrison, M.L.** (1999) The sequence of events around the epicentre of the 1929 Grand Banks earthquake: initiation of debris flows and turbidity current inferred from sidescan sonar. *Sedimentology*, **46**, 79–97.

Pirmez, C., **Beaubouef, R.T.**, **Friedmann, S.J.** and **Mohrig, D.C.** (2000) Equilibrium Profile and Baselevel in Submarine Channels: Examples from Late Pleistocene Systems and Implications for the Architecture of Deepwater Reservoirs. *Deep-Water Reserv. World 20th Annu.*, 782–805.

Pitman, J. (1999) Mutineer-1B Well Completion Report Interpretive Part 1 of 2 100032772. *Santos Ltd*.

Pitman, J. (2003) Mutineer 3 interpreted data report W20796A4. *Santos Ltd*.

Pizzi, M., **Whittaker, A.C.**, **Mayall, M.** and **Lonergan, L.** (2023) Structural controls on the pathways and sedimentary architecture of submarine channels: New constraints from the Niger Delta. *Basin Res.*, **35**, 141–171.

Plink-Björklund, P. and **Steel, R.** (2002) Sea-level fall below the shelf edge, without basin-floor fans. *Geology*, **30**, 115–118.

Pohl, F., **Eggenhuisen, J.T.**, **Cartigny, M.J.B.**, **Tilston, M.C.**, **De Leeuw, J.** and **Hermidas, N.** (2020) The influence of a slope break on turbidite deposits: An experimental investigation. *Mar. Geol.*, **424**, 106160.

Pope, E.L., **Cartigny, M.J.B.**, **Clare, M.A.**, **Talling, P.J.**, **Lintern, D.G.**, **Vellinga, A.**, **Hage, S.**, **Açikalin, S.**, **Bailey, L.**, **Chapplow, N.**, **Chen, Y.**, **Eggenhuisen, J.T.**, **Hendry, A.**, **Heerema, C.J.**, **Heijnen, M.S.**, **Hubbard, S.M.**, **Hunt, J.E.**, **McGhee, C.**, **Parsons, D.R.**, **Simmons, S.M.**, **Stacey, C.D.** and **Vendettuoli, D.** (2022) First source-to-sink monitoring shows dense head controls sediment flux and runout in turbidity currents. *Sci. Adv.*, **8**, eabj3220.

Porten, K.W., **Kane, I.A.**, **Warchoł, M.J.** and **Southern, S.J.** (2016) A Sedimentological Process-Based Approach To Depositional Reservoir Quality of Deep-Marine Sandstones: An Example From the Springar Formation, Northwestern Vøring Basin, Norwegian Sea. *J. Sediment. Res.*, **86**, 1269–1286.

Prather, B.E., **Booth, J.R.**, **Steffens, G.S.** and **Craig, P.A.** (1998) Classification, lithologic calibration, and stratigraphic succession of seismic facies of intraslope basins, deep-water Gulf of Mexico. *AAPG Bull.*, **82**, 701–728.

Prather, B.E., **Deptuck, M.**, **Mohrig, D.C.**, **Van Hoorn, B.**, **Wynn, R.B.**, and **.** (2012) Application of the Principles of Seismic Geomorphology to Continental-Slope and Base-of-Slope Systems: Case Studies from Seafloor and Near-Seafloor Analogues. *Appl. Princ. Seism. Geomorphol. Cont.-Slope Base--Slope Syst. Case Stud. Seafloor - Seafloor Analog.*, 5–9.

Prélat, A., **Covault, J.A.**, **Hodgson, D.M.**, **Fildani, A.** and **Flint, S.S.** (2010) Intrinsic controls on the range of volumes, morphologies, and dimensions of submarine lobes. *Sediment. Geol.*, **232**, 66–76.

Prélat, A. and **Hodgson, D.M.** (2013) The full range of turbidite bed thickness patterns in submarine lobes: controls and implications. *J. Geol. Soc.*, **170**, 209–214.

Prélat, A., **Hodgson, D.M.** and **Flint, S.S.** (2009) Evolution, architecture and hierarchy of distributary deep-water deposits: a high-resolution outcrop investigation from the Permian Karoo Basin, South Africa. *Sedimentology*, **56**, 2132–2154.

Prélat, A., **Pankhania, S.S.**, **Jackson, C.A.L.** and **Hodgson, D.M.** (2015) Slope gradient and lithology as controls on the initiation of submarine slope gullies; Insights from the North Carnarvon Basin, Offshore NW Australia. *Sediment. Geol.*, **329**, 12–17.

Privat, A.M.L.J., **Hodgson, D.M.**, **Jackson, C.A.L.**, **Schwarz, E.** and **Peakall, J.** (2021) Evolution from syn-rift carbonates to early post-rift deep-marine intraslope lobes: The role of rift basin physiography on sedimentation patterns. *Sedimentology*, **68**, 2563–2605.

Prosser, S. (1993) Rift-related linked depositional systems and their seismic expression. *Geol. Soc. Spec. Publ.*, **71**, 35–66.

Ravnås, R., **Nøttvedt, A.**, **Steel, R.J.** and **Windelstad, J.** (2000) Syn-rift sedimentary architectures in the Northern North Sea. *Geol. Soc. Spec. Publ.*, **167**, 133–177.

Ravnås, R. and **Steel, R.J.** (1997) Contrasting styles of Late Jurassic syn-rift turbidite sedimentation: A comparative study of the Magnus and Oseberg areas, northern North Sea. *Mar. Pet. Geol.*, **14**, 417–449.

Reading, H.G. and **Richards, M.** (1994) Turbidite systems in deep-water basin margins classified by grain size and feeder system. *Am. Assoc. Pet. Geol. Bull.*, **78**, 792–822.

Reeve, M.T., **Bell, R.E.**, **Duffy, O.B.**, **Jackson, C.A.L.** and **Sansom, E.** (2015) The growth of non-colinear normal fault systems; What can we learn from 3D seismic reflection data? *J. Struct. Geol.*, **70**, 141–155.

Reeve, M.T., **Bell, R.E.** and **Jackson, C.A.-L.** (2013) Origin and significance of intra-basement seismic reflections offshore western Norway. *J. Geol. Soc.*, **171**, 1–4.

Rivard, B., **Feng, J.**, **Gallie, A.** and **Sanchez-Azofeifa, A.** (2008) Continuous wavelets for the improved use of spectral libraries and hyperspectral data. *Remote Sens. Environ.*, **112**, 2850–2862.

Rodriguez, C., **Jackson, C.**, **Bell, R.**, **Rotevatn, A.** and **Francis, M.** (2019) Deep-water reservoir distribution on a salt-influenced slope, Santos Basin, offshore Brazil. *Physical Sciences and Mathematics*.

Romine, K.K., **J.M., D.**, **Cathro, D.L.** and **Bernardel, G.** (1997) Petroleum play prediction for the Cretaceous-Tertiary phase, Northern Carnarvon Basin. *APPEA J.*, **37**, 315–339.

Rose, P.T.S. (1999) Reservoir characterization in the Captain Field: integration of horizontal and vertical well data. In: *Petroleum Geology of Northwest Europe: Proceedings of the 5th conference* (Ed. A.J. Fleet and S.A.R. Bouldy), *Geological Society*, London, 1101–1113.

Rose, P.T.S. and **Pyle, J.R.** (2014) The habitat of bypassed pay in the Forties Field. *Geol. Soc. Lond. Spec. Publ.*, **403**, 333–354.

Rothwell, R.G., **Thomson, J.** and **Kähler, G.** (1998) Low-sea-level emplacement of a very large Late Pleistocene 'megaturbidite' in the western Mediterranean Sea. *Nature*, **392**, 377–380.

Saller, A., **Werner, K.**, **Sugiaman, F.**, **Cebastiant, A.**, **May, R.**, **Glenn, D.** and **Barker, C.** (2008) Characteristics of Pleistocene deep-water fan lobes and their application to an upper Miocene reservoir model, offshore East Kalimantan, Indonesia. *AAPG Bull.*, **92**, 919–949.

Schodlok, M.C., **Whitbourn, L.**, **Huntington, J.**, **Mason, P.**, **Green, A.**, **Berman, M.**, **Coward, D.**, **Connor, P.**, **Wright, W.**, **Jolivet, M.** and **Martinez, R.** (2016) HyLogger-3, a visible to shortwave and thermal infrared reflectance spectrometer system for drill core logging: functional description. *Aust. J. Earth Sci.*, **63**, 929–940.

Seilacher, A. (1967) Bathymetry of trace fossils. *Mar. Geol.*, **5**, 413–428.

Shanmugam, G., **Lehtonen, L.R.**, **Straume, T.**, **Syvertsen, S.E.**, **Hodgkinson, R.J.** and **Skibeli, M.** (1994) Slump and debris-flow dominated upper slope facies in the Cretaceous of the Norwegian and northern North Seas (61-67°N): implications for sand distribution. *Am. Assoc. Pet. Geol. Bull.*, **78**, 910–937.

Shanmugam, G. and **Moiola, R.J.** (1988) Submarine fans: Characteristics, models, classification, and reservoir potential. *Earth Sci. Rev.*, **24**, 383–428.

Shchepetkina, A., **Speta, M.**, **Gingras, M.K.**, **Rivard, B.** and **George Pemberton, S.** (2017) Hyperspectral imaging as an aid for facies analysis in massive-appearing sediments: A case study from the middle McMurray formation. *Bull. Can. Pet. Geol.*, **65**, 262–278.

Shepard, F.P., **McLoughlin, P.A.**, **Marshall, N.F.** and **Sullivan, G.G.** (1977) Current-meter recordings of low-speed turbidity currents. *Geology*, **5**, 297–301.

Simmons, S.M., **Azpiroz-Zabala, M.**, **Cartigny, M.J.B.**, **Clare, M.A.**, **Cooper, C.**, **Parsons, D.R.**, **Pope, E.L.**, **Sumner, E.J.** and **Talling, P.J.** (2020) Novel Acoustic Method Provides First Detailed Measurements of Sediment Concentration Structure Within Submarine Turbidity Currents. *J. Geophys. Res. Oceans*, **125**

Skibeli, M., **Barnes, K.**, **Straume, T.**, **Syvertsen, S.E.** and **Shanmugam, G.** (1995) A sequence stratigraphic study of lower cretaceous deposits in the northernmost North Sea. *Nor. Pet. Soc. Spec. Publ.*, **5**, 389–400.

Slagstad, T., **Barrére, C.**, **Davidsen, B.** and **Ramstad, R.K.** (2008) Petrophysical and thermal properties of pre-Devonian basement rocks on the Norwegian continental margin. *Geol Surv Nor. Bull*, **448**, 1–6.

Smith, R. (2008) Silled sub-basins to connected tortuous corridors: sediment distribution systems on topographically complex sub-aqueous slopes. *Geol. Soc. Lond. Spec. Publ.*, **222**, 23–43.

Sohn, Y.K. (1997) On traction-carpet sedimentation. *J. Sediment. Res.*, **67**, 502–509.

Sømme, T.O. and **Jackson, C.A.L.** (2013) Source-to-sink analysis of ancient sedimentary systems using a subsurface case study from the Møre-Trøndelag area of southern Norway: Part 2 - sediment dispersal and forcing mechanisms. *Basin Res.*, **25**, 512–531.

Sømme, T.O., **Jackson, C.A.L.** and **Vaksdal, M.** (2013) Source-to-sink analysis of ancient sedimentary systems using a subsurface case study from the Møre-Trøndelag area of southern Norway: Part 1 - depositional setting and fan evolution. *Basin Res.*, **25**, 489–511.

Southern, S.J., **Kane, I.A.**, **Warchoł, M.J.**, **Porten, K.W.** and **McCaffrey, W.D.** (2017) Hybrid event beds dominated by transitional-flow facies: Character, distribution and significance in the maastrichtian springar formation, north-west Vøring Basin, Norwegian Sea. *Sedimentology*, **64**, 747–776.

Southern, S.J., **Patacci, M.**, **Felletti, F.** and **McCaffrey, W.D.** (2015) Influence of flow containment and substrate entrainment upon sandy hybrid event beds containing a co-genetic mud-clast-rich division. *Sediment. Geol.*, **321**, 105–122.

Soutter, E.L., **Bell, D.**, **Cumberpatch, Z.A.**, **Ferguson, R.A.**, **Spychala, Y.T.**, **Kane, I.A.** and **Eggenhuisen, J.T.** (2021) The Influence of Confining Topography Orientation on Experimental Turbidity Currents and Geological Implications. Front Earth Sci. doi: 10.3389/feart.2020.540633

Soutter, E.L., **Kane, I.A.**, **Fuhrmann, A.**, **Cumberpatch, Z.A.** and **Huuse, M.** (2019) The stratigraphic evolution of onlap in siliciclastic deep-water systems: Autogenic modulation of allogenic signals. *J. Sediment. Res.*, **89**, 890–917.

Soutter, E.L., **Kane, I.A.**, **Martínez-Doñate, A.**, **Boyce, A.J.**, **Stacey, J.** and **Castelltort, S.** (2022) The Eocene-Oligocene climate transition in the Alpine foreland basin: Paleoenvironmental change recorded in submarine fans. *Palaeogeogr. Palaeoclimatol. Palaeoecol.*, **600**, 111064.

Spears, D.A. and **Amin, M.A.** (1981) A mineralogical and geochemical study of turbidite sandstones and interbedded shales, Mam Tor, Derbyshire, UK. *Clay Miner.*, **16**, 333–345.

Spencer, L., **Needham, J.**, **Edgecombe, S.**, **Foster, C.**, **Bradshaw, M.**, **Vizy, J.** and **Zuccaro, G.** (1992) Dampier sub-basin module. *Australian Geological Survey Orgnaisation*.

Sprague, **Garfield**, **Goulding**, **Beaubouef, R.**, **Sullivan**, **Rossen**, **Campion**, **Sickafoose**, **Abreu, V.**, **Schellpeper**, **Jensen**, **Jennette, D.**, **Pirmez, C.**, **Dixon, B.**, **Ying**, **Ardill**, **Mohrig, D.**, **Porter**, **Farrell** and **Mellere, D.** (2005) Integrated slope channel depositional models: the key to successful prediction of reservoir presence and quality in offshore West Africa.

Spychala, Y.T., **Hodgson, D.M.**, **Flint, S.S.** and **Mountney, N.P.** (2015) Constraining the sedimentology and stratigraphy of submarine intraslope lobe deposits using exhumed examples from the Karoo Basin, South Africa. *Sediment. Geol.*, **322**, 67–81.

Spychala, Y.T., **Hodgson, D.M.** and **Lee, D.R.** (2017a) Autogenic controls on hybrid bed distribution in submarine lobe complexes. *Mar. Pet. Geol.*, **88**, 1078–1093.

Spychala, Y.T., **Hodgson, D.M.**, **Prélat, A.**, **Kane, I.A.**, **Flint, S.S.** and **Mountney, N.P.** (2017b) Frontal and Lateral Submarine Lobe Fringes: Comparing Sedimentary Facies, Architecture and Flow Processes. *J. Sediment. Res.*, **87**, 75–96.

Spychala, Y.T., **Hodgson, D.M.**, **Stevenson, C.J.** and **Flint, S.S.** (2017c) Aggradational lobe fringes: The influence of subtle intrabasinal seabed topography on sediment gravity flow processes and lobe stacking patterns. *Sedimentology*, **64**, 582–608.

Stanbrook, D., Bentley, M., (2022) Practical turbidite interpretation: The role of relative confinement in understanding reservoir architectures. Marine and Petroleum Geology 135, 105372.

Steel, R.J. (2010) Triassic–Jurassic megasequence stratigraphy in the Northern North Sea: rift to post-rift evolution. *Geol. Soc. Lond. Pet. Geol. Conf. Ser.*, **4**, 299–315.

Stephenson, A.E., **Blevin, J.E.** and **West, B.G.** (1998) The paleogeography of the Beagle Sub-basin, northern Carnarvon Basin, Australia. *J. Sediment. Res.*, **68**, 1131–1145.

Stevenson, C.J., **Jackson, C.A.**, **Hodgson, D.M.**, **Hubbard, S.M.** and **Eggenhuisen, J.T.** (2015) Deep-water sediment bypass. *J. Sediment. Res.*, 1058–1081.

Stevenson, C.J., **Peakall, J.**, **Hodgson, D.M.**, **Bell, D.**, and **Aurélia Privat** (2020) TB or not TB: Banding in turbidite sandstones. *J. Sediment. Res.*, **90**, 821–842.

Stevenson, C.J., **Talling, P.J.**, **Wynn, R.B.**, **Masson, D.G.**, **Hunt, J.E.**, **Frenz, M.**, **Akhmetzhanhov, A.** and **Cronin, B.T.** (2013) The flows that left no trace: Very large-volume turbidity currents that bypassed sediment through submarine channels without eroding the sea floor. *Mar. Pet. Geol.*, **41**, 186–205.

Steventon, M.J., **Jackson, C.A.L.**, **Johnson, H.D.**, **Hodgson, D.M.**, **Kelly, S.**, **Omma, J.**, **Gopon, C.**, **Stevenson, C.** and **Fitch, P.** (2021) Evolution of a sand-rich submarine channel–lobe system, and the impact of mass-transport and transitional-flow deposits on reservoir heterogeneity: Magnus field, northern North Sea. Pet Geosci. doi: 10.1144/petgeo2020-095

Stow, D.A.V. and **Faugères, J.-C.** (2008) Chapter 13 Contourite Facies and the Facies Model. *Dev. Sedimentol.*, **60**, 223–256.

Stow, D.A.V. and **Johansson, M.** (2000) Deep-water massive sands: nature, origin and hydrocarbon implications. *Fuel Energy Abstr.*, **41**, 267.

Straub, K.M. and **Pyles, D.R.** (2012) Quantifying the Hierarchical Organization of Compensation In Submarine Fans Using Surface Statistics. *J. Sediment. Res.*, **82**, 889–898.

Sullivan, M., **Jensen, G.**, **Goulding, F.**, **Jennette, D.**, **Foreman, L.** and **Stern, D.** (2000) Architectural Analysis of Deep-Water Outcrops: Implications for Exploration and Development of the Diana Sub-Basin, Western Gulf of Mexico. *SEPM Society for Sedimentary Geology*, 0 pp.

Talling, P.J., **Baker, M.L.**, **Pope, E.L.**, **Ruffell, S.C.**, **Jacinto, R.S.**, **Heijnen, M.S.**, **Hage, S.**, **Simmons, S.M.**, **Hasenhündl, M.**, **Heerema, C.J.**, **McGhee, C.**, **Apprioual, R.**, **Ferrant, A.**, **Cartigny, M.J.B.**, **Parsons, D.R.**, **Clare, M.A.**, **Tshimanga, R.M.**, **Trigg, M.A.**, **Cula, C.A.**, **Faria, R.**, **Gaillot, A.**, **Bola, G.**, **Wallance, D.**, **Griffiths, A.**, **Nunny, R.**, **Urlaub, M.**, **Peirce, C.**, **Burnett, R.**, **Neasham, J.** and **Hilton, R.J.** (2022) Longest sediment flows yet measured show how major rivers connect efficiently to deep sea. *Nat. Commun.*, **13**, 4193.

Talling, P.J., **Masson, D.G.**, **Sumner, E.J.** and **Malgesini, G.** (2012) Subaqueous sediment density flows: Depositional processes and deposit types. *Sedimentology*, **59**, 1937–2003.

Talling, P.J., **Wynn, R.B.**, **Masson, D.G.**, **Frenz, M.**, **Cronin, B.T.**, **Schiebel, R.**, **Akhmetzhanov, A.M.**, **Dallmeier-Tiessen, S.**, **Benetti, S.**, **Weaver, P.P.E.**, **Georgiopoulou, A.**, **Zühlsdorff, C.** and **Amy, L.A.** (2007) Onset of submarine debris flow deposition far from original giant landslide. *Nature*, **450**, 541–544.

Tillmans, F., **Gawthorpe, R.L.**, **Jackson, C.A.L.** and **Rotevatn, A.** (2021) Syn-rift sediment gravity flow deposition on a Late Jurassic fault-terraced slope, northern North Sea. *Basin Res.*, **33**, 1844–1879.

Vollset, J. and **Dore, A.G.** (1984) A revised Triassic and Jurassic lithostratigraphic nomenclature for the Norwegian North Sea.

Wahyuni, F., **Escalona, A.**, **Augustsson, C.** and **Marin, D.** (2019) Early cretaceous tectonostratigraphic evolution of the Sogn Graben and Måløy Slope, northern North Sea (Agat Fm.). 81st EAGE Conf Exhib 2019. doi: 10.3997/2214-4609.201901079

Walker, R.G. (1978) Deep-Water Sandstone Facies and Ancient Submarine Fans: Models for Exploration for Stratigraphic Traps. *AAPG Bull.*, **62**, 932–966.

Wawryk, M. and **Hancock, L.** (2017) GSWA pXRD Analysis – Drillhole : Mutineer 1B. *GSWA*.

Weimer, P. and **Pettingill, H.S.** (2007) Deep-water Exploration and Production: A Global Overview. *Atlas Deep-Water Outcrops AAPG Stud. Geol. 56*, 7–11.

Wetzel, A. (1984) Bioturbation in deep-sea fine-grained sediments: Influence of sediment texture, turbidite frequency and rates of environmental change. *Geol. Soc. Spec. Publ.*, **15**, 595–608.

Wilkinson, R. (2022) NW Shelf JV awarded greenhouse gas permit over depleted Angel field. In: Oil Gas J. https://www.ogj.com/energy-transition/article/14282156/nw-shelf-jv-awarded-greenhouse-gas-permit-over-depleted-angel-field. Accessed 12 Apr 2023

Wonham, J.P., **Rodwell, I.**, **Lein-Mathisen, T.** and **Thomas, M.** (2014) Tectonic control on sedimentation, erosion and redeposition of Upper Jurassic sandstones, Central Graben, North Sea. 473–512 pp.

Woodside (1989) Wanaea-1 Completeion Report WA-28-P Volume 1 Part 2 Basic Data W3432A6V2.

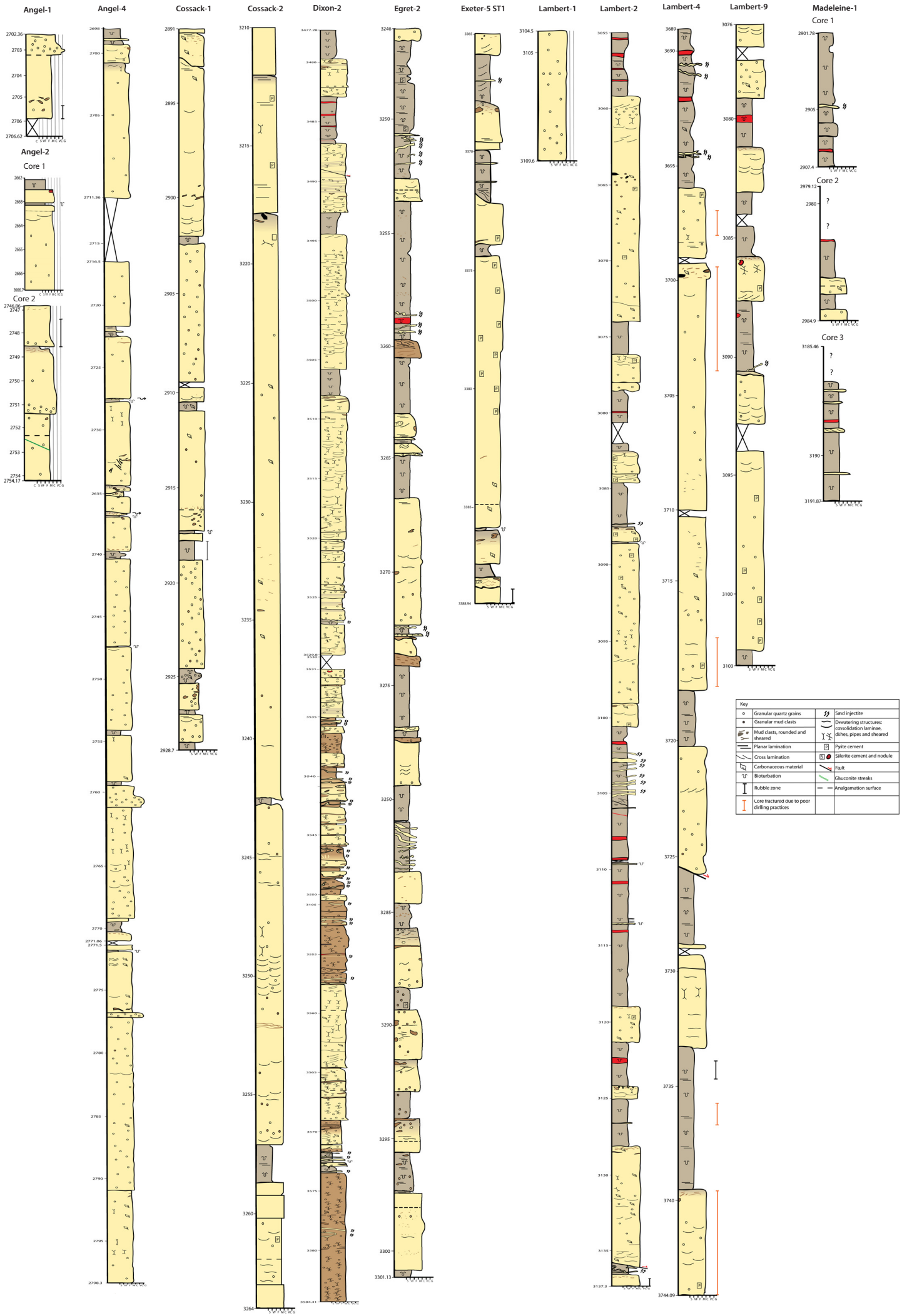
Wynn, R.B., **Kenyon, N.H.**, **Masson, D.G.**, **Stow, D.A.V.** and **Weaver, P.P.E.** (2002) Characterization and recognition of deep-water channel-lobe transition zones. *AAPG Bull.*, **8**, 1441–1462.

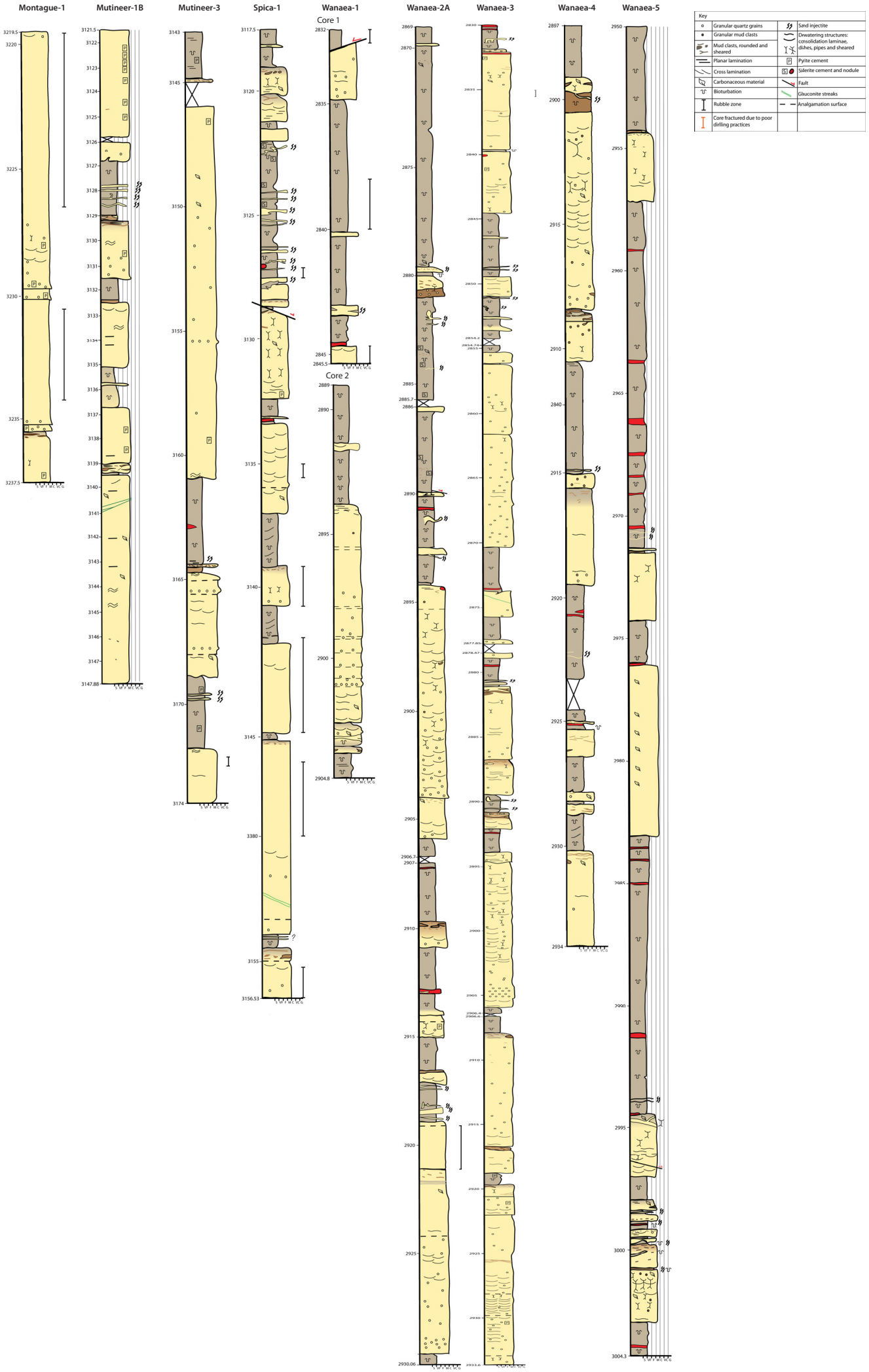
Zachariah, A.J., **Gawthorpe, R.**, **Dreyer, T.** and **Corfield, S.** (2009) Controls on early post-rift physiography and stratigraphy, lower to mid-Cretaceous, North Viking Graben, Norwegian North Sea. *Basin Res.*, **21**, 189–208.

8 Appendix

8.1 Appendix 1: Angel Core logs

Key			
o	Granular quartz grains		Sand injectite
●	Granular mud clasts		Dewatering structures: consolidation laminae, dishes, pipes and sheared
	Mud clasts, rounded and sheared		
	Planar lamination	P	Pyrite cement
	Cross lamination	S	Siderite cement and nodule
	Carbonaceous material		Fault
	Bioturbation		Glauconite streaks
	Rubble zone		Amalgamation surface
	Core fractured due to poor dirlling practices		


Angel-1
Angel-2
Core 1
Core 2
Angel-4
Cossack-1
Cossack-2
Dixon-2
Egret-2
Exeter-5 ST1
Lambert-1
Lambert-2
Lambert-4
Lambert-9
Madeleine-1
Core 1
Core 2
Core 3
Key
Granular quartz grains
Granular mud clasts
Mud clasts, rounded and sheared
Planar lamination
Cross lamination
Carbonaceous material
Bioturbation
Rubble zone
Core fractured due to poor dirlling practices
Sand injectite
Dewatering structures: consolidation laminae, dishes, pipes and sheared
Pyrite cement
Siderite cement and nodule
Fault
Glauconite streaks
Analgamation surface


Montague-1
Mutineer-1B
Mutineer-3
Spica-1
Wanaea-1
Core 1
Core 2
Wanaea-2A
Wanaea-3
Wanaea-4
Wanaea-5
Key
Granular quartz grains
Granular mud clasts
Mud clasts, rounded and sheared
Planar lamination
Cross lamination
Carbonaceous material
Bioturbation
Rubble zone
Core fractured due to poor drilling practices
Sand injectite
Dewatering structures: consolidation laminae, dishes, pipes and sheared
Pyrite cement
Siderite cement and nodule
Fault
Gluconite streaks
Analgamation surface

8.2 Appendix 2: Seismic well ties

Selection of synthetic well ties.

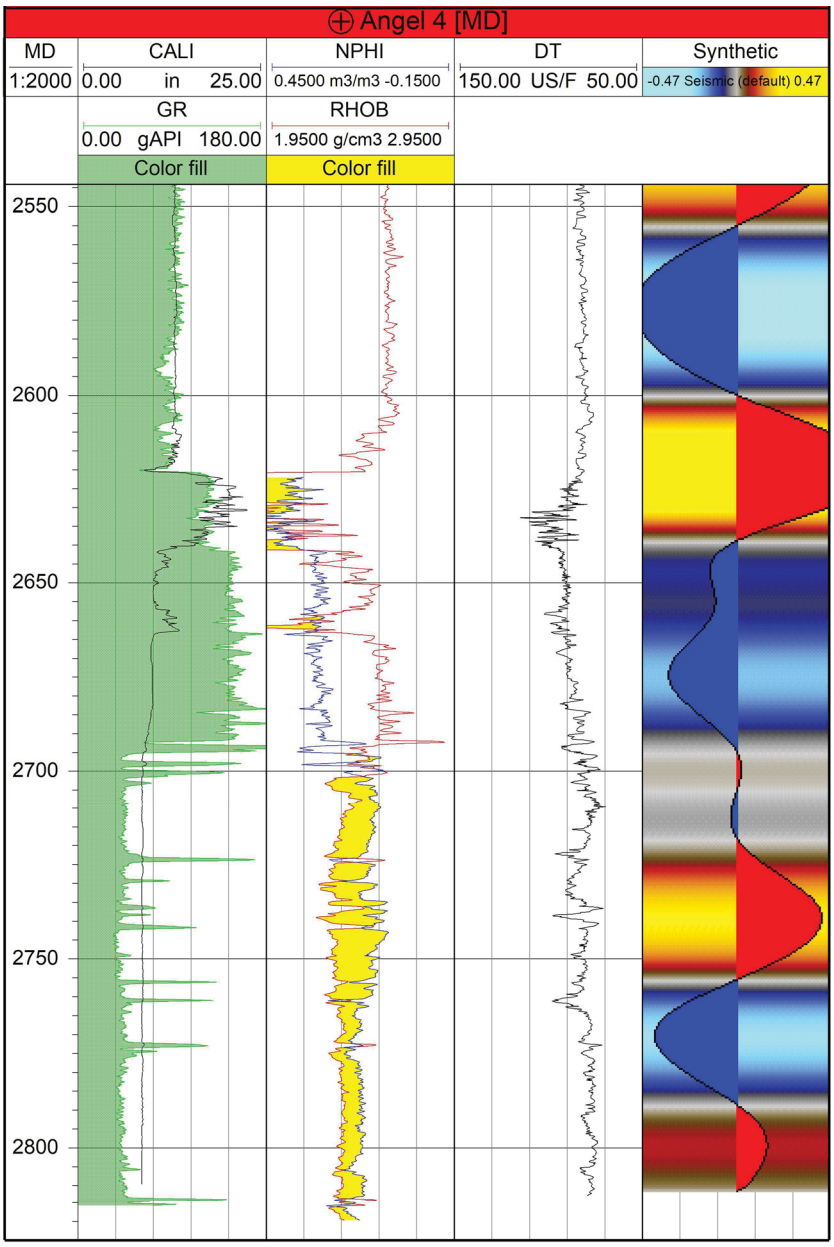
Top Legandre Fm. = H1

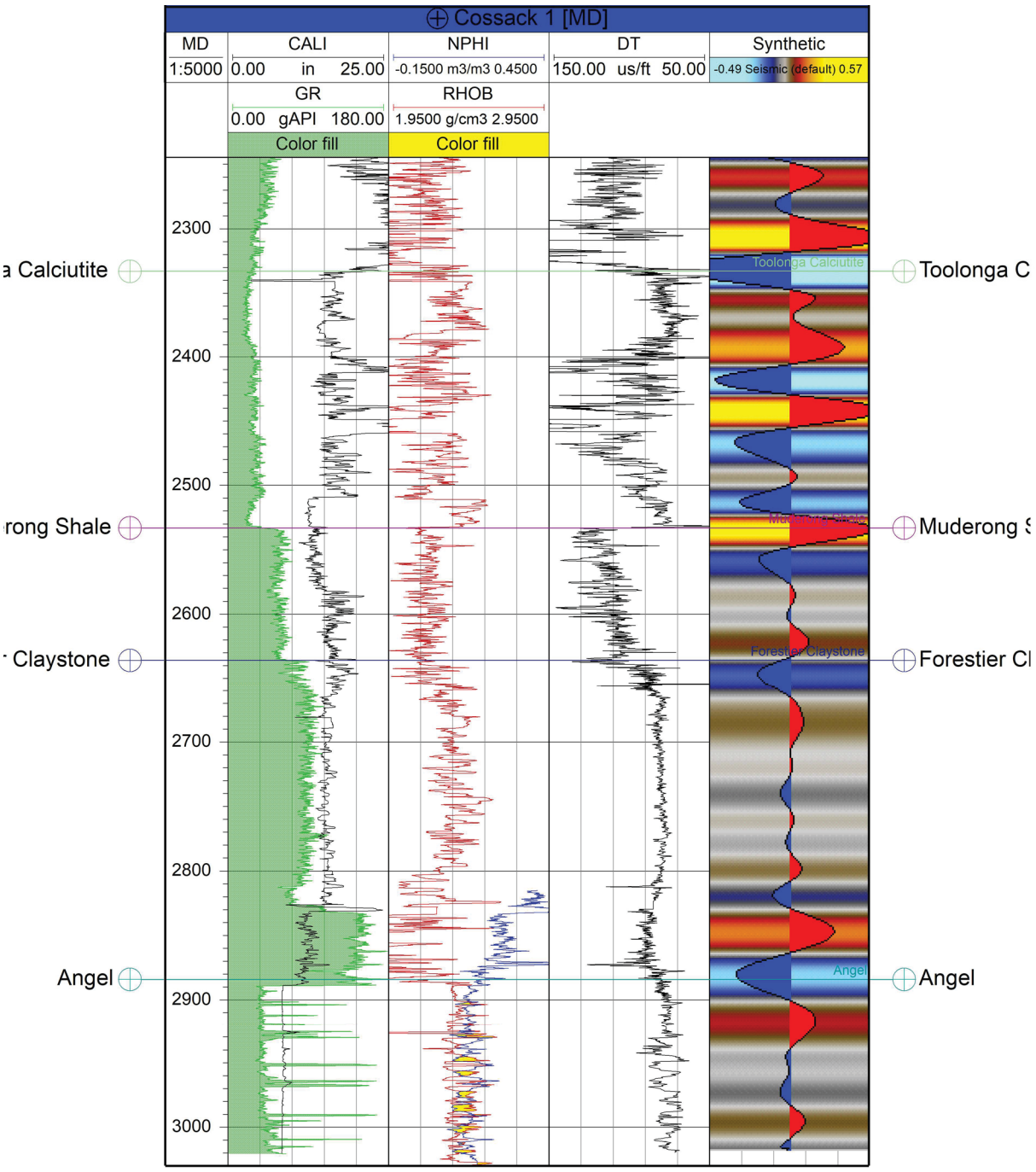
Top Dingo Fm./Base of Angel = H2

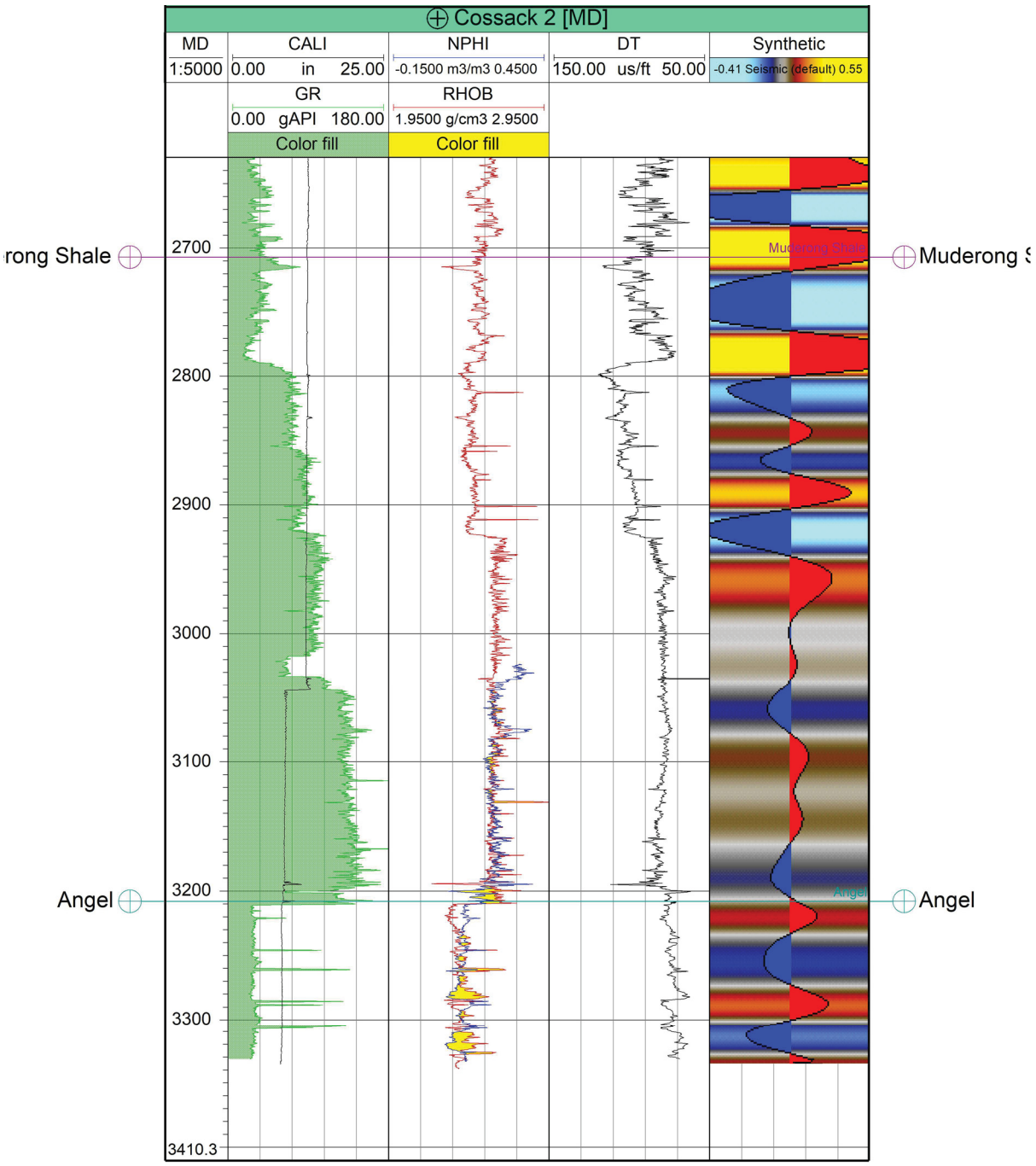
Top Angel Fm. = H3

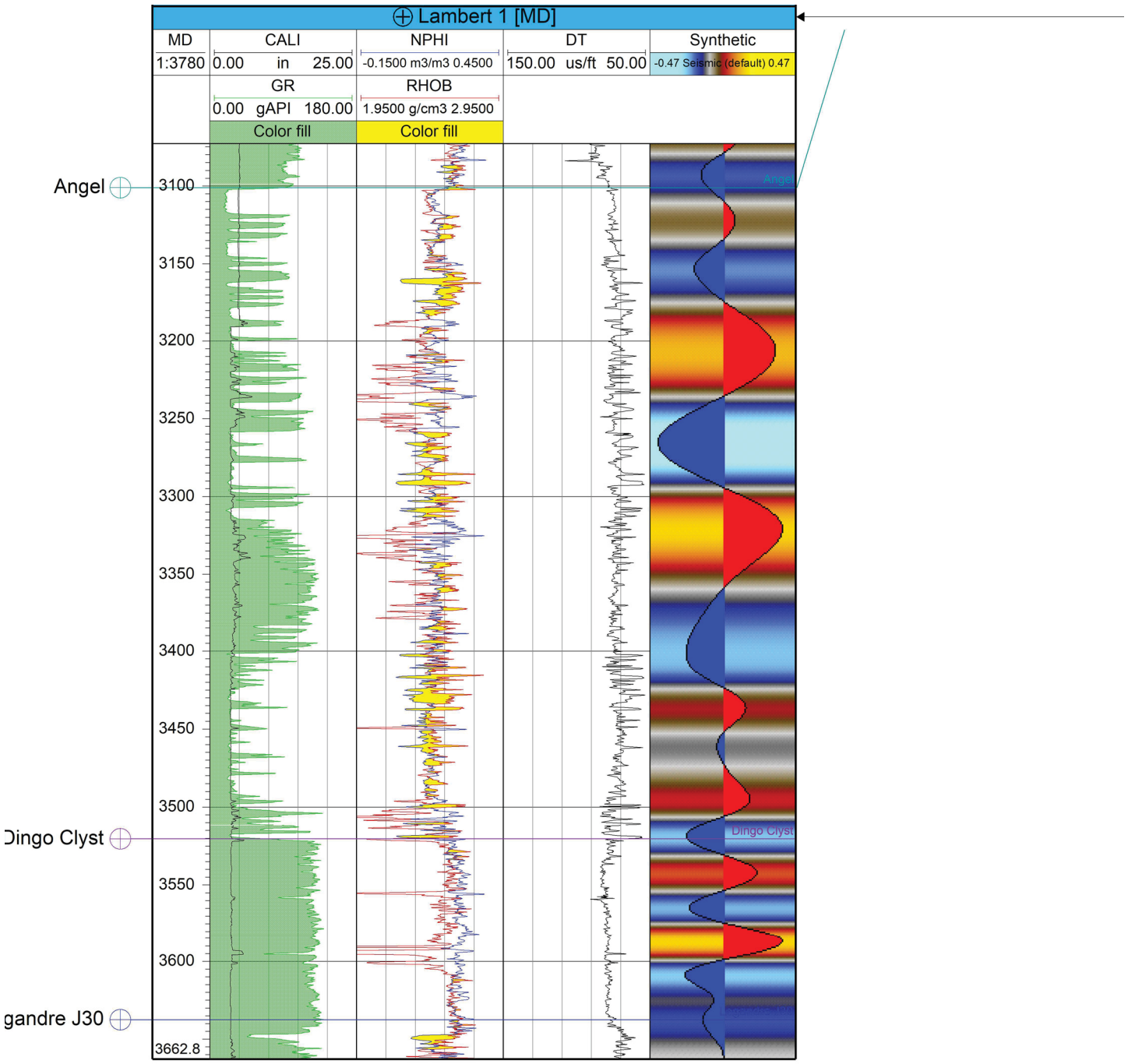
Top Forestier Claystone = H4

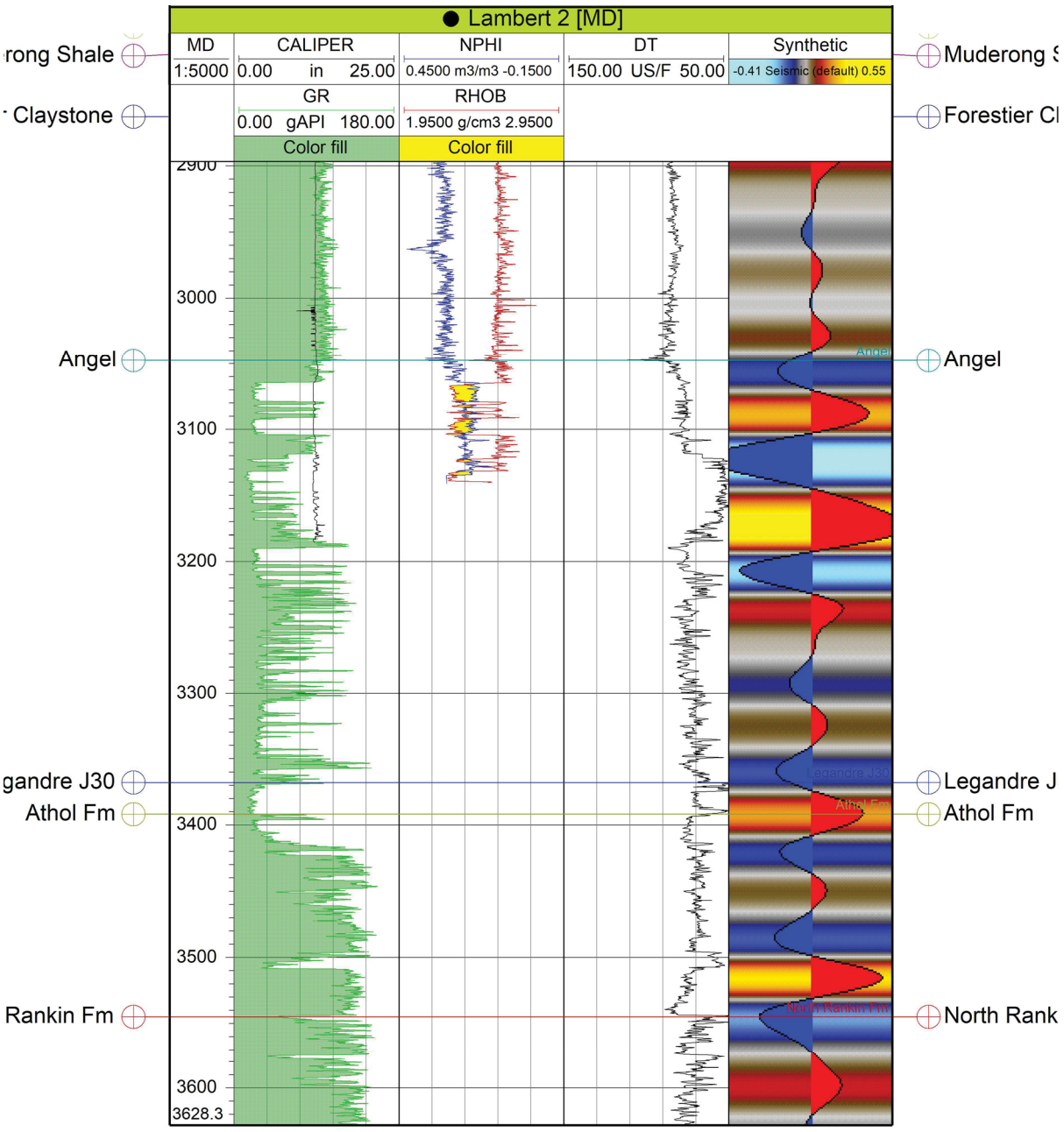
Top Muderong Shale = H5

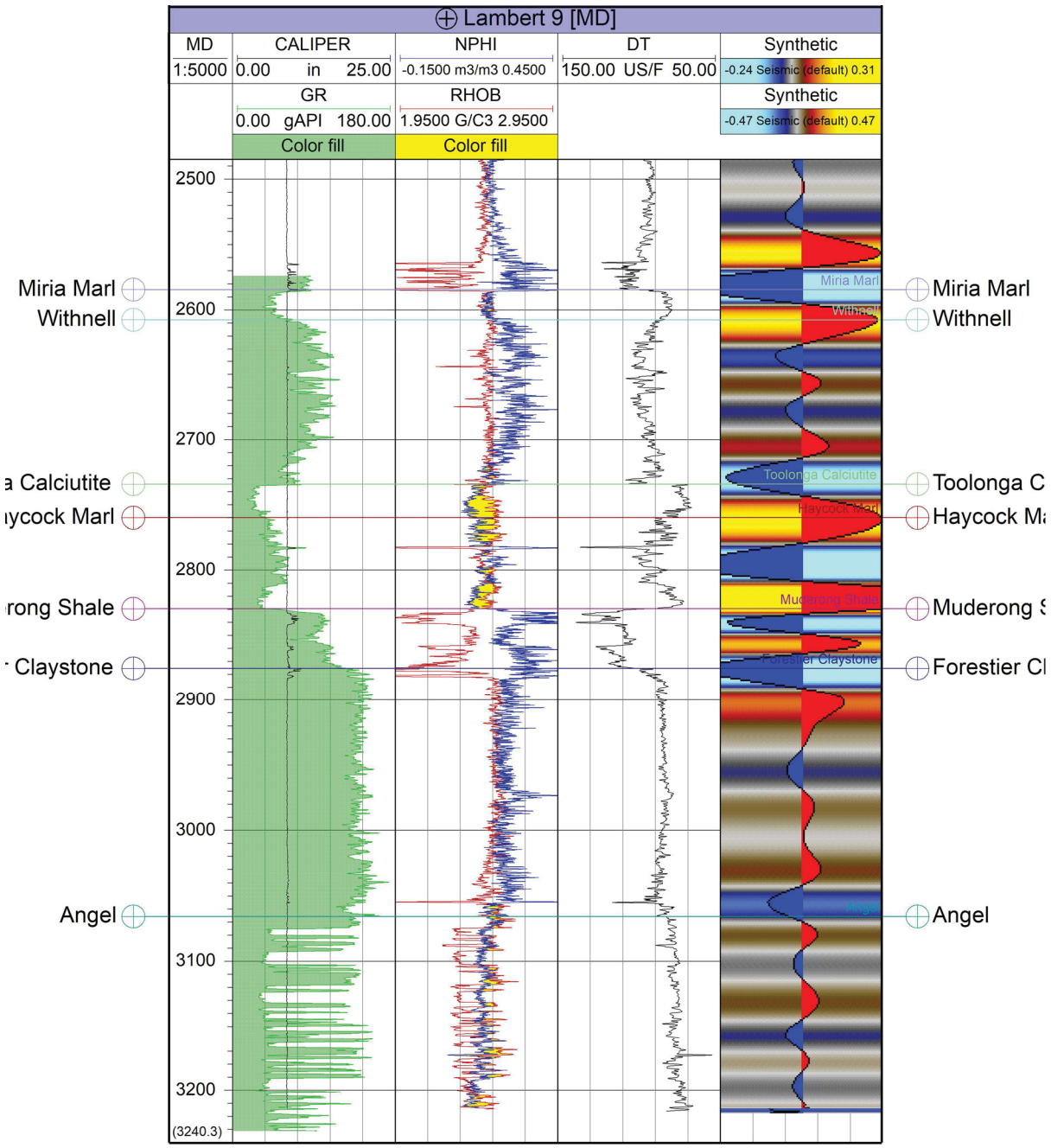

⊕ Angel 4 [MD]
MD
1:2000
CALI
0.00 in 25.00
GR
0.00 gAPI 180.00
Color fill
NPHI
0.4500 m3/m3 -0.1500
RHOB
1.9500 g/cm3 2.9500
Color fill
DT
150.00 US/F 50.00
Synthetic
-0.47 Seismic (default) 0.47
2550
2600
2650
2700
2750
2800

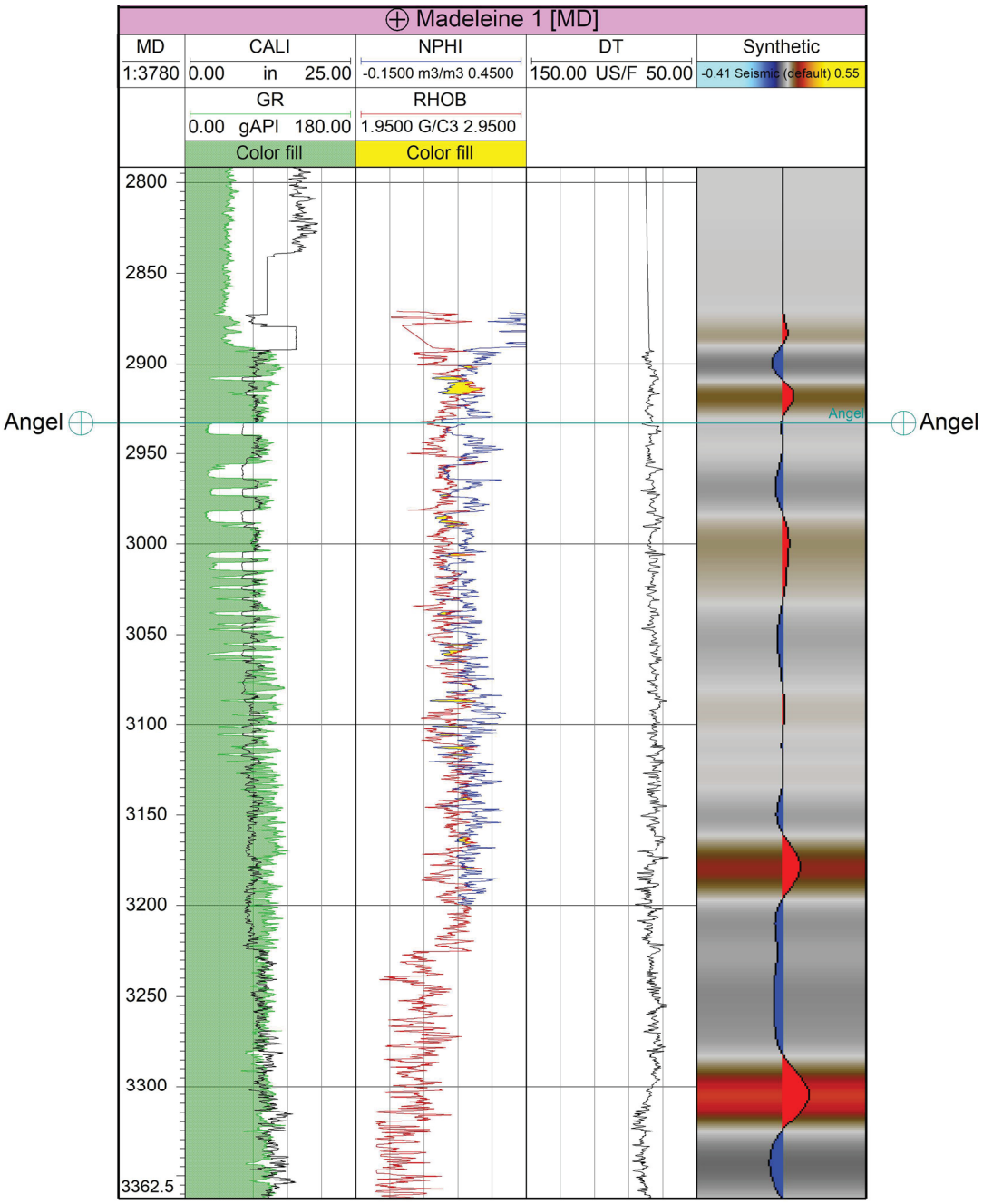

Cossack 1 [MD]
MD
1:5000
CALI
0.00 in 25.00
GR
0.00 gAPI 180.00
Color fill
NPHI
-0.1500 m3/m3 0.4500
RHOB
1.9500 g/cm3 2.9500
Color fill
DT
150.00 us/ft 50.00
Synthetic
-0.49 Seismic (default) 0.57
2300
2400
2500
2600
2700
2800
2900
3000
a Calciutite
rong Shale
Claystone
Angel
Toolonga Calciutite
Forestier Claystone
Angel
Toolonga C
Muderong S
Forestier Cl
Angel

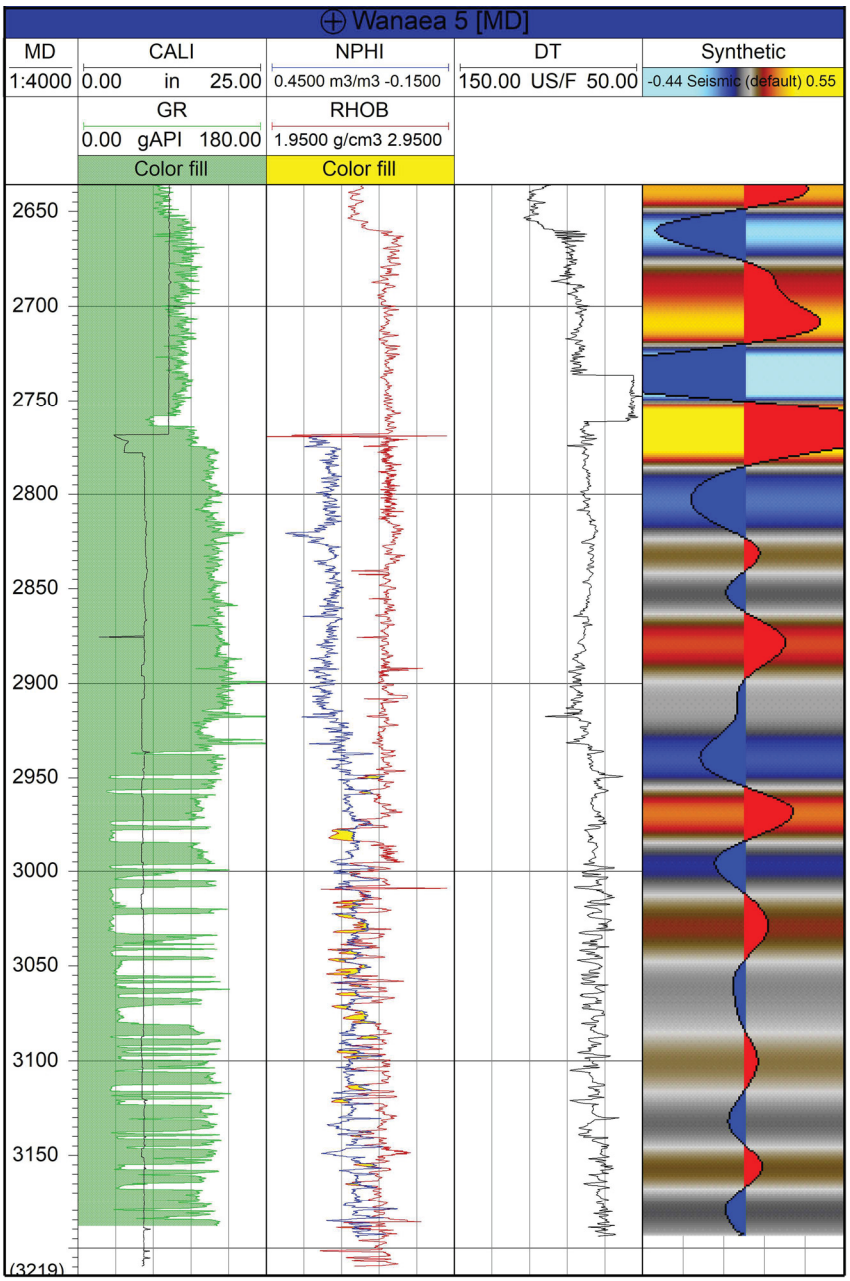

Cossack 2 [MD]
MD
1:5000
CALI
0.00 in 25.00
NPHI
-0.1500 m3/m3 0.4500
DT
150.00 us/ft 50.00
Synthetic
-0.41 Seismic (default) 0.55
GR
0.00 gAPI 180.00
RHOB
1.9500 g/cm3 2.9500
Color fill
Color fill
rong Shale
Muderong Shale
Muderong S
Angel
Angel
Angel
2700
2800
2900
3000
3100
3200
3300
3410.3


Lambert 1 [MD]
MD
1:3780
CALI
0.00 in 25.00
NPHI
-0.1500 m3/m3 0.4500
DT
150.00 us/ft 50.00
Synthetic
-0.47 Seismic (default) 0.47
GR
0.00 gAPI 180.00
RHOB
1.9500 g/cm3 2.9500
Color fill
Color fill
Angel
Dingo Clyst
gandre J30
3100
3150
3200
3250
3300
3350
3400
3450
3500
3550
3600
3662.8


Lambert 2 [MD]
MD
1:5000
CALIPER
0.00 in 25.00
GR
0.00 gAPI 180.00
Color fill
NPHI
0.4500 m3/m3 -0.1500
RHOB
1.9500 g/cm3 2.9500
Color fill
DT
150.00 US/F 50.00
Synthetic
-0.41 Seismic (default) 0.55
2900
3000
3100
3200
3300
3400
3500
3600
3628.3
rong Shale
Claystone
Angel
gandre J30
Athol Fm
Rankin Fm
Muderong S
Forestier Cl
Angel
Legandre J
Athol Fm
North Rank

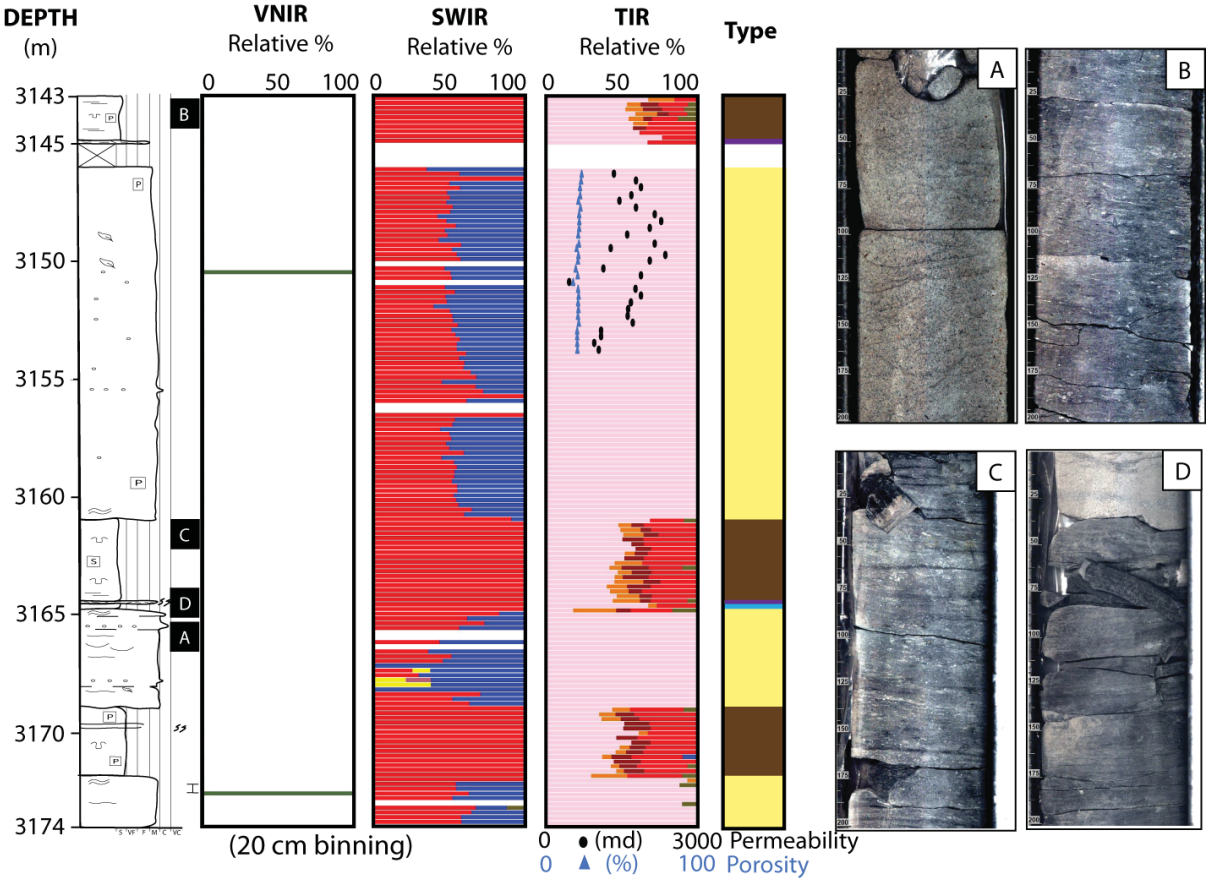

Lambert 9 [MD]
MD
1:5000
CALIPER
0.00 in 25.00
GR
0.00 gAPI 180.00
Color fill
NPHI
-0.1500 m3/m3 0.4500
RHOB
1.9500 G/C3 2.9500
Color fill
DT
150.00 US/F 50.00
Synthetic
-0.24 Seismic (default) 0.31
Synthetic
-0.47 Seismic (default) 0.47
2500
2600
2700
2800
2900
3000
3100
3200
(3240.3)
Miria Marl
Withnell
a Calciutite
ıycock Marl
rong Shale
· Claystone
Angel
Miria Marl
Withnell
Toolonga Calciutite
Haycock Marl
Muderong Shale
Forestier Claystone
Angel
Miria Marl
Withnell
Toolonga C
Haycock Ma
Muderong S
Forestier Cl
Angel


Madeleine 1 [MD]
MD
1:3780
CALI
0.00 in 25.00
NPHI
-0.1500 m3/m3 0.4500
DT
150.00 US/F 50.00
Synthetic
-0.41 Seismic (default) 0.55
GR
0.00 gAPI 180.00
RHOB
1.9500 G/C3 2.9500
Color fill
Color fill
2800
2850
2900
2950
3000
3050
3100
3150
3200
3250
3300
3362.5
Angel
Angel
Angel


⊕ Wanaea 5 [MD]
MD
1:4000
CALI
0.00 in 25.00
GR
0.00 gAPI 180.00
Color fill
NPHI
0.4500 m3/m3 -0.1500
RHOB
1.9500 g/cm3 2.9500
Color fill
DT
150.00 US/F 50.00
Synthetic
-0.44 Seismic (default) 0.55
2650
2700
2750
2800
2850
2900
2950
3000
3050
3100
3150
(3219)

8.3 Appendix 3: Spectral reflectance results

Mutineer-3 results



Key

- Granular quartz grains
- Bioturbation
- Mud clasts, rounded and sheared
- Carbonaceous material
- Glauconite fracture
- Injectite
- Wavy lamination
- Planar lamination
- Dewatering dish structures
- P Pyrite cement

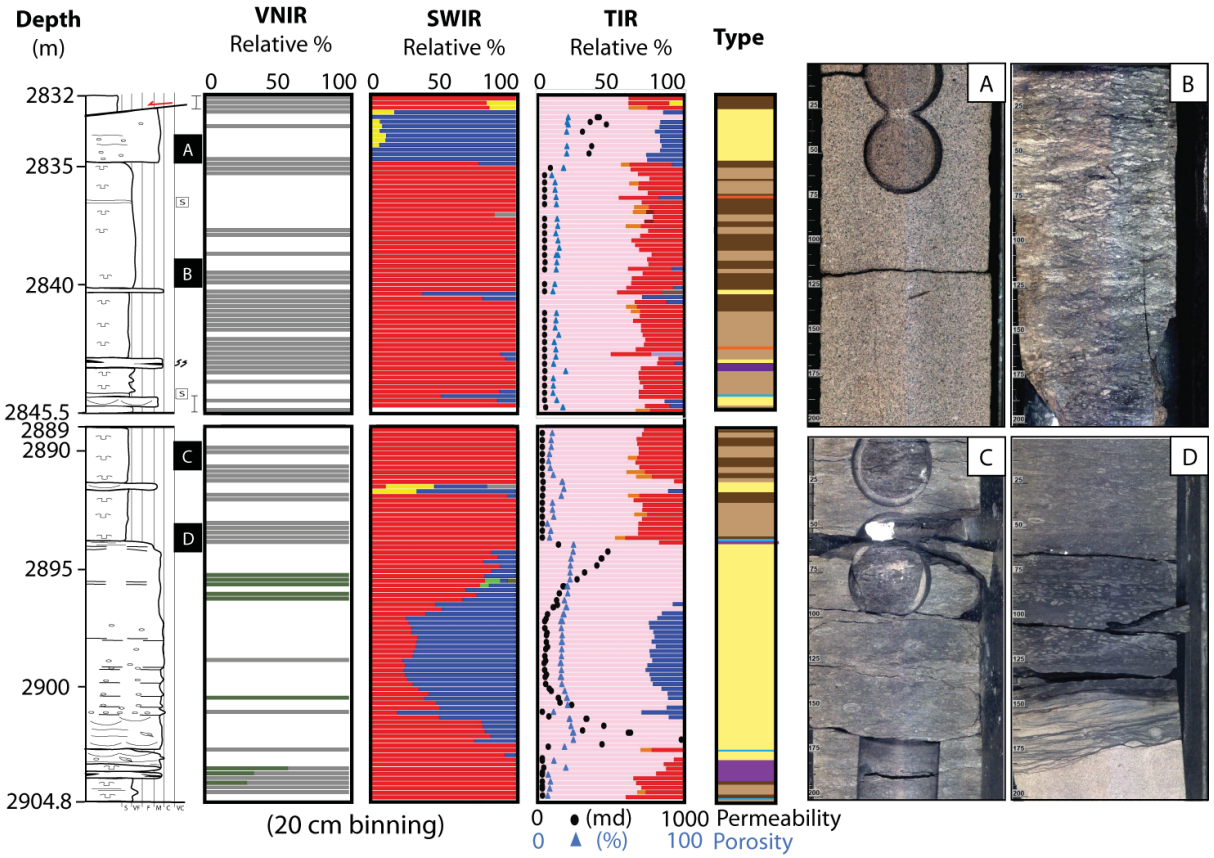
Mineral Group

- Sulphide
- Kaolin
- Carbonate
- White Mica
- Sulphate
- Silica
- K-Feldspar
- Plagioclase

Type

- Type 1
- Type 2A
- Type 2B
- Type 3
- Type 4
- Type 5

Wanaea-1 results



8.4 Appendix 4: Comparison of normalized thin section and XRF data to HyLogger data.

Normalised control data — **Anything <5% wont be detected by hylogger**

Mutineer 1B

WCR_Interpretive_Part_1_of_2_1000327772

Thin section analysis — QFR Compositions

Depth	Quartz	Chert	K-Feldspar	Plagioclase	Igneous Rock Fragm	Metamorphic Rock	Sedimentary Rock	Mica	Heavy min	Opaques	Ankerite	Phosphate	Glauconite	Clay	Quartz +Chr	Feldspar	Rock fragm	Quartz total %
3121.90	83.8%	0.3%	1.7%	0%	0%	0.3%	0.3%	0%	0%	7.1%	0%	0%	4.6%	1.7%	97.2	2	0.8	83.8%
3123.70	87.3%	2.7%	2.7%	0%	0.4%	0%	0.4%	0.4%	0%	1.8%	0%	0%	3.9%	0.6%	96.3	2.9	0.8	87.3%
3126.40	83.4%	1.8%	2.9%	0%	0.4%	0%	0.4%	0%	0%	1.4%	0%	0%	6.7%	3.2%	95.9	3.3	0.8	83.4%
3129.70	90.8%	0.4%	1.8%	0.4%	0%	0%	0%	0%	0%	1.2%	0%	0%	4.9%	0.6%	97.7	2.3	0	90.8%
3136.80	92.6%	0.6%	2.0%	0%	0%	0%	0%	0%	0%	1.2%	0.4%	0%	2.0%	1.2%	97.9	2.1	0	92.6%
3140.70	83.9%	1.7%	2.5%	0%	0%	0%	0%	0%	0%	8.7%	0%	0%	2.3%	0.9%	97.1	2.9	0	83.9%
3147.30	92.7%	0.8%	1.7%	0%	0.3%	0%	0.3%	0%	0%	0.8%	0%	0.3%	1.7%	1.2%	97.5	1.8	0.7	92.7%

WA-191-P The Angel Studies. Distribution, Stratigraphy and reservoir Quality Volume 3

Thin section analysis — Reservoir quality and distribution of the Late Jurassic sands, Dampier sub-basins, Western Australia, Matthew K. Dubsky BSc Thesis, University of Adelaide

Depth	Quartz	Feldspar	Rock Frag	Mica	Glauconv	Quartz	Dolomite	Cement Pyrite	Illite	Kaolin	Quartz total %
3130.90	85.6%	Tr	1.1%	Tr	5.6%	4.4%	0%	2.2%	1.1%	Tr	90.0%
3133.20	86.6%	1.1%	Tr	Tr	6.4%	4.3%	0%	1.6%	Tr	0%	90.9%
3138.90	83.3%	1.1%	Tr	Tr	5.6%	5.6%	0%	2.2%	2.2%	Tr	88.9%
3140.05	88.1%	1.2%	Tr	Tr	3.6%	6.0%	0%	1.2%	Tr	Tr	94.0%
3142.75	89.2%	1.2%	Tr	Tr	3.6%	6.0%	0%	Tr	Tr	Tr	95.2%
3147.88	88.9%	1.2%	Tr	Tr	2.5%	6.2%	0%	1.2%	Tr	Tr	95.1%

pXRD (Portable) — GSWA pXRD Analysis - Drillhole: Mutineer 1B. Wawryk & Hancock, 2017

Depth	Quartz	Kaolinite	Microdine	Muscovite	Unidentified clays
3135.88	Major	Minor	Minor	Tr	Tr
3134.30	Major		Minor	Tr	Tr

Major =>30%
Minor 5-30%
Tr = <5%

Mutineer 3 — Interpreted data report ENO22374_Mutineer3_Report — Accessory Incl. Zircon, Tourmaline Sphene , Monazite, Opaques

Thin section analysis

Depth	Quartz	Feldspar		Lithics	Mica		Accessor	Matrix		Authigenic Minerals				Quartz total %
	Quartz	K-feldspar	plagioclase	quartzite	other	muscovite	biotite	y	Glauconv	CO3	Quartz ov	Barite	Illite	Chlorite	Kaolin	Pyrite	
3146.10	85.0%	2.4%	0.5%	0.5%	1.5%	0.0%	0.0%	0.2%	0.0%	4.6%	1.0%	2.4%	0.2%	0.2%	0.0%	0.7%	87.4%
3147.90	84.7%	3.1%	0.5%	0.2%	1.7%	0.0%	0.0%	0.2%	0.0%	3.3%	2.6%	2.6%	0.0%	0.2%	0.0%	0.7%	87.3%
3148.50	85.1%	1.2%	0.2%	1.2%	2.1%	0.2%	0.0%	0.2%	0.0%	4.4%	0.5%	1.9%	0.0%	0.2%	0.0%	0.7%	86.9%
3150.60	85.3%	3.1%	0.0%	0.2%	1.4%	0.2%	0.0%	0.7%	0.0%	3.8%	0.7%	3.1%	0.0%	0.2%	0.0%	0.5%	88.5%
3150.90	74.7%	2.4%	0.0%	0.0%	2.6%	0.2%	0.0%	0.4%	0.0%	4.4%	0.7%	2.4%	0.0%	0.2%	0.0%	0.2%	77.1%
3152.70	84.0%	3.0%	0.2%	0.0%	2.3%	0.2%	0.0%	0.5%	0.0%	4.2%	1.2%	2.6%	0.0%	0.7%	0.0%	0.5%	86.5%
3153.05	85.4%	2.1%	0.2%	0.2%	2.4%	0.0%	0.2%	0.7%	0.0%	4.0%	0.7%	2.6%	0.0%	0.5%	0.0%	0.5%	88.0%
3153.30	84.7%	3.2%	0.5%	0.2%	3.2%	0.2%	0.0%	0.5%	0.0%	2.5%	0.7%	2.1%	0.0%	0.7%	0.0%	0.5%	86.8%
3153.60	81.5%	2.7%	0.5%	0.5%	2.5%	0.0%	0.2%	0.9%	0.0%	6.2%	0.9%	3.0%	0.0%	0.2%	0.0%	0.2%	84.4%
3153.90	84.5%	1.4%	0.2%	0.2%	2.8%	0.2%	0.2%	0.5%	0.0%	4.6%	0.7%	2.8%	0.0%	0.5%	0.0%	0.5%	87.2%
3156.30	76.8%	3.0%	0.2%	0.2%	1.1%	0.0%	0.0%	0.5%	0.0%	4.8%	0.7%	2.1%	0.2%	0.2%	0.0%	0.2%	78.9%
3156.90	75.2%	2.8%	0.2%	0.2%	2.1%	0.2%	0.2%	0.2%	0.0%	5.0%	1.4%	5.0%	0.0%	0.2%	0.2%	0.2%	80.1%
3158.70	82.1%	2.2%	0.4%	0.2%	2.0%	0.2%	0.2%	0.9%	0.0%	5.1%	0.2%	2.2%	0.2%	0.2%	0.2%	0.4%	84.4%
3160.50	82.9%	2.6%	0.0%	0.5%	2.1%	0.2%	0.0%	0.9%	0.0%	4.9%	0.9%	3.3%	0.2%	0.2%	0.0%	0.2%	86.2%
3165.80	78.5%	2.6%	0.0%	0.2%	4.1%	0.2%	0.2%	1.4%	0.0%	7.2%	0.2%	3.3%	0.2%	0.2%	0.0%	0.5%	81.9%
3166.70	70.4%	4.0%	0.9%	0.5%	4.0%	0.2%	0.2%	1.2%	0.9%	11.4%	0.2%	4.3%	0.2%	0.2%	0.0%	0.2%	74.6%
3168.50	76.1%	2.6%	0.5%	0.2%	3.0%	0.2%	0.2%	1.4%	0.0%	8.4%	0.0%	4.6%	0.2%	0.2%	0.0%	0.2%	80.7%

XRD — Peak Area Calculation

Depth	Quartz	Feldspar	Kaolin	Dolomite	Pyrite
3147.88	96.7%	0.9%	0.4%	1.0%	

Wanaea 1 — W34324 6V2

Depth	Quartz	Feldspar	Lithics	Framework Glauconite	Mica	Heavy Minerals	Matrix total	Matrix Carbonate	Phyllosilic	Opaques	Quartz total %
2833.60	75%	5%	2%	4%	<1	<1	11%	3%		0%	75.0%
2841.40	35%	5%	0%	7%		1%	1%	50%	?	46%	4%	35.4%
2843.20	78%	7%	1%	5%			100%	8%	?			77.6%
2891.50	75%	6%	1%	3%			100%	14%	?			74.7%
2897.80	74%	7%	2%	5%		<1		12%	?			74.0%

Hylogger Data															Hylogger interpretation	Difference between TIR and Control			
	VNIR		SWIR				TIR												
Depth	Min1	Min 1 Wt%	Min 1	WT%1	Min 2	WT%2	Min1	Wt%1	Min2	Wt%2	Min3	Wt%3			Type	Quartz	Feldspar	Glauconite	
3121.90							Quartz	100%							1	16%	-1.7%	-4.6%	
3123.70	Pyrite	100%					Quartz	100%							1	13%	-2.7%	-3.9%	
3126.40							Quartz	100%							1	17%	-2.9%	-6.7%	
3129.70							Quartz	100%							1	9%	-1.8%	-4.9%	
3136.80	Pyrite	100%					Quartz	100%							1	7%	-2.0%	-2.0%	
3140.70							Quartz	100%							1	16%	-2.5%	-2.3%	
3147.30							Quartz	100%							1	7%	-1.7%	-1.7%	
	VNIR		SWIR				TIR												
Depth	Min1	Min 1 Wt%	Min 1	WT%1	Min 2	WT%2	Min1	Wt%1	Min2	Wt%2	Min3	Wt%3			Type	Quartz	Feldspar	Glauconite	
3130.90							Quartz	100%							1	10.0%	-1.1%	-5.6%	
3133.20							Quartz	100%							1	9.1%		-6.4%	
3138.90			Kaolinite-WX	100%			Quartz	100%							1	11.1%		-5.6%	
3140.05			Kaolinite-WX	100%			Quartz	100%							1	6.0%		-3.6%	
3142.75							Quartz	100%							1	4.8%		-3.6%	
3147.88							Quartz	100%							1	4.9%		-2.5%	
	VNIR		SWIR1				TIR												
Depth	Min1	Min 1 Wt%	Min 1	WT%1	Min 2	WT%2	Min1	Wt%1	Min2	Wt%2	Min3	Wt%3			Type	Quartz			
3135.88			Kaolinite-WX	100%			Quartz	53%	Kaolinite-WX	29%	Orthoclase	18%			3				
3134.3							Quartz	100%							1				
	VNIR		SWIR				TIR												
Depth	Min1	Min 1 Wt%	Min 1	WT%1	Min 2	WT%2	Min1	Wt%1	Min2	Wt%2	Min3	Wt%3			Type	Quartz	Feldspar	Glauconite	
3146.10							Quartz	100%							1	12.6%	-2.9%	-4.6%	
3147.90			Ankerite	51%	Kaolinite-WX	49%	Quartz	100%							1	12.7%	-3.5%	-3.3%	
3148.50			Ankerite	53%	Kaolinite-WX	47%	Quartz	100%							1	13.1%	-1.4%	-4.4%	
3150.60			Ankerite	50%	Kaolinite-WX	50%	Quartz	100%					Plug missing nearest result		1	11.5%	-3.1%	-3.8%	
3150.90							Quartz	100%					Plug missing nearest result		1	22.9%	-2.4%	-4.4%	
3152.70			Ankerite	52%	Kaolinite-WX	48%	Quartz	100%					Plug missing nearest result		1	13.5%	-3.2%	-4.2%	
3153.05			Kaolinite-WX	57%	Ankerite	43%	Quartz	100%					Plug missing nearest result		1	12.0%	-2.4%	-4.0%	
3153.30			Kaolinite-WX	50%	Ankerite	50%	Quartz	100%					Plug missing nearest result		1	13.2%	-3.7%	-2.5%	
3153.60			Kaolinite-WX	58%	Ankerite	42%	Quartz	100%					Plug missing nearest result		1	15.6%	-3.2%	-6.2%	
3153.90			Kaolinite-WX	56%	Ankerite	44%	Quartz	100%					Plug missing nearest result		1	12.8%	-1.6%	-4.6%	
3156.30							Quartz	100%					Plug missing nearest result		1	21.1%	-3.2%	-4.8%	
3156.90			Ankerite	59%	Dickite	41%	Quartz	100%					Plug missing nearest result		1	19.9%	-3.1%	-5.0%	
3158.70			Kaolinite-WX	100%			Quartz	100%					Plug missing nearest result		1	15.6%	-2.7%	-5.1%	
3160.50			Kaolinite-WX	100%			Quartz	100%					Plug missing nearest result		1	13.8%	-2.6%	-4.9%	
3165.80							Quartz	100%							1	18.1%	-2.6%	-7.2%	
3166.70							Quartz	100%					Plug missing nearest result		1	25.4%	-5.0%	-11.4%	
3168.50			Siderite	62%	Kaolinite-WX	38%	Quartz	100%					Plug missing nearest result		1	19.3%	-3.0%	-8.4%	
	VNIR		SWIR				TIR												
Depth	Min1	Min 1 Wt%	Min 1	WT%1	Min 2	WT%2	Min1	Wt%1	Min2	Wt%2	Min3	Wt%3			Type	Quartz	Feldspar		
3147.88			Ankerite	51%	Kaolinite-WX	49%	Quartz	100%					Plug missing nearest result		1	3.3%	-0.9%		
	VNIR		SWIR				TIR												
Depth	Min1	Min 1 Wt%	Min 1	WT%1	Min 2	WT%2	Min1	Wt%1	Min2	Wt%2	Min3	Wt%3			Type	Quartz	Carbonate	Kaolinite	Feldspar	Glauconit
2833.6			Ankerite	70%	Tourmaline-Fe	30%	Quartz	81%	Calcite	14%	Siderite	5%			1	6.0%	3.0%		-5.0%	-4.0%
2841.4			Kaolinite-WX	100%			Quartz	63%	Albite	19%	Kaolinite-WX	18%			3	27.6%		-26.8%	-5.2%	-7.3%
2843.2			Ankerite	50%	Kaolinite-WX	50%	Quartz	91%	Calcite	7%	Siderite	2%			1	13.4%	?		-7.1%	-5.1%
2891.5			Siderite	59%	Muscovite	41%	Quartz	90%	Calcite	10%					1	15.3%	?		-6.1%	-3.0%
2897.8			Ankerite	63%	Kaolinite-WX	37%	Quartz	77%	Calcite	17%	Siderite	6%			1	3.0%	?		-7.0%	-5.0%

8.5 Appendix 5: Agat Core logs


36/7-4
35/7-4
2437
2440
2445
2450
2455
2460
2465
2470
2475
2480
2485
2490
2495
2500
2505
2510
2515
2520
2525
2530
2535
2540
2545
2550
2554.6 m
2695
2700
2705
2710
2715
2720
2725
2730
2730.8
Key
Granular clasts; Chlorite (gr), Siderite/phosphate (or), Bioclast (wh)
Mud clasts
Armoured mudclasts
Cross lamination
Ripple lamination
Mud-draped climbing ripples
Convolute laminations
Sand injectite
Small scale faults